Fibre-Sized Energy Generation in Multi-Functional Fabrics

A thesis submitted in fulfilment of the requirements for the degree of Doctor of Philosophy

Sania Waqar

B.Sc. Textile Engineering

(National Textile University, Pakistan)

M.Sc. Advanced Materials

(University of Bolton, United Kingdom)

School of Engineering

College of Science Engineering and Health

RMIT University

March 2018

To my parents, who mean the world to me

Declaration

I certify that except where due acknowledgement has been made, the work is that of the author alone; the work has not been submitted previously, in whole or in part, to qualify for any other academic award; the content of the thesis is the result of work which has been carried out since the official commencement date of the approved research program; any editorial work, paid or unpaid, carried out by a third party is acknowledged; and, ethics procedures and guidelines have been followed. I acknowledge the support I have received for my research through the provision of an Australian Government Research Training Program Scholarship.

Sania Waqar

March 2018

Acknowledgements

All praise be to God almighty, who has given me the strength to carry out my work.

I am greatly indebted to Professor Sabu John for his unwavering support, patience, and his diligent mentorship throughout the PhD. His wisdom, knowledge and commitment to highest standards inspired and motivated me. I would also like to extend my gratitude to Associate Professor Lijing Wang who guided me. I am equally grateful to Professor Chun Wang, who left before the completion of project, for his deep insights on especially challenging questions that kept me curious.

The project would not have been possible without the financial funding from Australian Research council ARC and Dr Floreana Coman, of FCST Pty. Ltd who have supported this project under the ARC Linkage Projects scheme - Grant number LP110100455.

I owe a deep sense of gratitude to Dr. Jesse McCarthy for his guidance throughout the thesis and his assistance in simulation work which would not have been possible without his help.

I would also like to thank Hue James for his insights in to intricate electrical measurement at School of Engineering and Martin Gregory at School of Textiles for their technical support in completion of various parts of this thesis.

I would like to admit that I will not be here without the unconditional guidance and support of Dr. Zafar Javed, my teacher, and mentor who has helped me even at the lowest times.

I owe a debt of gratitude to my husband, Imtiaz, who stood by me through thick and thin. I am lucky to have met him and I thank him for his friendship, love, and unyielding support.

And finally, I must thank my parents for believing in me, when the world stood against me. Thank you, Mama and Daddy.

Last, but not the least, is the recognition of support given by my friends and family worldwide.

Sania

Abstract

There is an increasing demand for powering on-person-devices (for communications, health-care purposes and soldier protection) without the burden of the parasitic weight and toxicity of conventional batteries. This demand calls for an alternative power source from minuscule piezoelectric generators. Miniature electronic devices can be powered with such generators for integration in an apparel structure. Earlier studies have shown that these kinds of devices could help power ultra-low energy devices. There are however several research questions that need to be addressed in this research area, related to the optimization of these piezoelectric generators.

The overall aim of this research is to answer some of the scientific impediments currently associated with generating energy in fabrics. This study investigates the prospects of manufacturing Piezo-fabrics with embedded piezoelectric yarns that have the potential to convert the human movement-induced mechanical strain on the fabric into electrical energy. An attempt has been made to answer several issues through simulation and experimental work related to wearable piezoelectric energy generators such as the effect of varying area, aspect ratio and loading magnitude at different frequencies on voltage, current and power output of a piezoelectric strip. Also investigated are the optimum poling conditions to manufacture high (β) beta-content melt spun piezoelectric yarns while using varying parameters such as the draw ratio, poling voltage, electric field intensity and poling assembly design. The impact of fabric architecture on electrical power output and the translation of simulated work into real electrical outputs through the experimental validation of the piezoelectric yarns was also investigated.

The piezoelectric material used in this investigation was polyvinylidene fluoride (PVDF), which has the highest dielectric constant amongst flexible materials. This research consists of two parts related to simulation and experimental work. A dual mode finite element parametric analysis was conducted in ANSYS with varying areas and frequencies of a PVDF patch incorporated on polyester fabric to examine the electric power output response. The effect of varying poling assembly design, and electric field strength on the melt spun PVDF yarns for electric output was examined in ANSYS by using two poling designs to pole monofilaments in the d_{33} mode. A representative volume element of spacer fabrics was evaluated in ANSYS to obtain electrical outputs at a low frequency range of 0-2Hz. The direction of poling was found to have a significant effect on the power output in the d_{33} mode. The fabric design was altered to create more a stable cross-linked spacer fabric which resulted in increased electrical output due to increased energy absorption at higher stress levels. The drawing of the PVDF filament was done at various settings, including: draw ratio, temperatures, and poling setups. The drawing phase was found to be extremely critical in achieving a high β-content output and was found to achieve an optimal β-output fraction of 0.77 at a temperature of 80°C with a draw ratio of 5:1. The results from the dual field simulations were used to develop a high dielectric PVDF monofilament using the novel poling assembly designed. The fibres were further investigated to determine the electrical output using the four-point bend test and compression tests. They were found to produce a maximum output of 1.88V at a frequency of 2Hz with a mean power output of 0.23 μW.

Table of Contents

List of Figures xii
List of Tables xvi
1 Introduction 1
  1.1 Research background 1
  1.2 Research aim and objectives 2
  1.3 Research methodology 2
  1.4 Thesis overview 4
  1.5 List of publications 4
    1.5.1 Book chapter 4
    1.5.2 Conference proceedings 5
2 Literature review 6
  2.1 Fuel source classification for energy generation 6
  2.2 Global energy trend according to fuel type 6
  2.3 Energy harvesting methods 8
    2.3.1 Mechanical energy harvesting 8
      2.3.1.1 Piezoelectric effect 8
      2.3.1.2 Triboelectric effect 9
      2.3.1.3 Electromagnetic energy harvesting 9
    2.3.2 Thermal energy harvesting 9
      2.3.2.1 Thermoelectric effect 9
      2.3.2.2 Pyroelectric effect 10
    2.3.3 Solar energy harvesting 10
  2.4 Energy through human motion 11
    2.4.1 Motions in the human body 12
    2.4.2 The human limbs 13
      2.4.2.1 Human elbow 14
      2.4.2.2 The knee 15
      2.4.2.3 Foot motion (heel strike) 15
    2.4.3 Optimisation of location of energy generator 15
  2.5 Parts of energy harvesting device 16
    2.5.1 Energy harvesting materials 16

2.5.2 Electrode materials 16
2.5.2.1 Metallic coated yarns 16
2.5.2.2 Metal yarns 17
2.5.2.3 Nanoyarns/carbon nanotubes (CNT) yarns 18
2.5.3 Integrated storage and circuitry 18
2.6 Piezoelectric materials 19
2.6.1 History of piezoelectricity 20
2.6.2 Basic principles of piezoelectricity 21
2.6.2.1 Charge formation and poling 21
2.6.2.2 Direct and converse effects 22
2.6.2.3 Piezoelectric nodes 23
2.7 Mechanical energy conversion 24
2.7.1 General theory 25
2.8 Different piezoelectric materials 26
2.8.1 Piezo ceramics 26
2.8.1.1 Lead zirconate titanate (PZT) 27
2.8.1.2 Barium titanate ($BaTiO_3$) 27
2.8.1.3 Lead titanate ($PbTiO_3$) 28
2.8.2 Piezopolymers 28
2.8.2.1 Polyvinylidene fluoride (PVDF) 28
2.8.3 Piezocomposites 31
2.8.3.1 Nanowires 31
2.8.3.2 Carbon nanotubes 32
2.8.3.3 Copolymers 33
2.9 Manufacturing piezo textiles 33
2.9.1 Piezo fibres manufacturing 33
2.9.1.1 Wrapping/twisting 34
2.9.1.2 Electrospinning 34
2.9.1.3 Meltspinning 35
2.9.2 Piezoceramic fibres 35
2.9.3 Piezopolymer fibres 36
2.9.4 Composite fibres 37
2.9.5 Piezo fabrics 38
2.9.5.1 Types of manufacturing techniques 39

2.10 Recent trends in energy harvesting 42
2.11 Flexible piezoelectric energy harvesting 44
2.11.1 Fabrics 44
2.12 Optimisation of fabrication for wearable energy harvesting 45
2.13 Testing of piezo fabrics for energy harvesting 49
2.14 Designing for comfort 50
2.15 Applications 50
2.15.1 Energy requirements 50
2.15.2 Feasibility of human powered wearable devices 51
2.15.3 Medical, military wireless uses 53
2.16 Challenges/gaps in Polyvinylidene fluoride energy harvesting 55
2.17 Future trends 55
2.18 Research gaps 56
3 Finite Element Simulations in textiles 58
3.1 Introduction 58
3.2 Piezo responses of fabric 60
3.3 Dual field analysis of poling design of Polyvinylidene fluoride fibres for energy harvesting applications 61
3.3.1 Model Setup: 62
3.3.2 Simulation Results: 63
3.3.3 Experimental Validation: 67
3.3.4 Characterization: 68
3.4 Simulation-based power output in fabrics 69
3.4.1 Harmonic analysis and piezo-response 70
3.4.1.1 Piezo-response 71
3.4.2 Electrical outputs and results 71
3.4.3 Mesh optimization study 71
3.5 Dual Field Finite Element Simulations of Piezo-Patches on Fabrics: parametric study 71
3.5.1 Model design 73
3.5.2 Meshing 75
3.5.3 Results of simulation 76
3.5.3.1 Harmonic Analysis 76
3.5.3.2 Effect of Increasing Area 77

3.5.3.3 Effect of Increasing Aspect Ratio 78
3.5.3.4 Effect of Increasing Input Loading Magnitude 79
3.5.3.5 Modal Analysis 80
3.6 Modelling and Analysis of Various Piezo Fibre Geometries on the Piezoelectric Properties for Energy Scavenging Applications 82
3.6.1 Theory 82
3.6.2 Meshing 84
3.6.3 RVE 85
3.6.4 Analysis and Results 86
3.6.4.1 Harmonic Analysis 86
3.6.4.2 Poling Direction 87
3.6.4.3 Linear Density 88
3.6.4.4 Effect of Inclination Angle 89
3.6.4.5 Distances between Electrodes 91
3.7 Modelling of cross-linked spacer fibres 91
3.7.1 Spacer fabric geometric model 92
3.7.2 Yarn inclination and crosslinking 93
3.7.3 Yarn thickness and cross-linking 94
3.8 Summary of Computational Findings 96
4 Yarn and Fabric Experimental Validation 97
4.1 Yarn production by Melt spinning 98
4.2 Poling Assembly design 99
4.2.1 Effect of voltage 100
4.2.2 Finding the optimal poling temperature 101
4.2.3 Draw ratio variations 101
4.3 Fabric Preparation 102
4.4 Morphological characterization 102
4.4.1 SEM 102
4.4.2 FTIR 103
4.4.3 XRD 105
4.5 Piezoelectric output characterization 106
4.5.1 Compression testing 107
4.5.2 4-point bending 108

4.5.3 Strain applied during testing ... 109
4.6 Electrical outputs and Mean power calculation for melt spun polyvinylidene fluoride yarns .. 110
4.7 Summary ... 111
5 Experimental Results and Discussion ... 113
5.1 Morphological characterisation of the polyvinylidene fluoride polymer ... 113
5.1.1 Effect of increasing plate distance on output ... 113
5.1.2 Effect of increasing hole diameter ... 116
5.1.3 Applied voltage ... 119
5.1.4 Effect of varying the drawing temperature ... 121
5.1.5 Effect of draw ratio ... 123
5.2 Testing of PVDF piezo outputs ... 125
5.2.1 Electrode distance ... 125
5.2.2 Effect of increasing electrode diameter ... 126
5.2.3 Applied voltage ... 127
5.3 Power outputs ... 127
5.4 Comparison between modelling and experimental values ... 132
5.5 Summary ... 134
6 Conclusions and Recommendations ... 136
6.1 Computational simulations – piezo strip and yarns ... 136
6.2 Computational simulations – poling configurations ... 137
6.3 Experimental electro-mechanical performance of the poled PVDF yarns ... 138
6.4 Summary ... 139
6.4.1 Real world applications ... 139
6.5 Recommendations for further work in this area ... 139
7 References ... 141
8 Appendix ... 157
8.1.2 Properties for piezoelectric material ... 157
8.1.3 Properties for polyamide ... 157
8.2 Electric field density ... 158
8.3 ANSYS ... 159
8.3.1 Dual field analysis of poling design of Polyvinylidene fluoride fibres for energy harvesting applications ... 159
8.3.2 Dual Field Finite Element Simulations of Piezo-Patches on Fabrics: parametric study ... 167

8.3.3 Modelling and Analysis of Various Piezo Fibre Geometries on the Piezoelectric Properties for Energy Scavenging Applications 175

8.3.4 Modelling of cross-linked spacer fibres 181

List of Figures

Figure 2.1 Global energy trend according to fuel type (Arab development portal: sourced from BP Statistical Review of World Energy 2016) 7
Figure 2.2: New global investment in renewable energy in 2015 (Amount in US $BN; UNEP Bloomberg New Energy Finance (McCrone et al. 2016)) 8
Figure 2.3: (a) Schematic drawing of a polymer-based organic solar cell on Indium Tin Oxide coated glass-based substrate; (b) drawing of a photovoltaic fibre based on the principle 11
Figure 2.4: The motions of human limbs and the forces acting on them in (a) standing, (b) walking, (c) running positions (Zatsiorsky 2002) 14
Figure 2.5: Scanning electron microscope image of the various type of conductive yarns with metallic coatings (Alagirusamy *et al.* 2013) 17
Figure 2.6: Figure 2.6: Scanning electron microscope images showing the making of yarns from CNT forest at (a) overall view, (b) CNT detachment, (c) convergence point, and (d) final yarn (Sears et al. 2010) 18
Figure 2.7: Relationship between ferroelectric, dielectric, piezoelectric, and pyroelectric materials (adapted from Kong *et al.* 2014) 19
Figure 2.8: Dipole reorientation on the application of an electric field 21
Figure 2.9: (a)–(e) The direct and converse piezoelectric effects, respectively (Moheimani & Fleming 2006) 23
Figure 2.10: Direction of forces in piezoelectric materials (adapted from Gusarov 2015) 24
Figure 2.11: Structure of a piezoelectric perovskite crystal, (a) before and (b) after polarisation (Moheimani & Fleming 2006) 27
Figure 2.12: Chain conformations in α, β, and γ phases of polyvinylidene fluoride (Martins *et al.* 2014) 29
Figure 2.13: Conversion of the various phases of polyvinylidene fluoride (adapted from Esterly 2002) .. 30
Figure 2.14: Transformation process from α-phase to β-phase of polyvinylidene fluoride by mechanical stretching (Li *et al.* 2014) 31
Figure 2.15: Fabrication process of the PVDF–ZnO hybrid nanogenerator (Li *et al.* 2014) 32
Figure 2.16: (a) Process of electrospinning, (b) scanning electron microscope image of electrospun polyvinylidene fluoride fibrous matt (adapted from Damaraju *et al.* 2013) 35
Figure 2.17: Schematic of a nanowire and its (a) coordinate system. (b) Longitudinal strain εz distribution in the nanowire, (c) longitudinal electric field distribution in the nanowire induced by the piezoelectric effect. (d) Potential distribution in the nanowire (Wang & Song 2006) 37
Figure 2.18: Various textile structures 39
Figure 2.19: Comparison of various fabrics (Li & Tao 2014) 41
Figure 2.20: Spacer fabric (a) showing optical image (b) structural side view (adapted from Yip & Ng 2008) 41
Figure 2.21: A schematic diagram of the device fabricated by Ahn *et al.* (2015) 42
Figure 3.1 showing the ANSYS model used for analysis 62
Figure 3.2 showing the poling setup with (a) hole configuration and with (b) slit configuration 63
Figure 3.3 (a) and (b) showing the comparison between the two plate thicknesses 64
Figure 3.4 Graph showing the relationship between the plate distance and hole diameter 64

Figure 3.5: (a) parallel plates with a hole diameter of 5 mm, the plate thickness of 3 mm and 3 mm apart. (b) same as (a) but with a distance of 10 mm 65
Figure 3.6 (a) parallel plates with a hole diameter of 10 mm, the plate thickness of 3 mm and 3 mm apart. (b) same as (a) but with a distance of 10 mm. 66
Figure 3.7 showing the setup used to extrude and pole polyvinylidene fluoride 67
Figure 3.8 showing the temperature of polyvinylidene fluoride filament at poling setup (Image taken using a thermal camera) 68
Figure 3.9 Graph showing the effect of increasing the plate distance on the β-content of PVDF monofilament 68
Figure 3.10: β-phase fraction obtained by varying the hole diameter in poling setup using a hole configuration. 69
Figure 3.11: Schematic diagram of the polyvinylidene fluoride patch. 74
Figure 3.12: Sketches showing (a) Direction of force as applied to the model where the force vector applied was along the edge of the fabric (b) Meshing (c) Meshing as seen in thickness. 75
Figure 3.13: Total deformation at 5Hz in the model showing (a) Flexible polyester (b) Piezo patch. 76
Figure 3.14: Displacement amplitude of piezo patch at 5Hz. 77
Figure 3.15: Effect of increase in Area on (a) power output (b) displacement (c) output current (d) output voltage at aspect ratio 4, and input load 0.005N. 78
Figure 3.16: Effect of increase in Aspect ratio on (a) power output (b) displacement (c) output current; and (d) output voltage at 1600 mm^2 area with input load 0.005N 79
Figure 3.17: Effect of increase in loading magnitude on (a) power output (b) displacement (c) output current; and (d) output voltage at aspect ratio 4, and 1600 mm^2 area. 80
Figure 3.18: Modal Analysis (for the 1st mode) for Polyvinylidene fluoride area patch of 400 mm^2 81
Figure 3.19: Spacer fabric model 85
Figure 3.20: Representative volume element with (a) 4 spacer fibres (b) 9 spacer fibres (c) 16 spacer fibres (d) 25 spacer fibres 85
Figure 3.21: Power output in various RVE 86
Figure 3.22: Figure showing imposed boundary condition 87
Figure 3.23: Effect of poling direction on (a) power output (b) voltage and (c) 88
Figure 3.24: Effect of Yarn Count on (a) power output (b) voltage and (c) current 89
Figure 3.25: The spacer fabric model showing spacer yarns at an inclination angle of (a) 45 and (b) 30 90
Figure 3.26: Effect of increase in Fibre angle with vertical on (a) power output (b) Voltage and (c) current 90
Figure 3.27: Effect of increase in thickness on (a) power output (b) voltage and (c) current 91
Figure 3.28: Spacer fabric model RVE 92
Figure 3.29: Effect of increasing inclination angle on (a) output power, (b) Voltage and (c) current 94
Figure 3.30:Effect of increasing yarn count on (a) output power, (b) Voltage and (c) current 95
Figure 4.1 showing the schematic of the setup used for Melt spinning 98
Figure 4.2: Extruder used for Melt spinning yarn 98
Figure 4.3 High voltage supply (Gamma High Voltage Research) 99
Figure 4.4 showing the temperature of polyvinylidene fluoride filament using Fluke camera at (a) extruder nozzle (b) poling setup 101
Figure 4.5 Setup used to extrude and pole polyvinylidene fluoride for validation 102
Figure 4.6: Spacer fabric prepared using poled yarns (a) front view (b)side view 102

Figure 4.7: SEM images of polyvinylidene fluoride yarn at magnification of (a)200x (b)400x (c) 1400x (d) 1600x (e)4800x 103
Figure 4.8: Perkin Elmer 400 Spectrometer at RMIT (Textiles) 104
Figure 4.9:FTIR absorbance Spectra of Polyvinylidene fluoride filament 105
Figure 4.10 XRD (a) sample prep (b) & (c) Bruker AXS D4 at RMIT School of Textiles 106
Figure 4.11 Sample preparation (a) Schematic diagram (b) actual sample being prepared 107
Figure 4.12 Instron Insta cyclic compression machine showing (a) test setup and (b) attached data acquisition unit 108
Figure 4.13 4-point bending test with the sample under stress. 109
Figure 4.14 The figure shows the schematic presentation of the four-point bending machine (Gusarov, 2015). 109
Figure 4.15 Voltage Output signal using DMM 110
Figure 5.1: β-fraction obtained on varying electrode distance 114
Figure 5.2: Fourier-transform infrared spectra of polyvinylidene fluoride yarns extruded using various electrode distance 115
Figure 5.3: X-ray diffraction of polyvinylidene fluoride yarns extruded using various electrode distances (D1 – D4) 116
Figure 5.4: β-phase fraction content at various electrode diameters 117
Figure 5.5: Fourier-transform infrared spectra of polyvinylidene fluoride yarns extruded using various electrode diameters (H1-H4) 117
Figure 5.6: X-ray diffraction analysis of polyvinylidene fluoride yarns extruded using various poling diameter (H1-H4) 119
Figure 5.7: β-fraction obtained for yarns extruded at various poling voltages (P1-P5) 120
Figure 5.8: Fourier-transform infrared spectra of polyvinylidene fluoride yarns yarns extruded using varying applied voltage (P1-P5) 120
Figure 5.9: X-ray diffraction analysis of polyvinylidene fluoride yarns extruded using varying applied voltage (P2-P5) 121
Figure 5.10: β-phase fraction content 122
Figure 5.11: FTIR spectra of PVDF yarns extruded using varying temperatures 123
Figure 5.12: β-fraction obtained for fibres extruded at various draw ratios 123
Figure 5.13: Fourier-transform infrared spectra of polyvinylidene fluoride yarns extruded using various draw ratios 124
Figure 5.14: Peak voltage outputs for varying electrode distance 125
Figure 5.15: Peak voltage outputs for electrode diameter 126
Figure 5.16: Peak voltage output at various poling voltages 127
Figure 5.17: (a) Voltage response (d_{33}), (b) Voltage response (d_{31}), (c) Current (d_{33}), (d) Current (d_{31}), (e) Strain (d_{33}), and (f) Strain (d_{31}) on sample H1 128
Figure 5.18: Power outputs for various diameters 129
Figure 5.19: (a) (a) Voltage response (d_{33}), (b) Voltage response (d_{31}), (c) Current (d_{33}), (d) Current (d_{31}), (e) Strain (d_{33}), and (f) Strain (d_{31}) for sample D1 130
Figure 5.20: Power outputs as a function of distance between plates 131
Figure 5.21: (a) Voltage response (d_{33}), (b) Voltage response (d_{31}), (c) Current (d_{33}), (d) Current (d_{31}), (e) Strain (d_{33}), and (f) Strain (d_{31}) for sample P5 132
Figure 5.22: Power outputs as a function of poling voltage 132

Figure 5.23: A figurative comparison of the simulated electric field intensity with the experimental output voltage for various electrode diameters 133
Figure 5.24 showing the comparison of the simulated results for electric field intensity on the output voltage for various electrode distances 134

List of Tables

Table 2.1: Electrical properties of various metallic monofilaments 17
Table 2.2: Properties of various commercially available piezoelectric materials (adapted from Vatansever et al. 2012) 22
Table 2.3: Design guidelines for wearability (adapted from Gemperle 1998).. 48
Table 2.4: Energy requirements for portable devices (adapted from Vullers et al. 2009 and Alto 2012) .. 51
Table 3.1: Material properties of flexible polyester.. 73
Table 3.2: Material properties for piezoelectric material, polyvinylidene fluoride 74
Table 3.3: Natural Frequencies for modal analysis for Polyvinylidene fluoride area of 400 mm^2 81
Table 3.4: Material properties of piezoelectric material polyamide used for this analysis......................... 84
Table 4.1: Polyvinylidene fluoride crystal planes with corresponding 2θ peaks (Martins et al. 2014) 105

List of Symbols

d piezoelectric coefficient (C/N or m/V)

d_{31}, d_{33} Piezoelectric charge coefficients (C/N or m/V)

g_{31}, g_{33} Piezoelectric voltage coefficients (Vm/N)

k_2 Piezoelectric coupling coefficient

T Temperature °C

λ pyroelectric coefficient

D Electric displacement field (C/m^2)

s elastic compliance of piezoelectric material (N/m^2)

ϵ Dielectric constant (F/m)

ϵ_0 Permittivity of free space (8.85×10^{-12} F/m)

E Electric field strength (N/C) or Elastic modulus (MPa, GPa)

T or σ Mechanical stress (N/m^2)

S or ε Mechanical strain

YM Young's modulus (Pa or N/m^2 or kg. m)

V Electric voltage (μV, mV, V)

V_{RMS} Root mean square voltage (V)

I Current (μA, mA, A)

I_{RMS} Root mean square (A)

P Power (μW, mW, W)

C Capacitance (F)

η Conversion efficiency

S Conductivity (S/m)

α Alpha crystalline phase (α-PVDF)

β Beta crystalline phase (β-PVDF)

List of Acronyms

APDL ANSYS - Parametric Design Language

CNT - Carbon Nano Tubes

DSC - Differential Scanning Calorimetry

FEM - Finite Element Modelling

FTIR - Fourier Transformation Infra-Red

ITO - Indium Tin Oxide

MEMS - Micro-Electro-Mechanical Systems

MWNT - Multi-walled carbon nanotubes

NMR - Nuclear magnetic resonance

NW - Nanowires

PDMS - Polydimethylsiloxane

PEDOT:PSS - Poly (Styrene Sulfonic acid)

PMMA - Poly(Methyl Methacrylate)

P(VDF-TrFE) - Poly(vinylidene fluoride-co-trifluoroethylene)

PVDF - Polyvinylidene Fluoride

PZT - Lead Zirconate Titanate Pb[ZrxTi1−x]O3

RVE - Representative Volume Element

SEM - Scanning Electron Microscope

SMA - Shape Memory Alloy

SWNT - Single-walled Carbon Nanotubes

VSSP - Viscous Suspension Spinning Process

XRD - Xray-Diffraction

ZnO - Zinc Oxide

1 Introduction

1.1 Research background

The topic of energy has been in limelight for several decades now and seems likely to continue to dominate scientific research and global policies in the future. From the world that mainly relied on renewable resources some three centuries ago, it is now shifting back to renewable energy sources due to the diminishing fossil reserves and the adverse environmental impact of burning fossil fuel (Abbasi *et al.* 2011; Covert *et al.* 2016).

A fast paced, growing, competitive, commercial environment and improved living standards have resulted in a rapid increase in energy demand, placing a continuous strain on existing global fossil reserves. This continuous strain has led to a depletion of fossil supplies, higher energy costs and resentful effect on the environment. Due to the continuous use of fossil fuels for power generation and transportation purposes, gases like CO_2, CO, NO_x, SO_2 and CH_4 are being released into the atmosphere causing a steady rise in the earth's temperature, depletion of the ozone layer, and health-related issues (Russell 2013). The recent rapid changes in global climate have led the human race to consider the repercussions arising from ever-increasing energy generation and its usage. Global warming and air pollution are two major threats which humans and other living species face (Jacobson 2009). An editorial quoted a World Health Organization study which stated that air pollution caused approximately 6.5 million deaths alone across the world in 2012 (Nature Energy 2017). Researchers are continuously working to address this grave issue, and renewable power generation holds a probable solution for this topic.

Advancements in wearable electronics have opened new horizons in smart textiles which have a considerable impact on sectors like health monitoring, military services, sportswear, portable energy generation, and energy storage (Yuksel & Unalan 2015). The increased interactive role of textiles and innovations in materials science has revolutionised the global technological system. Mitcheson *et al.* (2008) define energy harvesting as power generated through ambient sources. According to them, powering of low energy requirement devices through inexhaustible energy generation systems holds great interest. Why these energy harvesting techniques are so attractive can be mainly attributed to the decrease in the power requirements of electronic devices. Scavenging energy using generators through biomechanical human motion can produce electric power from milliwatts to watts (Romero-Ramirez 2010). Harvesting energy biomechanically from human motion offers us a clean substitute to charge batteries of portable electronic devices or even to replace the traditional batteries possibly by utilising the piezoelectric phenomenon. This research work presents robust fibre-based piezoelectric energy generation devices integrated within wearable fabrics that could be used to produce power through human motion on various body locations. The generated electric charge could be used to store electric energy on another wearable device and further power any 'on-person' electronic device.

1.2 Research aim and objectives

The main aim of this research is to tackle some of the scientific and technological impediments currently associated with generating energy in multi-functional fabrics. Hence, it considers the potential of harvesting energy through fibre-sized material utilising human body motion taking place at low-frequency vibrations. Energy harvesting from human body motion was critically reviewed from the available scientific literature. Based on this review and computational modelling work undertaken in this manuscript, a prototype device was designed and evaluated. The main objective of this dissertation was to develop an energy harvesting device from piezo fibres which uses human body movements to generate electrical energy. The main objectives of the thesis are as follows:

1. Integration and robust connection of conducting fibres and energy harvesting fibres (polyvinylidene fluoride (PVDF)) with non-conducting structural fibres.
2. In depth study of the process of on-garment energy harvesting using finite element simulations.
3. Characterisation and performance output evaluation of the piezo fibres and fabrics.

1.3 Research methodology

This work is divided into various sections including computational simulations, PVDF yarn production and poling, characterisation of yarns and fabric, and piezoelectric testing. The first section involves a novel simulation work on piezoelectric interaction using ANSYS software by Ansys Inc. to simulate finite elements. Various simulation studies were conducted to optimise the design parameters for a novel device for poling of PVDF yarns *in situ* with the melt spinning process. These simulations for in-line poling of continuous filament were conducted to enhance beta (β-phase) formation in PVDF. Several parameters were taken into consideration and the results were validated using an experimental approach followed by Fourier-transform infrared (FTIR) spectroscopy analysis.

To explore the feasibility of harvesting electrical energy from human motions, a computational study was carried out to simulate a wearable energy harvesting device embedded in textiles for elbow, knee, and finger joints. A dual field (electro-mechanical) computational analysis of a PVDF patch bonded onto a nominal representative flexible fabric was carried out with human locomotion frequency, which is in the range of less than 2 Hz. Different parameters such as the area, aspect ratio, and input loading magnitude were studied at different frequencies together with their effect on output power, voltage, current, and displacement. To simulate piezoelectric effect in a PVDF fabric, a finite element analysis of an idealised PVDF wearable textile using the Representative Volume Element (RVE) approach was conducted. The model was optimised using parametric analysis of the designs of 3D spacer fabric. Other parameters included the effect of fibre angle, thickness, linear density, and poling directions on output power at lower frequencies (1–2 Hz), with the results discussed in the context of the intended fabric applications.

The simulations were followed by production of PVDF yarns through simulated method poling design. The PVDF yarns were produced at a temperature of 170°C using a single monofilament extruder with a custom drawing assembly to accommodate in-line poling. These poled yarns were produced using several parameters and the effect of these parameters was studied using various morphological characterisations techniques such as scanning electron microscopy (SEM), FTIR, and X-ray diffraction (XRD). The results of these techniques were augmented with electro-mechanical outputs to validate the effect of piezoelectric activity in the PVDF yarns. A four-point bending test used to validate these outputs and the electrical outputs such as voltage (V) and current (mA) were collected using a digital multimeter. This was followed by calculations on obtained energy outputs using poled PVDF yarns. A piezo fabric was then produced using the optimised, poled PVDF yarns and the optimised spacer fabric model. The piezo fabric was subjected to similar evaluation to obtain electro-mechanical outputs.

1.4 Thesis overview

Chapter 1 contains a brief introduction to research background and energy harvesting through human motion. It explains the rationale behind the thesis and structure of the thesis.

Chapter 2 presents a detailed critical review of the energy harvesting concept, theory, and approach already published by various researchers which are relevant to the work in this thesis.

Chapter 3 demonstrates our novel work on finite element simulation on fibre-based textile structures using ANSYS software. Optimum energy generator structure and production conditions were formulated due to this work. The power output results in this work indicate the power availability from these generators.

Chapter 4 includes the energy generator description and the fabrication processes employed to manufacture prototype energy harvesters and various characterisation techniques that were used for yarn testing.

Chapter 5 comprises of assessment and analysis of the investigation undertaken in the previous chapters. A detailed insight analysis helps in determining the issues encountered during the research and the performance output of developed energy generators.

Chapter 6 outlines the main conclusions of the thesis with some recommendations for future work.

1.5 List of publications

1.5.1 Book chapter

1. Waqar, S, Wang, L & John, S 2015, ‘Piezoelectric energy harvesting from intelligent textiles’, Electronic Textiles, Woodhead Publishing. Pages 173-197,ISBN 9780081002018.

1.5.2 Conference proceedings

1. Waqar, S, McCarthy, JM, Deivasigamani, A, Wang, CH, Wang, L, Coman, F & John, S 2013, ‘Dual field finite element simulations of piezo-patches on fabrics: a parametric study’, *Fourth International Conference on Smart Materials and Nanotechnology in Engineering (SMN 2013)*, Gold Coast, Australia.
2. Waqar, S, John, S, Khan, IA, Wang, CH, McCarthy, JM, Ladigus-Grange, A, Wang, L & Coman, F 2014, ‘Modelling and analysis of various piezo fibre geometries on the piezoelectric properties for energy scavenging applications’, *ACAM 8*, Melbourne, Australia, Nov 23–26, 2014.
3. Waqar, S, John, S, Khan, IA, Wang, CH, McCarthy, JM, Ladigus-Grange, A, Wang, L & Coman, F 2015, ‘Dual field analysis of poling design of PVDF fibres for energy harvesting applications’, *APISAT*, Cairns, Australia, Nov 25–27, 2015.
4. Waqar, S, John, S, Khan, IA, Wang, CH, Coman, F 2015, ‘Optimization of fabric design for energy harvesting applications’, *ATC*, Geelong, Australia, Nov 3–6, 2015.

2 Literature review

Intelligent textiles are textiles that are capable of detecting changes in their surroundings and reacting to them (Zhang & Tao 2001). They are textiles that react to an external stimulus in their surroundings and produce a practical outcome. The induced stimulus and the consequent response could be chemical, electric, thermal or some other type in nature (Van Langenhove & Hertleer 2004). Intelligent textiles or smart textiles are interchangeably used words.

2.1 Fuel source classification for energy generation

Numerous fuel types are used to generate energy over the period (Waqar *et al*. 2014). Energy produced using various fuel types can be classified as conventional and non-conventional (alternative) fuel sources. Petroleum, gas, coal, and shale come under the conventional fuel source category. Conventional fuel sources are the dominant fuel source for energy generation and will continue to be the leading sources for world energy generation. These fuel sources are unsustainable and world reserves of these are decreasing every day. Non-conventional or alternative fuel sources are all other sources or elements used to produce energy, such as hydro, solar, wind, tidal, and biomass. These sources which replenish over time and are sustainable, are also termed as renewable energy resources (Koroneos *et al.* 2003). Renewable energy is explained as inexhaustible and replenishable energy. Renewable energy happens to be the most popular energy generation technique these days due to its minimal adverse effect on the environment.

2.2 Global energy trend according to fuel type

Conventional fuel sources remain the main source of global energy production with 86% of energy produced is derived from them (Figure 2.1). The main constituents of conventional fuel are oil, natural gas, and coal. These fuel types have their own set of drawbacks. Coal is considered the major pollutant, due to the contaminant emissions it produces when used. Natural gas is the least pollutant fuel type present in the conventional fuel category, however, it still has a huge overall impact on the environment. During recent years, a lot of investment has been seen in the renewable sector, mainly solar and wind energy, to counter climate change and help produce green energy. In Figure 2.2, according to United Nations Environment Program (UNEP) Bloomberg, New Energy Finance report a large investment could be seen in the renewable energy sector (McCrone *et al.* 2016). China is leading the way in global renewable investment but also trying to surpass Germany in solar power generation according to reports published recently.

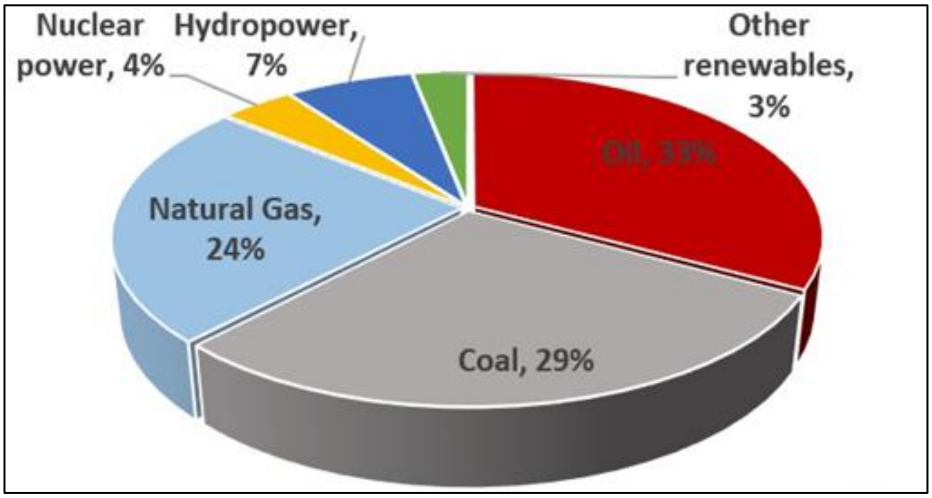

Figure 2.1 Global energy trend according to fuel type (Arab development portal: sourced from BP Statistical Review of World Energy 2016)

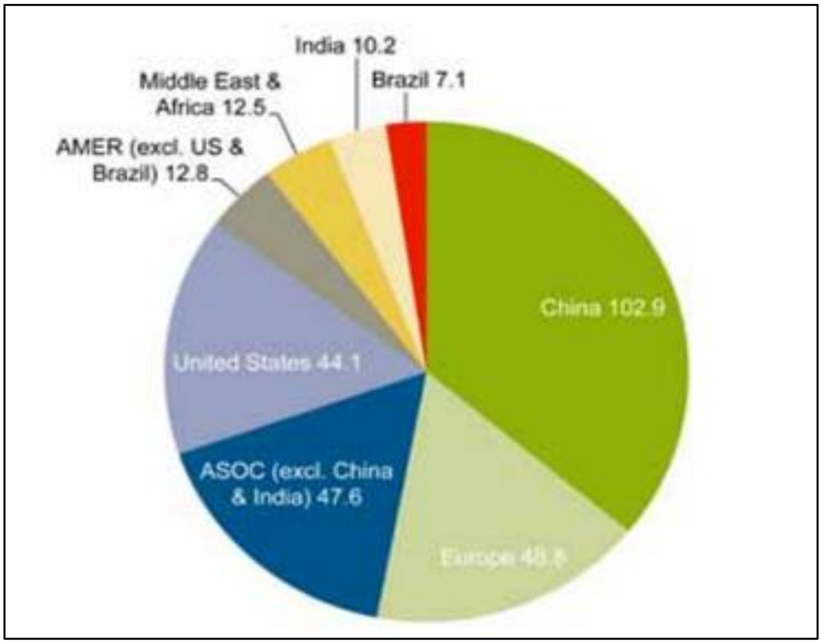

Figure 2.2: New global investment in renewable energy in 2015 (Amount in US $BN; UNEP Bloomberg New Energy Finance (McCrone et al. 2016))

Undoubtedly, the world is looking towards more diversified and greener power generation options. It is indeed a transgression from the long period of using fossil fuel for energy production. Still, it will take time and effort to shift from conventional to greener energy production. Global warming and climate change pose an imminent threat with enormous fatal implications for our planet.

2.3 Energy harvesting methods

Chalasani and Conrad (2008) have classified energy harvesting methods into mechanical, thermal, and solar.

2.3.1 Mechanical energy harvesting

2.3.1.1 Piezoelectric effect

The piezoelectric effect can be described as the ability of some materials to produce an electric charge in response to applied mechanical stress. The effect is due to shifting of positive and negative charge centres upon application of stress which creates an external electric field. This effect is reversible where placing the material in a strong electric field which tends to produce a stretch or compression in the material. The polarisation charge density due to the electrical dipole moment is proportional to the applied mechanical stress, which is given by:

$$\rho = dX \tag{2.1}$$

where ρ is the polarisation charge density, d is the piezoelectric coefficient, and X is the applied stress.

2.3.1.2 Triboelectric effect

The triboelectric effect is the result of some materials being electrically charged after coming into contact with another different material due to friction. The resultant electrostatically charged material is the result of charge transfer between the two, which retains its charge for a long time. This causes a potential between the two, driving induced electrons to flow between the two electrodes. Despite the long known static effect, the energy harvesting through triboelectric effect is a recent finding.

2.3.1.3 Electromagnetic energy harvesting

Electromagnetic energy harvesting is based on the principle of electromagnetic induction. This induction generates a voltage by changing the magnetic field around the conductor. This type of energy harvesting provides a reliable source of energy with improved damping due to reduced mechanical contacts (Chalasani & Conrad 2008).

2.3.2 Thermal energy harvesting

Thermal energy harvesting is based on the temperature gradient. Thermal energy provides a clean source to power electronic devices. It is widely used in space and terrestrial applications. The two main types of thermal energy harvesters are:

2.3.2.1 Thermoelectric effect

Thermoelectric energy harvesting is based on heat flux through a thermoelectric element, created by temperature differences. This effect is based on the Seebeck effect which produces a flow of charge carriers resulting in Seebeck voltage. Under identical temperatures between two surfaces, these charge carriers are distributed evenly. However, in the presence of a temperature gradient, there will be charge build-up at the surface with the higher temperatures, owing to higher kinetic energy at the surface. The Seebeck voltage can be calculated by:

$$V=\alpha_{ab}\cdot\Delta T=\alpha_{ab}\cdot(T_H-T_C) \qquad (2.2)$$

Where α_{ab} is the Seebeck coefficient of the junction between the materials a and b, and T_H and T_C, the temperature of hot and cold surfaces, respectively. The value of αab is determined by:

$$\alpha ab \sim \frac{V}{\Delta T}\ (at\ \Delta T\ \rightarrow 0) \qquad (2.3)$$

This current is created due to the presence of an electrical load in series with the thermogenerator and is dependent upon the temperature gradient between the hot and cold junctions. The Seebeck coefficients generally vary as a function of temperature, being positive for p-type materials and negative for n-type materials. Materials such as $NaCo_{1.9}M_{0.1}O_4$ and $NaCo_2O_4$ are high-Seebeck metals, exhibiting superior thermoelectric properties.

2.3.2.2 Pyroelectric effect

Pyroelectric effect is the result of a change in spontaneous polarisation due to temperature fluctuation. This effect is visible in certain anisotropic solids where a sequential change in temperature results in a flow of charge. This flow of charge occurs to or from the surface of materials and is called the pyroelectric current. This current in a homogeneous pyroelectric material can be calculated by the given equation (Xu 1991):

$$I = \frac{dQ}{dt} = S\,\lambda\,\frac{dT}{dt} \qquad (2.4)$$

where T is temperature (uniform), S is the electrode surface area, Q is the induced charge, and λ is the pyroelectric coefficient. The pyroelectric coefficient can be derived from Equation 2.5 where P_S is the electrical polarisation vector.

$$\lambda = \frac{dP_S}{dT} \qquad (2.5)$$

2.3.3 Solar energy harvesting

Solar energy harvesting is dependent on conversion of solar radiation to electrical energy in photovoltaic cells. When light falls upon a solar cell, the semiconductor absorbs it, causing its excitation and hole/electron separation leading to transport of charges to the electrodes. A typical solar energy harvesting cell consists of a transparent electrode such as Indium Tin Oxide (ITO), a poly (3,4-ethylenedioxythiophene: poly (styrene sulfonic acid) (PEDOT:PSS) layer, the photoactive material layer such as benzodithiophene-based polymers and fused-ring ladder-type molecules, and finally the metallic electrode to collect charges. Figure 2.3 shows the schematic drawing of a conventional solar cell on ITO-coated glass-based substrate. Solar harvesting is quite a mature technology for harvesting milliwatts up to megawatts range. The photoactive materials in solar cells are made from semiconductor constituents such as crystalline silicon (89%), amorphous silicon (10%), cadmium telluride (0.5%), gallium arsenide, copper indium, and diselenide. Apart from conventional solar energy harvesting, the principle has also been applied to search for wearable solar energy scavenging. Figure 2.3 shows one such flexible photovoltaic fibre, consisting of a PEDOT:PSS layer, the photoactive layer, and a metal-based electrode developed by Bedeloglu1 *et al*. (2010).

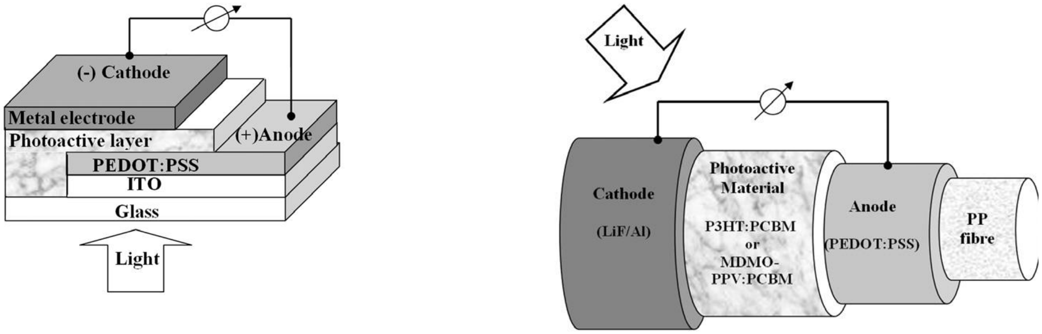

(a) **(b)**

Figure 2.3: (a) Schematic drawing of a polymer-based organic solar cell on Indium Tin Oxide coated glass-based substrate; (b) drawing of a photovoltaic fibre based on the principle

2.4 Energy through human motion

Harvesting energy biomechanically from human motion offers us a rather clean substitute to charge batteries of portable electronic devices or even to replace the traditional batteries. The piezoelectric phenomenon has been applied in many fields, with one of the significant uses being energy harvesting. Energy can be harvested from the human body by utilising movement of various parts of the body during motion, such as the knee, elbow, and shoulder joint motion, heel strike etc. Using human motion to create electric energy to charge micro devices is beneficial to society, providing green energy for its consumers continuously and in all places.

2.4.1 Motions in the human body

The main reason behind the notion of energy harvesting through the human body is that human body dissipates the energy throughout the day during everyday functions. While most of the human energy derived from carbohydrates, proteins, fats etc. is consumed for our bodily functions such as digesting food, keeping the body at a temperature, brain function and storing excess, a major chunk of energy is used for movement. Movements of limbs happen when the energy from food is delivered to, for example, the muscles in the arm to move it. By the definition of energy, 'Energy cannot be created or destroyed, it is transferred from one source to another source', it can be stated that the human food energy is converted into kinetic energy (Chen 2013). The energy harvested from human motion presents a promising future for the human race. It results in so many advantages over the current oversized, heavy and toxic batteries. Other forms of energy conversions include heat which is dissipated from a human body into the environment. The kinetic energy produced because of normal bodily functions can typically be used for arms and leg movements, respiratory process, eye movements, etc. Several researchers have previously worked on the utilising this kinetic energy.

The main challenge behind the utilising this kinetic to produce useable electrical energy is the conversion efficiency. Even the mechanical efficiency of human body lies between 15% and 30% (Winter 2005). Therefore, it can be stated that most of the energy the human body produces is used on heat dissipation. However, Riemer and Shapiro (2011) have shown that the efficiency of a heat conversion device at an environmental temperature of 0°C would be no more than 12%.

$$\text{Efficiency} = \frac{T_{body} - T_{ambient}}{T_{body}} * 100 \qquad (2.6)$$

$$= [(310 - 273)/310] * 100$$

$$= 12\%$$

where T_{Body} is the body temperatures and the $T_{Ambient}$ is the surrounding temperature in degrees Kelvin. The actual efficiency of a device to convert this energy was found to be no more than

2.5%. These above equations leave us with the kinetic energy, the second biggest energy conversion in the body.

2.4.2 The human limbs

The limbs in the body act in a sinusoidal way during normal movements. In simple bodily functions, such as walking, the legs would move forward but the actual torque applied is in a sine wave.

The muscles in the body go through the cycle of positive and negative work to produce motion. They first contract and by doing so generate motion after which they expand. This expansion requires energy but does not produce any motion and is therefore referred to as negative work. During positive work, the muscles apply torque at the joint which acts in the same direction as its angular velocity (Winter 2005). Conversely, when the torque applied is in opposite direction to the angular velocity of the joint, it is called negative work.

An energy harvester must perform in a way where the positive work is beneficial for conversion into electrical energy while the negative work period would be required to be sleep mode. In electrical terms, this can be achieved by signal rectifying which is discussed later.

In order to produce electricity, a continuous motion is required by the energy harvesting device, which can be used to generate some power, and does not affect the normal functions. This means that any natural movement of the body which is produced without any extra effort would be considered useful for the harvester. Continuous movements include torso expansion and contraction during breathing, eye blinking movements, and bending of arms and knees during walking.

The expansion and contraction of the torso is a continuous motion despite having no significant movements. However, this motion would require some close or tightly fitted chest band such as a heart rate monitor. Any tightly fitted device on upper body, particularly in the chest area, is likely to cause discomfort for our intended applications. Also, the chest movement is small and would require more work done.

The bending motion of limbs is found to have the highest torque in any movement of the body. (Riemer & Shapiro 2011). The elbow and knee joint act as hinge motion. During the simple process of walking, these limbs are continuously moving in a cycle with positive and negative work being done. As it is a hinge joint, the human elbow has two types of movements, the flexion-extension of the joint and the rotation of the radius. Figure 2.4 shows the forces acting on human limbs. The elbow is known to have an extension radius of only around 180°, being limited by the olecranon of the ulna, and the flexion is limited to the compression of the soft tissues around the elbow joint. Figure 2.4 shows the motion of limbs while running and walking. The arm motion in the human body occurs during walking. It involves a swinging back and forth motion which is composed of relative motion between the trunk and upper arm, and between the forearm and upper arm (Riemer & Shapiro 2011).

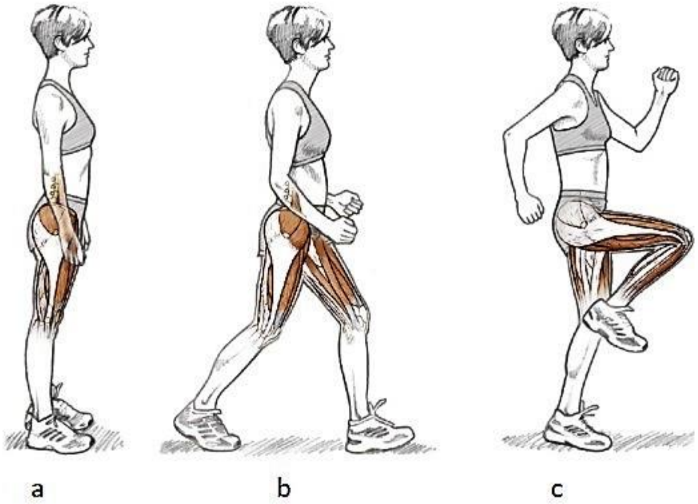

Figure 2.4: The motions of human limbs and the forces acting on them in (a) standing, (b) walking, (c) running positions (Zatsiorsky 2002)

2.4.2.1 Human elbow

During normal walking, the human elbow extends to only 30–40° from its rest position which can be approximately 180°. As we switch from walking to running, this extension/flexion can reach up to 140° depending on the speed. Some athletes, especially with large limbs, can flex up to maximum 165° during running. This sounds very promising for an energy harvester where more bending can result in higher torque. At running position, the frequency of the extension-flexion can reach up to 3–4 which is double that of the walking position.

2.4.2.2 The knee

The human knee has a similar hinge joint to that of the elbow. The human knee has the motion of flexion and extension. The rest position or standing position has 00 flexions whereas maximum flexion can be 1400–1500. During normal walking, the human knee flexes to 20°. This rate goes higher to 50° during running. This flexion and extension motion can be converted into useful electrical power using various energy resources.

2.4.2.3 Foot motion (heel strike)

Several devices have been built to generate energy from heel-strike motion. Some devices use the energy from the relative motion between the foot and the ground during the stance phase (the phase in which the foot is on the ground). Others use the energy from the bending of the shoe sole. In both cases, the device aims to use the energy that would otherwise have been lost to the surroundings. Zhao and You (2014) have designed an integratable shoe-embedded harvester for energy scavenging from human locomotion which provides an average output power of 1 mW at a frequency of approximately 1 Hz.

2.4.3 Optimisation of location of energy generator

The best place to place a generator would be in the highest strain area, the heel. However, the heel-based devices have a major issue of transfer of this energy to its desired location. As this transfer requires circuitry, this idea is complex.

Other strain areas on the body are the knee, elbow, shoulder, and fingers. Of these, our study shows the most feasible for an on-garment application is the elbow due to its location and comfort. The knee joint is also important, however, when at rest, elbows are more likely to be in operation than the knee. It is more feasible to produce a circuit in this case.

Proto *et al.* (2016), have harvested energy using lead zirconate titanate (PZT) and PVDF during locomotion activities. A tight suit was used with transducers placed in the proximity of the main body joints. These transducers were placed on the neck, shoulder, elbow, wrist, hip, knee, and ankle for the testing purposes; then, five locomotion activities, walking, walking up and down stairs, jogging, and running. The power obtained during these motions were reported in the range of 6–74 μW.

2.5 Parts of energy harvesting device

The geometry of the energy harvesting device is another major concern when optimising its applicability and efficiency. Considering the operating frequency and application domains, energy harvesting technologies will eventually need to have a wider range of implant ability. The geometrical configuration of an energy harvesting device will need to be managed depending on its operation site. However, power output and operating frequency of the conventional energy harvesting devices are greatly dependent on its geometry. Hence, future research needs to concentrate on these issues to optimise the related parameters before the devices can be used in many commercial operations.

2.5.1 Energy harvesting materials

In fabricating a device for energy harvesting, there are many important things to be considered, including the required output, materials and methods, life expectancy, performance, and environment. Typical energy harvesting devices consist of a sandwich structure. The main body or energy harvester is held between two electrodes used for transferring charge.

The requirements for piezoelectric materials are high dielectric constant, flexibility to be used in textiles, robust, can sustain wear and tear, and be practically lead-free if it is to be used on-garment. For electrodes, the material must be chosen based on flexibility along with high electrical conductivity. Both the electrode and piezo material must be incorporated which increases the maximum strain on the piezo while maintaining the contact with the electrode to transfer the induced charges.

The geometry of the harvester plays an important role in its performance (Ahmed *et al.* 2017). The output is also highly dependent on operating frequency of the harvester including its operation site.

2.5.2 Electrode materials

There are several possible electrode yarn materials for use in flexible electronics, including metallic yarns, metal-coated yarns, and other recent conductive fibres.

2.5.2.1 Metallic coated yarns

Metallic coated yarns are usually used for the manufactue of technical textiles. They are highly useful due to their anti-static, electromagnetic shielding properties. Many polymeric threads can be used with a metalised coating of silver, tin, copper, nickel etc. yarns such as X-static which is produced by coating conventional fibres with a metallic silver coating of up to 99% coverage (X-static 2014). Figure 2.5 shows conductive yarns with a metalised silver coating on single and plied yarns.

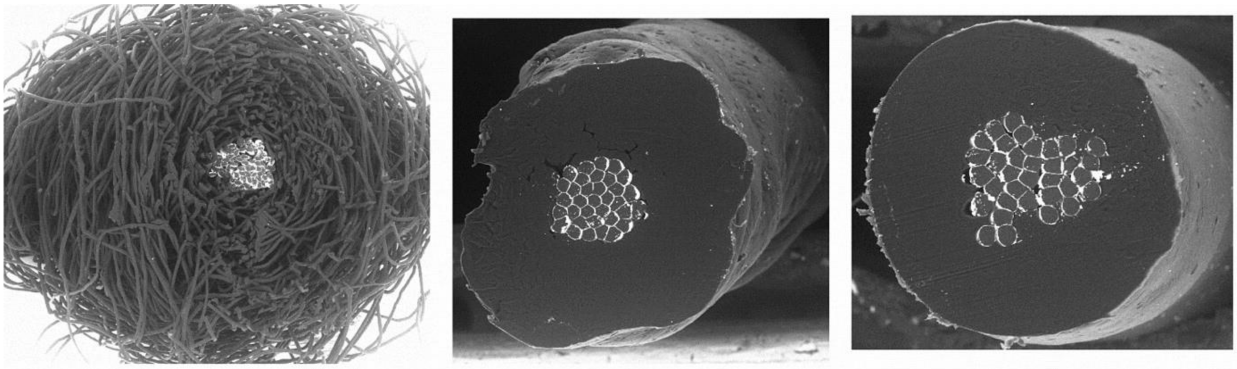

Figure 2.5: Scanning electron microscope image of the various type of conductive yarns with metallic coatings (Alagirusamy *et al*. 2013)

2.5.2.2 Metal yarns

Metallic yarns have long been used as conductive surfaces in textiles. Many metallic yarns are commercially available and can be chosen based on the requirement of end use. As a current collector in energy harvesting textiles, the yarns need to be flexible enough to withstand normal wear and tear, and therefore, are required to be flexible. Table 2.1 compares the properties of metallic nanofilaments. Metallic yarns such as stainless steel, copper, nickel etc. can be used directly as monofilaments, or plied with cotton or any other conventional textile yarns.

Table 2.1: Electrical properties of various metallic monofilaments

Electrical properties					
Conductivity (S·m mm^{-2})		Resistivity (Ω·mm^{2} m^{-1})		Thermal coefficient of resistance (10^{-6} K^{-1})	
Min		Typ		Max	
Cu	58.5	0.0171	3900	3930	4000
Cu/Ag	58.5	0.0171	3900	4100	4300
Ag 99%	62.5	0.0160	3800	3950	4100
Ms * 70	16.0	0.0625	1400	1500	1600
Ms/Ag	16.0	0.0625	1400	1500	1600
AgCu	57.5	0.0174	3800	3950	4100
Bronze	7.5	0.1333	600	650	700
Steel 304	1.4		0.7300	1020	
Steel 316L	1.3		0.7500	1020	

2.5.2.3 Nanoyarns/carbon nanotubes (CNT) yarns

Nanoyarn is spun from powder or solution-based polymers. It has superior functional properties owing to its high surface area. Lepro *et al.* (2010) have developed carbon nanotube (CNT) nano yarns from CNT forests grown on metallic substrates. They claim that the yarns have interesting electronic and mechanical properties and they could be used for various structural applications in electronic devices. Sears *et al*. (2010) have also developed high strength CNT yarns from closer CNT packing density forests with increased compressive stresses (Figure 2.6).

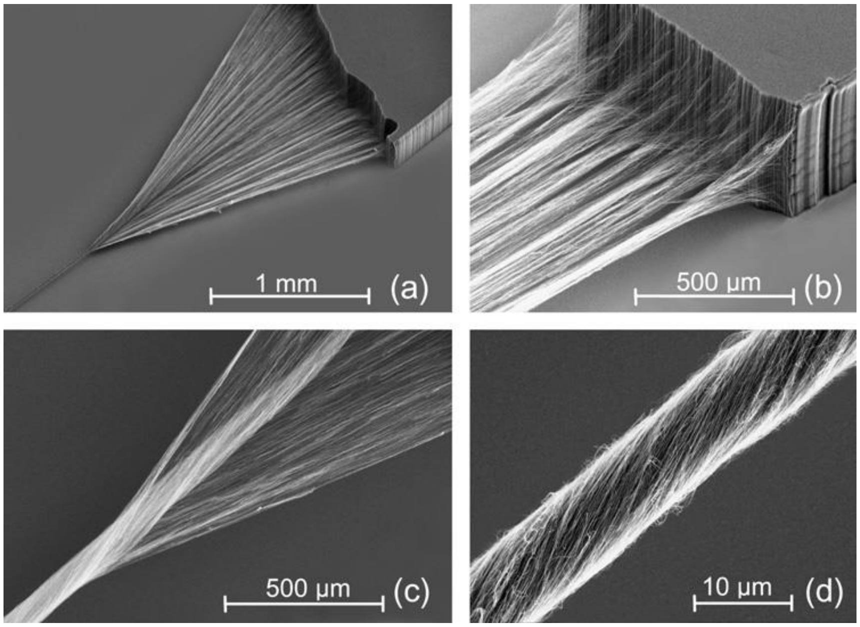

Figure 2.6: Figure 2.6: Scanning electron microscope images showing the making of yarns from CNT forest at (a) overall view, (b) CNT detachment, (c) convergence point, and (d) final yarn (Sears et al. 2010)

2.5.3 Integrated storage and circuitry

The harvested energy from a harvester needs to be transported to the required media. The device could be powered directly such as a pacemaker or stored in a storage system. The integrated storage would need to be designed in a way where it reduces the resistance between contacts. The integration of storage would directly enable the harvested energy useable in times when not in need. The charging of these storage devotes require constant current and voltage. However, most of the generators produce alternating voltage, which then requires an optimised circuit with an AC-

DC converter to charge the storage device (Lee *et al*. 2016). The harvester should be integrated into storage in a way that energy loss is minimised.

The scope of this research is to focus on fabrication of an energy harvesting device in which the energy harvesting materials play a key role. They are discussed at length here.

2.6 Piezoelectric materials

The piezoelectric phenomenon could be described as one of the substantial discoveries of the 19th century. The term piezo is derived from the Greek words *piezein*, i.e. pressure (Kholkin *et al.* 2008). Piezoelectricity is electricity produced due to pressure exerted on a piezoelectric material.

Piezoelectric, pyroelectric, and ferroelectric materials are often discussed simultaneously owing to their inter-relationship with each other at the crystalline structure level. For a crystalline structure to exhibit piezoelectricity there should be no symmetry at the inversion centre for point group(s) (Tilley 2006). A piezoelectric material can show both pyroelectricity, generation of electric charge on a crystal by the change of temperature, and ferroelectricity, a property of certain materials that have a spontaneous electric polarisation. The relationship between different types of materials is shown in Figure 2.7. The ferroelectric materials are known to have superior piezoelectric properties against their non-ferroelectric counterparts.

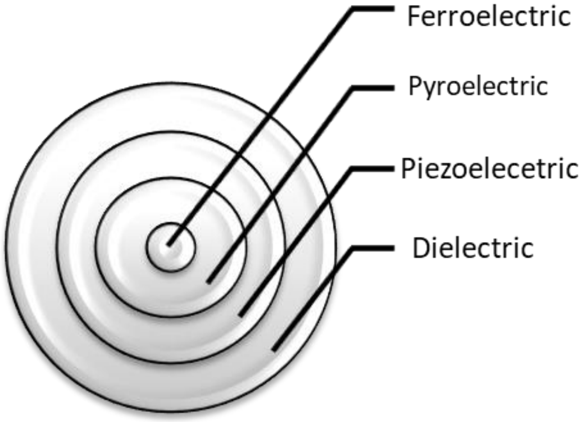

Figure 2.7: Relationship between ferroelectric, dielectric, piezoelectric, and pyroelectric materials (adapted from Kong *et al.* 2014)

There are different piezoelectric materials based on various crystalline properties. These materials can also be classed according to their source, such as natural or synthetic. Natural materials such as quartz, bones, tendons, enamel, and dentin etc. are known to exhibit piezoelectric properties. Generally, the crystalline structures can be classed according to seven basic crystal systems. These are triclinic, monoclinic, orthorhombic, tetragonal, rhombohedral (trigonal), hexagonal, and cubic. These form 32 various types of point groups, of which 21 are non-centrosymmetric. Of these, 20 are piezoelectric. Out of these, 10 are pyroelectric crystals which become permanently polarised in a certain temperature range (Kong *et al.* 2014). Pyroelectric crystals are different from thermoelectric crystals because the whole crystal (not just a portion of the device) undergoes a temperature change causing a temporary voltage. Among these 10 pyroelectrics are ferroelectric crystals such as $BaTiO_3$ and $PbTiO_3$ which are characterised by the formation of electrical dipoles due to asymmetrical shifts in the equilibrium positions of ions.

2.6.1 History of piezoelectricity

In a review regarding piezoelectricity, Ballato (1996) reveals that Coulomb was the first to suspect that electricity generation could be attained through applying pressure to materials. Katzir (2003) pointed out that Jacques Curie and Pierre Curie were the first to observe piezoelectricity in 1880. It is interesting to note that in 1881 it was not the Curie brothers but Lippmann (1881) who announced the existence of a converse piezoelectric effect. Basically, this converse effect is a deformation of a piezoelectric material due to the influence of an applied electrical field. Lippmann (1881) postulated the existence of this effect through mathematical prediction by applying basic thermodynamic principles to reversible processes. Curie and Curie (1881) verified and established the converse piezoelectric effect experimentally soon after.

In early years after this discovery, theories governing the effect were formed and modified. It was not until the First World War that the earliest applications of the piezoelectric effect were developed in the form of sonar devices to detect submerged metal objects in the water (Katzir 2006). As indicated by Sharapov (2011), shortly after the first sonar device was built other devices such as piezoelectric microphones, sound recording and receiving equipment, together with measuring instruments for force, acceleration, and vibration were created based on piezoelectric principles. Since then, a lot of studies have been made on the uses of piezoelectric materials, particularly for energy generation.

A recent and novel approach is energy generation using nanostructured piezoelectric devices called nanogenerators. These transform kinetic energy into electrical energy using different types of materials such as ZnO, ZnS, GaN, CdS, PVDF, and $BaTiO_3$.

2.6.2 Basic principles of piezoelectricity

2.6.2.1 Charge formation and poling

The piezoelectric materials are a part of the ferroelectric family, in which the molecular structure orientation causes the formation of electrical dipoles due to localised charge separation (Figure 2.8). A group of dipoles with parallel orientation are called Weiss domains. These Weiss domains tend to be randomly oriented in a raw piezoelectric material (Figure 2.8(a)) hence the material does not show any piezoelectric response. However, when the material is heated above its Curie temperature (T_c) in the presence of a strong electric field, these dipoles reorient themselves in the direction of the applied field (Figure 2.8(b)). On cooling, the material tends to maintain the dipolar orientation achieved during heating (Figures 2.8(c) and 2.9).

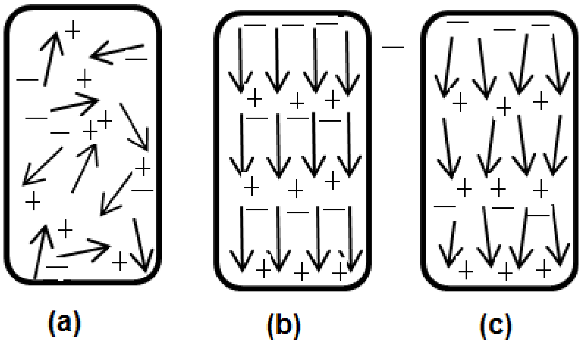

Figure 2.8: Dipole reorientation on the application of an electric field

Table 2.2 shows a comparison between various piezoelectric materials and their properties. The piezoelectric coefficients in ceramics are higher than in polymers. Hence, on the application of pressure, the electrical output tends to be higher for piezoceramic materials. The electro-mechanical coupling constant (k_{31}) for ceramics such as PZT (($Pb[Zr_xTi_{1-x}]O_3$ $0 \leq x \leq 1$) is 2.5 times higher than PVDF ($-(C_2H_2F_2)_n-$), showing the enhanced ability of ceramics to convert stress to an electrical output. However, the piezoelectric voltage coefficient in PVDF is higher than in ceramics (21 times that of PZT).

Table 2.2: Properties of various commercially available piezoelectric materials (adapted from Vatansever et al. 2012)

Property	**Units**	**$BaTiO_3$**	**PZT**	**PVDF**
Density	103 kg m^{-3}	5.7	7.5	1.78
Acoustic impedance	(106) kg m^{-2}-s	30	30	2.7
Relative permittivity	$\varepsilon/\varepsilon_0$	1700	1200	12
Piezoelectric strain coefficient (d_{31})	10^{-12} C/N	78	110	23
Piezoelectric voltage coefficient (g_{31})	10^{-3} Vm N^{-1}	5	10	216
Pyroelectric voltage coefficient (*Pv)*	V µm K^{-1}	0.05	0.03	0.47
Electro-mechanical coupling constant (k_{31})	%@1 kHz	21	30	12

2.6.2.2 Direct and converse effects

The idea of putting pressure on a material to produce electrical output can be referred as a 'direct piezoelectric effect'. The electrical output generated in the direct effect is due to the applied mechanical stress on the material, which produces an electric charge on the surface of the crystals. Figure 2.9(b) and (c) show the effect of applying tension and compression to a piezoelectric material (direct effect). The polarity of the charge produced can be inverted by changing the direction of the strain. This effect can also be reversed producing a 'converse' piezoelectric effect. The application of an electric field across the crystal results in a mechanical deformation realised as a change in its dimensions (Figure 2.9(d) and (e)) (Damjanovic 1998; Haertling 1999; Kong *et al.* 2001; Kong *et al.* 2008).

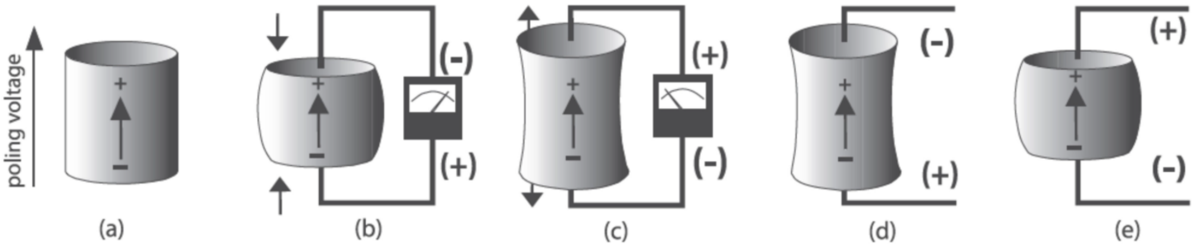

Figure 2.9: (a)–(e) The direct and converse piezoelectric effects, respectively (Moheimani & Fleming 2006)

2.6.2.3 Piezoelectric nodes

As discussed earlier, piezoelectric materials are highly anisotropic materials due to their crystallographic structure, therefore, the orientation of the crystal dictates their properties. Figure 2.10 shows the orientation axis 1, 2 and 3 of the crystal. Axis 3 is normally placed along the thickness and axis 1 is along the longest side.

The characteristic piezoelectric material behaviour needs to be fully understood for which there are 36 flexibility coefficients (s), 18 piezoelectric coefficients (d) and 9 permittivity coefficients (ε). Moreover, there are 63 coefficients which are used to fully characterise the piezoelectric behaviour. However, these can be reduced owing to the sufficient symmetry present in the piezoelectric crystal. The coefficient matrices for piezoelectric materials are given below (IEEE 1988) where s, d and ε are shown:

$$\varepsilon_{ij} = \begin{pmatrix} \varepsilon_{11} & 0 & \varepsilon_{13} \\ 0 & \varepsilon_{22} & 0 \\ \varepsilon_{13} & 0 & \varepsilon_{33} \end{pmatrix} \qquad (2.7a)$$

$$d_{ij} = \begin{pmatrix} d_{11} & d_{12} & d_{13} & 0 & d_{15} & 0 \\ 0 & 0 & 0 & d_{24} & 0 & d_{26} \\ d_{31} & d_{32} & d_{33} & 0 & d_{35} & 0 \end{pmatrix} \qquad (2.7b)$$

$$s_{ij} = \begin{pmatrix} s_{11} & s_{12} & s_{13} & 0 & s_{15} & 0 \\ s_{12} & s_{22} & s_{23} & 0 & s_{25} & 0 \\ s_{13} & s_{23} & s_{33} & 0 & s_{35} & 0 \\ 0 & 0 & 0 & s_{44} & 0 & s_{46} \\ s_{15} & s_{25} & s_{35} & 0 & s_{55} & 0 \\ 0 & 0 & 0 & s_{46} & 0 & s_{66} \end{pmatrix} \tag{2.7c}$$

Where d_{ij} is the Piezoelectric Strain coefficient, s_{ij} elastic compliance, ε_{ij} dielectric permittivities for the piezoelectric crystals in point group m. The mechanical and electrical parameters of piezoelectric materials are tensors of a different order. As they are to be measured in a different axis, the piezoelectric and elastic coefficients are hence presented in a matrix form above. They are denoted as d_{ij}, i being the direction of generated voltage and j being the direction of applied stress (Figure 2.10).

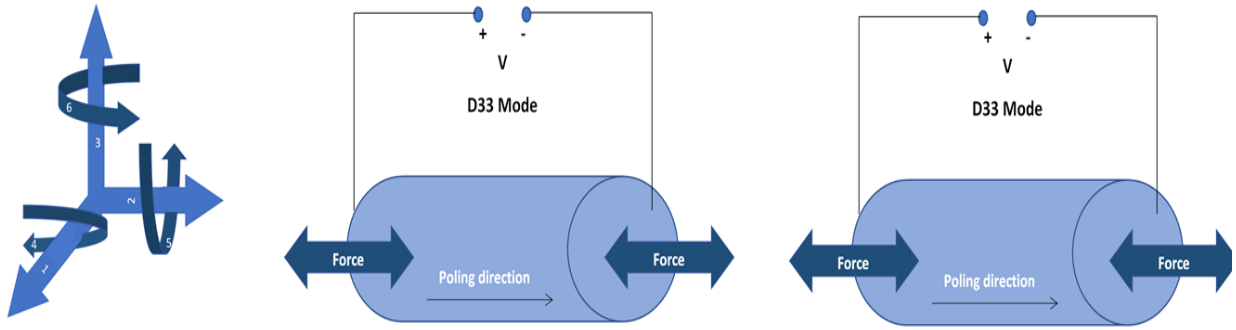

Figure 2.10: Direction of forces in piezoelectric materials (adapted from Gusarov 2015)

2.7 Mechanical energy conversion

Piezoelectric materials work on the basic phenomenon of conversion of structural vibrations into electrical outputs. Piezoelectric materials tend to produce electricity when pressure is applied. This pressure causes a change in the polarity of the dipoles, which results in an imbalance between the two surfaces where the two ends become polarised. The types of deformations which cause this effect can result from bending, mechanical compressive stress, mechanical strain, tensile stress, and strain. Piezoelectric generators can produce relatively high voltage outputs but low electrical currents. Output impedance also tends to be high with piezoelectric materials (>100 kΩ) (Beeby

& White 2010). Lee *et al.* (2012) have demonstrated that the M13 of certain bacteriophages can be utilised for the piezoelectric energy harvesting.

2.7.1 General theory

The piezoelectric coupling factors (e.g. k_{33}, k_{31}, and k_p), refer to the overall strength of electro-mechanical effects. These are the square root of the ratio of electrical energy output to the mechanical energy input. The value of k is always less than unity due to the inability of complete conversion of electrical to mechanical energy and vice versa. The coupling factor k_{xy} measures the effectiveness of a piezoelectric material and can vary in different directions within a material. The piezoelectric charge coefficient, also known as the piezoelectric modulus with the symbol d, describes the change in volume on the application of an electric field. Values of d have magnitudes of the order of 10^{12} C/N (direct effect). This can become 10^{-12} m V^{-1} in the case of the converse effect. There can be many piezo coefficients, i.e. d_{xy}, where x relates to the direction of generation of polarisation in electrodes perpendicular to the vertical direction whereas y refers to the applied mechanical stress in the lateral direction. For example, d_{31} means that this piezoelectric coefficient relates to the generation of polarisation (direct effect) in the electrodes perpendicular to the vertical direction (3) with the stress being mechanically applied in the lateral direction (1), while d_{33} indicates the polarisation generated in the vertical direction (3) when the stress is applied in the same direction. Hence, d is an important indicator for piezoelectric materials.

The piezoelectric voltage constant, also known as the g factor, denotes the electric field generated by materials per unit mechanical stress applied. Like the piezoelectric charge constant, these values can also be classed in terms of directions, i.e. g_{xy}.

Permittivity is defined as the dielectric constant, ε. This value quantifies the dielectric displacement obtained per unit electric field applied. ε^T and ε^S denote the permittivity at constant stress and strain, respectively, with terms such as $\varepsilon^T{}_{11}$, $\varepsilon^S{}_{11}$, $\varepsilon^T{}_{33}$, and $\varepsilon^S{}_{33}$.

Elastic compliance, s, is the reciprocal of Young’s modulus, or the strain produced as a result of applied mechanical stress. s^D and s^E are two types of elastic compliances, which denote compliance under constant electric displacement and electric field, respectively. The direction of applied stress or strain is represented by s_{xy} where x is the direction of strain and y is the direction of stress.

Young’s modulus is the measure of the elasticity or stiffness of a material and is denoted by Y. It is a ratio of stress applied to strain produced.

The constitutive equations (Uchino 2010) for piezoelectric finite element analysis which define how the piezoelectric material’s stress (T), strain (S), charge-density displacement (D), elastic compliance of piezoelectric material (s), piezo coefficient (d), permittivity (ϵ), and electric field (E) interact are:

$$S=s.T+d.E \qquad (2.8a)$$

$$D=d.T+\epsilon.E \qquad (2.8b)$$

2.8 Different piezoelectric materials

2.8.1 Piezo ceramics

Piezo ceramics, a significant group of piezoelectric materials, are ferroelectric materials with polycrystalline structures (perovskite, tetragonal/rhombohedral crystals). Above the Curie temperature, these crystals exhibit simple cubic symmetry in structure. There are no dipoles present in this state as the positive and negative charge sites are coincident due to the centrosymetric structure. However, this symmetry is no longer present below the Curie temperature, where the charge sites are no more coinciding. This results in built-in electric dipoles, which are reversible. Neighbouring dipoles realign locally to form Weiss domains. Figure 2.11 shows the structure of a typical piezoelectric ceramic crystal where (a) is the structure of the crystal at temperatures above Curie point. The positive and negative charges coincide hence there is not net dipole moment. At temperatures below Curie point the crystal structure changes to perovskite (tetragonal lattice) as shown in figure 2.11(b). The dipoles are aligned in one direction resulting in an overall dipole moment.

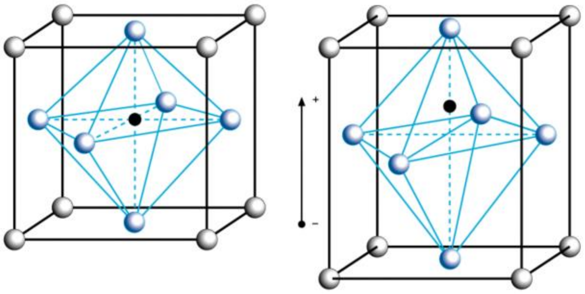

(a) **(b)**

Figure 2.11: Structure of a piezoelectric perovskite crystal, (a) before and (b) after polarisation (Moheimani & Fleming 2006)

Lead zirconate titanate (PZT), barium titanate ($BaTiO_3$), lead titanate ($PbTiO_3$), potassium niobate ($KNbO_3$), lithium niobate ($LiNbO_3$), lithium titanate ($LiTaO_3$), sodium tungstate (Na_2WO_3), and zinc oxide (ZnO) are some of the most typical piezo ceramics. Of these, PZT is the most widely used due to its superior performance. However, the toxicity of lead has raised concerns over the use of PZT. A restriction on the amount of lead present has been placed and is focused on eliminating its use eventually. Nevertheless, PZT has no rival at present. Table 2.2 above summarises the properties of different piezoelectric materials.

2.8.1.1 Lead zirconate titanate (PZT)

Lead zirconate titanate is a ferroelectric ceramic material. It has a high density (7500 kg m^{-3}), and a high Piezoelectric Strain coefficient (d_{31}) $1.8e^{-10}$ mV^{-1} and Young's modulus for PZT is 63 GPa. It has been used for the manufacture of ultrasonic devices and hydrophones. PZT has square polarisation loops leading to easy poling and de-poling.

2.8.1.2 Barium titanate ($BaTiO_3$)

Barium titanate is a ferro-piezoelectric oxide with perovskite structure. It has a very high dielectric constant and low temperature coefficient. The cubic phase of $BaTiO_3$ exhibits paraelectricity due to high symmetry in its structure. The crystal structure deforms to a tetragonal structure below Curie temperature (120–130°C) causing a spontaneous polarisation and ferroelectric behaviour. It has a high electro-mechanical coupling factor (k_{33}) of 0.50 and Piezoelectric Strain constant (d_{33}) of 190 pC/N (Villafuerte-Castrejón *et al*. 2016). It has widely been used in sensors, actuators, and sonars. The piezoelectric qualities of $BaTiO_3$ are inferior to

PZT, however, as a lead-free piezoelectric ceramic material, it is a popular choice for wearable microelectromechanical systems (MEMS) devices.

2.8.1.3 Lead titanate ($PbTiO_3$)

Lead titanate is a ferroelectric ceramic material with a strong anisotropic structure. At high temperatures, it attains a cubic perovskite assembly. Its material properties include high Curie temperature, high pyroelectric coefficient, low dielectric constant, and high spontaneous polarisation making it easy to pole (Chaudhari *et al*. 2013). It is widely used in the manufacturing of capacitors, ultrasonic transducers, thermistors, and optoelectronics (Kuwabara 1990).

2.8.2 Piezopolymers

Piezopolymers are a fascinating piezoelectric group of materials having good piezo performance and much higher flexibility than piezo ceramics. Natural polymers such as polysaccharides, proteins, and polynucleotides have shown some piezoelectric properties (Fukada 2000). The polymers have superior benefits over other materials due to their ability to form yarns and fabrics. Polyvinylidene fluoride, a piezoelectric polymer with remarkable piezo properties and suitable textile performance, is discussed below in more detail.

2.8.2.1 Polyvinylidene fluoride (PVDF)

Polyvinylidene fluoride is a semicrystalline thermoplastic polymer synthesised by the polymerisation of vinylidene difluoride. It has a monomer $-CH_2-CF_2-$ and it is 50% amorphous with a Curie temperature of 110°C.

Polyvinylidene fluoride has high tensile strength and impact properties due to its chemical structure. In small thin sections such as yarns and films, the polymer is quite flexible thus highly suitable for its uses in wearable devices. It has excellent piezoelectric properties due to high dielectric constant; hence it is a popular polymer for use in sensors and actuators, for use in wearable devices. In general, PVDF has exceptional properties such as high strength and resistance to ultraviolet radiations, high thermal stability, and high chemical resistance and weathering, therefore, it has been used in many applications in space (Tuzzolino 1996; Dargaville *et al.* 2005; Gary *et al.* 2005).

Polyvinylidene fluoride is present in five distinct crystalline phases: alpha(α), beta(β), gamma(γ), delta(δ), and epsilon(ε). The different phases are the result of different chain conformations: TTT (all-trans) planar zigzag for the β-phase, TGTG' (trans-gauche-trans-gauche) for the α and δ phases and T3GT3G' for γ and ε phases (Lovinger 1982). Of these five phases α, β, and γ are the most investigated forms of PVDF (Martins *et al.* 2014). Figure 2.12 shows the molecular chains conformations in α, β, and γ phases.

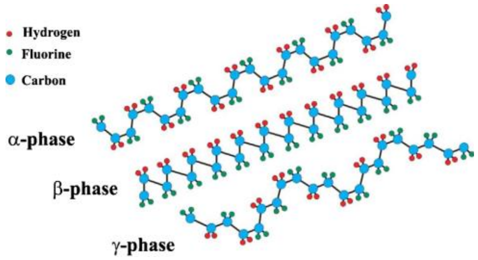

Figure 2.12: Chain conformations in α, β, and γ phases of polyvinylidene fluoride (Martins *et al.* 2014)

These different crystalline phases are dependent on preparation conditions. These conditions are summarised in Figure 2.13 which govern the final form of PVDF. The PVDF monomer unit has strong electrical dipoles moment (5–8 × 10^{-30} C.m) which is the result of electronegativity of fluorine atoms ($-(C_2H_2F_2)\ n-$) (Giannetti 2001). Of all the phases, β-phase has the highest dipole moment (8 × 10^{-30} C.m), resulting in superior piezoelectric properties over other phases. These chain arrangements, when packed in a parallel configuration, result in a net dipole moment. This dipole moment is non-existent in α and ε phases, due to antiparallel packing. In ceramic materials, dipole reorientation takes place resulting in piezoelectricity, whereas in polymers, such as PVDF, volumetric electrostriction causes a change in their shape under the application of an electric field resulting in a negative d_{33} and g_{33} (Salimi & Yousefi 2003).

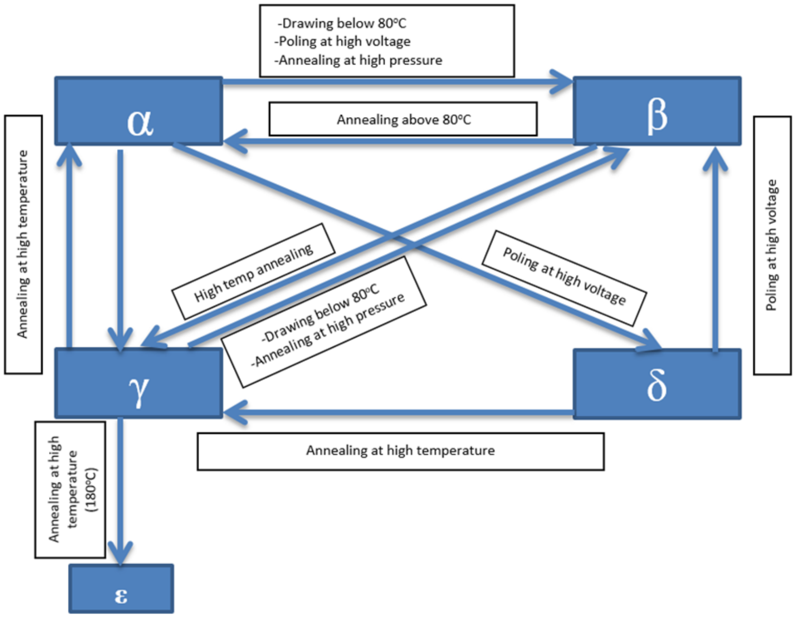

Figure 2.13: Conversion of the various phases of polyvinylidene fluoride (adapted from Esterly 2002)

The direct melting of polymer yields a semicrystalline state, which is mostly the non-polar α. Figure 2.14 shows transformation process from α-phase to β-phase of PVDF by mechanical stretching. The α and ε phases are non-polar due to antiparallel packing. Polymer chains in β, γ, and δ phases are packed within the crystalline in a confirmation which causes a global dipolar moment, therefore, these phases possess a permeant dipole. However, β and γ are more electrically active than δ. Of all the PVDF phases, the α, β, and γ are of more interest for scientific research owing to their properties.

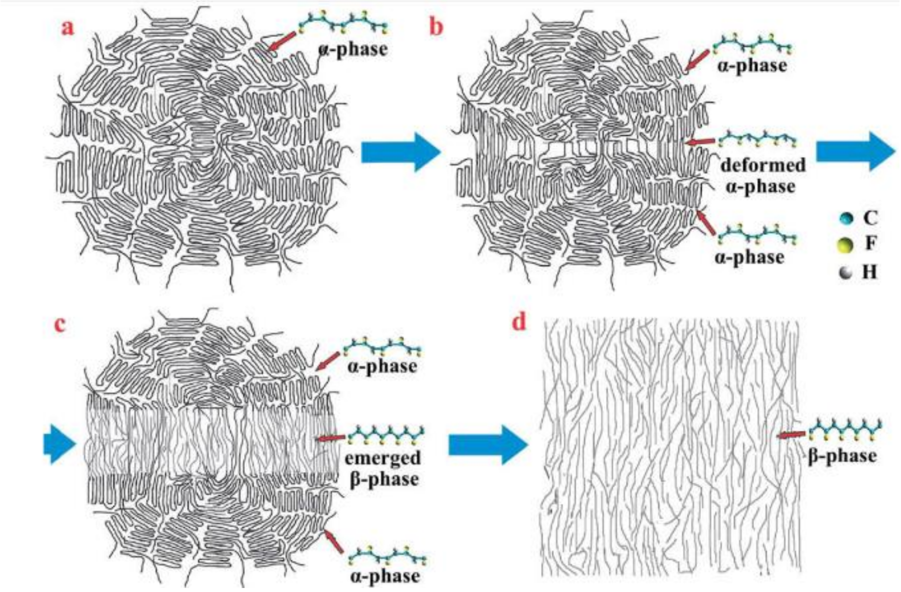

Figure 2.14: Transformation process from α-phase to β-phase of polyvinylidene fluoride by mechanical stretching (Li *et al.* 2014)

2.8.3 Piezocomposites

Some materials may have excellent piezo properties but are not suitable for certain applications due to their characteristics. Piezo ceramics are a classic example of such materials where the brittleness of these limits their advantages. In such cases, a piezocomposite can be formed consisting of piezo ceramics. These may be arranged in several shapes and geometries such as rods, diced, honeycomb, and shell structures (Tressler 1999). Also, the piezoelectric properties of certain materials can also be enhanced by the addition of some additional substances. Mokhtari *et al.* (2017) has compared the piezoelectric response of various additives used in electrospun PVDF nanofibre composites and has reported that ZnO each of the additives (LiCl, PANI, CNT, ZnO) was found to alter the piezo response. Carbon nanotubes were found to favour the formation of β-phase and have the highest output voltage whereas Polyaniline (PANI) had the least.

2.8.3.1 Nanowires

Nanowires (NW) can be described as minute structures having diameters in orders of less than or equal to nanometres (1 nm = 10^{-9} m) and can be of an unspecified length. In piezoelectric materials, these NWs are shown to enhance the piezoelectric effect. Li *et al.* (2013) have used silver (Ag) NW doped PVDF and found that the β-phase contents were enriched using these NWs.

Zeng *et al.* (2013) have used $NaNbO_3$ NWs mixed in PVDF in electrospun non-woven webs. Yang *et al.* (2012) have demonstrated the use of ZnO NWs which yielded a peak open circuit voltage of 58 V and a corresponding maximum power density of 0.78 Wcm^{-1}. Li *et al.* (2014) have also incorporated ZnO NW on PVDF using hydrothermal process. Figure 2.15 shows the schematic of growing NWs on PVDF film substrate. They have presented a pulse DC-like type generation from their nanogenerator and claim that the β-phase of PVDF was not only achieved but also maintained. Some other materials such as InN, GaN, CdS, and $KNbO_3$ can also be used in a similar manner (Lin *et al.* 2008; Huang *et al.* 2010; Lin *et al.* 2011; Yang *et al.* 2012(a)).

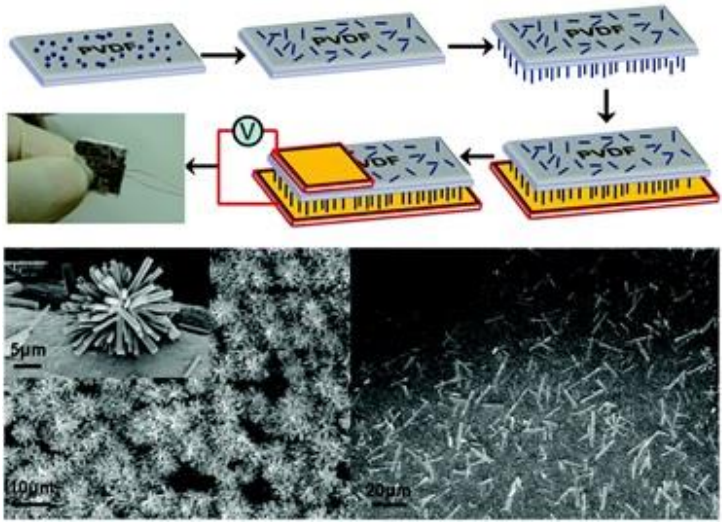

Figure 2.15: Fabrication process of the PVDF–ZnO hybrid nanogenerator (Li *et al.* 2014)

2.8.3.2 Carbon nanotubes

Carbon nanotubes are nanostructured materials with superior mechanical thermal and electrical properties. They can be classed as single-walled nanotubes (SWNT) or multi-walled nanotubes (MWNT). SWNT can be thought of as a one atom thick layer of graphite whereas MWNT as multiple concentric rolled layers of carbon atoms. They are highly useful in contributing to the properties of nano-scale structures. The CNTs are an important organic filler due to their low mass density and a large aspect ratio. These properties help in obtaining a unique combination of mechanical, thermal, and electroactive (Kabir *et al.* 2017). However, agglomeration of CNTs remains a major issue in the fabrication of PVDF-CNT composites. Levi *et al.* (2004) have investigated the properties of a PVDF-CNT matrix. They used both SWNT and MWNT and claimed that the piezoelectric and pyroelectric behaviour was enhanced remarkably over their parent polymer. Bodkhe *et al.* (2014) have reported an increase of up to 74.34% in β-phase content on the addition of CNT to PVDF matrix.

2.8.3.3 Copolymers

Polyvinylidene fluoride copolymers have been investigated for their piezo properties and for uses in various applications such as sensors. An example of a PVDF copolymer is polyvinylidenefluoride-co-trifluoroethylene, [P(VDF-TrFE)] which is a ferroelectric, crystalline polar polymer that exhibits inherent piezoelectric and pyroelectric responses with low acoustic impedance. Such properties provide an optimistic approach towards the use of these polymers for various applications in near future. Higashihata *et al.* (1981) compared the piezoelectric constants of PVDF and P(VDF-TrFE) and observed that much larger values were obtained for P(VDF-TrFE) under the same polarising conditions. The special interest in this copolymer is also due to the evidence reported by Furukawa *et al.* (1981) that the PVDF–TrFE copolymer can be annealed to 100% crystallinity as opposed to 50% in PVDF. Other copolymers have also been explored to determine an enhanced piezo effect (Poulsen & Ducharme 2010).

2.9 Manufacturing piezo textiles

There are many piezoelectric devices such as sensors, actuators, frequency controllers, and transducers, etc. (Uchino 2010). Piezo textiles could be developed using various types of piezo fibres along the lines described below.

2.9.1 Piezo fibres manufacturing

Depending on the type of manufacturing technique used for constructing piezo fabrics, either piezo fibres or yarns would be required. A piezo fibre could be either a short or continuous filament fibre having a high length to thickness ratio. The best suitable resources to produce such fibres would be flexible materials such as polymers which have the tendency to bend and form into fibres. Fibres could also be produced directly from piezo materials such as piezo ceramics. In addition to energy harvesting, the piezoceramic fibres could have other benefits as well such as better piezoelectric activity and higher working temperatures. However, for obvious reasons, ceramic fibres are less feasible for use in garment applications. Another broad area is the development of composite piezoelectric fibres. Pinet (2008) suggested that such high aspect ratio fibres could be used for *in vivo* endovascular imaging and acoustic microscopy inside acoustically opaque organs.

2.9.1.1 Wrapping/twisting

Wrapping is a type of yarn formation technique whereby parallel fibres as a thick inner core are wrapped by the wrapping material. This process imparts extra strength specially to staple filaments. The resulting yarn is a high strength structure with properties combining of both the core and wrapping material. The core may be fully or partially enveloped. In electronic textiles, this technique helps in the formation of conducting yarns. Zeng *et al.* (2013) have used wrapped conducting yarn for the formation of knitted electrodes as current collectors for energy harvesting PVDF–NaNbO3 nanofibre non-woven fabric. The core was segmented polyurethane on which a silver-coated polyamide yarn was wrapped to transfer the generated current. Huang *et al.* (2008) have also fabricated a yarn based on a wrapping technique for a piezo-resistive sensor.

2.9.1.2 Electrospinning

Electrospinning is a process of producing fabric consisting of a nanofibrous web. Figure 2.16 shows schematic of the process of manufacture. Bicomponent electrospinning technique can produce core sheath structures in which one type of material forms the core and the other forms an outer shell. Several variations are possible, including having materials side by side or one material in a different shape such as a star, pie wedge, sea islands or even a custom design across the cross section embedded in an outer sheath.

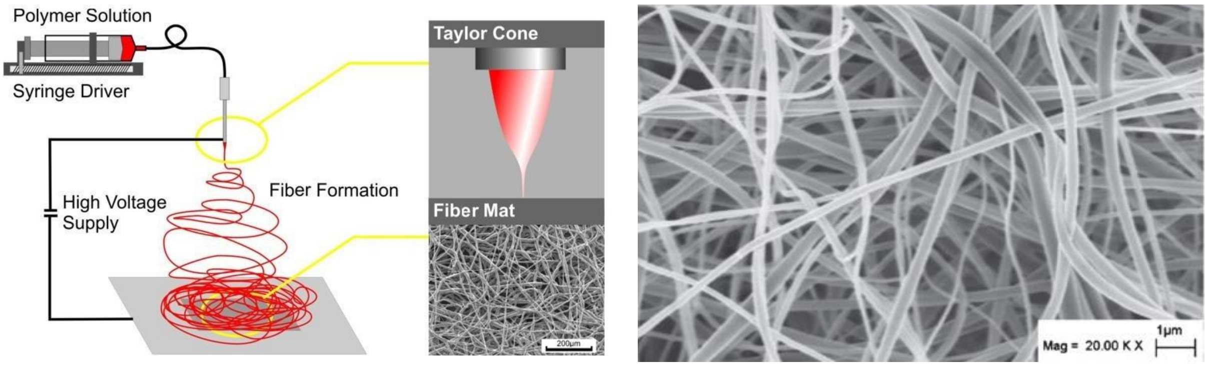

(a) **(b)**

Figure 2.16: (a) Process of electrospinning, (b) scanning electron microscope image of electrospun polyvinylidene fluoride fibrous matt (adapted from Damaraju *et al.* 2013)

2.9.1.3 Meltspinning

Meltspinning is a process of forming objects with a fixed cross section. The process requires the material to be passed through a mould or a die forming a specific cross-sectional shape. The mould could also be reshaped to accommodate shapes having different core materials. Such bicomponent fibres would be beneficial for producing crimp in some textile structures. Another important use of these materials is the manufacture of non-woven fabrics where thermal bonding is required. Thus, when heat is applied, the outer material melts to form glue hence bonding the web together. These structures could also be used to provide special core properties such as strength, conductivity, elasticity, and comfort. Glauß *et al.* (2013) produced one such PVDF fibre with a conductive polypropylene core for energy harvesting applications.

2.9.2 Piezoceramic fibres

Piezoceramic materials are chemically inert and physically strong. In fibre form, they have anisotropic structures. Usually, ceramic fibres are produced by the spinning of an organic or mineral precursor fibre, followed by heat treatment and pyrolysis (Hearle 2001). Piezoceramic fibres comprising of lead zirconate/lead titanate exhibit better sensitivity in terms of piezoelectric activity and elevated operating temperatures (Swallow *et al.* 2008). Lead zirconate titanate fibres can be manufactured by various processes such as sol-gel, viscous suspension spinning (VSSP), extrusion and viscous plastic processing, some of which are already commercially available

(French & Cass 1998; Meyer *et al.* 1998; Strock *et al.* 1999; Meister *et al.* 2003; Bowen *et al.* 2006).

Generally, ceramic fibres are expected to have high strength and stiffness and for this reason, they would be expected to be best suited for reinforcement of composite materials. Nevertheless, owing to superior electrical properties such as high dielectric constant, and high charge coefficient, such as in PZT, these materials could also be used for energy harvesting in fabrics. However, their rigidity, brittleness and, in some cases, environmental unfriendliness may inhibit their usage in textiles.

French *et al.* (1997) have reported a method for producing continuous fine PZT filaments through a VSSP. These continuous filaments can then be woven, wound, or braided and can produce large outputs from small volume fractions. These PZT fibres can be formed into 2D and 3D textiles structures for its use in composites and other areas such as vibration generation and transducers, etc. These filaments are also capable of producing large output strokes from small volumes due to the large extension ratio (20 microns per linear inch) of PZT.

Chen *et al.* (2010) reported production of PZT nanofibres aligned in interdigitated platinum wire electrodes. The structure was packaged in the soft polymer, poly-(dimethyl siloxane) (PDMS). When stress was applied to the polymer, a charge was produced between two electrodes, owing to bending and tensile stresses in the PZT nanofibres. The output voltage produced was 1.63 V with an output power 0.03 μW.

2.9.3 Piezopolymer fibres

Polymeric fibres such as PVDF have the advantage of high flexibility allowing them to be easily incorporated into flexible structures such as textiles for energy harvesting. PVDF is a lightweight, tough polymer and is available in a wide range of thicknesses. Although its thermal stability and electrochemical coupling coefficient are less than ceramics, it is still one of the most widely researched materials for engineering energy harvesting fabrics. The working temperature of PVDF lies below 100°C, however, new copolymers such as in polyvinylidenefluoride-co-trifluoroethylene, [P(VDF-TrFE)] as mentioned above have been developed, extending the working temperature to 135°C (Swallow *et al.* 2008).

2.9.4 Composite fibres

Piezocomposite fibres can be embedded in polymer matrices to form piezo fibres with a conducting core, or a composite fibre consisting of many coated layers for energy harvesting applications.

Qin *et al.* (2008) have demonstrated a textile fibre-based nanogenerator by growing ZnO NW radially around Kevlar 129 fibres using a hypothermal method. The device works as a dual fibre nanogenerator with one fibre covered with ZnO NW entangled around another fibre with gold-coated NWs. One fibre was fixed, and the other was allowed to slide over the other fibre. A short circuit current and the open voltage were obtained due to brushing motion between the two fibres. The authors claim that fibres with grown ZnO NW can be used to fabricate an energy harvesting garment. Also, the fibres when bundled could produce much higher outputs than the reported power density of 20–80 mWm^{-2}. The operating frequency of the device is also claimed to be very low, making it a viable energy harvesting device from low-frequency human movements, heartbeats, etc.

Wang & Song (2006) used piezoelectric zinc oxide nanowire (NW) arrays to convert minute mechanical energy into electrical output. The NWs were deflected using a conductive atomic force microscope tip. Due to semiconducting and piezoelectric properties of zinc oxide, strain field resulted in induced charge separation in NW as they were bended. This phenomenon can be seen in Figure 2.17 (a-d) below.

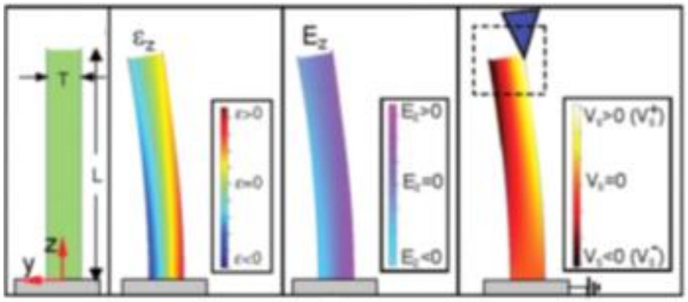

(a) (b) (c) (d)

Figure 2.17: Schematic of a nanowire and its (a) coordinate system. (b) Longitudinal strain εz distribution in the nanowire, (c) longitudinal electric field distribution in the nanowire induced by the piezoelectric effect. (d) Potential distribution in the nanowire (Wang & Song 2006)

Egusa *et al.* (2010) have developed a multi-material piezoelectric fibre consisting of shells of a 700 µm-thick layer of P(VDF-TrFE) and a 250 µm-thick layer of carbon-loaded poly(carbonate) (CPC) assembled with indium filaments and a poly(carbonate) cladding. The fibre can be used for communication applications as well as for energy harvesting.

Siores *et al.* (2010) have developed a fibre structure that can be used to convert mechanical and light energy into electrical energy. The hybrid energy conversion device consists of piezoelectric polymeric structure coated with a photovoltaic system. The fibre is claimed to be flexible enough to be converted into textiles for energy harvesting.

Glauß *et al.* (2013) have reported the development of a PVDF fibre with a conductive core. The meltspun bicomponent fibre consisted of a conductive polypropylene core (containing 10 wt % CNT and 2 wt % sodium stearate (NaSt)) covered with a PVDF sheath. The piezoelectric effects were achieved by draw winding which favours the all-trans β-phase formation.

Lin *et al.* (2013) have investigated the mechanical strength and piezoelectric characteristics of a PVDF/MWNT nanofibre developed using the near-field electrospinning technique. They have reported that the fibres formed by this method have excellent structural stability, enhanced flexibility, and a high Piezoelectric Strain coefficient (d_{33} 57.6pmV^{-1}).

2.9.5 Piezo fabrics

Piezo fabrics are the type of smart textile fabrics used typically for energy harvesting and related smart textile applications in wearable devices. These fabrics are a new class of fabrics and can be made by conventional fabric manufacturing processes which will be discussed further.

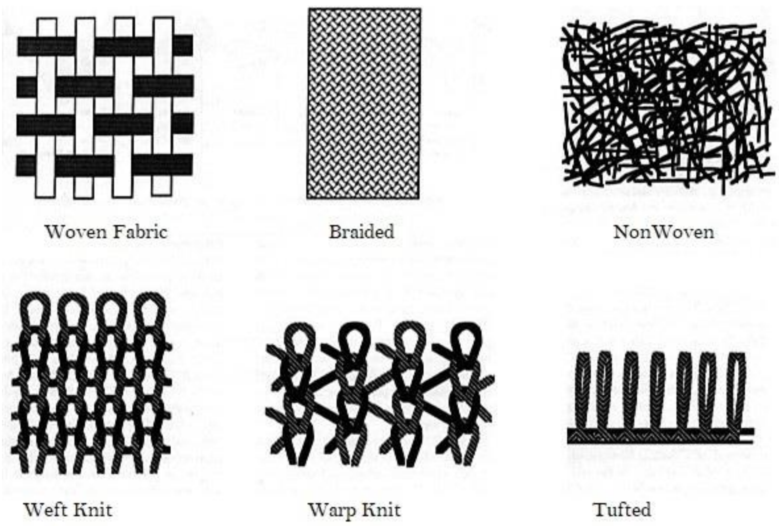

Figure 2.18: Various textile structures

2.9.5.1 Types of manufacturing techniques

Various textile structures can be employed to design a garment for embedded wearable technology. Fabric structures such as woven, knitted, braided, non-woven and other textile structures are possible depending on the requirements of the system. Figure 2.18 defines different types of fabric structures. Each type of fabric type has its unique properties which can play a major role in the functionality of the system. Most of these types of textile structure are used for electronic textiles, such as embroidery etc. Nevertheless, these structures find uses in many smart textiles used today.

A woven structure offers high strength and stability when compared with other structures. Woven structures can be single, double, or multi-layered fabrics. Hence a woven fabric can be engineered to achieve desired characteristics such as tensile strength, tear strength, shear strength, air permeability, drapeability, air and water absorbency, crease resistance, and many others (McCann *et al.* 2009). The interlacing of warp and weft yarns form a woven fabric, perpendicular to each other. There are practically endless number of ways of producing woven fabrics.

Knitted structures are made of loops of yarn interconnected with each other. The size of the loop can be altered to produce a fabric as per required characteristics. Some knitted structures offer robustness and are suitable for many technical applications. Knitted structures are mainly classed as weft knitted or warp knitted. Weft knitted fabrics are highly stretchable and hence are extremely useful for undergarments and sportswear production. They are formed by intermeshing from a single yarn in a horizontal way. This fabric is formed on a circular or flat form on the crosswise basis. The yarn is fed is one yarn at a time, leading to multiplication of several yarns as desired. A single yarn being dropped from the structure, leads to the fault also known as 'ladder' effect. Most of the weft knitting is done in tubular form.

Warp knitting is a method of fabric forming in which the loops are made in a vertical way along the length of the fabric using yarns. In warp knitting, numerous ends of yarns are being fed simultaneously, requiring larger feed packages in the form of yarn beam. The warp yarn and intermeshing of loops occur lengthwise basis in a flat, open width form. Warp knitted fabrics do not unravel as easily as weft knitted structures and have significant insulating properties. Warp knitting is highly suitable for technical textiles production such as geotextile and medical textiles. In piezoelectric harvesting textiles, knitted structures offer extensibility, which is advantageous for wearable piezoelectric textiles allowing wearer comfort.

Non-woven structures can be employed in manufacturing smart textile structures. Non-wovens are classed according to their type of manufacturing. The three main processes involved in non-woven making are web formation, web bonding and finishing process. Non-woven structures offer high absorbency, and this accounts for their enormous use in the medical industry. For piezoelectric textiles, these structures could provide higher surface areas, resulting in increased the power density. Figure 2.19 provides a comparison of various fabric types. As discussed, it can be concluded that knitted fabrics provide a higher flexibility than woven and non-woven fabrics.

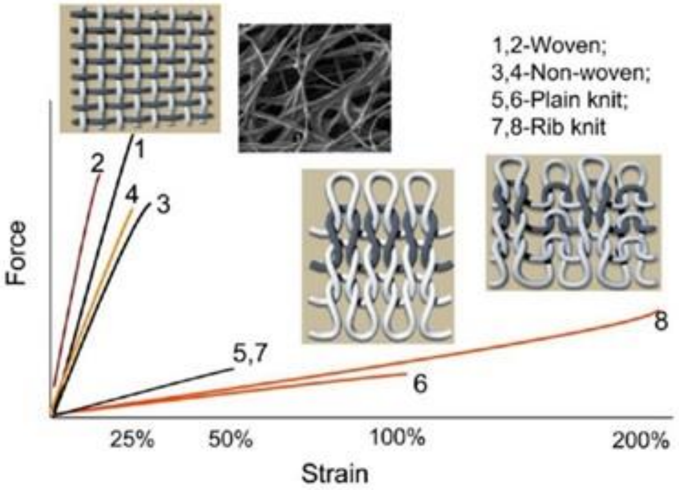

Figure 2.19: Comparison of various fabrics (Li & Tao 2014)

Structures such as braided, tufted, felts, films, foams, laminated, and bonded, stitched through, nets, embroidery, quilts, and laced structures can also be formed. Textile composites and fibre reinforced composites are also another form of textile structures consisting partly of textile materials (Corbman 1983).

A composite structure can be formed with more than one component such as non-woven and knitted structures, which combine the best features of both types of assemblies to address specific application requirements, such as enhanced performance characteristics, higher power output, device functionality, wearer comfort, etc. Yet the optimal integration of piezoelectric fibres in a wearable fabric for maximum energy output remains to be established.


(a) **(b)**

Figure 2.20: Spacer fabric (a) showing optical image (b) structural side view (adapted from Yip & Ng 2008)

A Spacer fabric is a three-dimensional knitted structure consisting of two separate knitted fabrics, joined together by spacer yarn (Figure 2.20). Spacer fabrics are widely used in different products such as car seat covers, dashboard cover, composites, anti-decubitus blankets, sports textiles, and foundation garments. Spacer fabric is highly breathable and comfortable. They offer a distinct sandwich structure which can be modified according to the requirements. The properties such as compression, air permeability, and thermal conductivity are significant to spacer fabrics and are highly useful in technical applications.

2.10 Recent trends in energy harvesting

Hyeon *et al.* (2015) have produced an energy harvesting device based on o-ply piezoelectric yarn-type generator using an electrospun PVDF–TrFE mat and a commercially available silver-coated nylon fibre. The 2D piezoelectric PVDF–TrFE mat was rolled to a 1D fibre. Then silver-coated nylon fibre rolled in PVDF–TrFE was plied with another similar fibre to make a flexible two-ply piezoelectric yarn. The yarn has been reported to generate 0.7 V when compressed.

BaTiO3 NWs and PVC polymer were used by Zhang *et al.* (2015) to develop a nanogenerator which they claim have an output large enough to power an LCD. The BaTiO3/PVC nanogenerator can generate 1.9 V output voltage and 24 nA output current.

A highly flexible piezo device was fabricated by Ahn *et al.* (2015) (Figure 2.21). Piezoelectric strips were woven on hollow tubes when stretched, maximum peak open circuit voltage reported is 51 V at a frequency of 6 Hz with power output being 850 μW.

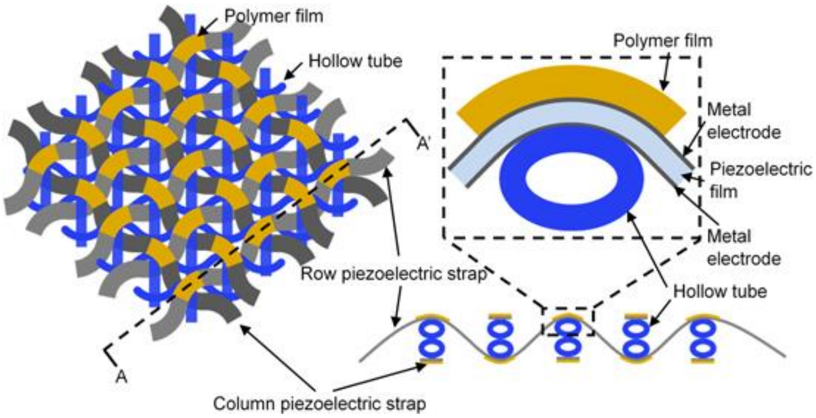

Figure 2.21: A schematic diagram of the device fabricated by Ahn *et al.* (2015)

Ray and Anton (2017) have reported a piezoelectric harvesting device using piezoelectric foam in multilayer stack configuration. The foam was excited in compression state at low frequencies. The

20-layer stack was excited at 0.5 g, which resulted in a 100-µF capacitor being charged to 1.45 V in 15 min and produced a peak power of 0.45 µW. The same setup was used 40-layer stack, which charged 100-µF capacitor to 1.7 V in 15 min when excited at 0.5 g and produces a peak power of 0.89 µW.

Amini *et al.* (2015) have employed generalised Hamilton's principle for electro-mechanical materials to develop finite element models for simulating the functionally graded piezoelectric harvesters in unimorph or bimorph (series or parallel connections) configurations. The predictions of the results of the finite element models are verified by that of the analytical solutions. They analysed the produced voltages, with different power indices (n) and load resistance values of functionally graded (FG) harvesters (unimorph and bimorph). They have reported that the value of n influences the produced voltage and power.

Zabek *et al*. (2016) have modelled PVDF films for thermal energy harvesting using micro-sized patterned meshed electrode. They claim that the use of meshed electrodes has significantly improved the open circuit voltage (from 16 to 50 V) and closed-circuit current (9–32 Na).

Another fabric nanogenerator has been proposed by Pu *et al.* (2016) using electric induction effect of electrified charges in the parylene film results in the flowing of electrons between the Ni-coated cloth strip and parylene-Ni-coated cloth strip. The generator produces an open circuit peak-to-peak voltage of 40 V with contact-separation at 5 Hz.

Jung *et al.* (2015) have proposed a flexible piezoelectric generator with a curved structure. The device consists of PVDF as the piezoelectric layer, joined on the curved polyimide (PI) assembly applied force across the piezoelectric layer. The harvester produces ~120 V of peak output voltage and ~700 µA of peak output current during one cycle.

Kim *et al.* (2017) have developed an energy harvesting device based on PVDF and PDMS. The device has the potential to perform in multiple directions. The harvester was tested in the direction of 0°, 45°, and 90° with an input force of 4 N at 2 H. The output was reported at 1.75, 1.29, and 0.98 V, respectively.

2.11 Flexible piezoelectric energy harvesting

2.11.1 Fabrics

To date, numerous knitted, woven, non-woven, and composite structures have been employed to produce energy harvesting fabrics. However, Vatansever *et al.* (2011) suggest that weaving is the best possible method of fabric production for smart textiles. Using piezoelectric, conductive, and conventional textile fibres, different arrangements of warp and weft yarns are possible for the production of suitable woven fabrics. However, the conductive fibres must interweave with the same pole of piezoelectric fibres in order to avoid a short circuit. The woven fabric suggested by Vatansever *et al.* (2011) can be used to harvest energy using mechanical stress and strains.

Magniez *et al.* (2013) have demonstrated a method to produce piezoelectric woven fabrics from melt spun PVDF fibres, which were spun using a Busschaert bicomponent extruder. The PVDF fibres were assembled with conductive fibres and were integrated into various woven structures such a plain weave and 2 × 2 twill weave. A non-conducting nylon yarn was used as insulation between two electrodes to prevent short circuiting. The warp yarns were PVDF and the weft yarns were silver-coated nylon. The fabrics were tested for electrical output using a 70 N impact force at a 1 Hz frequency and a maximum output of 6 V was produced.

Bai *et al.* (2013) have also demonstrated woven nanogenerators made from ZnO NW as warp and ZnO NW with a Pd coating as weft. The Pd-coated wires are attached to a slider while the other wires remained fixed. As the slider moves, the NWs on fixed wires were deformed by friction causing a peak output electrical current of about 17 pA.

Soin *et al.* (2014) have produced a 3D knitted spacer piezo fabric. Meltspun PVDF yarns as spacer yarns were incorporated between two knitted faces made of silver-coated polyamide yarns. They claim the piezo fabric can produce a power output density of 1.10–5.10 μWcm^{-2} at applied impact pressures in the range of 0.02–0.10 MPa.

Fang *et al.* (2011) have demonstrated a simple, efficient, cost-effective, and flexible setup to produce piezoelectric fabrics through an electrospinning process. A PVDF solution comprised of PVDF pellets in dimethylformamide (DMF) was electrospun at 15 kV to produce a nanoweb. The nanoweb was sandwiched between two aluminium electrodes to obtain an output voltage. Under

1 Hz compressive impacts, the average peak voltage output obtained was 0.43 V. When the impact frequency was increased to 5 Hz, the voltage output became 2.21 V. A further increase to 10 Hz produced a higher output voltage of 6.3 V.

Apart from manufacturing piezo fabric through above-mentioned textile processes, various materials and/or structures could be combined to produce composite fabric assemblies. Such a structure could be a sandwich structure with one layer being an energy harvesting assembly and the other layers could function as a current collector, reinforcement, or insulation assembly. The piezoelectric fibre composite developed by Williams *et al.* (2002) is comprised of piezoelectric fibres, such as those produced by Cass *et al.* (2003), impregnated in a polymer matrix. This composite resulted in superior properties and higher efficiency due to increased surface area.

Zeng *et al.* (2013) have demonstrated a fibre nanogenerator made from PVDF-$NaNbO_3$ nanofibre non-woven web which is capable of generating a peak open circuit voltage of 3.4 V and a peak current of 4.4 µA in a cyclic compression test. The non-woven web was sandwiched between elastic conducting knitted fabrics made from segmented polyurethane yarns wrapped with silver-coated polyamide multifilament yarns. The whole device was packaged between layers of PDMS to enhance its mechanical robustness.

Swallow *et al.* (2008) have reported the formation of a piezoelectric fibre composite-based energy harvesting device intended to be used as a glove for tremor suppression. They have investigated the use of both PVDF and PZT in fibre composites to produce electrical outputs. The piezoelectric fibre composite containing PZT produced a power output of ~11 µW, as compared to the power output of 0.3 µW of the PVDF material alone.

2.12 Optimisation of fabrication for wearable energy harvesting

Designing a wearable electronic device is a complex exercise. Depending on its intended end use and the technology to be incorporated, several factors should be considered. To meet the needs of the end-user, expertise from textile specialists, modern day technologies, and electronics, skills of clothing and fashion designers and eventually the capability of the manufacturer should be brought together in order to utilise its maximum potential (McCann & Bryson 2009). Ideally, the wearable energy harvesting device should be thin, elastic, and integratable with skins in addition to its required performance output, to realise a self-sustainable system (Gong & Cheng 2017).

Since its realisation in the 1990s, wearable computing has come a long way. With the advancement of computing technologies, it seems that there are no boundaries. From health monitoring devices such as garment-based electrocardiographs (ECG) (Gopalsamy 1999), respiration and temperature monitors, to other wearable computing devices such as MP3 player jackets, textile keypads, electronic ski suits, smart shirts and much more, are applications that combine textiles with electronics (Moeli 2002). The terms E-textiles, smart textiles, wearable electronics and Textronis are some of the terms used to describe such kind of devices. Smart textiles for wearable technology utilise several recent developments which make it possible to incorporate electronics with textiles. Conductive textile materials are one example of a new technology which is widely used in these applications. Conductive textile materials, including conductive fibres, yarns, and fabrics, are commonly used for flexible sensors, electromagnetic interference shielding, dust and germ-free clothing, data transfer in clothing, as well as camouflage and stealth technologies for military applications. Conductivity in textiles is imparted by the addition of carbon, steel, nickel, or silver, in the form of wires, fibres, or micro- and nanoparticulate matter. Conductive polymers have been developed by the processes of solvent spinning, solvent casting, or spinning as blends with conventional polymers. They can be used as coating materials, or embedded particles in fibres. A more recent focus has been on the use of conductive inks which can be employed to impart conductivity to specific areas on a garment. Conductive particles such as nickel, silver, gold, carbon, and copper can be added to conventional inks which can then be used to form patterns by using various printing techniques.

The use of flexible sensors in wearable electronics has reduced discomfort while wearing the garments. The size of the sensors can now be reduced particularly with the advent of micro-technologies and nanotechnologies. Flexible sensors also are very suitable when the contact surface area is of prime importance. Optical fibres or conductive fibres embedded within a fabric can be useful for wireless technology integration in the textiles for data transfer as they are unaffected by electromagnetic radiation and do not generate heat. As conventional batteries are bulky, there was a need to develop some alternate forms of energy source for these devices. Solar cells have now been developed which utilise textile materials as the substrate. Research utilising piezoelectric materials to harvest energy is also underway (Tang 2006).

As new technologies are being introduced, the problems associated with the design of wearable electronic devices are also evolving. The major problems that occur in designing wearable electronics include the incorporation of electric junctions into the device when a garment must undergo processes involving mechanical stresses, washing, ironing and some other threats such as moisture, sweat, temperature, light, some chemical substances, dimensional changes, and creasing. The electric supply to a device is also a major problem as the traditional batteries are large and heavy. However, ambient energy sources such as photovoltaic, thermogenerators, and piezoelectric device have a small capacity. Hence, it is necessary to develop systems where these problems can be overcome to produce an ideal smart textile complying with the comfortability and functionality of the device (Gniotek 2004). The connections in integrated circuits in textiles also need to be modified to overcome the problems mentioned above.

In designing wearable devices, there are several factors to be considered. The focus should be that it does not hinder the wearer’s movements unless intended for that purpose. Also, other important factors include the service life, reusability, the element of design, comfort level, and functionality. The placement of the components highly affects garment comfort and appearance. Table 2.3 shows a summary of design guidelines laid down for wearable systems.

Table 2.3: Design guidelines for wearability (adapted from Gemperle 1998)

Guidelines for wearability	
Placement	Explains where extra components should be placed on body
Form Language	Defines shape for additional components
Human Movement	Considers the dynamic parts of human body structure
Proxemics	Perception of space by human brain
Sizing	Should be able to fit several users
Attachment	Extra components that can be fixed to the body comfortably
Containment	Considering what is inside the form
Weight	Balance across the human body, should not hinder human movement
Accessibility	Additional components should be easily approachable
Sensory Interaction	Active or passive interaction between user and component
Thermal	Thermal comfort to the wearer
Aesthetics	Appearance or perceptual appropriateness
Long-term Use	Effects of prolonged use of the body and mind

Whenever a garment is designed for many different wearers, the knowledge of diverse sizes and shapes is required. Some of the areas in the human body are quite feasible for placement of additional components on the body such as non-moving parts with large surface areas. The additional components should be designed in such a way that they do not have any sharp edges and conform to body contours. The components should also have minimal weight to reduce discomfort. Limbs and other parts of the body should be unrestricted in movement. It would be inconvenient to place large components on the body area. Any special requirement such as when the user has to interact with an extreme environment has to be considered when designing apparel (Haanikainen 2006). It is also feasible to utilise places on the body such as wrists to place heart beat sensors (Martin 2002). It is also suggested to use the neural networks for ‘event prediction’, generating alert signals for integrated communication wearable systems, thus creating a new class of intelligent textiles (Lymberis 2008).

2.13 Testing of piezo fabrics for energy harvesting

Since their discovery, piezoelectric films, fibres, and fabrics, etc., have been investigated for their outputs via different methods. The testing methods vary in terms of the intended end use, type of force applied, and fabrication methods.

Most commonly for shoe inserts, it is understood that the heel strike would mimic the impact of force acting on a body. Therefore, impact testing is one of the most preferred test methods for energy harvesting. It has also been used to test the effect of a force applied on the output power in piezo fabrics (Vatansevar *et al.* 2012; Mangniez *et al.* 2013) have used an Instron with a drop weight of 1.02 kg at several different heights to test the voltage output by a piezoelectric fibre composite.

Dynamic impact force pulses produced with restrained pulse pressures and a range of frequencies can be used to investigate possible power outputs (Zeng *et al.* 2013). Soin *et al.* (2014) have designed an experiment where they used an Instron system compression test by attaching a compression plate to the load cell. The impact pressure applied was in the range of 0.02–0.10 MPa and this generated an output power density of 1.1–5.1 μWcm^{-2}.

Apart from these popular tests, Yun and Yun (2013) have used a method in which they stretched a woven PVDF fabric. The fabric was fixed at one end and the other end was mounted on a custom designed linear actuation system. The movement of the actuator system was controlled using a stepper motor which controlled the distance moved and the operational frequency. An oscilloscope was used to record the output voltage. It was claimed that a peak output power of 1.1 mW was achieved using 20% stretching at 8 Hz (~0.63 $mWcm^{-2}$).

Fang *et al.* (2011) subjected their electrospun PVDF fabric to 5 Hz repeated compressive impact and release cycles. They received steady outputs and also observed that with the increasing impact frequency, the output voltage increased. Yang and Yun (2012) have produced a flexible wearable shell structure using PVDF in fabrics. As the intended application of the device was for elbows and fingers, they applied bending forces to the structure through a custom designed linear actuator system. The bending angle was constant at 80° and the folding and unfolding frequency was 2 Hz.

2.14 Designing for comfort

The general idea behind on the go energy generation is the continuous power supply for applications such as portable devices for the public or for the military personnel use. If the wearer of this generator has slight discomfort, they are not likely to wear it over long periods of time and eventually would cause the concept to fail. Therefore, it is important to consider several factors when designing the generator such as the location of the harvester, the weight of the device, wearability, useability, and safety, etc.

2.15 Applications

2.15.1 Energy requirements

During recent years, there has been a significant increase in demand for powering on-person devices. As the sizes of these devices shrink, the energy requirements have also been reduced. This miniaturisation has also encouraged the emergence of embedded wearable applications. Hence, overall decreasing size and power requirements both present a feasible notion for energy harvesting using various power sources. Several modern wireless protocols such as Bluetooth transceiver have sub-watt power consumption (Sebald *et al.* 2008). More recently, concession setup and data transfer as fast as 3 ms has also been supported using Bluetooth Low Energy technology (BLE) (Bluetooth.com 2017).

Table 2.4 shows the energy requirements for several portable devices. It is worth mentioning here that the requirements shown can vary depending on different manufacturers, model, and usage. Some of the devices require only a few microwatts.

Table 2.4: Energy requirements for portable devices (adapted from Vullers et al. 2009 and Alto 2012)

Portable Device	Power Consumption	Energy Autonomy
Quartz Watch	5 µW	5 years
Cardiac Pacemaker	50 µW	7 years
Wireless Sensor Node	100 µW	Lifetime
Hearing Aid	1 mW	5 days
MP3 Player	50 mW	15 h
Smartphone	1 W	5 h
Tablets (iPad)	1–2 W	24–48 h
Laptops	50–80W	3–6 h

2.15.2 Feasibility of human powered wearable devices

The ever-growing demand for green energy has made energy harvesting from renewable sources a mandatory requirement. The rapid increase in miniaturisation of electronic devices would mean that in future the power requirement would go down to a few microwatts. Hence, energy scavenging from microwatt-based generators could become highly attractive. More important is the fact that the energy is not only renewable but also available all the time, especially for handheld devices. This can be termed as 'energy on the go' and can be available in highly indigent circumstances.

The first device utilising human motion for energy scavenging was a self-winding wrist watch invented in the 18th century. Since then, energy scavenging has been utilised for watches for many years. Starner (1996) was the first researcher to describe the possibility of piezo energy harvesting through human motions. He reported that the simple human motion such as walking produced about 67 W of energy. This 'lost' energy with about 12.5% piezoelectric material conversion efficiency could be translated into 10 W of power which is more than adequate to power milliwatt-based wearable devices. Since then, many studies have been carried out in an attempt to convert this 'lost' energy into useable electrical power. In the human motion, energy also is available through other continuous and discontinuous activities such as breathing and heartbeats (Gonzalez *et al.* 2002). Breathing allows energy harvesting via exhalation as well as changes in chest perimeters. Changes in blood pressure and heart beat are another important source of energy harvesting for implantable devices such as pacemakers (Karami & Inman 2012). Of all the discontinuous movements, walking provides maximum power outputs when compared to the rest of the body. This area has been widely explored by researchers.

Kymissis *et al.* (1998) integrated different harvesters a PZT unimorph (a cantilever that consists of one piezoelectric layer and one inactive layer), a PVDF stave and a rotary magnetic generator into the heel of a shoe to harvest impact energy. They reported an output of 80 mW achieved using the PZT unimorph. Shenck and Paradiso (2001) have also discussed the use of piezoelectric shoe inserts to produce energy. It is claimed that the upper limb movement could also be used to harvest power up to 60 W (Gonzalez *et al.* 2002). Yang and Yun (2012) have demonstrated a textile-based flexible energy harvester that can be worn on fingers and elbow joints. Waqar *et al.* (2013) have also presented a parametric study of finite element simulations of piezo strips on fabric. Such fabric could be used to harvest energy merely from vibrations. Typing is another possible energy harvesting source where impact energy could be transferred to useable electrical energy (Berridge 2011). Bhaskaran *et al.* (2011) have demonstrated a method to produce energy harvesting key boards and are working on integrating it into laptops using piezoelectric thin film technology. Energy harvesting from peculiar sources, such as ear canals, have also been explored by some researchers using flexible PVDF sheets. Delnavaz and Voix (2013) have fabricated a device mounted in the headset and placed in the ear canal. The device deforms during mouth movements, giving electrical outputs.

Allameh *et al.* (2007) have proposed to power a drug delivery system that delivers the drug to localised ailing cells. The system could be powered by the movements of body fluids or solids. Energy harvesting tiles are now commercially available (http://www.pavegen.com/home), which are being installed at public locations such as train stations, and other main transport hubs. Energy harvesting tiles mounted at West Ham underground station, London generated enough power to light up the station. Energy harvesting floors are already installed as dance floors in clubs such as Club Surya in London which claims to be an eco-club (Henderson 2009).

Recently, Young Cha (2017) has theoretically investigated the idea of harvesting of energy from flexible piezoelectric materials during walking. The author estimated the harvested power from PVDF and derived the contour maps with respect to the harvested power as a function of the load resistance and walking frequency. It is suggested that for the same walking cycle, the frequency for each body part is different. Furthermore, the hip is found to have the fundamental harmonic effect followed by the ankle. The effect is comparable to the knee.

Knee-based harvesting can offer uninterrupted, especially for combats, and emergency power sources. Commercial knee harvesting devices such as the PowerWalk™ are already being used (Bionic Power Inc. 2017) and claim to be producing up to 12 W of useable power.

2.15.3 Medical, military wireless uses

There are numerous possible applications of energy harvesting through flexible textile materials. Edmison *et al.* (2002) described an initial prototype of a glove for user input that employs piezoelectric elements to sense the movement of the hands to illustrate the design issues involved in using piezoelectric material. Swallow *et al.* (2008) developed a micro composite-based energy reclamation device for gloves. This non-invasive system can be used to harvest waste mechanical energy produced and can be utilised to suppress tremors or be directly stored. A similar principle has been used by Zieba *et al.* (2010) to measure breathing frequency and develop an energy harvesting vest. Wang (2012) has also proposed harvesting respiration energy using piezoelectric polymer thin films.

Soldiers during combat need the energy to power up many accessories they carry. Wireless networking, such as cellular radio and satellite communications, all require a source or power. The weight of the batteries, as well as their limited life, are critical factors for a soldier who may be relying on them for communication, light, and in extreme cases, survival chances. Military equipment such as night goggles, GPS systems, radios, etc., all need batteries. Hence, a soldier may need to carry around a number of such devices weighing 16–20 lbs (7.26–9.07 kg) (Johnson 2012).

In such cases, the energy harvesting textiles could prove to be a breakthrough. Advances in solar energy harvesting have proven to be helpful where many companies are now trying to weave flexible solar panels into a soldier’s uniform (Daileda 2013; He *et al.* 2013). Yet, it is stated that the power outputs could vary during the day due to a soldier's movements in a battlefield under shady areas. Conversely, a soldier could benefit from the darkness at night and be even be more engaged. Being in continuous motion at all these times may provide a continuous source of ambient energy to harvest. Furthermore, batteries are a finite source of power supply and could be worn out when they are needed the most. Such an event in remote areas or in the case of an unexpected prolonged stay in certain situations, such as during warfare or catastrophic circumstances, could prove to be life threatening. Energy harvesting textiles could be employed independently or in addition to flexible solar panels, increasing the amount and availability of energy. Energy harvesting knee braces (Bionic Power Inc. 2017) and shoe inserts are also available.

Granstrom *et al.* (2007) have proposed an energy harvesting backpack, capable of generating 45.6 mW of power output. The backpack has flexible PVDF films integrated into the shoulder straps used to convert mechanical strains into electrical outputs.

Antennae can be integrated into a person's clothing (Massey 2001). Such a system could be utilised for obtaining locations on a soldier's movement. It is also extremely useful for people working or holidaying in remote areas. The antenna would require only a small amount of energy and could be powered by human movements through piezo fabrics, hence providing location signals at all times.

In the medical field, many textiles-based devices using piezoelectric materials as sensors and actuators have been developed. Medical ECG chest, sleep monitor, patient care tremor suppressor, and a breast cancer detection bra are some of the many devices that employ various forms of piezo materials. Several portable types of health monitors are used for observing patient conditions. Such devices constantly need power supplies. The weight and limited life of batteries could prove to be life threatening in some cases. Another important concern is the toxicity of these batteries (Bernardes *et al.* 2004). The battery systems contain electrolyte which especially in the case of lithium batteries are mostly toxic and flammable. Recycling of these batteries could provide benefits as suggested by Bernardes *et al.* (2004), but for applications such as those described above for military personnel and medical applications, it is not feasible. In these events, energy scavenging through human motion could potentially eliminate the need for battery systems and provide an efficient and reliable power source.

2.16 Challenges/gaps in Polyvinylidene fluoride energy harvesting

The flexible energy harvesting to date faces many challenges, and despite being a bright area for future, the research is limited. The performance of these devices is mostly limited to micropower and efforts are being made to increase the outputs. However, portability and size of these devices make them extremely promising for new technologies. Furthermore, in this era where global warming has reached extreme levels, the idea of zero toxicity is remarkable and opens a huge world of possibilities. Nevertheless, it is needed to improve the efficiency of these devices to make them a reality for every household.

2.17 Future trends

There is a genuine need for energy harvesting for on-person wearable devices. Recent developments in piezo fibres, fabric architectures, enhancement of piezo properties, etc., present a promising future for powering electronics. Metal powders, NWs, nanotubes, and copolymers have already been used to enhance piezoelectric properties. There are still possibilities of exploring other organic and inorganic materials producing hybrid piezoelectric structures to improve piezo properties. Another focus is on reducing toxicity from these fabrics, such as lead (PZT etc.), which has made materials like PVDF a significant alternative option. Several types of research have been conducted on the production of piezo fibres using various processes for energy harvesting such as melt spinning, electrospinning, etc. The focus currently is on faster, cheaper, and more reliable methods for production of piezo fibres, and the corresponding piezo fabrics.

Further work will continue to enhance the dielectric constants of materials used for piezo fabrics, improvements in fabric architecture and the easy integration of these piezo fibres with other flexible conductors, sensing and actuating fibres can lead to a new generation of smart fabrics. Smart fabrics could possibly reduce the need to provide parasitic batteries, especially for on-person low power devices.

There are still problems regarding the durability, laundering, and robustness of piezo fabrics. Zeng *et al.* (2013) have claimed to enhance the durability of peizo fabrics by encapsulating the whole structure in PDMS packaging. If, somehow, the whole piezo fabric could be made washable without damage, it could bring the next breakthrough in piezo fabric energy harvesting and its integration into smart textiles.

Another important research area which requires further exploration is standardisation of testing of these fabrics. Most of the researchers so far are using different testing methods for investigating the electrical output. The locations of these fabrics on a person and how much strain is imparted in various body locations will be one of the factors dictating the outputs.

Due to the ever-increasing user demand for wearable electronic gadgets and the reducing power requirements for these devices, a much-needed approach is for textile technologists to work closely with electronic manufacturers in order to make both worlds compatible. Multidisciplinary teams consisting of designers and engineers could provide productive results to change the functional profile of textiles. Working closely with end-users and understanding their needs (i.e. military personnel, peers, family, older people, and patients) would also help us shape their lifestyle by designing these fabrics to meet their aspirations.

Finally, the ultimate goal would be the adaptability and user friendliness of these fabrics in which form and function are integrated. In addition, size, shape, proportion, comfort, fit, combined with the overall aesthetic style of the fabrics are achieved.

2.18 Research gaps

Since the discovery of piezoelectric effects in the 19th century, much progress has been made towards the realisation of its uses for viable energy generation. One of them is the development of piezo textiles for energy harvesting. From piezo fibre development such as piezopolymers, piezo ceramics, and composite fibres to hybrid piezofabrics incorporating electrodes, piezo, insulating and conducting fibres, the notion of textile as a flexible material for covering the human body has been redefined.

This chapter has covered at length, the various aspects of piezoelectric energy harvesting fabrics as an alternative power source, especially for low energy requirements. Various developments in the field of energy harvesting fabrics in terms of fibre production and fabric architecture have also been reviewed. An insight into existing and potential materials for these fabrics, and the design parameters for fabric architecture and garment production have also been summarised. The feasibility of powering devices through human motion has been explored and is expected to become more focused on changes in lifestyles.

The need for powering on-person wearable devices can be easily addressed through textiles which potentially could supply energy for data communications, health monitoring, and emergency power supply for survival and surveillance tactics in military and medical sectors. Moreover, portable devices such as mobile phones, note pads, and GPS etc., all need reliable, consistent, and sustainable sources of power, especially as a backup in catastrophic situations. In such cases, energy scavenging fabrics could provide an abundant source of power any time of the day (photovoltaics would only be active in daylight) as a standalone system, or part of an integrated hybrid power system incorporating a photovoltaic power system and storage media. These fabrics are envisioned to make the users independent and enhance their autonomy in a power dependant world.

3 Finite Element Simulations in textiles

3.1 Introduction

The main idea behind The Finite Element Method (FEM) is that a randomized body is divided into various smaller parts, referred to as elements. In this work, FEM analysis has been used to optimize the design parameters of a device for poling of Polyvinylidene fluoride (PVDF) yarns to enhance β-phase formation. As shown by Martins *et al.* (2014), stretching increases the β-phase percentage from 37 to 80. The poling of these yarns further enhances the phase output from 80 to 83. Therefore, computational studies were carried out to simulate electric field in poling device under high electric field as shown in section 3.3 (dual field analysis of poling device of PVDF yarns for energy harvesting applications). For these simulations, the finite element simulations-based software, ANSYS has several modules such as, electromagnetic field analysis which includes high and low frequency, cable bundle electromagnetic compatibility (EMC), printed circuit board (PCB), signal integrity (SI) and others. Such simulation methods have been utilized by Chen *et al.* (2014) in strain gauges, conductor surface field strength, electric field distribution in high voltage transmission line assembly to optimize the size of fixture structure and assembly of each part. They were successfully able to improve the design by using a curved chamfer, to avoid the discharge at the tips under extreme temperatures and increase the fillet radius. Huang *et al.* (2017) were able to increase the maximum electric field in a Medium frequency transformer using six kinds of typical non-interleaved windings. These simulations could be used for improving electric field distribution in a transformer.

Another major area of interest is the scavenging of energy by using PVDF yarns and PVDF films incorporated in flexible fabrics. To date, many research studies have been carried out to simulate the fabric to investigate their performance based on their properties. Farnsworth *et al.* (2014) have modelled a cantilever-based piezoelectric energy harvester aimed at optimizing the targeted resonant frequency response against the power generation efficiency. Almusallam *et al.* (2013) have modelled a screen printed piezo energy harvester. Their modelled harvester produced the output of 3V. The actual harvester open circuit voltage was 2V lower than predicted value owing to reduced poling field for the device. Wu *et al.* (2015), have demonstrated the use of ANSYS to optimize a cantilever beam for energy harvesting using human motion. They studied the length, width, and thickness, to determine a geometry which has a resonant frequency close to a human motion frequency range of 2Hz. The experimental results obtained are in agreement with the proposed geometry giving an open circuit voltage output of 120mV at a frequency of 20.4 Hz using vibration acceleration of $2m/s^2$.

In a study conducted by Li *et al*, (2015) they have proposed a low frequency and wide-bandwidth harvester design with quintuple piezoelectric cantilever lead zirconate titanate (PZT-5H) beams. The harvester has been modelled in COMSOL to obtain the resonant frequency using the Eigenfrequency Study and the output voltage performance was calculated using, ‘Frequency Domain Study’. The proposed energy harvester achieves a maximum open-circuit voltage of 65V, and maximum output power 4.5 mW. A similar study was carried out by Kaur *et al.* (2016), utilizing COMSOL Multiphysics, to simulate various shapes and materials of a piezoelectric energy harvesting system. In addition to (PZT-5H,) they have compared aluminium nitride (AlN), and barium titanate ($BaTiO_3$) to determine the power output. They observed that the maximum power output of 382.5 µW was achieved using barium titanate with a rectangular shape geometry. Tien and Goo, (2010) have utilized ANSYS to conduct a finite element analysis of a piezo-composite generating element for stress distribution. The piezo-composite consists of piezoelectric lead zirconate titanate ceramic (PZT), layers of carbon/epoxy, and glass/epoxy cured at an elevated temperature. The variations in the layup process of this piezo-composite significantly affect the voltage outputs. Moreover, residual stresses are also found to alter the voltage outputs after curing process. Seo *et al.* (2015) have presented FEM simulation on piezoelectric energy harvester (PZT) and a flexible body beam. They indicated that the smaller beam spring constant k_2 leads to lower resonant frequencies. It was also found that by using a low spring constant (k_2), the first two resonant modes can be localized. They also concluded that a flexible structure reduces the multi-mode resonant frequencies within a more realistic vibrational range.

The finite element method-based approach was also undertaken by Chen *et al.* (2015), followed by experimental validation, to propose an optimal frame design for energy harvesting. The designed harvester can generate 20.7mW/g^2 at the resonance frequency of 160Hz for a single stage harvester and 487mW/g^2 at the resonance frequency of 38.9Hz as a dual stage harvester. Lee *et al.* (2009) have modelled a PVDF energy harvester mounted on brass resonator to harvest ambient energy into electrical power. The harvester has been verified through modal analysis of mode 1 to 4. The frequency of 1st mode was found to be 400Hz which was equal to the resonant frequency of the diaphragm attached.

3.2 Piezo responses of fabric

In this research, a novel approach has been taken to determine the electrical voltage and power outputs through simulations of energy scavenging fabrics. Some assumptions have been made and are highlighted where applicable. The experimental validations of the results prove that they are in accordance with the simulated outputs.

Computational simulations in the mechanical package of ANSYS have been carried out to investigate the viability and production of energy harvesting fabrics. The output from these fabrics was highly dependent on the variables and hence these results are adaptable. However, the investigations have shown that these results can be predicted based on the validations that were achieved. The simulations have been used to optimize the design of energy harvesting fabric. ANSYS 14.0 to 17.0 were used to run these simulations. The findings of these simulations have since been used to answer many of the ambiguous questions in research such as their electrical response based on mechanical stimulus. The focus of the research was to obtain the piezo-electrical response of these fabrics which is innovative. This practice would help in not only designing a suitable energy harvesting fabric but also customizing it to localized body parts with higher energy outputs.

3.3 Dual field analysis of poling design of Polyvinylidene fluoride fibres for energy harvesting applications

This study presents the dual field simulations of various methods for in-line poling of continuous filament PVDF fibres. The model was examined for various hole diameters, plate distance and direction of poling. The model was validated using Fourier-transform infrared spectroscopy (FTIR) results of various samples to confirm the presence of β-phase. The results obtained shows enhanced energy outputs while using the optimized parameters for the poling design.

As discussed in Chapter 2, Piezoelectric materials become electrically polarized when subjected to a stress, resulting in a change in dimension owing to variation in bond lengths between cations and anions due to applied stress. This direct piezoelectric effect is the phenomenon used in mechanical-to-electrical energy conversion, it is applied in energy harvesting, sensing or vibration damping, especially in aerospace industry. When a ferroelectric material is heated above the Curie temperature and then allowed to cool down, several domains are formed consisting of continuous crystallographic orientation and polarization. These domains are self-compensated under the absence of any forces due to an electrical field, hence resulting in a zero-net polarisation. Therefore, in order to achieve piezoelectricity in such materials, it is possible to re-orientate these domains by applying a high electric field (Anderson *et al.* 2011).

In this study, the PVDF yarns are poled by passing between two aluminium electrodes having a potential difference of 6kV. For this, an ANSYS simulation was performed to determine the optimum shape of the electrode such as a slit or a hole configuration, dimensions of that configuration, and spacing between electrodes.

The equation for a constant electric field, similar to that between two parallel plates is:

$$E=V/d \qquad (3.1)$$

E represents the field energy; V is the voltage applied to the plates and d is the distance between them, measured in meters. Hence, the units for E are volts per meter.

From this equation, it can be seen that as the distance increases while keeping the voltage the same, the electric field intensity will decrease and vice versa. Also, if the diameter is kept constant, then increasing the voltage will increase the electric field intensity.

The β-phase of the PVDF is determined by the following which is explained in Chapter 2.

$$F(\beta) = A\beta/((X\alpha/X\beta)\,A\beta + A\beta) \qquad (3.2)$$

3.3.1 Model Setup:

In order to pole the PVDF fibres, a poling method was devised to work in situ with the melt extrusion process. Just after coming out of the melt extrusion nozzle, the fibre passes through two aluminium plates that are charged with 6 kV. The top plate has the positive charge and the two plates are separated by an air gap. In one setup, there was a hole in the centre of the two plates, where the fibre will pass through. The setup is shown below in Figure 3.1.

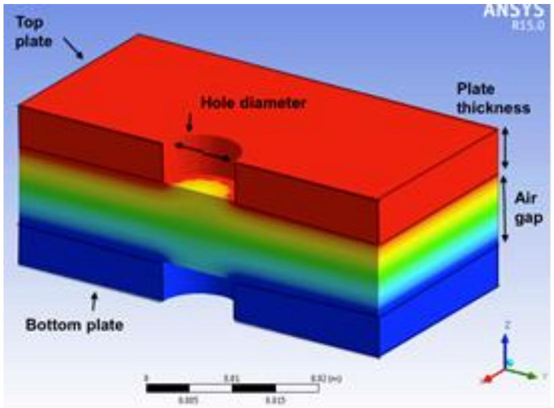

Figure 3.1 showing the ANSYS model used for analysis

One of the problems with this setup was that the electric field intensity is extremely low between the two holes in the plates. ANSYS was used to find the most efficient hole geometry, plate thickness, and air gap distance. Along with the hole in the centre of the two plates, a slit was also simulated in ANSYS to analyse the electric field intensity. This model is shown in Figure 3.2.

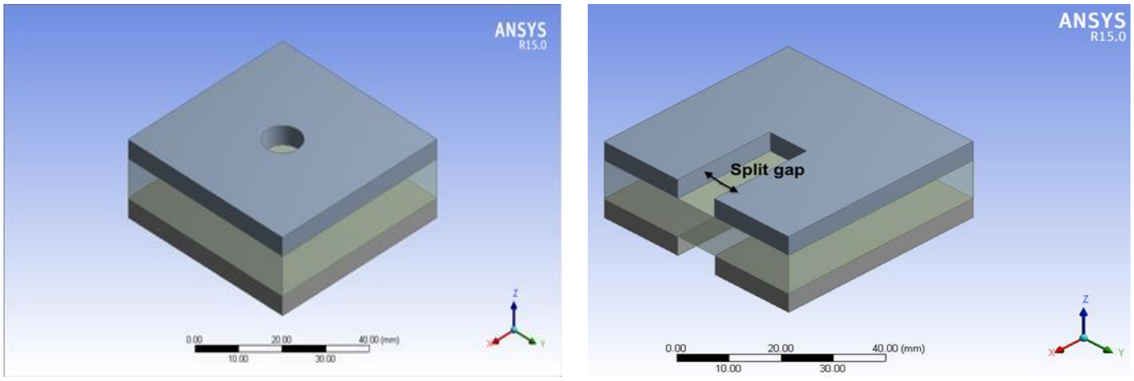

Figure 3.2 showing the poling setup with (a) hole configuration and with (b) slit configuration

The two parallel plates were 50 mm x 50 mm and differently sized splits, diameters and heights were observed.

3.3.2 Simulation Results:

In Table 8.4, shown in Appendix, the best plate geometry combination appears to be the 5 mm diameter centre hole with 3 mm thick plates, which were situated 10 mm apart. According to the ANSYS electric field representation, this combination also has the best-shaped electric field, with constant field vectors headed straight down through the hole to the negative plate. Overall, the slit had a lower field intensity than the hole geometry. Therefore, the hole combination will be looked in further detail. A separate study was conducted in which the 3 mm thick plates (50mm x 50mm x 3mm) was found to have a higher electric field intensity than the 10 mm (50mm x 50mm x 10mm) plates.

To expand on these results, further simulations were done focusing on the ratio between hole diameter, the distance between the plates, and electrical field intensity. Since the 3 mm thick plates (50mm x 50mm x 3mm) produced a higher electric field than 10 mm plates (50mm x 50mm x 10mm), 3 mm plates were also compared to 5 mm plates (50mm x 50mm x 5mm) to observe any differences. Figures 3.3 (a) and (b) show the comparison between 3 mm and 5 mm thick plates. A detailed report for the simulation has been reported in Appendix 8.3.1.

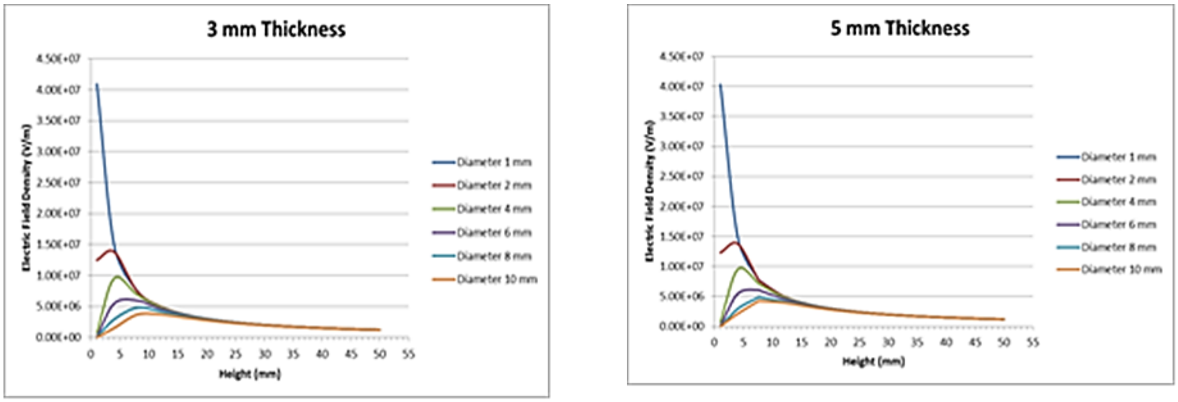

(a) **(b)**

Figure 3.3 (a) and (b) showing the comparison between the two plate thicknesses against the plate distance (height in mm)

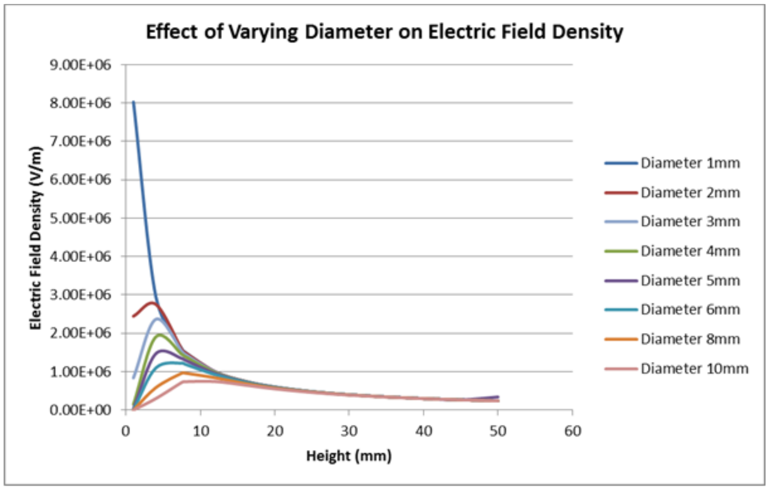

Figure 3.4 Graph showing the relationship between the plate distance (height in mm) and hole diameter

The height in the graphs above represents the distance between the two parallel plates. The electrical field intensity was the maximum result taken in the centre of the hole, midway between the plates. Figure 3.4 shows the effect of varying the plate distance and hole diameter on the electric field intensity. It can be observed that between 1 mm to approximately 10 mm in height, the electrical field intensity varies significantly depending on the diameter. However, after around a gap of 10 mm, the electrical field intensity becomes constant between the different diameters.

If the diameter is increased, the electric field intensity decreases at a given height. This is due, in part, to the electrical field not forming correctly between the two plates. If the plates are too close together and the diameter too large, the electrical field lines do not reach the centre of the hole. This results in a lower electrical field intensity. If the plates are spaced reasonably apart, the electrical field has time to form and creates a field that is more constant in the centre of the hole. This means the fibre will pass through a high electrical field intensity for longer.

The figures 3.5 (a-b) and 3.6 (a-b) show the electric field lines in the air gap between the two plates for the different diameters and heights. If a height greater than 10 mm is chosen, then the only way to increase the electrical field intensity is to increase the voltage used to charge the plates.

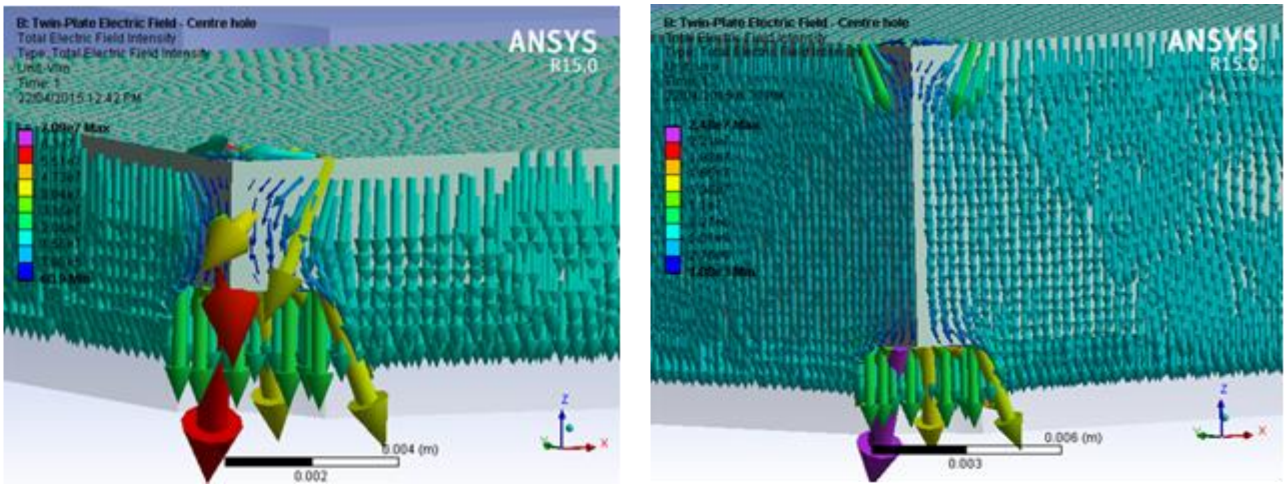

(a) (b)

Figure 3.5: (a) parallel plates with a hole diameter of 5 mm, the plate thickness of 3 mm and 3 mm apart. (b) same as (a) but with a distance of 10 mm

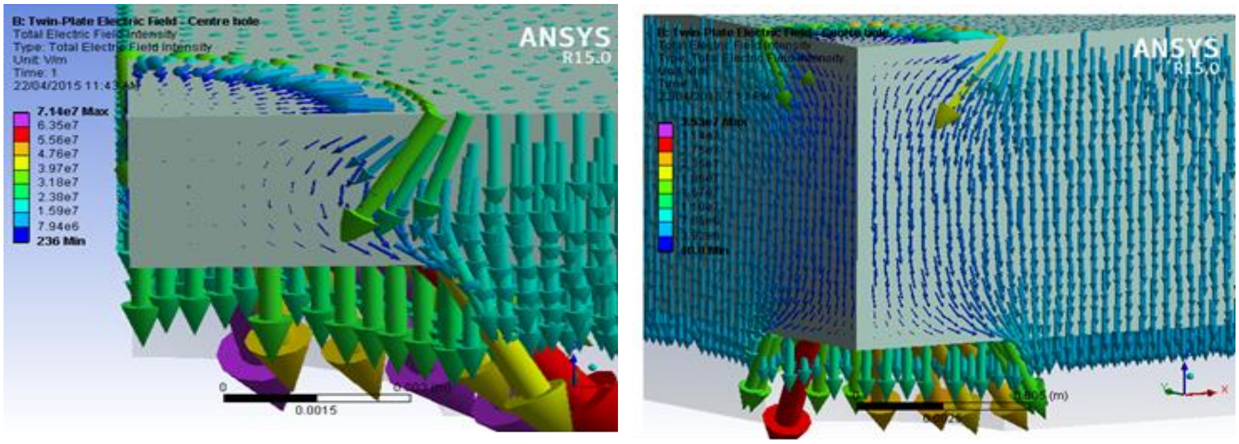

(a)

(b)

Figure 3.6 (a) parallel plates with a hole diameter of 10 mm, the plate thickness of 3 mm and 3 mm apart. (b) same as (a) but with a distance of 10 mm.

At a height of 7.5 mm, the average field intensity across the diameters is 6.36 MV/m. In previous studies, the typical field strength needed to permanently pole the β-phase chains is between 50-300 MV/m (Nilsson *et al.* 2013). However, poling can be carried out at an elevated temperature and/or a longer poling time to help reduce the electric field required.

The simulations suggest approximately no difference between the 3 mm and 5 mm thick plates as seen in the figures 3.3 (a) and (b). The 5 mm thick plates produce a slightly higher field intensity, approximately averaging 98 kV/m depending on the selected diameter. This could be due to the errors associated with the simulation and the added thickness to the charged plates creating a stronger electric field. Some of the simulation errors might include low mesh density and the use of probing method to capture the approximate maximum field intensity between the plates. To increase the accuracy of the model, a targeted selection in between the plates was assigned a smaller element size. This increased the mesh density in the area that was the focus of our investigation, while keeping the mesh density in the areas of little concern down, saving computational memory. As the height increased between the two plates, the model grew in memory size until a height of approximately 20 mm, where the model size exceeded the available limit. When this occurred, the targeted selection was removed, lowering the mesh density. This could have created less accurate results for heights above 20 mm.

3.3.3 Experimental Validation:

To validate these results, 5 mm thick plates were used with the hole configuration having a diameter of 5 mm and a varying distance in a range of 10 mm – 28 mm between the plates. The plates used in the computational simulations were 50 mm x 50 mm. In the validation of these results, the plates were made up of 50 mm x 100 mm. A quick alteration in ANSYS shows almost identical results to the plates used previously. Figure 3.7 shows the setup used for testing the poling design.

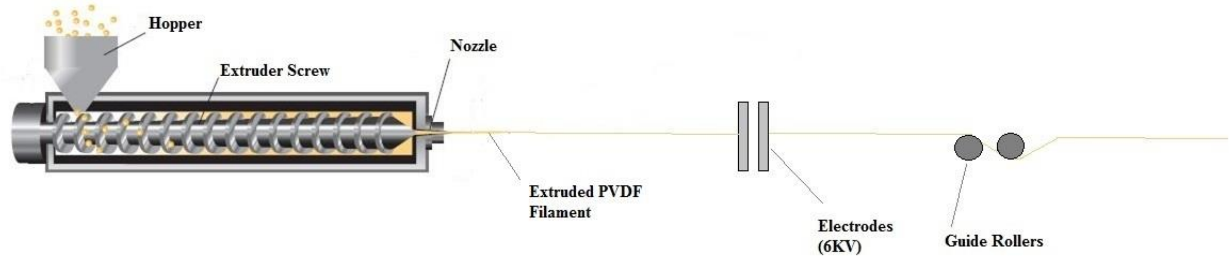

Figure 3.7 showing the setup used to extrude and pole polyvinylidene fluoride for validation (Refer to Fig 3.2)

The plates used were made from Aluminium, mounted to a Perspex (Polymethyl methacrylate, PMMA) sheet. A voltage of 6kV was applied to the plates while the fibre was extruded. The single yarn filament extruder was used to extrude yarns, stretching at the constant draw ratio of 3:1, and was simultaneously poled. The procedure was repeated for various distances between the plates as modelled. The extrusion temperature was 220 °C which dropped to 75.6 °C at poling (figure 3.8).

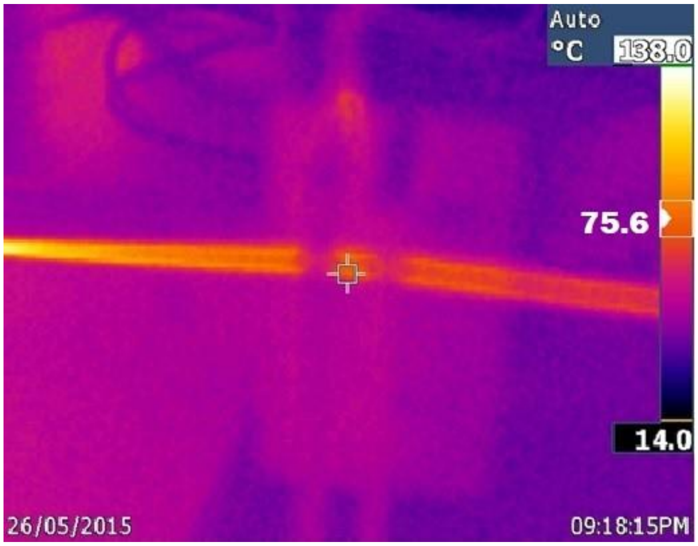

Figure 3.8 showing the temperature of polyvinylidene fluoride filament at poling setup (Image taken using a thermal camera)

3.3.4 Characterization:

The yarns obtained were tested using FTIR for infra-red spectra. The amount of β-phase was calculated as per the equation (3.2) above. The results were analysed for maximum β-phase output. The higher the β-phase fraction, the better the piezoelectric behaviour due to its highest dipolar moment per cell unit (Martins *et al.* 2014).

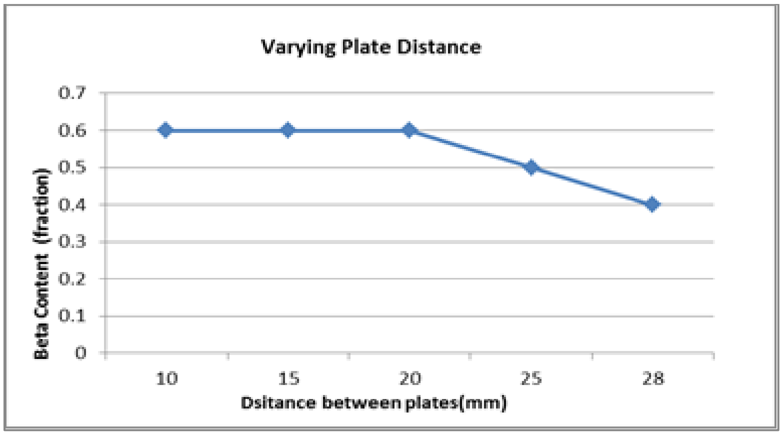

Figure 3.9 Graph showing the effect of increasing the plate distance on the β-content of PVDF monofilament

Figure 3.9 shows that increasing the plate distance decreases the β-phase fraction. Due to the limitations of the poling plates, a distance lower than 10.0 mm was not possible but will be considered in future work. It was observed in simulation results that decreasing the plate distance decreases the electric field intensity. The figure above coincides with our previous observations arguably that the decrease in electric field intensity (V/m) results in lower spontaneous reorientation of the dipoles.

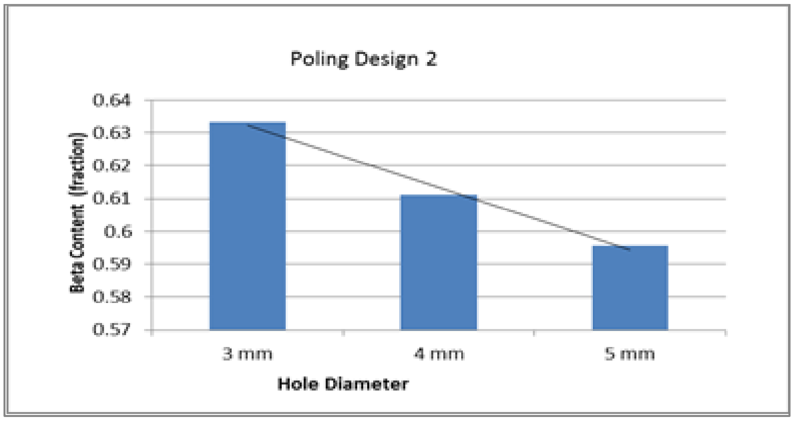

Figure 3.10: β-phase fraction obtained by varying the hole diameter in poling setup using a hole configuration.

Figure 3.10 shows the β-fraction obtained at the constant plate distance of 10 mm for various hole diameters; increasing the diameter to 5 mm decreases the β-fraction as seen. This is primarily due to the increase in the electric field intensity which is also observed in the simulation results.

In this study, two poling design setups have been modelled to pole PVDF monofilaments in d_{33} mode. The poled PVDF filament is then tested for the presence of β-phase conversion. In this study, the hole configuration results obtained via ANSYS simulations were found to produce higher electric field intensity along the path of the yarn as compared to the slit configuration. This is also evident in the high β-phase fraction as seen in graphs. The hole configuration was further analysed for optimum plate distance and diameter. It was observed that increasing the diameter of the hole in the plates resulted in decreasing the electric field intensity, which is confirmed by the FTIR results. Furthermore, the increase in plate distance also produces a weaker electric field intensity and a hence lower β -phase fraction. The higher electric field intensity thus is accepted as the one responsible for the higher β-phase in the hole configuration. This novel approach of poling PVDF yarns can be used for in-line poling of yarns to be used for energy harvesting purpose.

3.4 Simulation-based power output in fabrics

There are many softwares that can be used to determine the behaviour of fabric under mechanical stress. These softwares have been used to simulate mechanical outputs such as stress in woven designs, drapability, fibre orientation distribution, and other properties. However, the electrical response of fabrics is still under research and has not been (fully) explored.

3.4.1 Harmonic analysis and piezo-response

A harmonic analysis is used to study the structural response under constant steady state sinusoidal loading at a frequency; also known as frequency response. This response makes use of Young's modulus, Poisson ratio and mass density of the materials. However, damping is considered a global property and not a material property. Therefore, it has not been specified in the study other than using a constant damping ratio where applicable. Modal analysis can be used to determine a structure's vibration characteristics using natural frequencies and mode shapes.

The general equations of motions are as such

$$M]\{\ddot{x}\} +[C]\ \{\dot{x}\}+[K]\{x\} = \{F\} \qquad (3.3)$$

The loading and response of the structure assumed to be harmonic.

$$\{F\} = \{F_{max}e^{j\Psi}\}\ ej^{\Omega t} \qquad (3.4a)$$

$$\{x\} = \{x_{max}e^{j\Phi}\}\ e^{j\Omega t} \qquad (3.4b)$$

$$(-\Omega^2[M] +j\Omega[C] + [K])\ \{x_1+jx_2\} =\{F_1+jF_2\} \qquad (3.5)$$

The above equations are explained in chapter 2 in detail.

There are many types of equation solvers, such as direct and iterative methods. The direct sparse equation solver was used in these simulations due to its high speed and low memory usage. It is also useful in ill-conditioned matrices such as that in poorly shaped elements. At each node, the stresses are calculated under the given condition and using the specified solver. At this point, the maximum memory of the system is being used due to enormous equations running in the background.

The model used for simulations in this project was based on the basic 2D model designed in CAD. In some of the simulations, the model consisted of a representative volume element of the fabric which was generally a repeatable unit cell of the fabric.

3.4.1.1 Piezo-response

To obtain the outputs from our model, it was subjected to mechanical stimuli, such as a force. There are several types of analysis present: static, modal, harmonic, transient, spectrum, sub-structuring and Eigen buckling. In the simulations, we have used harmonic and modal analysis.

3.4.2 Electrical outputs and results

Post-processing of results is required to fully utilise the simulations. This helps in the interpretation of the results into easy, understandable content. The results are post-processed using the general postprocessor tab. After solving both static and dynamic models and obtaining the numerical values, the results can be animated using animation tools.

3.4.3 Mesh optimization study

Mesh density is highly significant in determining the accuracy of results. It is generally accepted that a higher mesh density would produce more accurate results. However, the time constraint and computer utilization are some important factors to consider and therefore, mesh density is considered important. In order to evaluate these investigations, a mesh optimization study was conducted for each of the simulations. The influence of mesh sensitivity in terms of mesh sizing on load outputs is shown in the results which are summarized below. Three types of mesh configurations were used, coarse, medium, and fine with element sizes. The brick elements used were 20 node 3D brick elements.

3.5 Dual Field Finite Element Simulations of Piezo-Patches on Fabrics: parametric study

In this simulation, a dual-field computational analysis, combining harmonic and piezoelectric models, has been undertaken using the ANSYS Finite Element package. The scope of this study was to undertake a dual field (electro-mechanical) computational analysis of a PVDF patch bonded onto a nominal representative flexible fabric. A PVDF patch bonded to a material representative of a flexible fabric has been modelled in ANSYS. The electrodes are connected to a resistor that was matched to the piezo properties and loading conditions. The parametric variables used in this study include surface area of the piezo-patches, aspect ratio, input force amplitude, and the operational frequency. The complex interaction of these variables to the power output was explored and discussed in the context of the intended application. A harmonic analysis was carried out using ANSYS Finite Element package and the complex interactions of different surface areas, aspect ratios, input force magnitudes and the frequencies were studied.

The constitutive equations for piezoelectric finite element analysis which define how the piezoelectric material's stress (T), strain (S), charge-density displacement (D), elastic compliance of piezoelectric material (s), piezo coefficient (d), permittivity (ϵ) and electric field (E) interact (Uchino, 2010) are:

$$S = s.T + d.E \tag{3.6}$$

$$D = d.T + \epsilon.E \tag{3.7}$$

When deformed, mechanically, the total induced electrical charges Q, assuming a linear relationship between stress and strain can be expressed (Yang & Yun, 2012) as:

$$Q = dYA\left(\frac{\Delta \mathrm{l}}{l_0}\right) \tag{3.8}$$

Where *Y* is Young's modulus, *A* is the surface area, l_0 is the initial length, and Δl is the differential length of the piezoelectric material. Differentiating both sides, we get the output current and voltage for any resistive load as:

$$I = \frac{V}{R} = \dot{Q} = dYA\,\frac{1}{l_0}\,\dot{\Delta l} \tag{3.9}$$

Where *I* is the current, *V* is the output voltage, *R* is the load resistance. Moreover, the electrical energy *W*, from the stored charge is related to the capacitance *C* as:

$$W = \frac{Q^2}{2C} \tag{3.10}$$

The capacitance *C* depends on the separation between electrodes *t*, dielectric constant ϵ for piezoelectric materials, and the area of electrode *A*.

$$C = \frac{\epsilon A}{t} \tag{3.11}$$

Substituting Q, we get:

$$W = \frac{At}{2\epsilon}\, d^2 Y^2 \left(\frac{\Delta l}{l_0}\right)^2 \tag{3.12}$$

The relations above show the dependence on output energy and power on various factors such as thickness (t) and area (A).

3.5.1 Model design

In this computational study, a piezoelectric material, PVDF patch was bonded onto a flexible fabric (polyester). The model was composed of two rectangular patches, the piezo patch and the fabric patch. The piezo patch will have varying dimensions for the parametric study and the fabric patch was 0.12 m x 0.1 m, with both having a thickness of 0.0002 m. The back of the piezo patch was bonded onto the face of the flexible polyester fabric. The material properties of both the polyester and the PVDF are included in Tables 3.1 and 3.2. For this study, the area of the piezo patch was varied to study the effect of a change in the area, aspect ratio, and input load while the dimensions of flexible polyester were kept constant. A schematic and cross-sectional view of the piezo patch and the polyester fabric is shown in Figure 3.11.

Table 3.1: Material properties of flexible polyester

Material properties for Polyester	
Property	Value
Young’s Modulus (MPa)	4410
Poisson’s Ratio,	0.403
Bulk Modulus (MPa)	7577.3
Shear Modulus (MPa)	1571.6
Density Kg/m^3	1400

Table 3.2: Material properties for piezoelectric material, polyvinylidene fluoride

Material properties for polyvinylidene fluoride	
Property	Value
Young’s Modulus (MPa)	4000
Poisson’s Ratio	0.3
Bulk Modulus (MPa)	3333.3
Shear Modulus (MPa)	1538.5
Density Kg/m^3	1780
d_{31} 10^{-12} C/N	23
d_{32} 10^{-12} C/N	3
d_{33} 10^{-12} C/N	-33

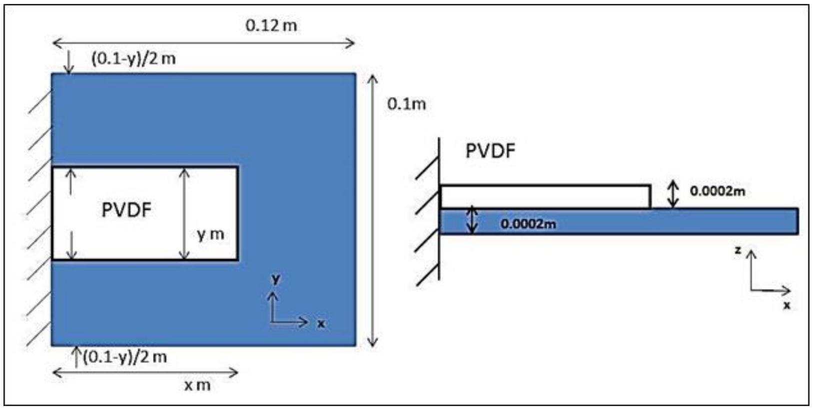

Figure 3.11: Schematic diagram of the polyvinylidene fluoride patch.

The electrodes in the patch were connected to a resistor that was matched to the piezo properties and the loading conditions. The top and the bottom face of the piezo material was defined as terminal 1 and 2 respectively in order to select the master node in each element and eventually allow the voltage to flow through the terminals and the resistance elements.

The model was fixed by using displacement boundary condition with the *x*, *y*, *z* components as 0.0 m. The model was fixed about the face through the thickness of flexible polyester. A distributed force along the edge with a magnitude range of 0.005N to 0.05N in Z direction was applied to the flexible polyester as seen in Figure 3.12a. It should be noted that the effect of gravity was not considered in this analysis, hence the planar fabric configuration is shown in Figure 3.12. The magnitude of this force was varied to study the effect of input loading and the resultant power output. The detailed properties of materials assigned are mentioned in Appendix 8 (table 8.1, 8.2)

3.5.2 Meshing

Due to the small thickness of the model, the finely divided mesh was used to mesh the piezo having two elements through the thickness of both piezo and the polyester material as seen in Figures 3.12 (b) and (c). This was done by selecting the edges and setting the number of divisions to two. The mesh generated was optimized and included the piezo brick elements for the piezo patch whereas the flexible polyester consisted of the standard brick elements. The brick elements were 20-node 3D elements, with the PVDF having the piezoelectric version of the 20-node brick elements. The piezoelectric elements are directly (or fully) coupled. Hence, the equation solver solves the coupled electrical and structural fields directly (and not iteratively) with these elements.

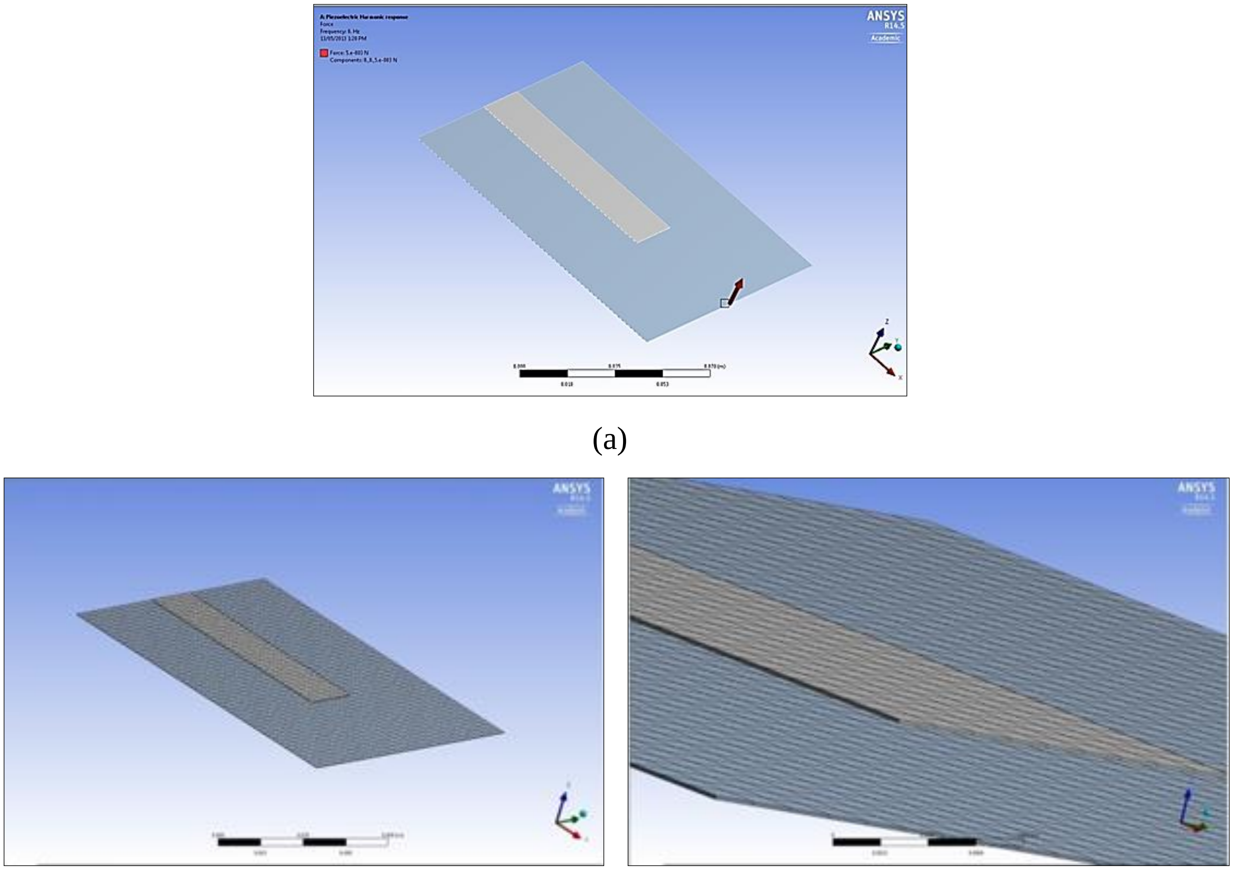

(a)

(b)

(c)

Figure 3.12: Sketches showing (a) Direction of force as applied to the model where the force vector applied was along the edge of the fabric (b) Meshing (c) Meshing as seen in thickness.

3.5.3 Results of simulation

3.5.3.1 Harmonic Analysis

The model described above was subjected to full steady-state harmonic analysis in Mechanical APDL using Finite Element Method. For this analysis, the dimensions (x, y) of the piezo patch were varied, to study the effect of changing area, the aspect ratio, and the input force magnitude at various frequencies. The harmonic analysis was performed for frequencies from 0 to 5Hz with 10 intervals. However, in case of the PVDF area of 400 mm^2, we looked at further frequencies of 6-10Hz with a constant damping ratio of 0.005 applied. The results were obtained using Mechanical ANSYS Parametric Design Language (APDL) with the sparse equation solver to obtain a direct solution of the global electro-mechanical coupled matrix. Figures 3.13 and 3.14 show the total deformation at the piezo patch at 5Hz and maximum displacement respectively.

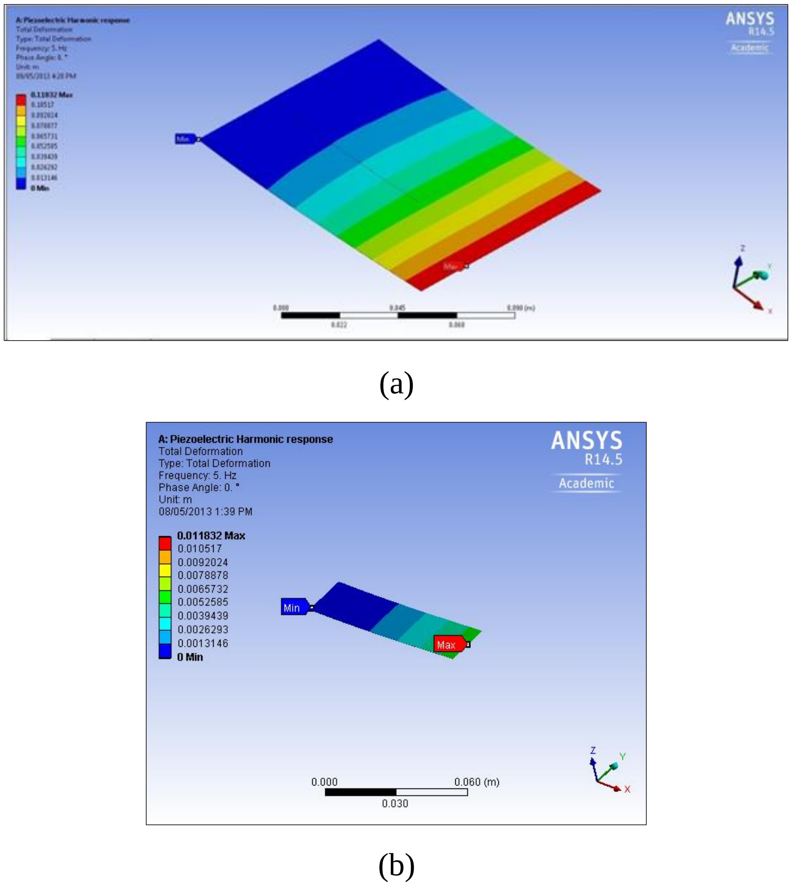

(a)

(b)

Figure 3.13: Total deformation at 5Hz in the model showing (a) Flexible polyester (b) Piezo patch.

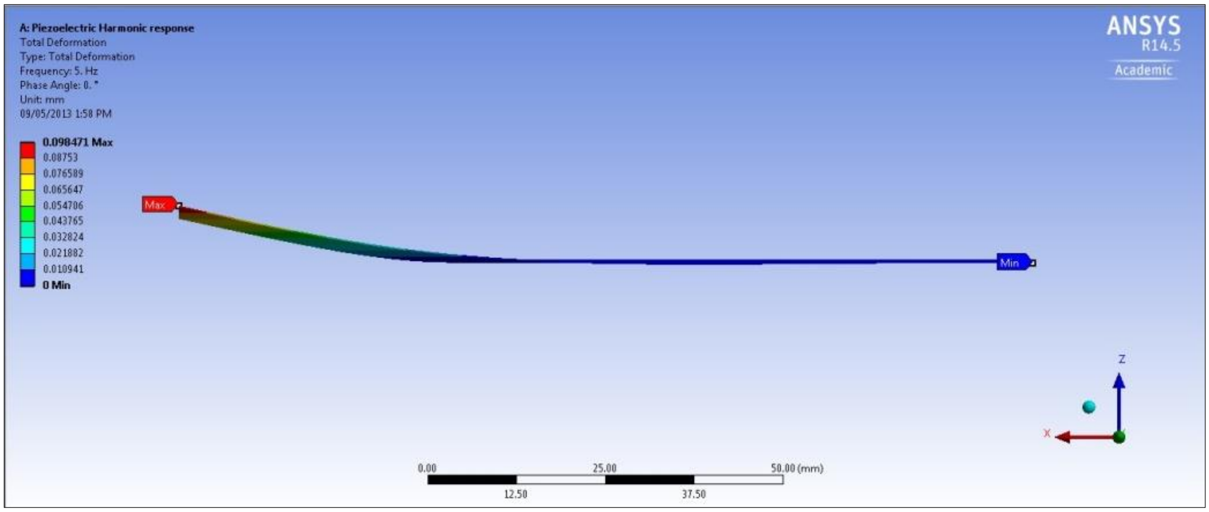

Figure 3.14: Displacement amplitude of piezo patch at 5Hz.

3.5.3.2 Effect of Increasing Area

The results of the simulations suggest that increasing area of the piezoelectric material has a direct effect on the output power, voltage, current, and displacement amplitude. The results show that as the area of PVDF material increased from 400 mm^2 to 2500 mm^2, the output generally increases with increasing frequency until it reaches a frequency of 5Hz as seen in Figure 3.15. At this point, the output power is highest for the smallest area, giving an output of 43.4μW. For this area of 400 mm^2 of PVDF material, the analysis was conducted for the frequency range of 0 till 10Hz. The power output appears to decrease after 5Hz. The modal analysis below, which shows that the fundamental natural frequency indeed occurs at 5 Hz, accounts for the post-5Hz energy drop.

Similarly, it is visible from the results that an increase in the area also increases the amplitude displacement. However, the displacement is maximum for 400 mm^2 at 5Hz having a displacement amplitude of 8.9 mm, which decreases after 5Hz. Increasing the area has an inverse effect on the output voltage and current and both voltage and current decrease for an increasing frequency. This could be attributed to the increased flexural stiffness for the larger areas and hence, reduced strain, which in turn reduces the output voltage and current for a fixed load.

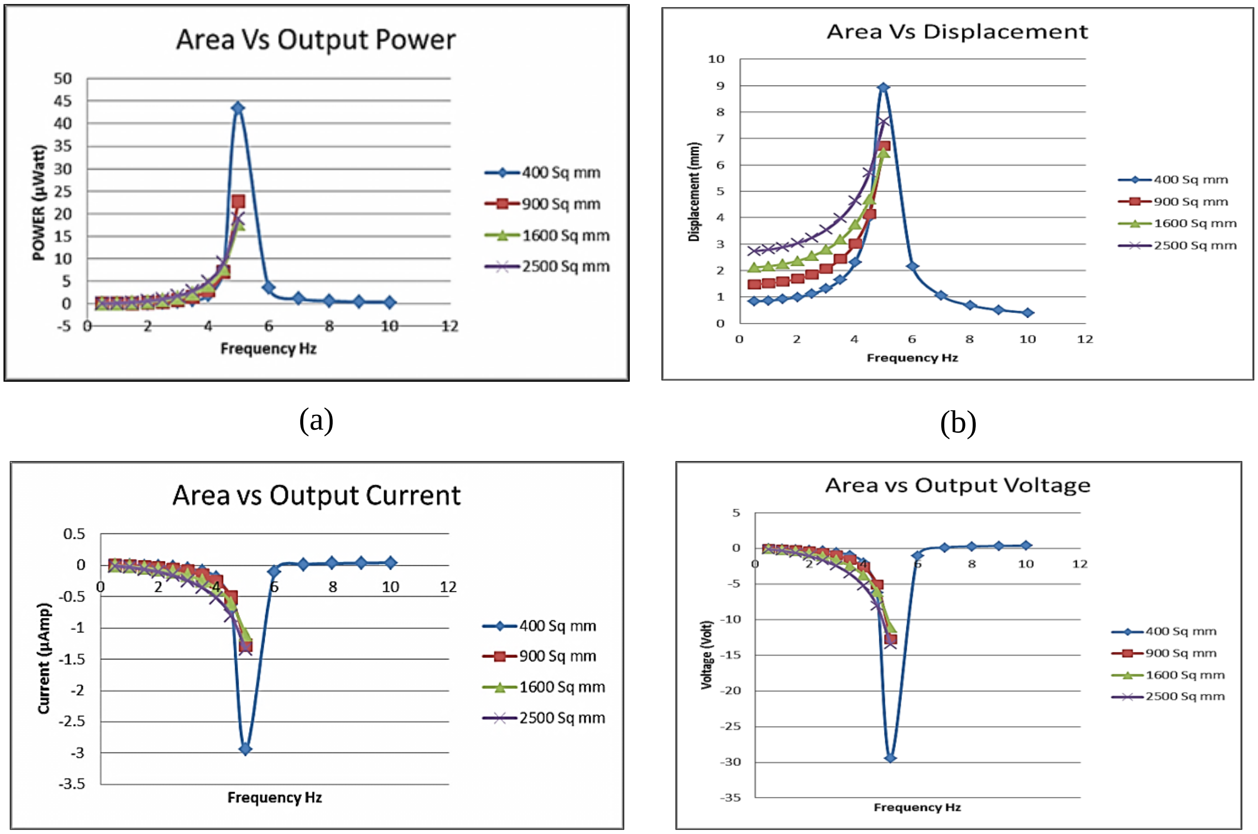

(a) (b)

(c) (d)

Figure 3.15: Effect of increase in Area on (a) power output (b) displacement (c) output current (d) output voltage at aspect ratio 4, and input load 0.005N.

3.5.3.3 Effect of Increasing Aspect Ratio

Increasing the aspect ratio increases the power output for the piezo patch with an increase in frequency. The power output obtained for aspect ratio 8 at a frequency of 5Hz is 54.7µW (figure 3.16(a). The displacement amplitude also increases with an increasing aspect ratio and a displacement of 25.4 mm is attained at maximum frequency. Figures 3.16 a-d show the trend that increasing aspect ratio has on output power, voltage, displacement, and current. This is somewhat expected since the increased aspect ratios result in increased deflection and hence strain, due to its increased compliance with aspect ratios.

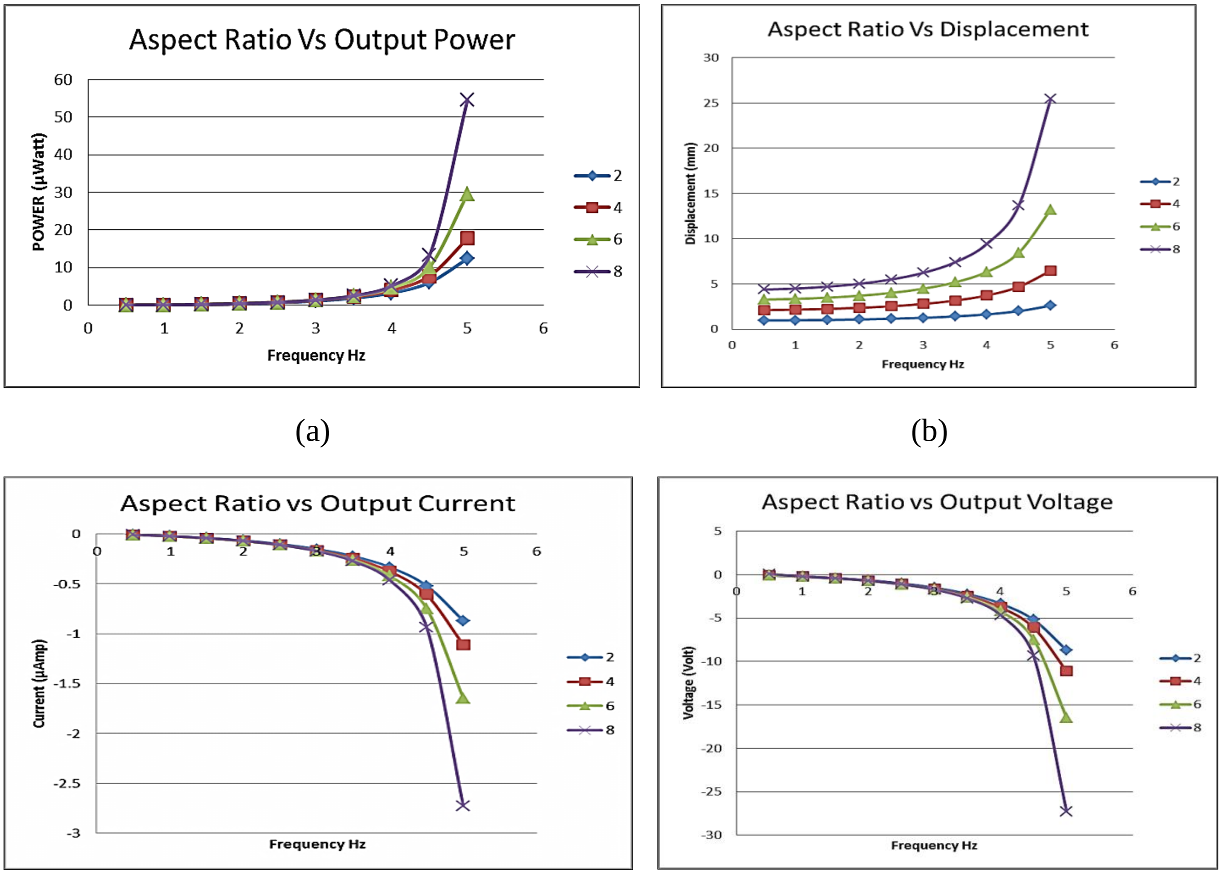

(a) (b)

(c) (d)

Figure 3.16: Effect of increase in Aspect ratio on (a) power output (b) displacement (c) output current; and (d) output voltage at 1600 mm^2 area with input load 0.005N (Legend in the figures 3.16 (a-d) show aspect ratios 2, 4, 6 and 8)

3.5.3.4 Effect of Increasing Input Loading Magnitude

As the input load is increased on the model from 0.005N to 0.05N, it is quite evident that the output power increases. Moreover, increasing the input load from 0.01N to 0.05N increases the output power considerably from 0.8mW to 1.8mW at a frequency of 5Hz. This trend is also similar in displacement amplitude, output voltage and current as seen in Figure 3.17.

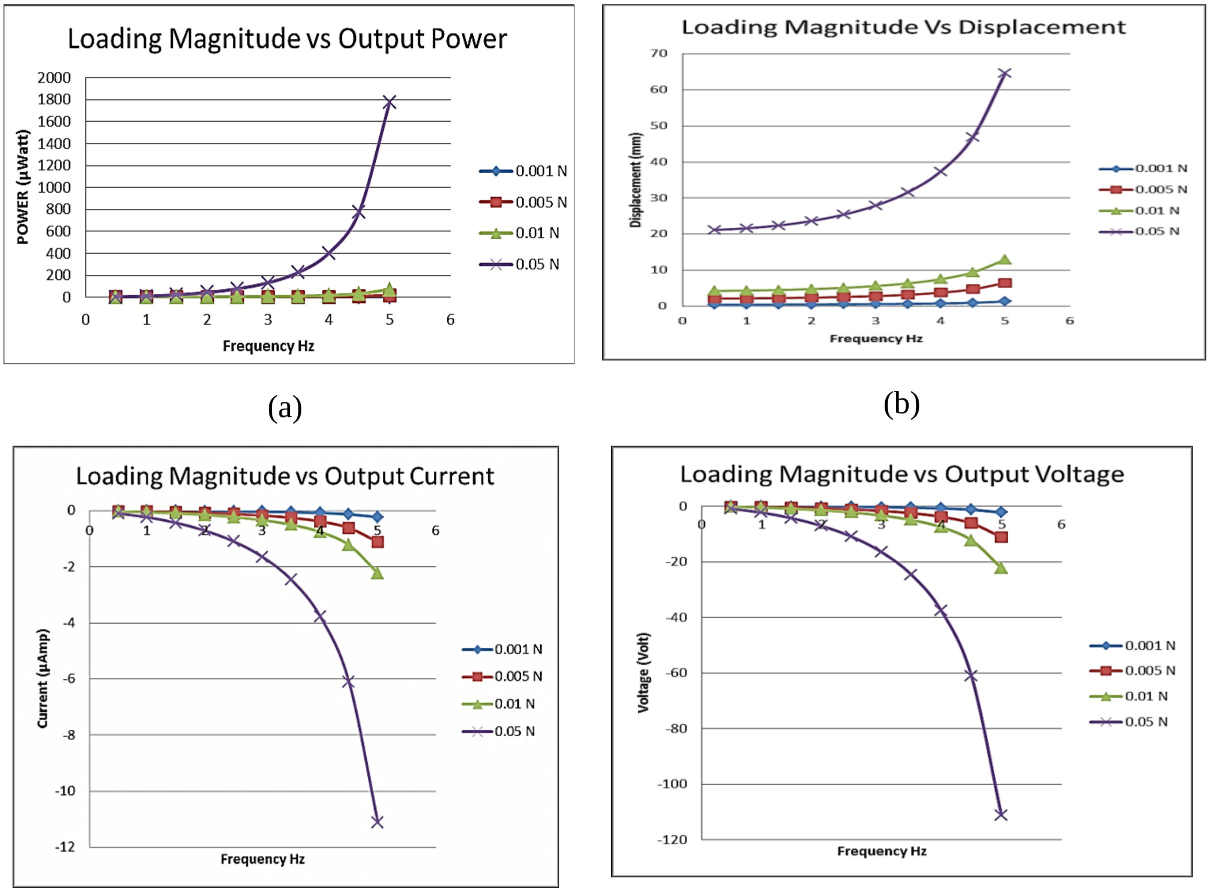

(a) (b)

(c) (d)

Figure 3.17: Effect of increase in loading magnitude on (a) power output (b) displacement (c) output current; and (d) output voltage at aspect ratio 4, and 1600 mm^2 area.

3.5.3.5 Modal Analysis

Modal analysis is the method of measuring and predicting the mode shape in a system. The mode shape is the well-defined characteristic deformation due to relative amplitudes at a single natural frequency, resulting in ultimate positions of vibration in a system.

A modal analysis as seen in Figure 3.18 was also carried out for the PVDF area 400 mm^2 to confirm the results obtained in Figure 3.15. The model was subjected to same geometry as described above and a fixed boundary condition was applied. The meshing was similar to that of fine mesh as used in harmonic analysis with a relevance of 100. It was observed in the analysis that the natural frequency for the 1st mode is indeed 5Hz, which explains the maximum power output and maximum displacement. Table 3 shows the natural frequencies obtained for modal analysis conducted for the PVDF of area 400mm^2.

Table 3.3: Natural Frequencies for modal analysis for Polyvinylidene fluoride area of 400 mm^2

Mode	1	2	3	4	5	6	7	8	9	10
Frequency (Hz)	5.0481	11.829	27.134	41.239	44.861	74.946	81.747	88.712	112.96	133.86

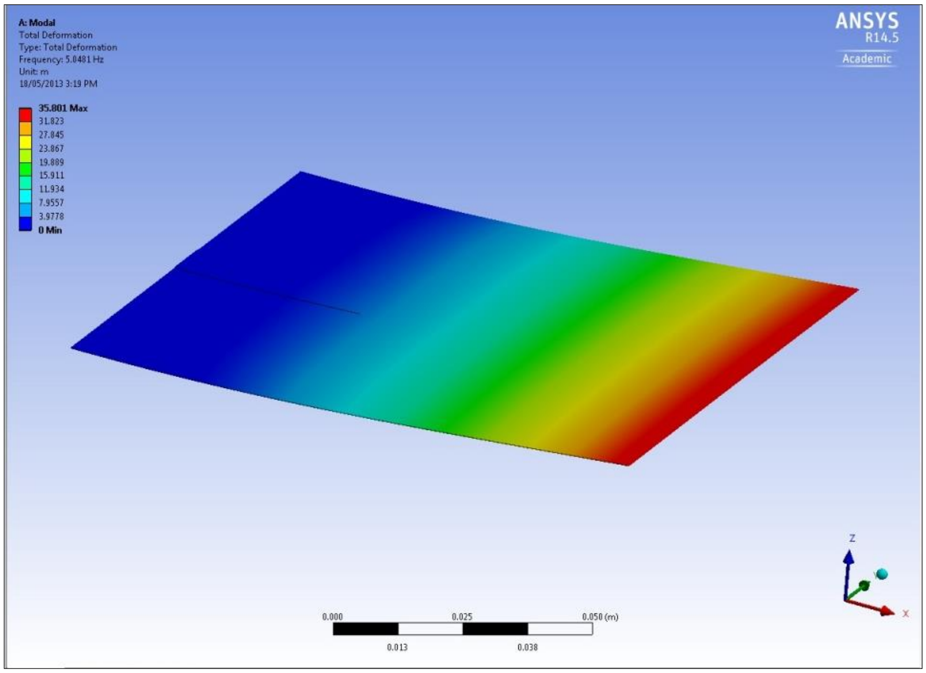

Figure 3.18: Modal Analysis (for the 1st mode) for Polyvinylidene fluoride area patch of 400 mm^2

In this study, finite element simulations have been performed for a piezo patch bonded on a flexible polyester using harmonic analysis. The modelling was to explore the feasibility of harvesting electrical energy from human motions such as wearable energy harvesting devices embedded in textiles for the elbow, knee, and finger joints. Different parameters such as the area, aspect ratio, and input loading magnitude were studied at different frequencies and their effect on output power, voltage, current and displacement were also studied. For the parametric study carried out here, there appears to be an optimal dimension of about 400 mm^2 of PVDF operating about 5Hz for maximum energy output in the microwatt range, which makes it viable as an energy scavenging system for powering many micro-watt-based communications and medical devices. However, it should be noted that nominal frequencies during human motion and locomotion are in a range of less than 2Hz. It is, therefore, more likely that the piezo patch on wearable fabrics will be operating at non-optimal frequencies and hence, sub-maximum power outputs will be expected from this configuration. These findings, never the less, augur well for the experimental program; which is the next research step. This research step is designed around integrating these PVDF patches (in sub-mm form) with wearable fabrics. Appendix 8.3.2 details the ANSYS reports for this simulation.

3.6 Modelling and Analysis of Various Piezo Fibre Geometries on the Piezoelectric Properties for Energy Scavenging Applications

3.6.1 Theory

A finite element analysis of an idealised PVDF wearable textile using the Representative Volume Element (RVE) approach. The RVE model consisted of PVDF fibres attached between flexible electrodes and exhibited a nonlinear increase in power output due to a similar increase in a number of fibres. A parametric analysis was then carried out on the effect of fibre angle, thickness, linear density, and poling directions on output power at lower frequencies (1 - 2Hz), with the results discussed in the context of the intended fabric applications.

As an alternative to woven piezoelectric fabrics, 3D knitted spacer fabrics could provide the required power output and could possibly obtain higher efficiencies. 3D spacer fabrics have two fabric substrates separated by spacer fibres (Yip & Ng, 2008), connected between two outer walls. These 3D spacer fabrics can be warp or weft knitted. The two outer fabrics act as the electrodes and a study conducted by Soin *et al* (2014) suggested the use of silver-coated polyamide multifilament yarns. 3D fabrics are commonly used for car interiors, medical textiles, and sportswear. Incorporating PVDF fibres into 3D spacer fabrics could yield a higher power output than solely weaving them throughout a simple single layer of fabric. Also, spacer fabrics are relatively breathable and for human applications, this is a good property for reducing moisture. The yarns, used as spacer yarn configuration, play a vital role in fabric construction and its resultant properties. The thicker the spacer yarns, the more resistant it would be to compression. Furthermore, the angle of spacer yarns also affects the stability of these fabrics. These spacer yarns can also be introduced as inter-crossed arrangement providing more stability. However, this is beyond the scope of this study. A few studies have been conducted on the mechanics and performance of these 3D spacer fabrics in terms of compression resistance.

Arranging the spacer fibres perpendicular to the two outer fabrics provides a higher compression resistance than other angles (the angle θ between fibre and electrode plate), as the fibres at lower angles collapse under compressive force. Therefore, Yip & Ng (2008), used a V-shaped orientation for better compression resistance. The resistive force of a spacer yarn is given as:

$$F_{Resistance} = F \sin \theta \qquad (3.13)$$

Where F is the force applied and θ is the angle between the spacer fibre and the substrate. From this equation, a larger angle gives a greater resistive force. The power output from Soin *et al*. 3D spacer fabrics was 1.10 – 5.10μWcm^{-2} with 0.02 – 0.10MPa. This was stated to be higher than any existing 2D piezoelectric assemblies.

In this study, 3D spacer fabric is computationally modelled in ANSYS to investigate possible power outputs from different configurations. The model consists of an RVE of spacer fabric, which consists of PVDF monofilament yarns attached between silver-coated polyamide electrodes (Appendix 8.3). Since the compressive resistance is related to the spacer-yarn arrangement, different arrangement angles are compared to determine the optimal angle. The effect of changing the diameter of the PVDF yarns and poling direction in those yarns is also assessed. Another crucial factor analysed is the thickness between the two electrodes, also known as the fabric thickness. A small frequency of 1-2Hz is used in the computations, as the frequency of human movement is extremely low. Table 3.4 below shows the material properties for polyamide used in this analysis. The material properties for PVDF used were same as described in table 3.1, section 3.5.1.

The constitutive equations show that when the mechanical stress is applied to the materials, it will cause an electrical output. The charge stored in a capacitor is:

$$C = \varepsilon \frac{A}{d} \qquad (3.14)$$

Where *C* is capacitance, *ε* epsilon, *A* area and *d* distance between the plates. The energy stored in a capacitor is:

$$E = \frac{1}{2}CV^2 \tag{3.15}$$

Where *C* is capacitance in farads and *V* is voltage. Since Power is the energy transferred per unit time, substituting the two equations, we have

$$P = \frac{\varepsilon A V^2}{2dt} \tag{3.16}$$

Table 3.4: Material properties of piezoelectric material polyamide used for this analysis

Property	Polyamide
Young's Modulus (MPa)	4000
Poisson's Ratio	0.39
Bulk Modulus (MPa)	6060
Shear Modulus (MPa)	1438
Density kg/m^3	1130
d_{31} 10^{-12} C/N	-
d_{32} 10^{-12} C/N	-
d_{33} 10^{-12} C/N	-

3.6.2 Meshing

In this model, the medium sized mesh comprising of 20-node 3D brick elements was used. The PVDF spacer yarns comprised of a piezoelectric version of the 20-node brick elements as seen in figure 3.19. The piezoelectric elements are directly (or fully) coupled. Figure 3.19 below shows the model including meshed elements.

.

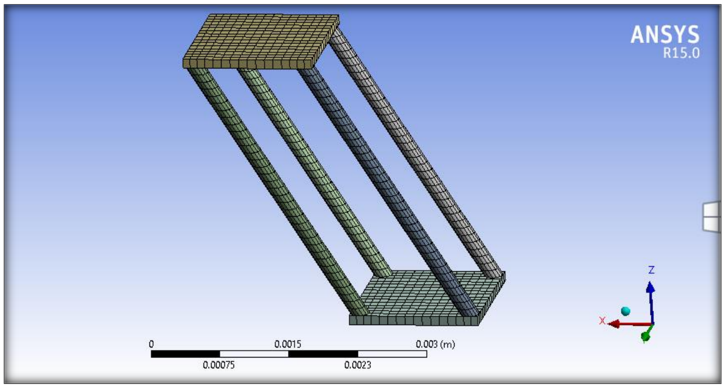

Figure 3.19: Spacer fabric model

3.6.3 RVE

The spacer fabric model was represented as an RVE in order to reduce computational resources. To verify the model to be used as representative volume element, the power output was plotted against a number of fibres. Figures 3.20 (a-d) show the variations in repeat unit to determine the optimal RVE.

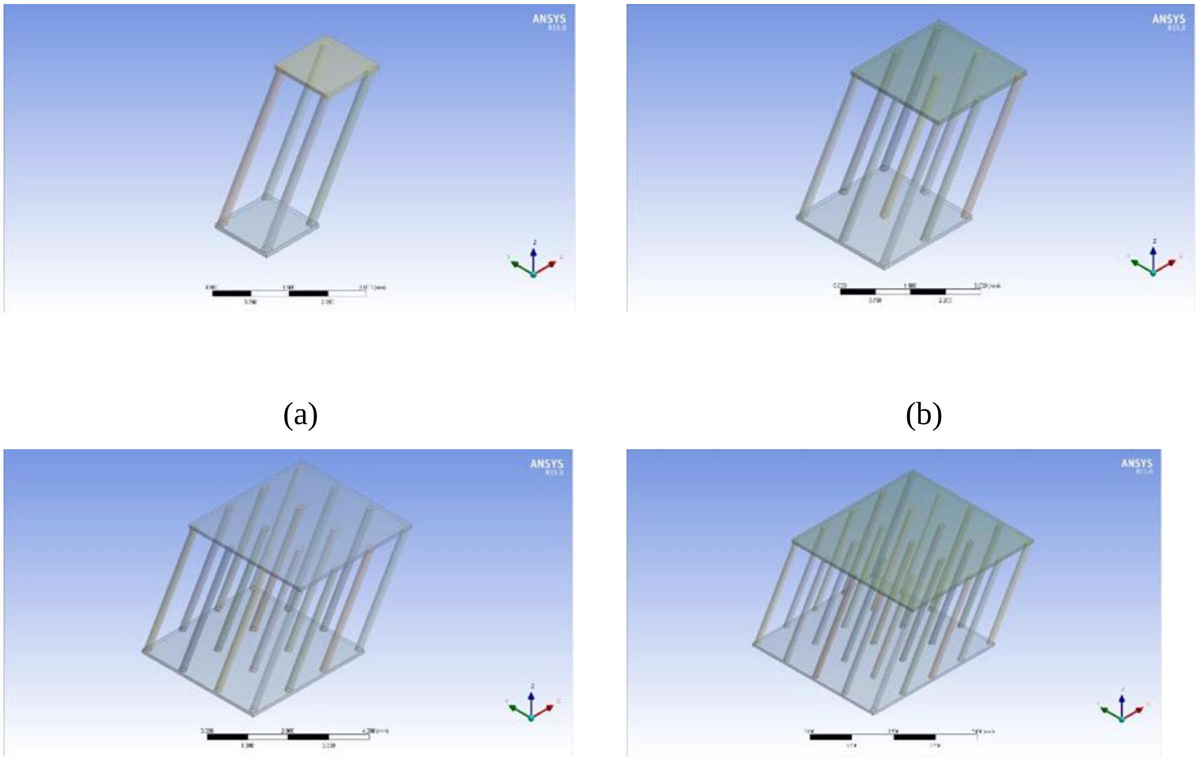

(a) (b)

(c) (d)

Figure 3.20: Representative volume element with (a) 4 spacer fibres (b) 9 spacer fibres (c) 16 spacer fibres (d) 25 spacer fibres

It was observed that with the increasing number of fibres, the power output increases exponentially. However, the increase is non-linear owing to a non-linear increase in the number of fibres. Figure 3.21 shows the resultant power output with increasing of fibres in the model.

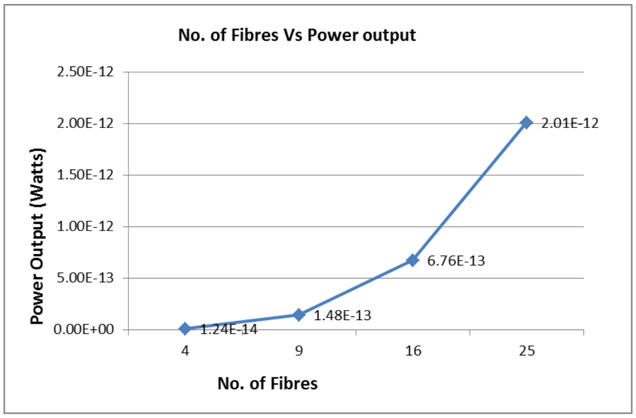

Figure 3.21: Power output in various RVE

3.6.4 Analysis and Results

3.6.4.1 Harmonic Analysis

The fabric model was subjected to a full, steady-state harmonic analysis in utilising Mechanical APDL in ANSYS. A full harmonic analysis does not consider material or structural non-linearities and solves the displacements and forces directly using the finite element method, as opposed to employing the mode superposition solution method. The full solution requires more computational resources, but the displacements and internal forces are obtained directly from the nodes, resulting in a more accurate solution at the frequencies of interest. The distance between the two electrodes, count of yarns, the inclination angles these yarns make with vertical and the poling direction was varied. A displacement boundary condition of 2.85×10^{-5}m in Z-direction was applied to the top electrode (Figure 3.22). The bottom electrode was subjected to fixed boundary conditions of 0.0m. It should be noted that the top and bottom polyamide electrodes were not modelled with electrical properties; to simplify the model. The harmonic analysis was performed for frequencies 0-2Hz owing to its intended application. The model was subjected to a parallel resistance of 0.46MΩ. The sparse equation solver was used for the direct solution of global electro-mechanical coupled matrix. The mesh used was optimized and a constant medium meshing size was used in all results. The material model was assumed to be linearly elastic and effect of damping was ignored.

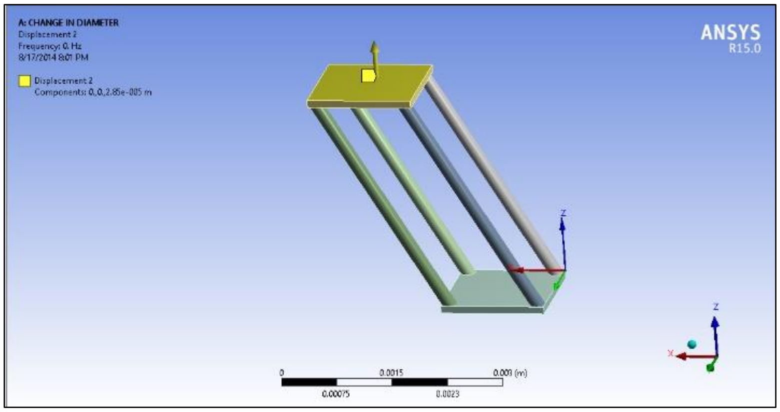

Figure 3.22: Figure showing imposed boundary condition

3.6.4.2 Poling Direction

The model was tested for the power outputs in different poling directions. The transverse d_{31} and longitudinal d_{33} poling directions for PVDF were explored. Figures 3.23 (a-c) below shows the current, voltage, and power output in these modes. It was observed that a significantly higher power output of 2.77×10^{-12}W was obtained in the d_{33} mode.

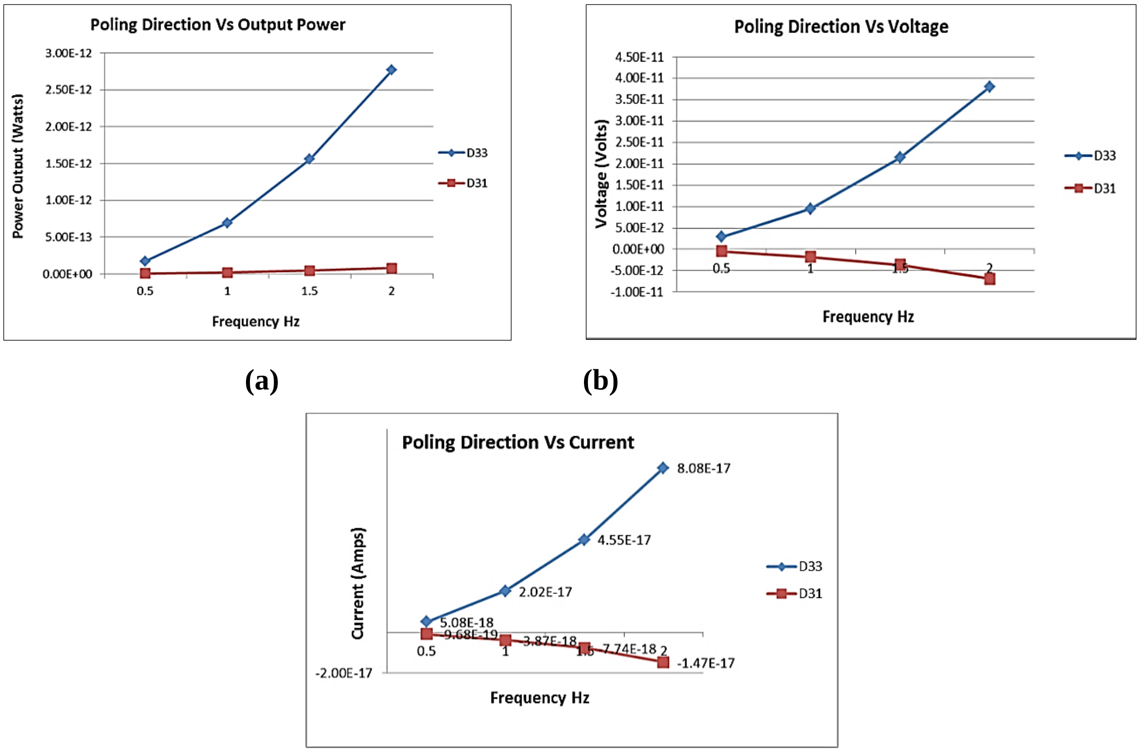

(a) (b)

(c)

Figure 3.23: Effect of poling direction on (a) power output (b) voltage and (c) current

3.6.4.3 Linear Density

When the linear density or fineness of yarn is changed, it modifies the diameter of yarn and effective cross-sectional area. Thus, in a fabric, altering yarn fineness modifies the overall properties of the fabric. The model was subjected to the displacement boundary condition at a constant inclination angle of 30° to the global Z-axis (Figure 3.22). This value was based on the fact that mostly spacer fabrics are formed with angles ranging between 0°-30° to vertical. The other dimensions of the model were also kept constant. Figures 3.24 (a-c) below shows the results obtained of varying the fineness of spacer yarns from 240Dtex to 390Dtex. It is observed that increasing the yarn linear density increases the output power, current and voltages. From these results, it can be deduced that increasing the linear density causes more absorption of energy at higher stress levels; which results in the higher electrical output.

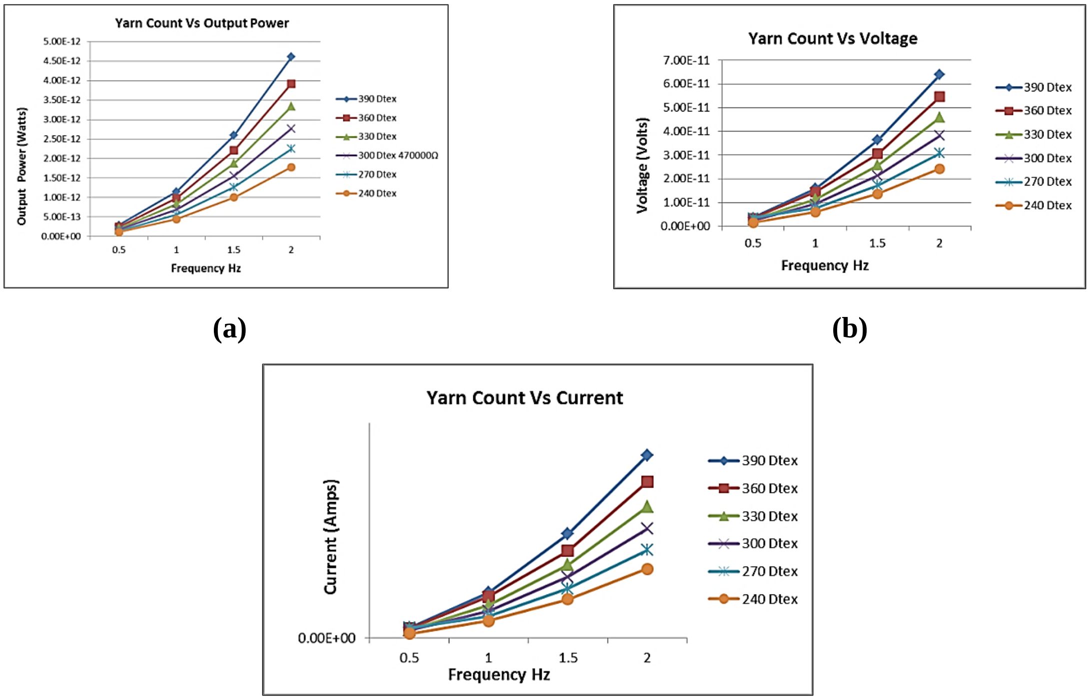

(a) **(b)**

(c)

Figure 3.24: Effect of Yarn Count on (a) power output (b) voltage and (c) current

3.6.4.4 Effect of Inclination Angle

To study the effect of a change in inclination angle, the thickness of the fabric i.e. the distance between the two plates was kept constant at 2.85mm and yarn linear density was also steady at 300Dtex. The angle of inclination of spacer yarns i.e. the angle between the spacer yarn and vertical axis was varied between 0°-60°. Figures 3.25 (a) and (b) show the model at an inclination of 45 and 30 degrees. Generally, it can be observed in the results (figures 3.26 a-c) that as the angle of spacer yarn increases, the power output decreases. At an angle of 60° with vertical, the fibres tend to have lower induced stresses before reaching its maximum position. However, as the angle is decreased, the induced stresses along fibre axis due to displacement loading increases and becomes maximum at 0°. Although a higher current and voltage is obtained at 0°, the output power is higher at 15°.

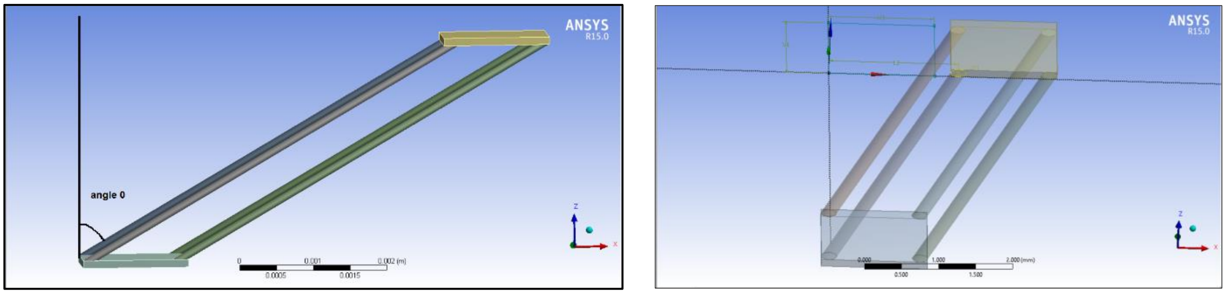

(a) (b)

Figure 3.25: The spacer fabric model showing spacer yarns at an inclination angle of (a) 45 and (b) 30

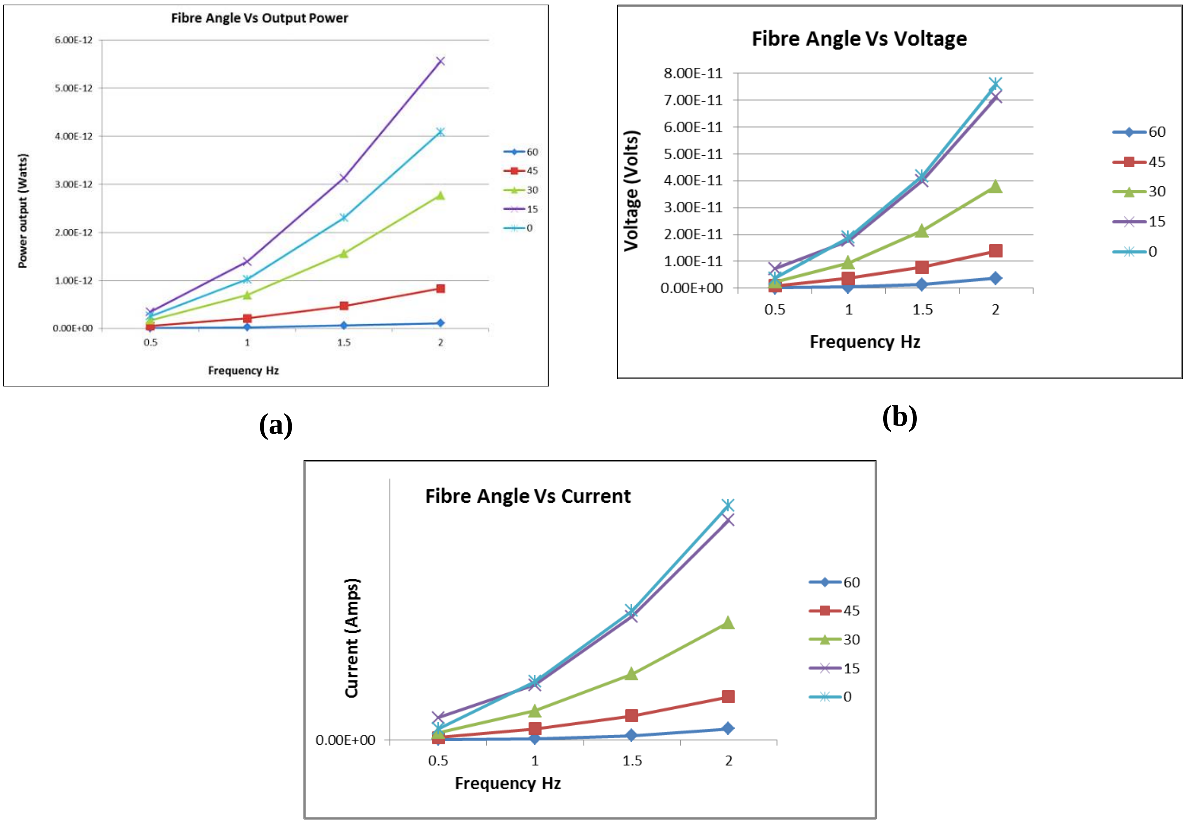

(a) (b)

(c)

Figure 3.26: Effect of increase in Fibre angle with vertical on (a) power output (b) Voltage and (c) current (Legend in figures 3.26 (a-d) refer to spacer yarn angle 0, 15, 30, 45, and 60 degrees with vertical)

3.6.4.5 Distances between Electrodes

The distance between the two electrodes (fabric thickness) was altered while keeping the fibres at 0°. It was observed that increasing the distance between the two electrodes decreases the power output. The increase in power output is due to the higher resultant stress at the lower thickness, which causes it to absorb more energy (Figures 3.27 a-c) (Liu *et al.* (2011). The constitutive equations stated above, a higher stress causes an increase in electrical field strength hence causing higher power outputs. It can also be seen in the power equations above, that the power decreases as the distance increases.

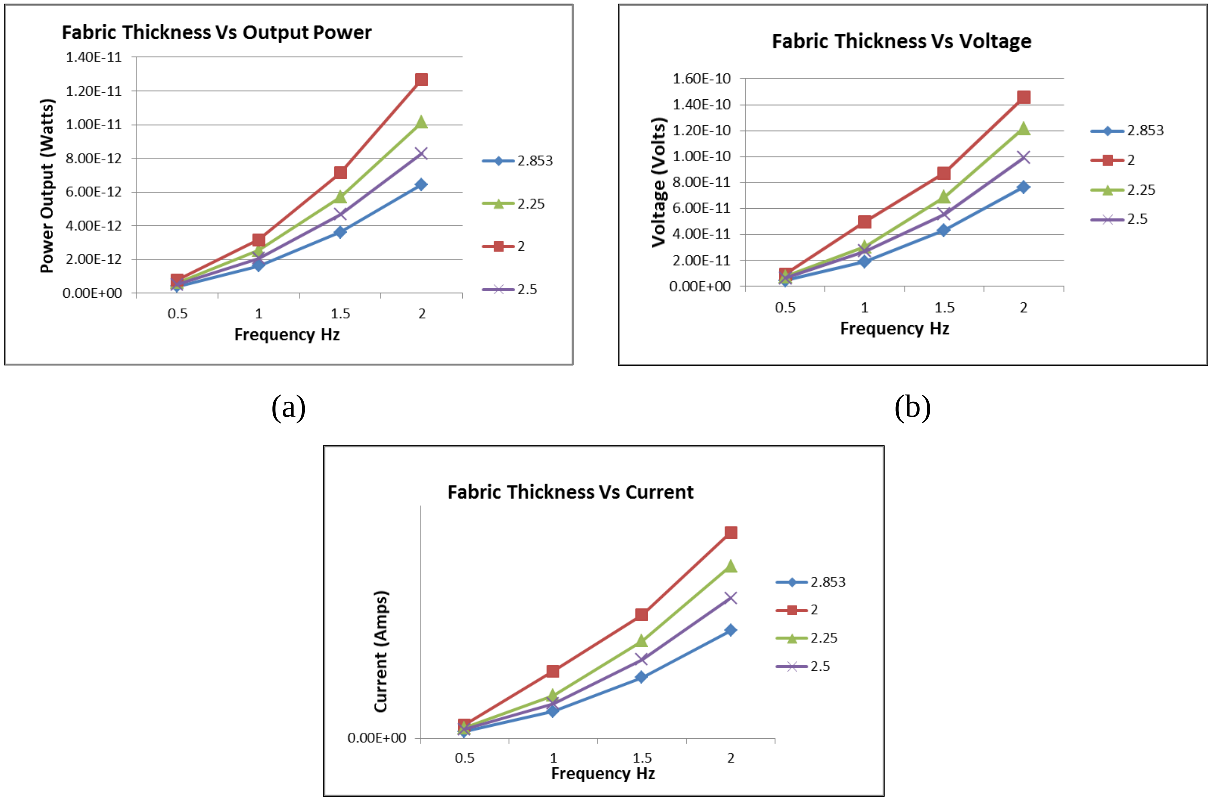

(a)

(b)

(c)

Figure 3.27: Effect of increase in thickness on (a) power output (b) voltage and (c) current (Legend in figures 3.27 (a-c) refer to fabric thicknesses 2, 2.25, 2.5, and 2.853 in mm)

3.7 Modelling of cross-linked spacer fibres

In this study, a representative model of spacer fabric using PVDF spacer yarns has been modelled. The results suggest that by altering the various structural parameters of the fabric, its electrical output can be optimized. The direction of poling has shown a significant effect on power output in d_{33} mode. The increase in yarn fineness has also shown to improve electrical output. The increase in yarn inclination angle has shown to decrease the power output. In addition to this, increasing the distance between the plates has shown to decrease the power output. The actual compression behaviour of the spacer fabric is expected to be somewhat different to the near-idealised model used in this study. Only bending of spacer yarns is considered in this model and realistically the deformation would cause buckling, rotating, and shearing of these fibres thus might yield results different to that reported in this study.

3.7.1 Spacer fabric geometric model

The model used in section 3.6.1 above was modified to study the effect of variation in the design of PVDF spacer fabric. The fabric was simulated by using a model consisting of 19 fibres attached with electrodes was used as the representative volume element of the fabric as shown in Figure 3.28. A medium sized mesh was used which was optimised. The model was created using 20 node 3D brick elements assigned to polyamide electrodes while the PVDF spacer yarns were assigned piezoelectric version of the 20 node bricks.

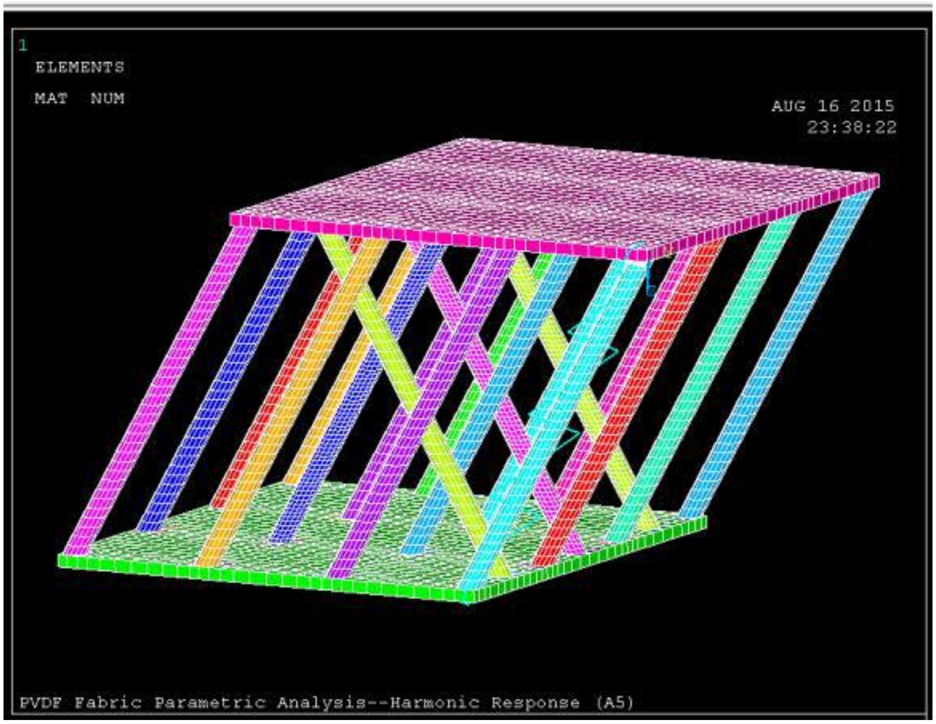

Figure 3.28: Spacer fabric model RVE

A steady-state full harmonic analysis was carried out in Mechanical APDL of ANSYS 15.0. A displacement boundary condition of 2.85x10-5m was applied in the *Z* direction to the top electrode. The bottom electrode was stationary using a fixed boundary condition of 0.0m. In order to simplify the model, only the spacer fibres were the part of the solver and the electrical properties of the top and bottom electrodes were suppressed. A sparse equation solver was used for the analysis which is a direct solver and well suited for linear and nonlinear applications with ill-conditioned matrices. The model was subjected to a low-frequency range of 0-2Hz with 4 intervals. A parallel resistance of 0.46MΩ was applied across the resistor. In this analysis, the model was assumed to be linearly elastic and any effect of damping was ignored. The mesh used for the results was medium sized mesh which was optimised. The electrodes were assigned material properties of polyamide. 38 contact regions between the fibres and electrodes were defined in the model. The distance between the electrodes was kept at 2.853mm. The spacer yarns were assigned the poling direction of d_{33}.

3.7.2 Yarn inclination and crosslinking

In a typical spacer fabric, yarn spacer angle lies between 10°-40°. However, the simulations were carried out for a wider range of inclination angles (0°-60°). Figure 3.29 (a-c) show the results obtained from these simulations. The yarn diameter was constant for the simulations (300Dtex) and the distance between the electrodes was constant at 2.853 mm. It was observed that decrease in yarn angle increases power outputs. However, 15 degrees was found to be the optimal angle with highest power output. At an angle of 60° with vertical, the fibres tend to have lower induced stresses before reaching its maximum position. However, as the angle is decreased, the induced stresses along fibre axis due to displacement loading increases and becomes maximum at 0°.

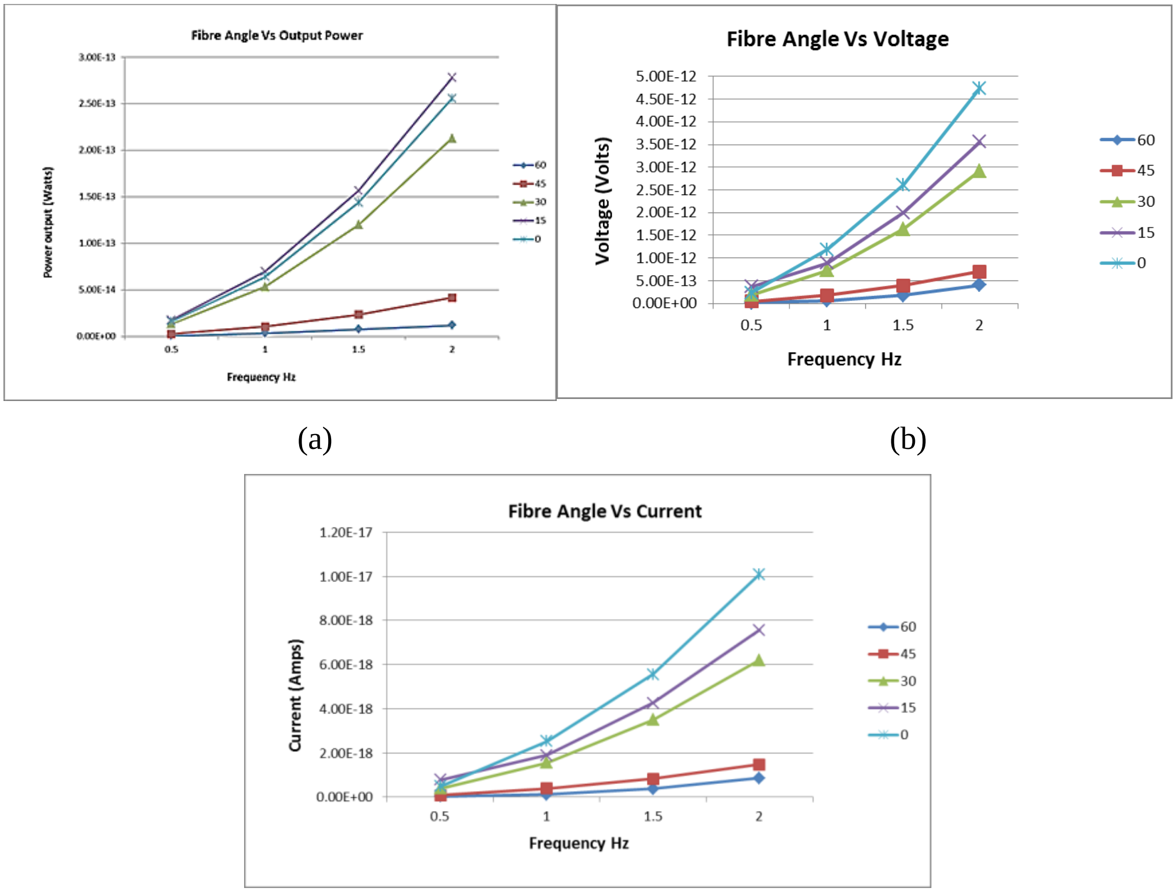

(a) (b)

(c)

Figure 3.29: Effect of increasing inclination angle on (a) output power, (b) Voltage and (c) current

3.7.3 Yarn thickness and cross-linking

The yarn count was varied from 200 to 400 deniers. The effect of these variations was recorded and are presented in Figures 3.30 (a-c) below. The model was subjected to the displacement boundary condition at a constant inclination angle of 30° to the global Z-axis. The other dimensions of the model were also kept constant. It was observed that increasing the yarn linear density increases the output power, current. This is due to increased absorption of energy at higher stress levels.

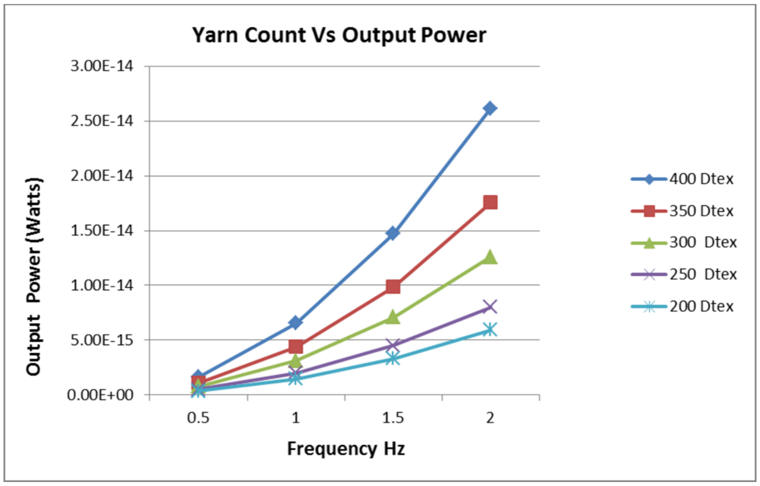

(a)

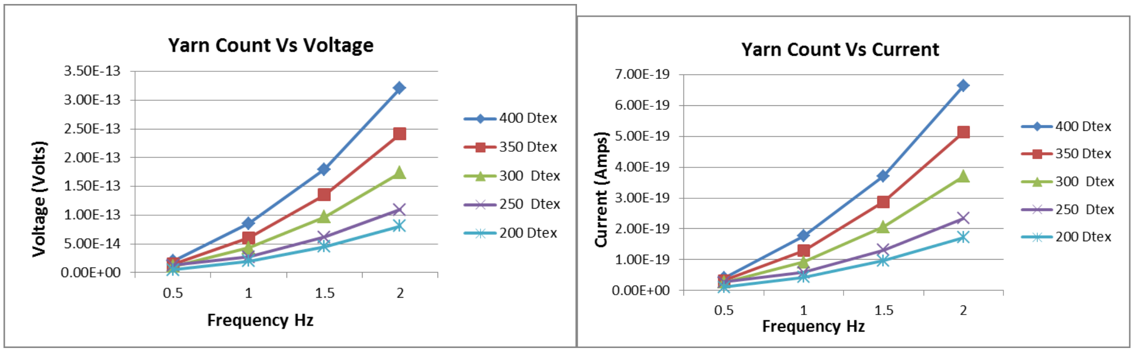

(b) (c)

Figure 3.30:Effect of increasing yarn count on (a) output power, (b) Voltage and (c) current

In this study, a spacer fabric in the form of its representative volume element using PVDF spacer yarns has been modelled. Various parameters of the RVE were modified and the results suggest that by altering its geometry, we are able to achieve higher power outputs. The results help in improving our understanding of the behaviour of spacer fabrics when deformed mechanically. The increase in a number of fibres has shown an increase in output power of the harvester. The yarn diameter has also been found to increase the outputs when using coarser yarns. It was also learnt that decreasing the inclination angle gives a higher output until reaching an optimal angle. The challenge is now to transfer the electrical energy generated in this fabric harvester to the required source which would be explored in the following chapters.

3.8 Summary of Computational Findings

A series of dual field finite element simulations have been done using ANSYS in this research. Two different poling configurations were simulated to achieve high electric field strength in order to pole the PVDF monofilament. The hole configuration, which was found to produce superior results was further investigated for central hole diameter, plate distance and plate thickness. It was observed that increasing the diameter of the hole in the plates result in decreasing the electric field intensity, which is confirmed by the FTIR results in the form of higher beta-content. Furthermore, the increase in plate distance also produces weaker electric field intensity and hence lower beta phase fraction.

A dual field finite element model was developed to explore the feasibility of energy harvesting using bonded PVDF patch onto a polyester and was subjected to harmonic and modal analysis. Various parameters such as the area, aspect ratio, and input loading magnitude were studied at different frequencies and their effect on output power, voltage, current and displacement were noted. The research found an optimal dimension of about 400 mm2 of PVDF operating at about 5 Hz to be able to harvest electrical energy from vibrational sources.

The optimisation of piezoelectrical output was also explored using a representative volume element of a spacer fabric using PVDF monofilament as spacer yarn. The results suggest that by altering the various structural parameters of the fabric, its electrical output can be optimized. The direction of poling has shown a significant effect on power output in d33 mode. The increase in yarn fineness has also shown to improve electrical output. The increase in yarn inclination angle has shown to decrease the power output. In addition to this increasing the distance between the plates has shown to decrease the power output. However, some limitations to the model include the actual buckling, rotating, and shearing of these fibres since only bending has been considered during simulations.

4 Yarn and Fabric Experimental Validation

In this chapter, the method for preparing PVDF yarns, and the fabric has been discussed. The produced samples were characterized using FTIR, and X-ray Diffraction (XRD) techniques. The samples were also tested using machines for electrical outputs. In these experimental work, PVDF pellets (MW 175,000, Sigma-Aldrich), were used to make electrospun Nano-fibrous web. The pellets were then used to make melt spun mono-filament yarn using single yarn extruder. These yarns were simultaneously poled with a novel poling assembly using high voltage to convert α-phase to β-phase. The phase conversions were verified using various techniques.

The high β-phase has been shown to increase the dipole moment as discussed. The higher the β-phase fraction, the better the piezoelectric behaviour due to its highest dipolar moment per cell unit (Qin et al. 2008). This high β-phase is the result of making PVDF fibres under certain conditions as discussed in Chapter 2. Briefly, it can be said that the high β-phases resulted from manufacturing under elongation, and with temperature up to 80°C. A strain of up to 550% is shown to favour β-phase formation.

The method of testing of PVDF fibres for electrical outputs has been equivocal. Several researchers have used a drop weigh method. However, only a few have discussed outputs under applied low stress. In his chapter, a 4-point bending test, has been used. This has been done by placing the yarns under strain, and then applying force to cause bending, to determine electrical outputs from PVDF yarns.

4.1 Yarn production by Melt spinning

Melt spinning is a process of forming objects with a fixed cross-section (Chapter 2). The process requires the material to be passed through a mould or a die forming a specific cross-sectional shape. The mould could also be reshaped to accommodate shapes having different core materials.

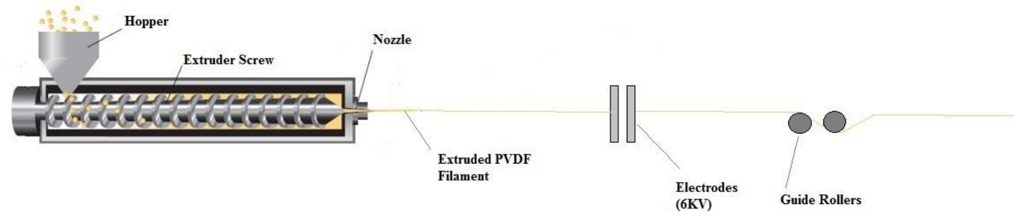

Figure 4.1 showing the schematic of the setup used for Melt spinning

In order to obtain the yarns, PVDF pellets were obtained from Goodfellow UK (Goodfellow.com, 2017). The polymer had a molecular weight of 175000. The melting point of the polymer was found to be 174°C and glass transition temperature was -32°C. the elongation at break of the polymer was 40%. To prepare yarns, FILABOT single screw melt extruder was used with modified drawing assembly. Figure 4.1 shows the schematic of the setup used for drawing of yarns. The extruder had nozzle diameter ranging from 0.5 mm-5 mm.

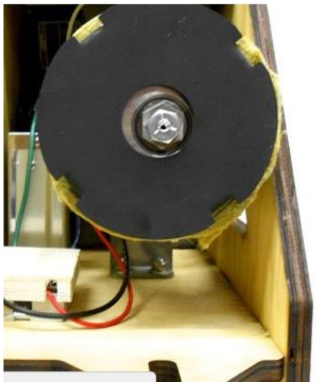

Figure 4.2: Extruder used for Melt spinning yarn

The draw ratio was varied using the drawing assembly with a controlled voltage reduction method. The drawing speed of the extruder was 4 m per minute at a draw ratio of 1. The draw ratio of yarn can be calculated by the ratio diameter of extruder nozzle to the actual diameter of the yarn. The yarn diameters were tested using the laser meter at various places. The polymer granules were fed to the hopper slowly. The poling assembly was followed by a set of rollers along with a customised winding assembly with two rollers and yarn guide. The extruder temperature was maintained constant 210^0C. A thermal camera FLUKE was used to measure the temperature of the extruded and drawn yarns at various gaps.

Figure 4.3 High voltage supply (Gamma High Voltage Research)

4.2 Poling Assembly design

Experimental procedure

To achieve the poling in these yarns, two aluminium plates were placed between the extruder nozzle and the steel rollers. Two 5 mm thick aluminium plates were used for the poling process. These plates had a maximum distance of 37.5 mm and a minimum distance of 7.5 mm. The electrodes were connected to a high voltage power supply, shown in Figure 4.3, with the range of 0-30kV and a variable output current range of 0-200μA. The speed of winding assembly was varied to achieve the required draw ratio. The environmental temperature including all poling conditions was changed accordingly to be able to achieve the required yarn. The entire poling assembly including the aluminium plates and the connectors were placed in a housing made of Perspex to minimize the health and safety risk as seen in Figure 4.5. The housing was connected to an earth connection and was also secured using the oscillating switch. This ensured that no one can be in direct contact with the high voltage while the experiments are running. The process was carried out in a single step and no post-poling was involved. This was to eliminate the risk of any variations that could be contracted.

The poling of these yarns was the d_{33} direction which indicates that the direction of poling in same as the direction of applied stress as discussed in Chapter 2 (2.7.1). The plates were placed horizontally in line with the fibre extrusion direction. The electric field present was perpendicular to the length of the fibre inducing a d_{31} field. Hence, to obtain d_{33} poling, the plates were placed vertically, and a hole was produced in the centre of each plate. For d_{31} the plates were horizontal with no holes. The hole configuration had a diameter of 5 mm and a varying distance in the range of 10 mm - 28 mm between the plates.

The centre hole diameter along with the distance between the two plates was optimized using an ANSYS simulation which was further validated. These simulations gave us a co-relation that between 1 mm to approximately 10 mm in height (electrode gap), the electrical field density varies greatly depending on the diameter (figure 3.4). However, after around a gap of 10 mm, the electrical field density becomes constant between the different diameters. If the diameter is increased, the electric field density decreases at a given height. This is due, in part, to the electrical field not forming correctly between the two plates. If the plates are too close together and the diameter too large, the electrical field lines do not reach the centre of the hole. This results in a lower electrical field density. If the plates are spaced reasonably apart, the electrical field has time to form and to create a field that is more constant at the centre of the hole. This means the fibre will pass through a higher electrical field density for a longer time.

4.2.1 Effect of voltage

The effect of field strength was determined by varying the applied voltage strength. The plates used were made from Aluminium, mounted to a Perspex (PMMA) sheet. A voltage of 6kV was applied to the plates while the fibre was extruded. The single yarn filament extruder was used to extrude yarns, stretching at the constant draw ratio of 5:1, and was simultaneously poled. The procedure was repeated for various distances between the plates as modelled. The extrusion temperature was 220°C which dropped to 75.6°C at poling (Figure 4.4).

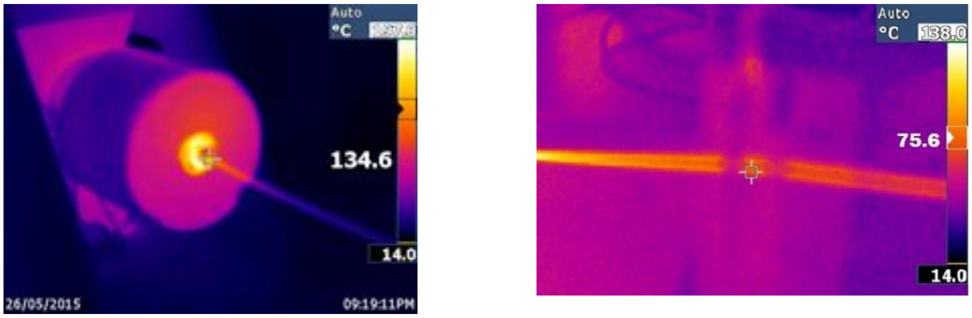

(a) **(b)**

Figure 4.4 showing the temperature of polyvinylidene fluoride filament using Fluke camera at (a) extruder nozzle (b) poling setup

4.2.2 Finding the optimal poling temperature

The yarns were drawn at various temperatures and were tested using Fluke Ti10 Infrared Camera. Figures 4.4 shows the fluke camera outputs at the nozzle and various sections of the drawing. Samples were prepared at various temperatures and their FTIR analysis was compared.

4.2.3 Draw ratio variations

To validate these results 5 mm thick plates were used with the hole configuration having a diameter of 5mm and a varying distance in the range of 10 mm - 28 mm between the plates. The plates used in the computational simulations were 50 mm x 50 mm. In the validation of these results, the plates were made up of 50 mm x 100 mm. A quick alteration in ANSYS shows almost identical results to the plates used previously as seen in Chapter 3 (Section 3.3). Figure 4.5 shows the setup used for testing the poling design.

One major concern on conducting high voltage experiments especially at high temperatures is that the surrounding air becomes ionized which increases the probability of arcing. This means that although the surrounding air is a non-conductor, plasma discharge can occur. This is the result of the production of current at one electrode which causes it to flow even through a non-conductor. In such an instance, any major accident can occur which in certain cases could be fatal. To avoid this and establish a safe working procedure, a safe and optimal distance was found to be 10 mm between the plates and all the experiments were conducted at that point. The voltage density used was 0.636MV/m. This is a large voltage density and is sufficient to induce poling in such thin yarns.

Figure 4.5 Setup used to extrude and pole polyvinylidene fluoride for validation

4.3 Fabric Preparation

The yarns produced from drawing of fibres, as discussed above, were used to produce spacer fabric. The spacer fabric has found many uses in the consumer world such as active wear, high absorbency medical applications and more recently in car seats. However, the possibility of using it for energy generation has been explored in this thesis. The knitted spacer structure made it possible to produce a fabric with a sandwich assembly. The spacer fabric was produced on SHIMA SEIKI Japan machine. The poled PVDF yarn with a 265 Den was used. Fine stainless-steel yarn plied with cotton yarn was used. Stainless steel yarns had a diameter of 85 microns, while the cotton yarn was 220 Den.

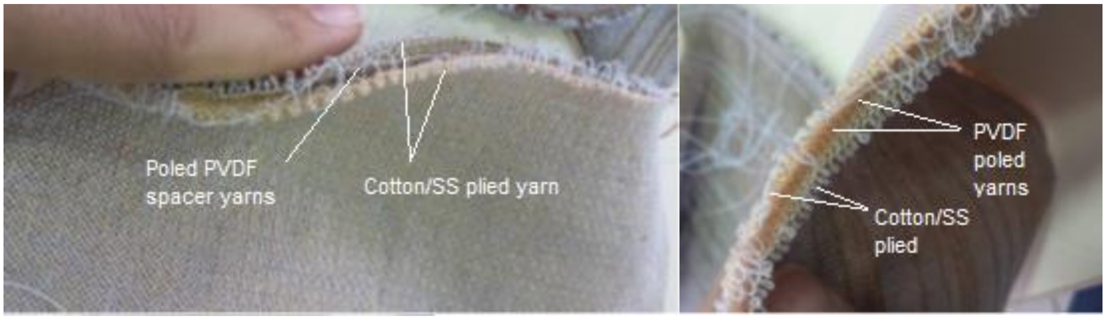

(a) (b)

Figure 4.6: Spacer fabric prepared using poled yarns (a) front view (b)side view

4.4 Morphological characterization

4.4.1 SEM

FEI Quanta 200 Environmental Scanning Electron Microscope (ESEM) (2002) was used to obtain the Scanning electron microscope (SEM) images of the produced fibres. The micrographs were acquired at the voltage of 15kV using a low vacuum. These were done without coating. The SEM images show a consistent yarn surfaces as seen in Figure 4.7.

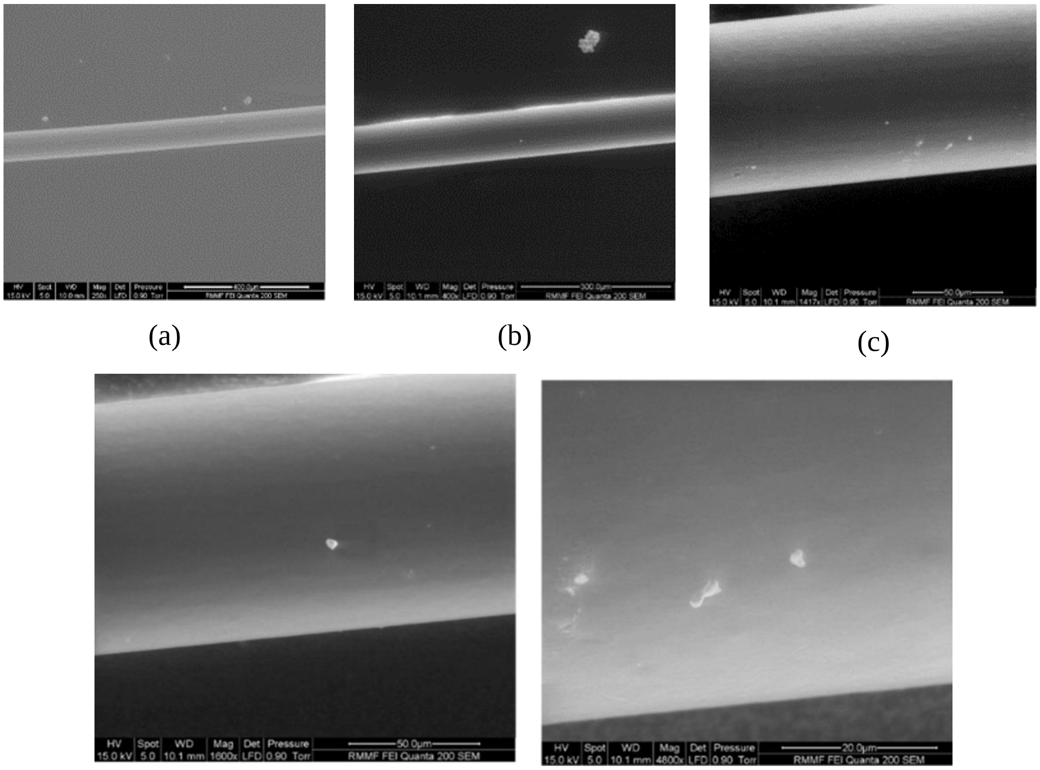

(a) (b) (c)

(d) (e)

Figure 4.7: SEM images of polyvinylidene fluoride yarn at magnification of (a)200x (b)400x (c) 1400x (d) 1600x (e)4800x

4.4.2 FTIR

The Fourier transformation Infrared is a technique used to identify the materials based on its infrared (IR) spectrum. Perkin Elmer 400 Spectrometer with universal attenuated total reflectance (ATR) sampling accessory attachment was used to obtain the infrared spectra of the poled and un-poled samples of PVDF. The spectrum (Figure 4.8) shows absorbance bands at 760, 790, and 970 which correspond to α-phase while the peaks at 840, 1430 which are characteristic bands of β-phase.

If IR absorption follows the Lambert-Beer law, the A_α and A_β absorbance at 764 and 840 cm^{-1}, respectively, are given by:

$$A_{\alpha,\beta} = Log\left(\frac{I^{0}_{\alpha,\beta}}{I_{\alpha,\beta}}\right) = C_{\alpha,\beta}K_{\alpha,\beta}X_{\alpha,\beta}L \tag{4.1}$$

for a sample with thickness *L*, and an average monomer concentration *C*. The subscripts α and β refer to the crystalline phases; I^0 and *I* are the incident and transmitted intensities of the radiation, respectively; *K*, the absorption coefficient at the respective wave number, and *X* is the degree of crystallinity of each phase.

For the polymer having α- and β-, the relative fraction of β-phase can be calculated as:

$$F(\beta) = \left(\frac{X_\beta}{X_\alpha + X_\beta}\right) = \left(\frac{A_\beta}{\left(\frac{K_\beta}{K_\alpha}\right)A_\alpha + A_\beta}\right) = \left(\frac{A_\beta}{1.26A_\alpha + A_\beta}\right) \qquad (4.2)$$

The value of K_α is 6.1×10^4 and K_β is 7.7×10^4 cm^2/ mol.

The yarns obtained were tested using FTIR for infra-red spectra. The amount of β-phase was calculated as per the equation (4.2) above. The results were analysed for maximum β-phase output.

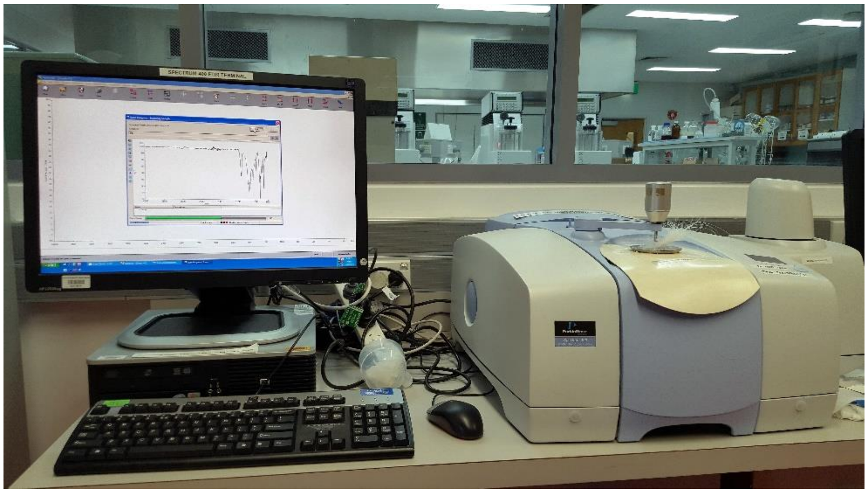

Figure 4.8: Perkin Elmer 400 Spectrometer at RMIT (Textiles)

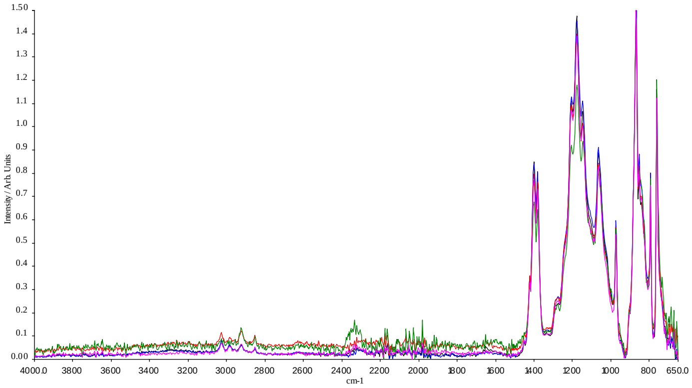

Figure 4.9:FTIR absorbance Spectra of Polyvinylidene fluoride filament

4.4.3 XRD

Bruker AXS D4 at RMIT University was used to obtain X-ray Diffraction (XRD) spectra of the samples produced. XRD results have been widely used to determine phases of PVDF (table 4.1) (Esterly, 2004, Martins et al. 2014, He et al. 2013). In XRD spectra, the results are obtained based on the identification of peaks at different degrees at two-theta (2θ). Some planes have similar peaks overlapping each other, however, each phase has at least one characteristics peak, which helps in identification of a phase. In XRD results, $K\alpha_1 = 1.5405600Å$, an α, β, and γ are known to show peaks around 20°. However, the β-phase has a characteristic well-defined peak at 20.26° (Martins et al., 2014). To obtain XRD spectrum, the samples were prepared as shown in Figure 4.10 (a). The samples were continuously scanned on XRD with 2θ angles between 5 and 90 degrees with a chopper increment of 0.04.

Table 4.1: Polyvinylidene fluoride crystal planes with corresponding 2θ peaks (Martins et al. 2014)

α-PVDF		β-PVDF		γ-PVDF	
Crystal plane	2θ	Crystal plane	2θ	Crystal plane	2θ
(100)	17.7	(110)	20.26	(020)	18.5
(020)	18.4	(200)	20.7	(002)	19.2
(021)	19.9	(020)	36.6	(110)	20.1
(111)	27.8	(101)	36.6	(101)	20.3
(200)	35.7	(221)	56.1	(022)	26.8
(002)	39			(200)	36.2

(022)	57.4	(211)	38.7

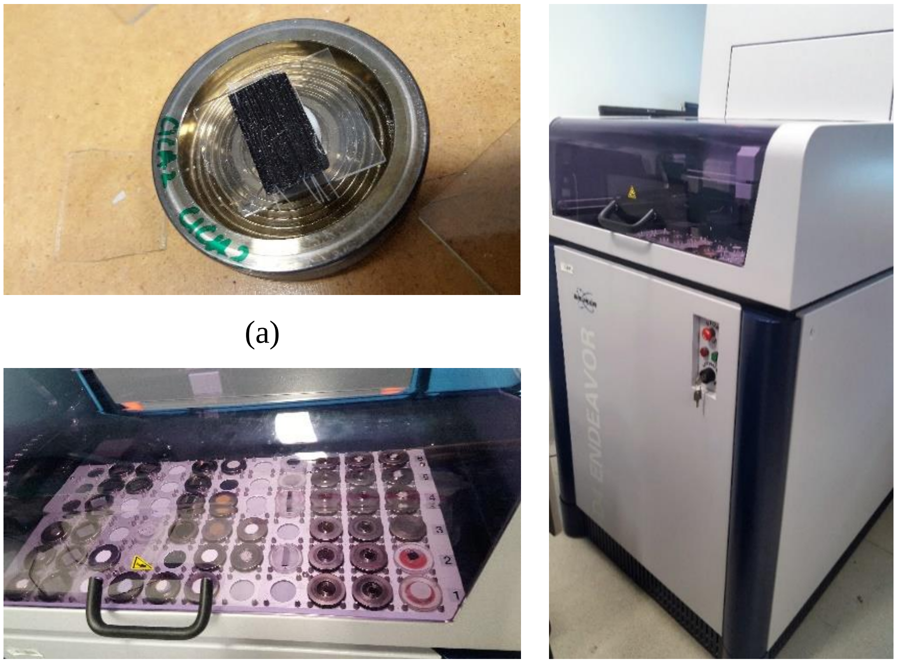
(a)

(b)

(c)

Figure 4.10 XRD (a) sample preparation (b) & (c) Bruker AXS D4 at RMIT School of Textiles

4.5 Piezoelectric output characterization

As seen in the literature review, most of the current test methods used for testing of PVDF yarns and fabric involve impact testing, such as American Society for Testing and Materials (ASTM) D 3763 standard impact test method. In this test, the sample is placed in an impact test rig and is connected to a digital oscilloscope. A weight e.g. 1.0 kg is dropped from a height and the subsequently produced voltage is recorded. In scenarios where sudden jerk, such as in impact, is present on a human body, correlates only with the heel strike. Therefore, this method seems highly suitable for the shoe-mounted piezo harvesting devices. in the fabric form, different forms of forces as acting. The fabric is continuously compressed against the skin under strain. In this study, two methods have been proposed based on it desired application as spacer yarn in the 3D fabric. The yarns are tested for direct piezoelectric voltage and energy using compression in axial loading, and a high precision four-point bending system with uniform stress. The corresponding open-circuit voltage is measured using digital multi-meter.

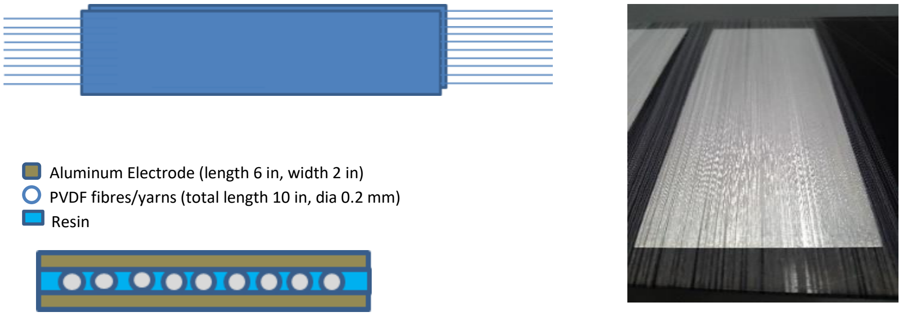

(a) (b)

Figure 4.11 Sample preparation (a) Schematic diagram (b) actual sample being prepared

In order to characterize the piezoelectric properties of the poled PVDF fibres, various experimental tests were conducted, and resultant output energy was calculated. The samples were prepared using uniformity tester by placing the equal number of yarns between two aluminium plates (figure 4.11 a-b). The polyester resin was used to restrain the fibres in their position. The yarns were subjected to equal strain and were left to cure for three days before removing from the machine. The electrical outputs were obtained by connecting Keysight digital multi-meter across the samples to collect open circuit voltage and closed circuit current outputs.

4.5.1 Compression testing

Instron insta cyclic compression machine was used to test PVDF fibres by applying axial loading. The cyclic tester formed series of dynamic impact force pulses with controlled sinusoidal force or displacement pulse ranging from -3 kN to 3kN. The samples were held between the wedge-shaped mounts and were insulated by using soft plastic bars between sample and wedges. When the samples were subjected to cyclic compression, the fibres sandwiched between electrodes were bent, deforming in the direction of the length of fibres.

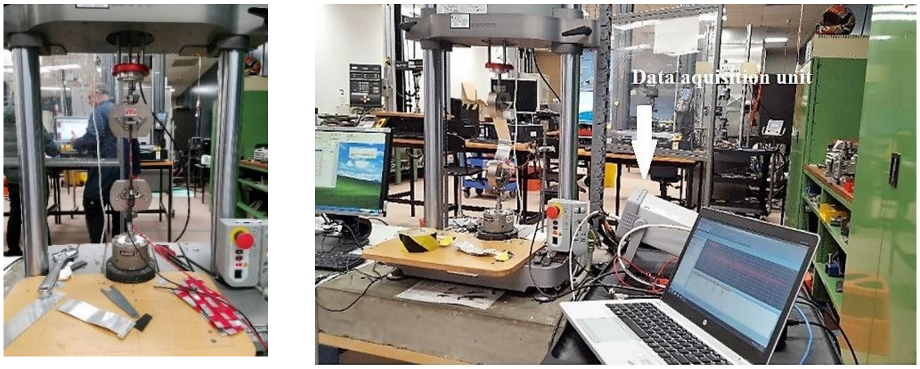

(a) (b)

Figure 4.12 Instron Insta cyclic compression machine showing (a) test setup and (b) attached data acquisition unit

The machine was set to compress the sample to a displacement of 2.5 mm at 2 Hz frequency. A data acquisition unit was connected to the electrodes on each side and sample scan rate was 100Hz. The integrated force sensor in the machine measures the applied uniform force. The data outputs were noted in the form of load, and displacement and were stored for further processing.

The stress in the sample can be calculated by:

$$\sigma = \frac{F}{w.t} \tag{4.3}$$

where F is a force (N), σ is stress (Pa), w(m) and t(m) are width and thickness respectively.

4.5.2 4-point bending

To determine the d_{31} voltage outputs in yarns, the 4-point bending test was used. A 4-point bending test is usually used for composite materials for flexural rigidity testing. In this test, the specimen lies in a span and force is applied. The load is uniformly distributed across the sample. The samples were placed between the span as seen in Figure 4.14. A data acquisition was connected to samples using wires. The process was repeated for all samples.

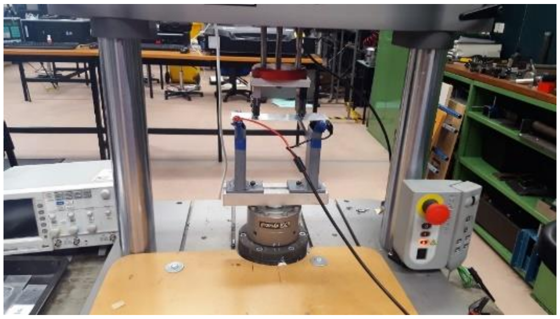

Figure 4.13 4-point bending test with the sample under stress.

The induced stresses in the material are obtained by the equation:

$$\sigma = \frac{3\,.F\,.(l-b)}{2\,.\,w\,.h^{2}} \qquad (4.4)$$

where σ is the induced stress, F is the load (force) [N], l is the span between the outer points, b is the span between the inner points, w is the width and h is the thickness of the substrate. The procedure was repeated for fabrics.

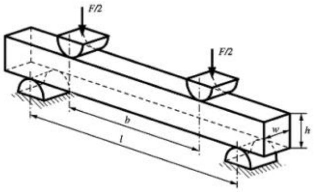

Figure 4.14 The figure shows the schematic presentation of the four-point bending machine (Gusarov, 2015).

4.5.3 Strain applied during testing

The strain was obtained by using Young’s modulus of the sample. It is assumed that the sample behaves quasi-isotopically for small displacements, and there are no voids in the sample, Young’s modulus of the sample is calculated based on the rule of mixtures. The tensile modulus of the materials is noted as:

$$E_c = V_f E_f + V_r E_r \qquad (4.5)$$

Where the tensile modulus of Aluminium is 7.00E+10 N/m^2, modulus of PVDF yarn 9.2E+8 N/m^2, and the modulus of Polyester Resin is 3.45E+9 N/m^2, the calculated modulus of the sample was 4.72E+10 N/m^2.

The flexural modulus was calculated using the 4-point bending test and found to validate the calculated modulus of 4.72E+10 N/m^2 above.

Assuming that the sample obeys hooks law, the strain can be calculated for the applied stress values based on:

$$E = \text{Stress/Strain}\left({}^{\sigma}/_{\varepsilon}\right) \tag{4.6}$$

4.6 Electrical outputs and Mean power calculation for melt spun polyvinylidene fluoride yarns

The PVDF yarn harvester means power was calculated using Eq.4.2, which is stated below. The voltages and the currents generated by the harvesters were recorded using data acquisition software and DMM (digital multimeter) both produced by Keysight technology. The samples were connected to DMM via wires.

The DMM 34410A by Keysight technologies that were used, having a basic accuracy of 0.0030% in DC, and 0.06% AC. The internal impedance of multimeter was 10 MΩ. A typical output piezo voltage signal can be seen in fig 4.15. The current measurements were recorded using a resistance of 0.46MΩ.

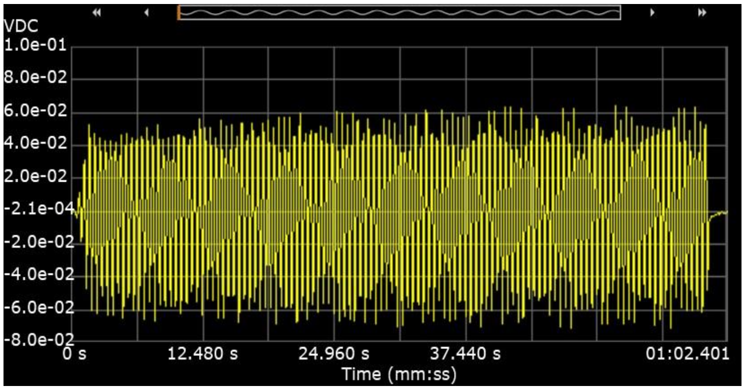

Figure 4.15 Voltage Output signal using DMM

All readings were taken at 2Hz frequency which was taken in regard to mimicking human motion. Coaxial wires and insulating tapes were used to reduce noise produced in voltage signals generated by PVDF harvesters. Still small amount of noise was detected in the system, but filtering of the signal was not performed because of the low power output allied with PVDF yarn harvester. To calculate the Mean Power of energy harvester the voltages and current values were converted into root mean square values. The distinct time-varying voltage signal values were converted to voltage root meant square (VRMS) by using Eq.4.1. where *n* is the number of voltage samples.

$$V_{RMS} = \sqrt{\frac{1}{n}}\ (V_1^2 + V_2^2 + \cdots V_n^2), \qquad (4.7)$$

As these values are calculated through the resistive circuit, the voltage and current values remain in phase with each other. It is assumed that the power factor is unity during the experiment i.e the energy is transmitted effectively between source and load network, hence the following:

$$\text{Power}_{\text{MEAN}} = \text{V}_{\text{RMS}} \text{ x } \text{I}_{\text{RMS}} \qquad (4.8)$$

4.7 Summary

The process of melt spinning is a widely used method for polymer fibre manufacturing at industrial scales. In this research, melt-spun monofilament was extruded and simultaneously poled using a novel poling assembly to validate the results obtained by simulating the device in ANSYS (chapter 3). Various process parameters such as temperature, poling voltage, draw ratio were studied to obtain results. The poling assembly was tested for the distance between plates and hole diameters in accordance with the simulation parameters. The characterisation of the produced PVDF yarns was performed using several techniques such as SEM, FTIR, XRD. The FTIR and XRD spectra were then evaluated to compare with the simulation results.

The testing of piezo fibres is still in its initial stages, although a number of tests are available, yet they are specific to their application. Some of those testing methods have been used in this research for the purpose of confirming the earlier conclusions. The 4-point bending test and compression test have been used to test the fibres for their electrical outputs through d_{31} and d_{33} bending modes. The results are discussed in the next chapter. The optimised yarns were then used to produce PVDF spacer fabric using flat-bed knitting machine. The detailed findings are discussed in next chapter.

5 Experimental Results and Discussion

To achieve the optimum design, we must consider the actual scenario of how yarns would behave individually, and collectively when applied with the same force. The morphological characterisation of yarns is generally conducted using several morphological techniques such as FTIR, XRD, SEM, and nuclear magnetic resonance spectroscopy (NMR). In practice, the FTIR results alone have been discussed to confirm the β-phase of PVDF. However, Martins *et al.* (2014) have shown that FTIR alone is not enough and has to be augmented with either X-ray diffraction (XRD) or differential scanning calorimetry (DSC) to support the obtained results. During characterisation of PVDF yarns, XRD technique was used to support the acquired FTIR spectrum results. The piezo output of yarns can be determined using direct voltage measurements such as through impact testing and then obtaining the outputs through a millimeter. The atomic force microscopy can also be used to obtain the piezoelectric constant d_{33} to investigate the outputs. In this manuscript, direct piezo voltages were obtained on application of strain parallel and perpendicular to the fibre axis, and the current outputs were noted.

Various parameters were tested for output response as discussed. The outputs are discussed in the sub-sections below. To eliminate noise from the testing machine, the insulating tape was used to protect any electrical noise, in addition to the thin plastic bars used to hold the samples. The output voltages were obtained at a low frequency of 2 Hz and duration of 60 s. The results were analysed using Origin (OriginLab, Northampton, MA) and MS Excel software (Ms office 365 pro plus).

5.1 Morphological characterisation of the polyvinylidene fluoride polymer

5.1.1 Effect of increasing plate distance on output

A set of PVDF yarns were extruded using the setup discussed in Chapter 4. The yarns were poled using 6 kV and the drawing temperature was kept constant at 80°C. The yarns were drawn at a ratio of 5 and all other parameters were kept constant. The yarns were passed between electrodes with varying distances and the produced yarns were tested for FTIR and XRD.

As seen in simulated results in Chapter 3 (Section 3.3.4.5), the effect of increasing plate distance was observed as a function of electric field intensity. It was observed that the field density decreased with increasing plate distance. Figure 5.1 shows the result of β-phase content result of the fibres produced using various plate heights. A decrease in the β-content fraction from 10 to 15 mm plate distance can be ascribed to decreased electric field intensity. Upon further increasing the plate distance, the β-content falls abruptly.

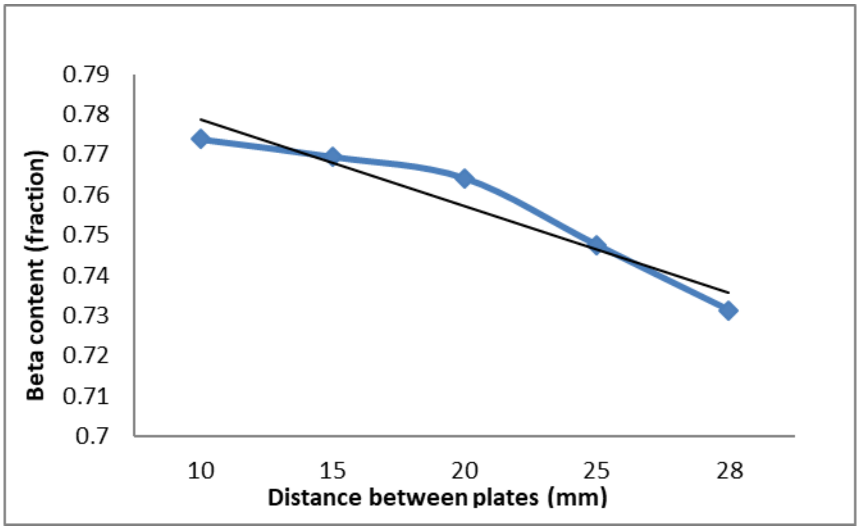

Figure 5.1: β-fraction obtained on varying electrode distance

The infrared spectra seen in Figure 5.2 shows the details of β-peaks and α-peaks observed at various wavelengths. Increasing plate distance can be attributed to decreasing field intensity as discussed in Chapter 3 (Figure 3.4). At low field intensity, a slight peak at 760 cm^{-1} can be seen (CF_2 bending). On increasing the field intensity, this peak is reduced while the peak at 840 cm^{-1} is slightly increased CH_2 rocking) and 1280 cm^{-1} (CF_2 stretching). The maximum field intensity at 10 mm indicates the strongest field with the increase in β-fraction of almost 4.5%, due to higher peak at 840 cm^{-1}. These shifts in the β-fraction results are comparable to the results of Gupta and Doughty (1980), who indicated that this change is due to a shift in molecular conformation on the application of a high electric field owing to crystal phase transition.

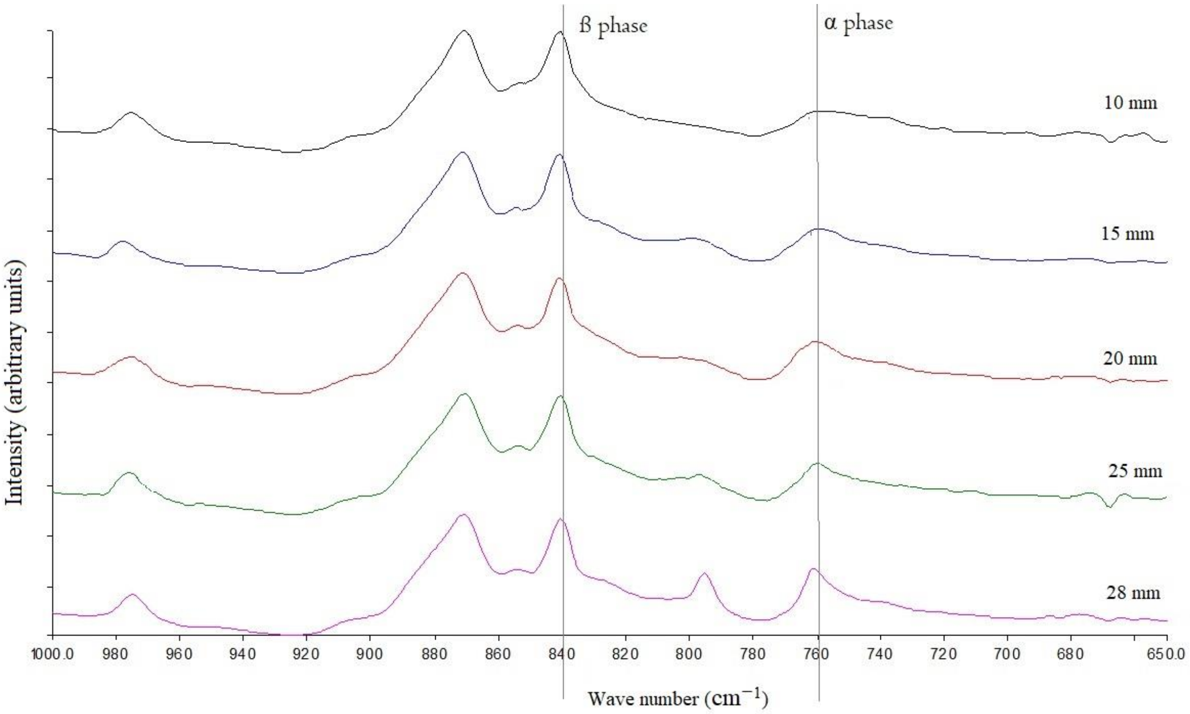

Figure 5.2: Fourier-transform infrared spectra of polyvinylidene fluoride yarns extruded using various electrode distance

The complete disappearance of the miniscule peak of 760 cm^{-1} suggests a shift in polar forms. It can be established that the results agree with the results predicted using computational simulations. The simulations in Chapter 3 had indicated that the field density is maximum at pre-10 mm. However, due to safety issues, it was not possible to reduce the plate distance below 10 mm. The result is further supported by the XRD data obtained for the four samples (figure 5.3). The samples D1–D5 represent electrode distance of 10, 15, 20, 25 and 28 mm, respectively as discussed in chapter 4. The most prominent peak was presenting (110) and (200) crystal planes, occurring at a two-theta angle of 20.26° as reported by Esterly & Love (2004) and Gregorio (2006) in the literature. The peaks of the X-ray results were greater in intensity at 20.26° than at other angles. A corresponding peak at 36.0° appears which can be attributed to (101) and (020) crystal planes (Buckley *et al*. 2006).

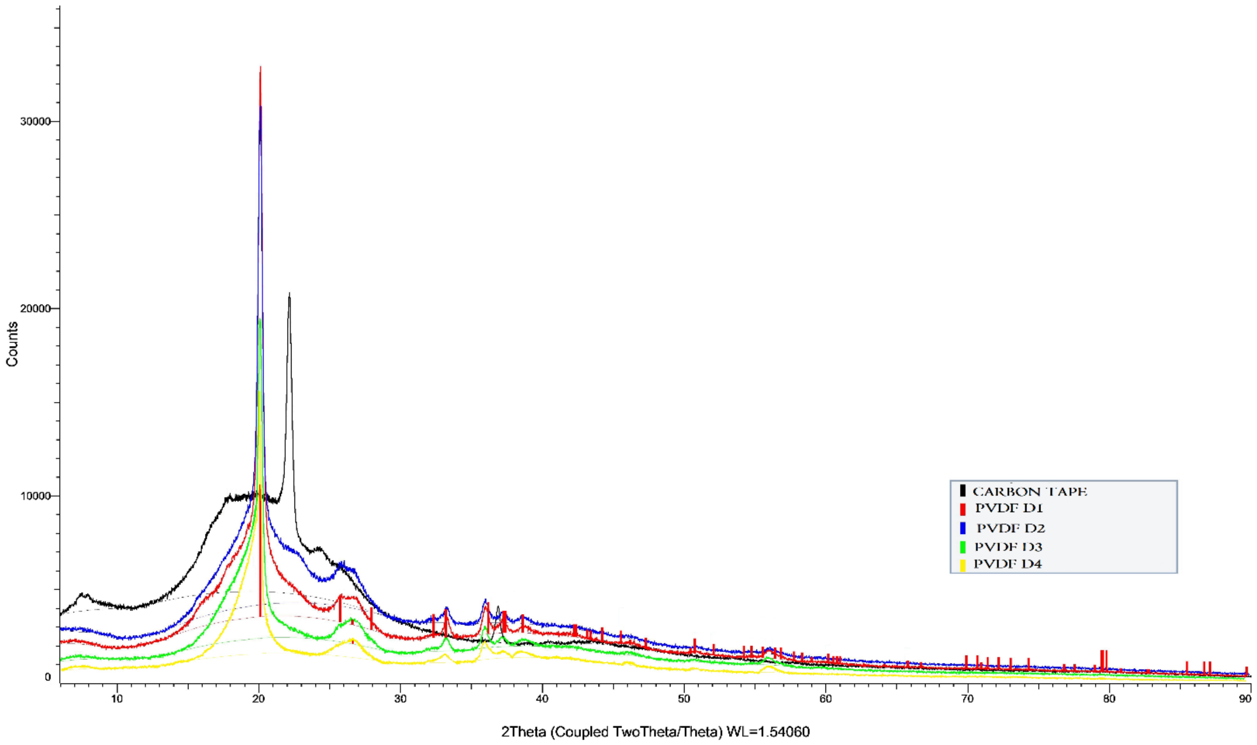

Figure 5.3: X-ray diffraction of polyvinylidene fluoride yarns extruded using various electrode distances (D1 – D4)

5.1.2 Effect of increasing hole diameter

The effect of the design of poling assembly for PVDF fibres has been simulated in Chapter 3. The use of two different poling designs was considered and it was found that design 2 (centre hole configuration) has much higher electric field intensity than slit configuration. To validate those results, several yarns were extruded with applied poling voltage of 6 kV. These yarns were drawn with a draw ratio of 5:1 and distance between the plates was fixed at 10 mm. The poling assembly was encased in a Perspex box with an oscillating switch to reduce external effects such as variations in temperature, draft around the poling area, in addition to providing isolation for safety (Occupational Health and Safety requirement).

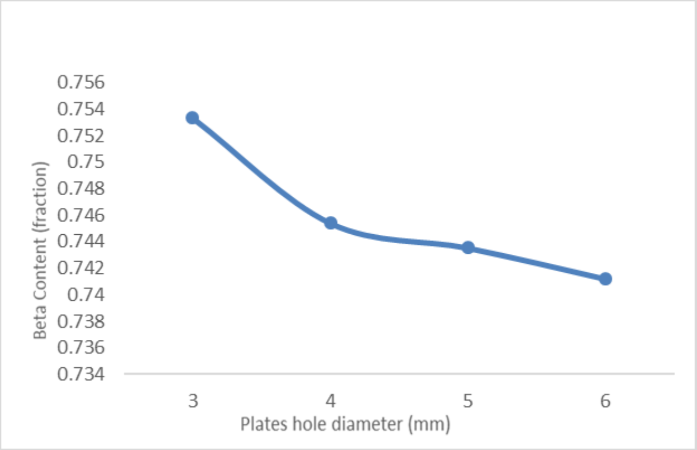

Figure 5.4: β-phase fraction content at various electrode hole diameters

Figure 5.4 shows the effect of increasing the hole diameter on β-phase fraction calculated as discussed in Chapter 4. It can be deduced that the lower the diameter is, the higher the β-phase is attributed. The β-fraction was calculated based on the peaks observed in FTIR spectrum Figure 5.5. The spectra show peaks present at 870 cm^{-1}, 840 cm^{-1}, and 760 cm^{-1}.

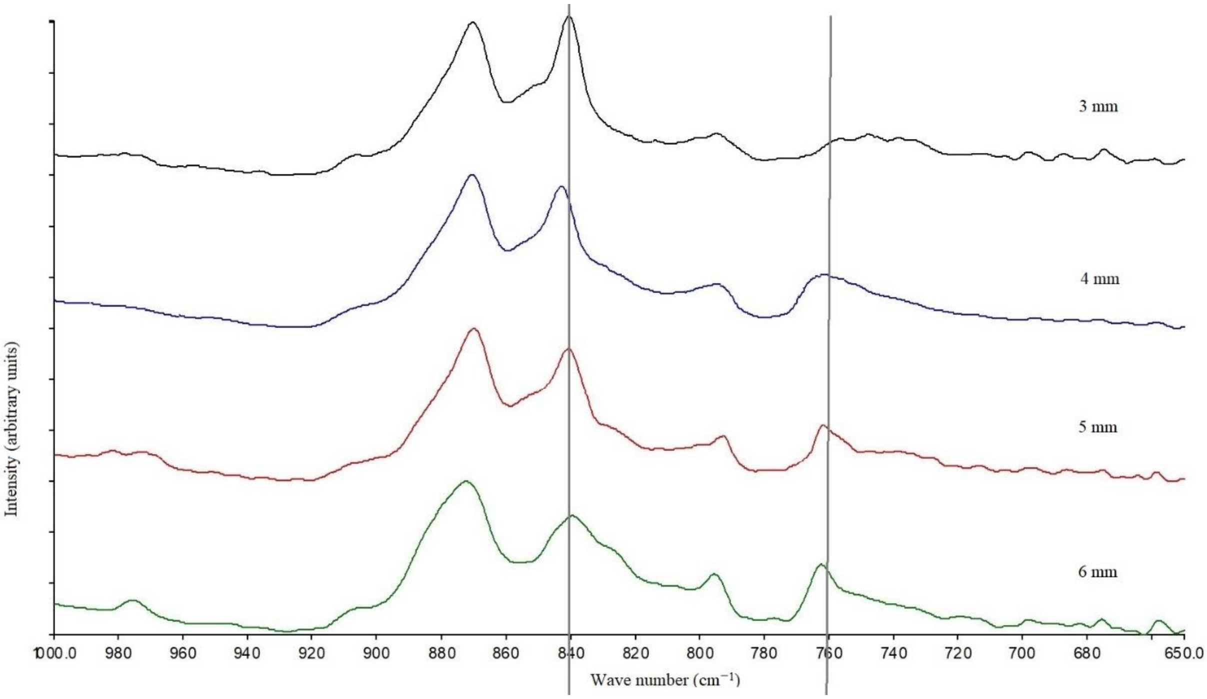

Figure 5.5: Fourier-transform infrared spectra of polyvinylidene fluoride yarns extruded using various electrode hole diameters (H1-H4)

As discussed earlier, the distinct peak at 840 cm^{-1} is the indication of the presence of β-phase. The height of peaks determines the fraction of the presence of each phase as depicted in Figure 5.4. The presence of a strong electric field between 3 mm and 6 mm diameter has caused a slight shift in the β-presence causing morphological conformation to change. This is consistent with the work of Davis *et al*. (1978) where it is mentioned that the high electric field causes the non-polar α-crystal to polarise resulting in a phase transformation to the highly polar β-phase. Gupta and Doughty (1980) have also agreed on the fact that although the uniaxially stretching causes a molecular realignment of chains, there are orientation dislocations due to chain twisting as indicated by Takahashi and Odajima (1978). These ‘dislocations’ can be adjusted by the applications of a strong electric field under which the odd molecules may be rotated in parallel positions. The removal of these ‘defects’ causes an overall improvement in crystallinity and net polarisation. Referring to Figure 5.4, it can be stated that effect is insignificant between diameters ranging from 3 mm to 5 mm. However, at 6 mm, the β-phase falls extremely low, nearly 0.74 which is due to the sample showing a small peak at 760 cm^{-1}. Figure 5.4 shows the β fraction is lowest for 6 mm samples, indicating a lower α- to β- conversion.

Figure 5.6 shows the XRD spectrum for various hole diameter assemblies. A clear distinct peak is present at 20.26° (Gregorio 2006) for all samples. The reduction in β-peak at 2theta in XRD is in admittance of the FTIR spectra (Figure 5.5). The appearance of a small peak at 18.0° in 6 mm diameter means that α-phase was present (100) (Gregorio 2006).

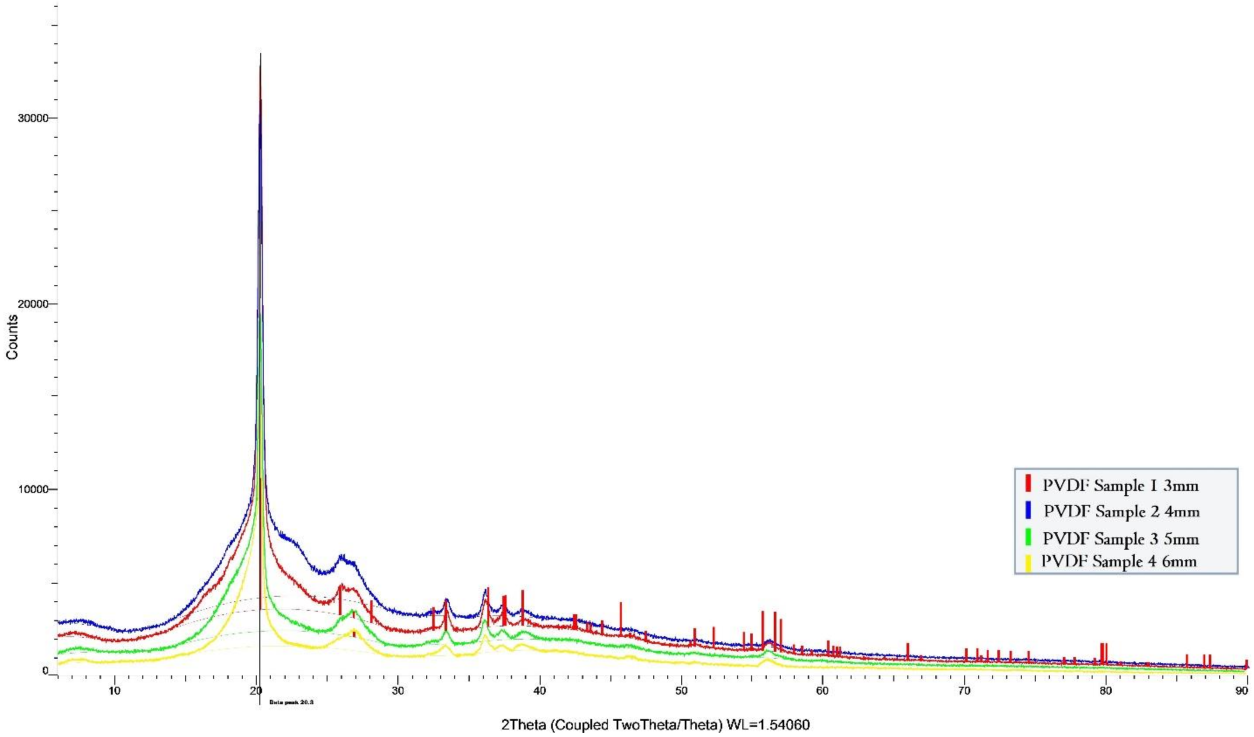

Figure 5.6: X-ray diffraction analysis of polyvinylidene fluoride yarns extruded using various poling diameter (H1-H4)

5.1.3 Applied voltage

To investigate the effect of applied voltage, PVDF yarns were extruded with varying applied voltages up to 6 kV. The draw ratio of yarns was constant at 5:1 and the distance between the electrodes is 10 mm. The yarns were then characterised using FTIR. The relation as discussed in Chapter 2 was used to determine the fraction of the β-content present in each yarn. Figure 5.7 shows the effect of increasing electric field intensity by increasing the applied poling voltage on β-fraction. The increase in β-fraction owing to higher poling voltage is suggestive of a change in molecular conformation as suggested by Davis *et al*. (1978).

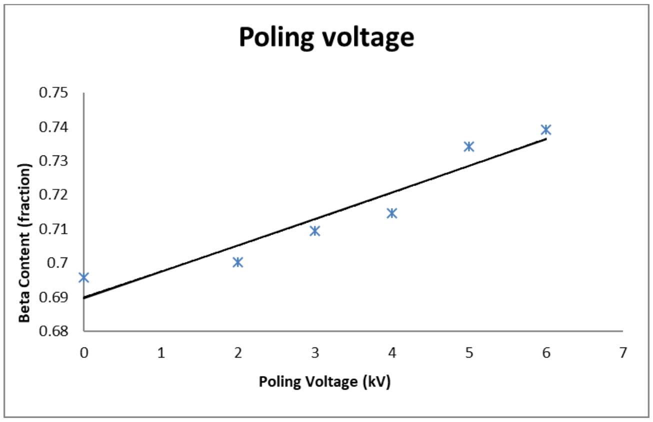

Figure 5.7: β-fraction obtained for yarns extruded at various poling voltages (P1-P5)

The detailed FTIR spectra (figure 5.8) of the variable applied field shows an increased peak at 840 cm^{-1}. The presence of a peak at 840 cm^{-1} indicates that all the samples have a strong presence of β-form. The difference in peak heights signifies an increase in overall polarity of the samples. The spectra also suggest a small peak at 760 cm^{-1}, diminishing on an increased voltage. The general effect of the application of a poling voltage from low to high has overall resulted in increasing β-fraction. The XRD spectra obtained for applied voltage is indicative of a presence of a strong peak at 20.26° as seen in figure 5.9.

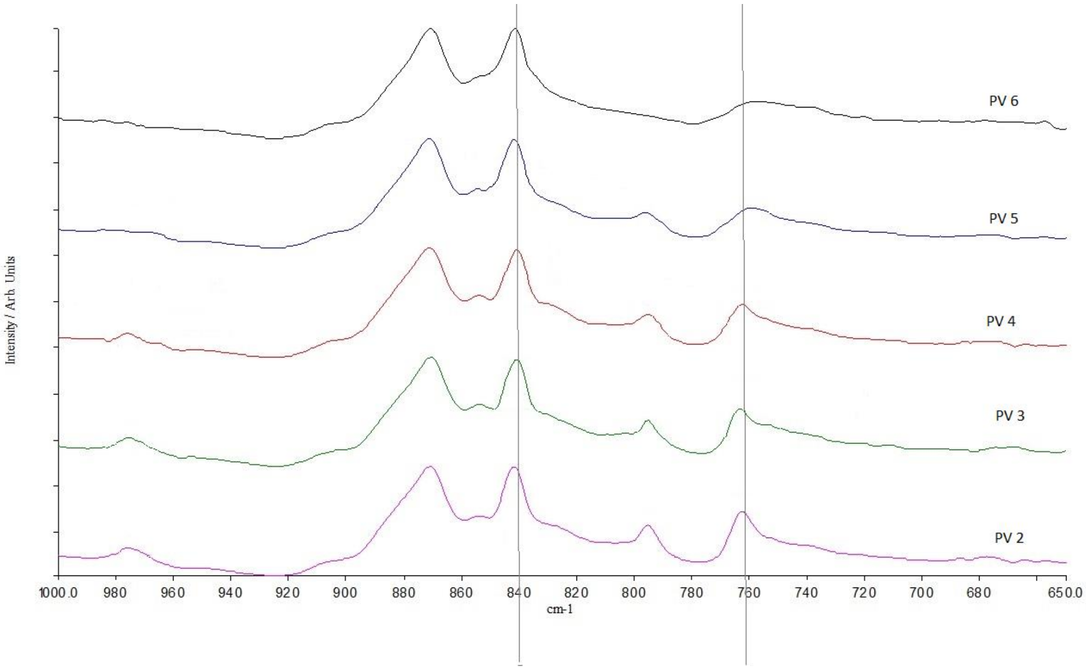

Figure 5.8: Fourier-transform infrared spectra of polyvinylidene fluoride yarns yarns extruded using varying applied voltage (P1-P5)

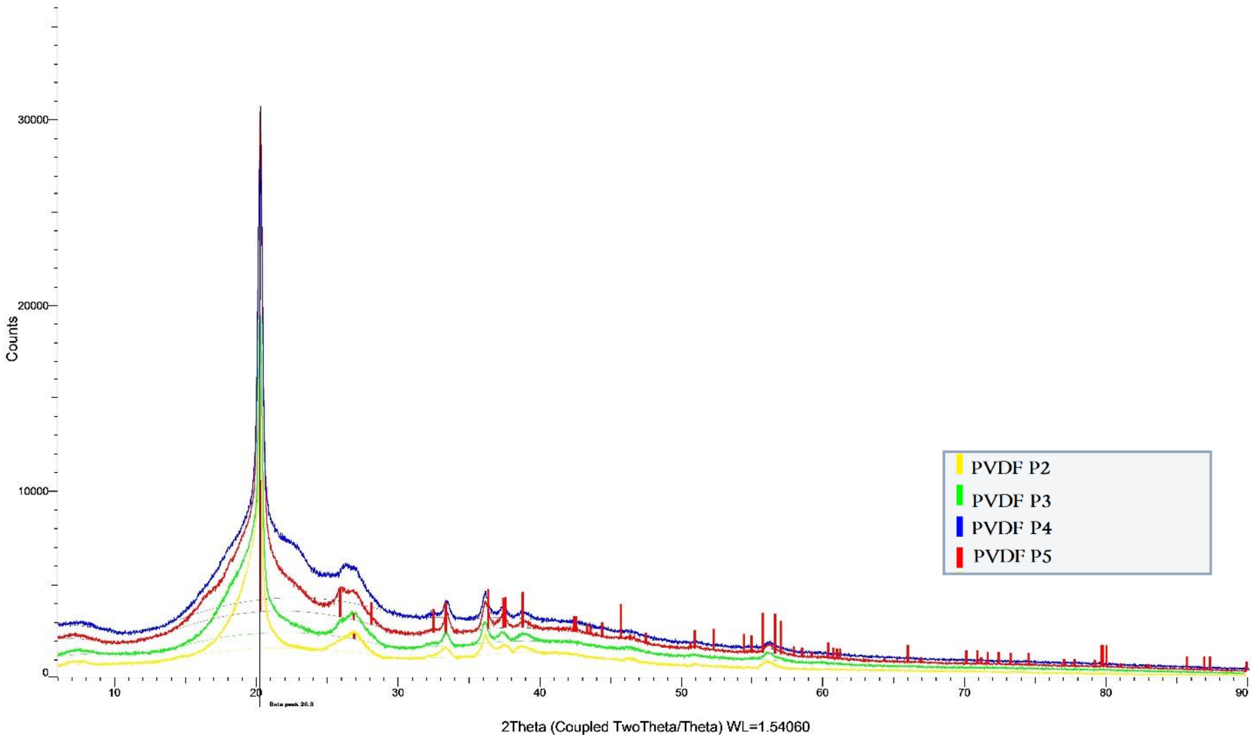

Figure 5.9: X-ray diffraction analysis of polyvinylidene fluoride yarns extruded using varying applied voltage (P2-P5)

5.1.4 Effect of varying the drawing temperature

The temperature dependence of piezoelectric activity in PVDF is widely researched and has shown to affect the formation of β-phase in PVDF yarns. The yarns were simultaneously extruded and poled at 6 kV. The draw ratio was consistent while varying the temperatures. The outcome of temperature variation on β-phase fraction can be seen in Figure 5.10.

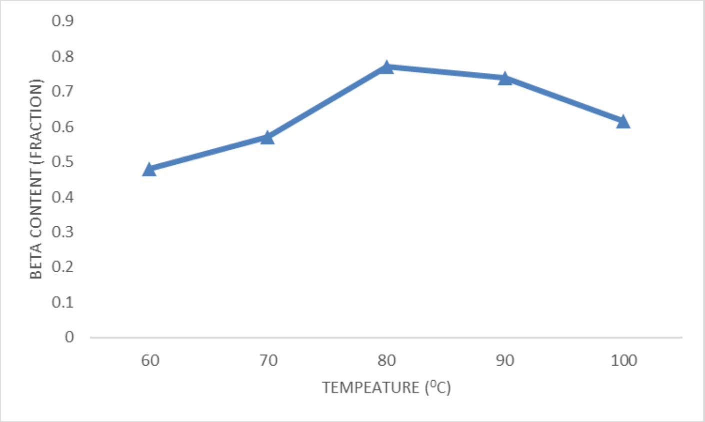

Figure 5.10: β-phase fraction content

The detailed FTIR spectrum in Figure 5.11 shows a distinct peak at 840 cm^{-1} which is indicative of conversion of β-phase (Lanceros-Méndez *et al*. 2001). A shift in the peak at 760 cm^{-1} can be seen while increasing the temperature from 60° to 70°. The peak decreases in height which nearly flattens out at 80°–90° and resurfaces at 100°. The β-fraction is calculated based on the absorbance spectrum and the summary of these were plotted in Figure 5.7. The results reveal that on increasing the drawing temperature from 60° to 70°, the β-fraction is marginally increased by 6%. However, increasing the drawing temperature to 80° shows a considerable increase the β-fractions by 32%. On reaching 90°, the β-phase fraction reaches a slight drop at 0.74 and continues to fall on drawing the filament at 100°. The highest fraction can be achieved at 80°. The increasing temperature is associated with decreasing viscosity of the polymer which becomes more ductile. This results in easier alignment of polymer chains along drawing direction. Hence, it results in orientation of dipole especially the CF_2 bonds dipole moments being optimised. This remains the case until 80°C is reached. The further increase favours the formation of α-phase. Sencadas *et al*. (2009) have stated that between 70° and 80° no major transformation of α to β takes place. In fact, the higher β-fractions obtained are mainly due to chain alignment which reaches its maximum at 80°C where the α to β transformation efficiency was found to decrease.

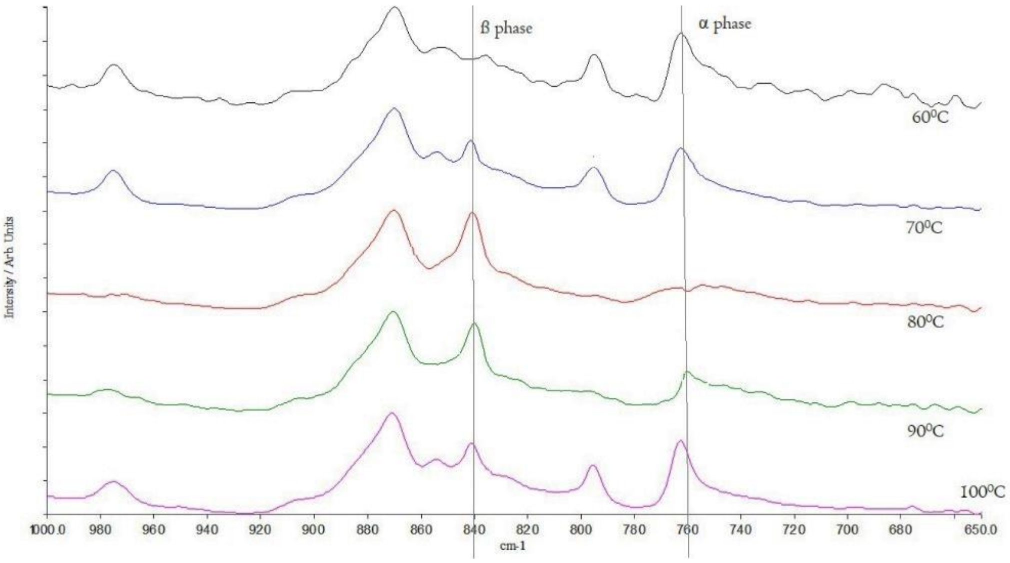

Figure 5.11: FTIR spectra of PVDF yarns extruded using varying temperatures

5.1.5 Effect of draw ratio

The yarns extruded for investigating the effect of draw ratio were poled using 6 kV. The draw ratio was varied using the varying take-up speeds. Different nozzles were used to extrude yarns at varying drawing speeds. The draw ratio above 5:1 was not possible due to repeated breakages. Figure 5.12 shows the effect of variation in draw ratio on resultant β-content. The drawing is an important step in the formation of β-phase and is found to significantly affect the results. The FTIR results obtained suggest that the draw ratio of 4:1, the β-fraction obtained is 0.67 which increases to 0.73 at 5:1.

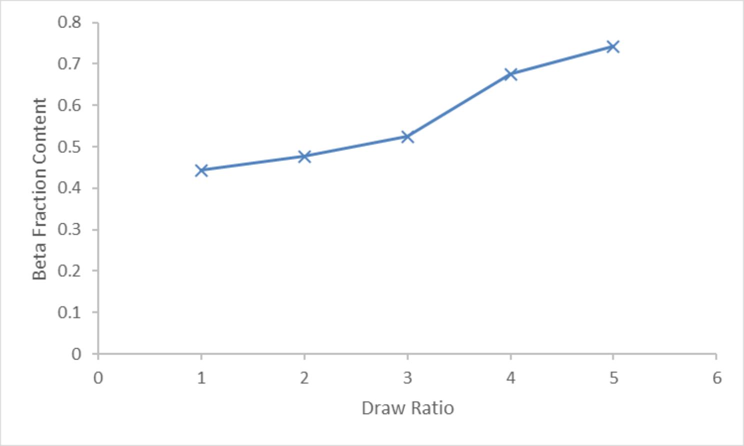

Figure 5.12: β-fraction obtained for fibres extruded at various draw ratios

Figure 5.13 shows the changes in the relevant peaks at 840 and 760 cm^{-1}. It is worth mentioning here that the simulation suggested the increase in yarn count (390Dtex) led to a higher power output. As the increasing draw ratio is associated with decreasing yarn diameter, a lower draw ratio has practically resulted in lower β-fraction. These results can be attributed to decreasing molecular chain conformation along the axis. Sencadas *et al*. (2009) have also agreed that the stretch ratio has a more prominent effect on attaining a higher β-phase than temperature variations. At higher draw ratios, the polymer chains get oriented and the crystalline structure is more packed increasing the dipole density (Gomes *et al.* 2010). Gregorio and Ueno (1999) clarify that at this stage as the packing density further increases, the chain mobility is hindered, hence affecting the orientation of dipoles. If the temperature is further increased at this point, the tension on molecules could be released which is present due to drawing but the molecules may reorient differently.

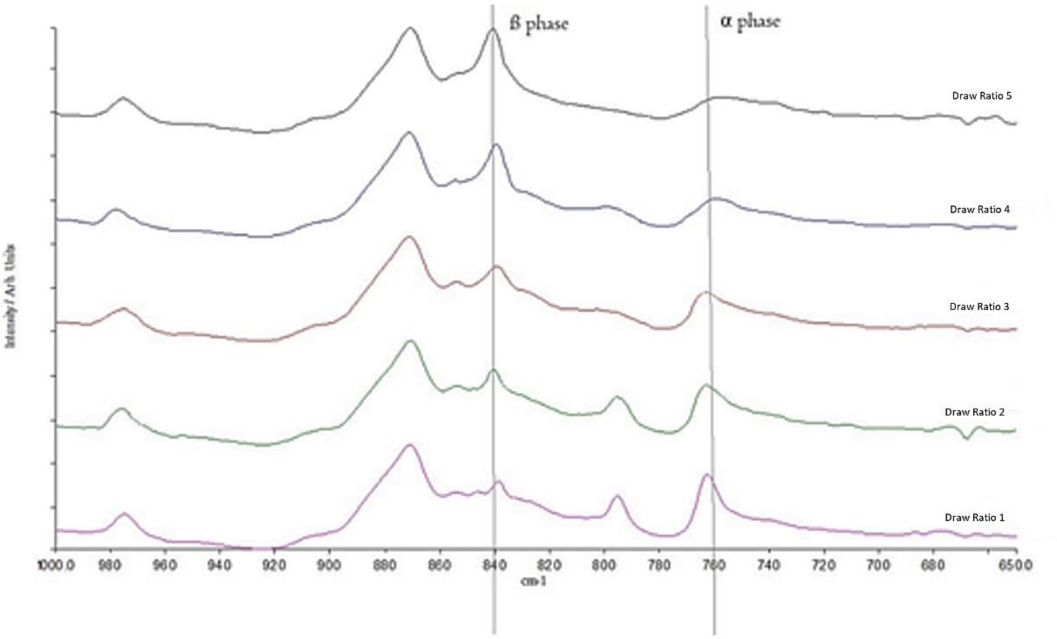

Figure 5.13: Fourier-transform infrared spectra of polyvinylidene fluoride yarns extruded using various draw ratios

5.2 Testing of PVDF piezo outputs

The resultant piezo output of PVDF fibres was tested using test methods described in Chapter 4. The open circuit voltage and current produced by the testing methods have been recorded and subsequent power has been calculated. The yarns were tested for both d_{31} mode (perpendicular) and d_{33} mode (parallel). The open circuit voltage outputs and currents were measured for samples produced as discussed in Chapter 4. Figure 5.14 shows the output voltage and current obtained for various samples. Open circuit voltage for PVDF fibres was tested using compression testing, while a resistance 0.46 MΩ was used to acquire the current output.

5.2.1 Electrode distance

The peak voltage outputs and corresponding current are presented in Figure 5.14. The yarns were drawn at a ratio of 5:1 and the drawing temperature was 80°C. The overall trend in peak voltages presents an endorsement of the simulation made in Chapter 3, Section 3.2. The electrode distance is essentially affecting the output voltages. Further evaluation of the power outputs suggests that the trend is consistent. At higher plate distances, the output voltage is marginally increased from 0.96 V to 1.067 V. However, as we further decrease the distance between the electrodes, the effective field intensity increases.

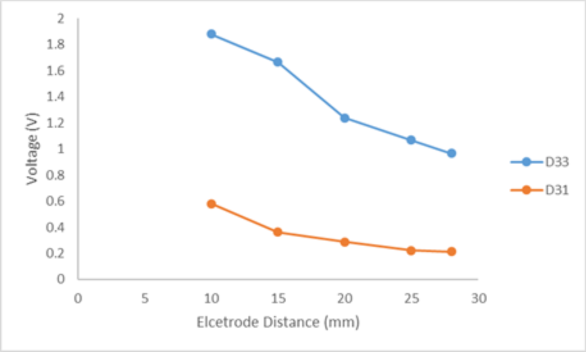

Figure 5.14: Peak voltage outputs for varying electrode distance

The FTIR spectrum of these samples has also confirmed the increase in β-fraction. The increase in electrode distance results in decreasing output voltage and resultant current signal. The peak voltage recorded for the 10 mm gap is 1.88 V which drops to 1.65 V when the gap is increased.

This is in admittance of simulation results. It would have been advantageous to see the sub-10 mm power outputs which were not conducted.

5.2.2 Effect of increasing electrode diameter

The simulation results showed an interesting relation between the diameter of the opening in plates and resultant electric field. Figure 5.15 shows the comparison of peak voltages obtained as a result of varying the electrode diameter. The minimum diameter which had the strongest electric field has resulted in a peak voltage output of 1.65 V. However, increasing the diameter has not majorly affected the output voltage.

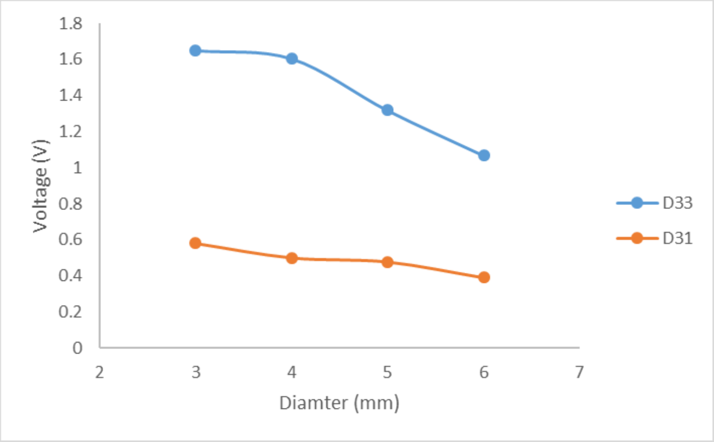

Figure 5.15: Peak voltage outputs for electrode hole diameter

In the simulation work carried out in Chapter 3 (section), the varying diameter was found to affect the electric field intensity at the centre of the electrode. It was seen that as the geometry changes, the electric field intensity at a given point is affected. However, the results suggest that changing the diameter from 3 to 4 has not affected the outputs. On increasing diameter further, the field lines are weaker, and this is evident from the resultant output. The field lines along the edge act in a different way than along between two plates. At the edge, the lines are more curved reducing the field intensity around that area. However, in a hole assembly, the field lines were found to 'overlap' resulting in a higher field intensity than any point between the plates. As the potential difference between the plate is constant, the varying voltage outputs can be attributed to the changing field intensity along the fibre axis.

5.2.3 Applied voltage

Although no significant claims have been made about the effect of increasing voltages in such poling method, however, Lund *et al*. have reported a peak output at 2 kV which decreases upon increasing electric field intensity. The higher electrical output as seen in figure 5.16 can be ascribed to the residual polarisation which occurs due to the presence of strong electric field causing the dipole realignment.

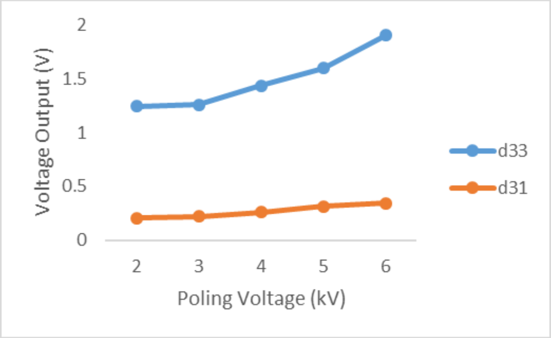

Figure 5.16: Peak voltage output at various poling voltages

Mahadeva *et al.* (2013) reported piezoelectric charge constant (d_{33}) at grid voltage of 2 kV through corona poling, decreasing upon increasing poling voltage, however, in this case, the result has been equitably orthodox generally, increasing with increase in voltage. It would have been interesting to see the effect of further increasing the poling voltage. The high voltages, in case of corona poling, results in electrical parasitic corona discharge which can result in reduced d_{33} constant (Hong *et al*. 2005).

5.3 Power outputs

The power outputs were calculated using the root mean square (RMS) voltages and current values. Assuming that the sample is quasi-isotropic, Young's modulus of the composite was used to acquire strain outputs from the calculated stresses. The strain for the samples is shown in figures below along with their corresponding voltage and current outputs.

Figure 5.17 shows the voltage, current output, and the corresponding loading applied to the sample H1 (3 mm diameter of the electrode) for the given time. The figures suggest a higher voltage output for d_{33} as compared to d_{31} outputs. The voltage outputs in the longitudinal direction show peak at

1.65 V while in the transverse direction, the peak is nearly 0.58 V. The strain applied is around the same in both test directions, whereas the outputs vary considerably. The current output obtained for the sample in the longitudinal direction (parallel) is 157 nA. This value falls to 117 nA in the transverse direction.

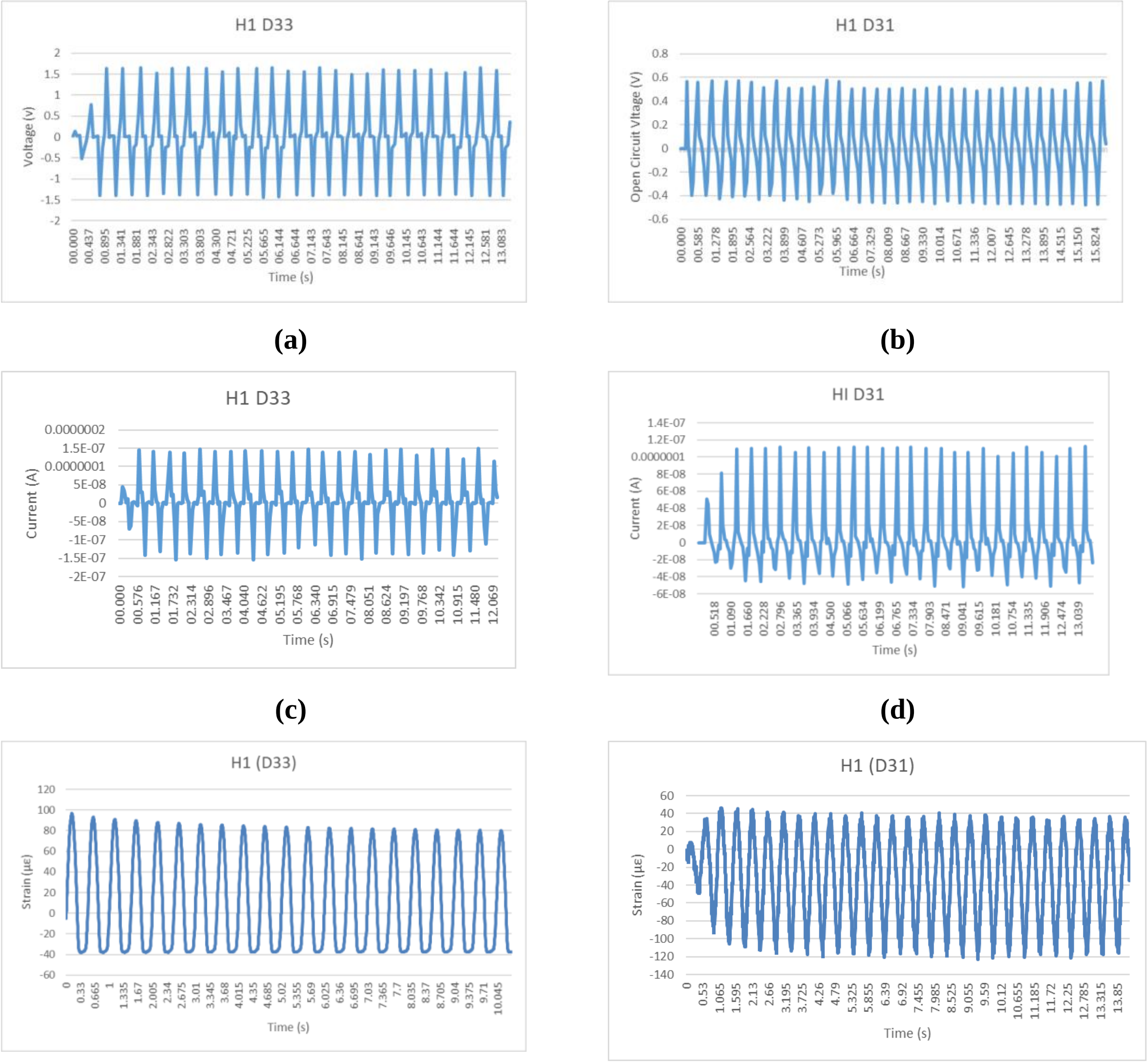

(a) (b) (c) (d) (e) (f)

Figure 5.17: (a) Voltage response (d_{33}), (b) Voltage response (d_{31}), (c) Current (d_{33}), (d) Current (d_{31}), (e) Strain (d_{33}), and (f) Strain (d_{31}) on sample H1

Figure 5.18 shows the peak power outputs and the average power outputs calculated as a function of the diameter. The figure indicates the maximum output power (peak) (0.245 μW) is achieved for minimum diameter. It can be confirmed from these that the increasing the diameter indeed effects the produced current and eventually the power outputs.

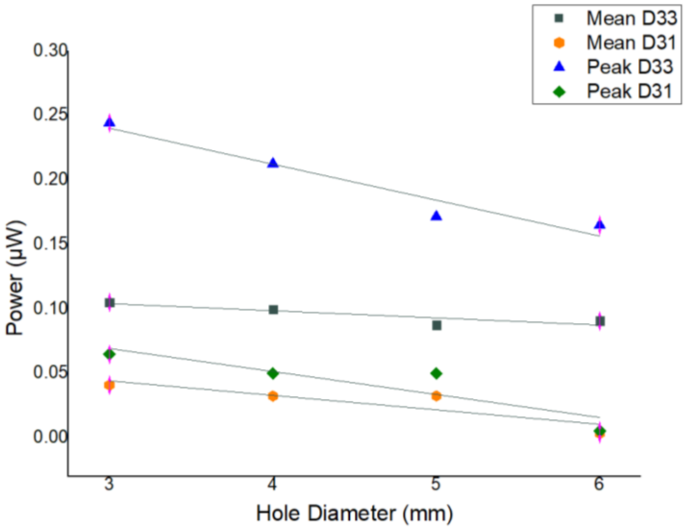

Figure 5.18: Power outputs for various diameters

The output signals for sample D1 with an electrode distance of 10 mm and the field intensity of 0.6 MV/m are shown in Figures 5.19 (a–f). The open circuit voltage outputs and current are recorded against the applied stain and the resultant peak power and average power are reported in Figure 5.20. In Figure 5.19 (a) and (b) it can be seen that the voltage output for D1 is 1.55 V and the current is 180 nA in the longitudinal direction which falls to 0.57 V and 33 nA in the cross direction. The peak power 0.29 µW is recorded for the maximum field intensity. The average power values are seen in figure 5.20, where it can be seen that the mean power outputs are maximum at the smallest gap. The average power output was found to be 0.15 µW.

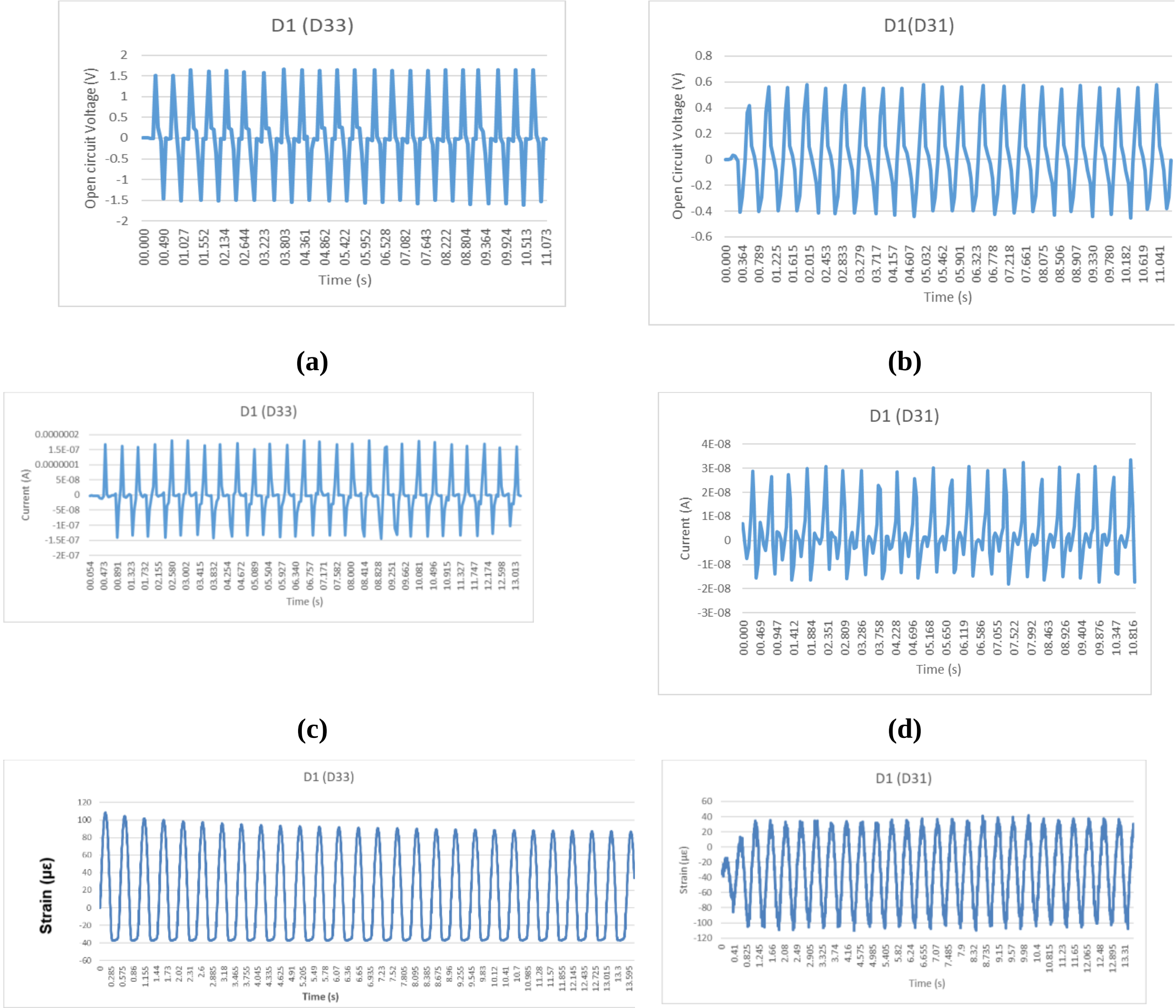

(a) **(b)**

(c) **(d)**

(e) **(f)**

Figure 5.19: (a) (a) Voltage response (d_{33}), (b) Voltage response (d_{31}), (c) Current (d_{33}), (d) Current (d_{31}), (e) Strain (d_{33}), and (f) Strain (d_{31}) for sample D1

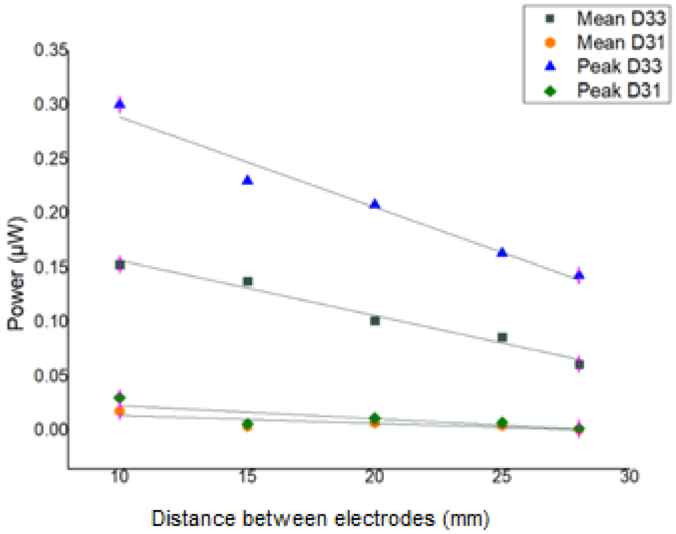

Figure 5.20: Power outputs as a function of distance between plates

Figure 5.21 shows the voltage, current output, and the corresponding loading applied to the sample P5 (poling voltage 6 kV) for the given time. The peak voltage for d_{33} mode is 1.804 V while in d_{31} mode is 0.341. The short circuit current in d_{33} mode is 319 nA while in d_{31} mode is 40 nA. The maximum power output (peak) is 0.57 µW, for the maximum applied voltage. The general output trend is higher for d_{33} mode as compared to d_{31} mode (figure 5.22). The average output is lower than peak power at about 0.23 µW.

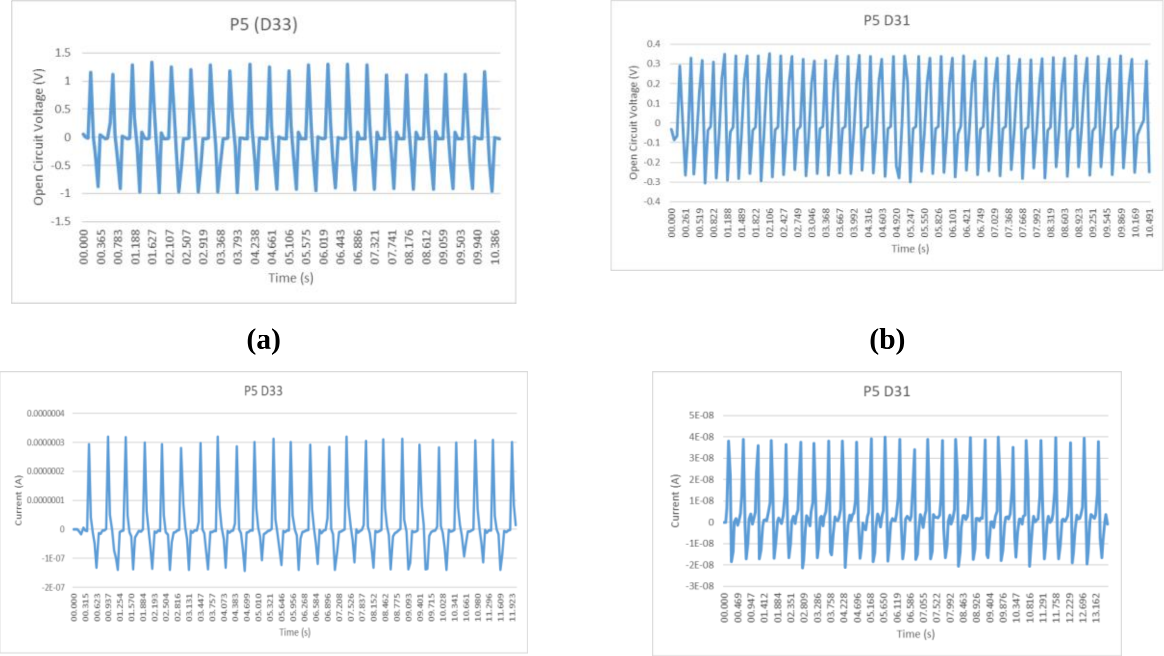

(a) **(b)**

(c) **(d)**

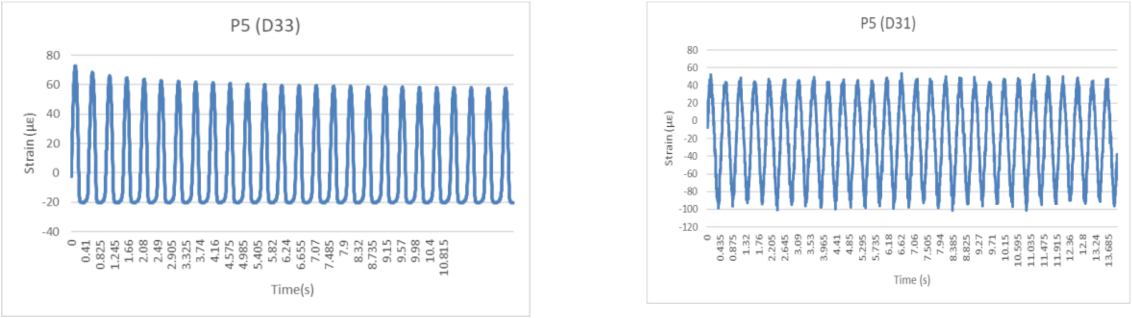

(e) **(f)**

Figure 5.21: (a) Voltage response (d_{33}), (b) Voltage response (d_{31}), (c) Current (d_{33}), (d) Current (d_{31}), (e) Strain (d_{33}), and (f) Strain (d_{31}) for sample P5

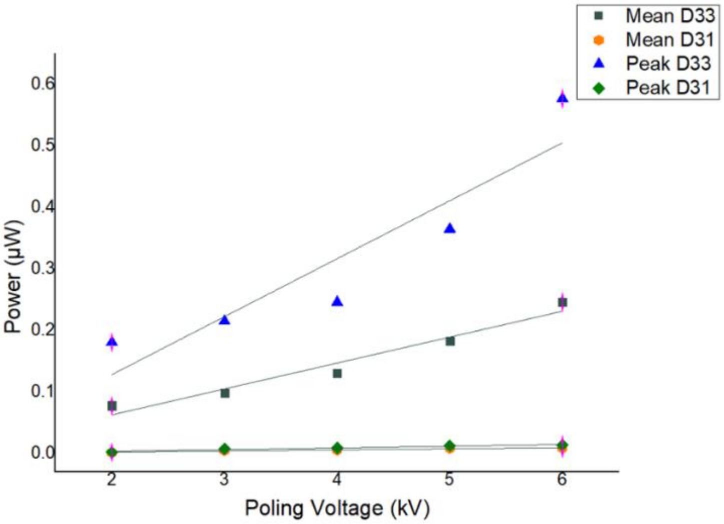

Figure 5.22: Power outputs as a function of poling voltage

5.4 Comparison between modelling and experimental values

The results from the user defined ANSYS simulations were corroborated with experiments. A realistic but simple approach was adopted in the model. A sparse equation solver was used in order to achieve the realistic calculations in the model. Medium-sized meshing was used to reach a compromise between the computational expense and time.

The validation for the poling equipment was done by subjecting the yarns to similar stresses in the model. The results predict a general corroboration of the simulated trends. It was seen that the increase in electric field intensity between the plates effected the output. These yarns were able to produce open circuit peak output voltage of 1.88 V. The yarns were also modified to produce higher output using high electrical field and mechanical stretching. Figure 5.23 shows the comparison between the effect of changing electric field intensity at various electrode distances. As seen in figure 5.14 above, the electric field intensity typically effects the β-phase changing the d_{33} constant of PVDF, hence, resulting in the varying outputs voltages as seen in figure 5.23. A similar comparison was undertaken for the hole diameter variation in the electrode.

The ANSYS simulation was used to predict the electric field intensity at the yarn position with various electrode hole diameters. As seen in figure 3.4 above, it can be seen that initially the electric field intensity increases with the increase in the distance between the plates for all diameters. This intensity reaches a maximum value and then starts to drop. The distance at which this maximum field intensity occurs varies for each hole diameter such as for the hole diameter of 10mm, the peak occurs at the distance of 7mm between the plates. This is contrary to the belief that the electric field intensity decreases with increasing distance. As simulated in ANSYS Figure 3.6 (a), this occurs due to the parabolic path of field lines at the edges. However, when testing this phenomenon, an electrical arc seemed to develop at plate distance below 10mm. Hence, the actual experimental validation was restricted to post 10mm plate distance owing to OHS issues. The experimental vs simulated results can be seen in figure 5.24, where the downward trend is noticeable.

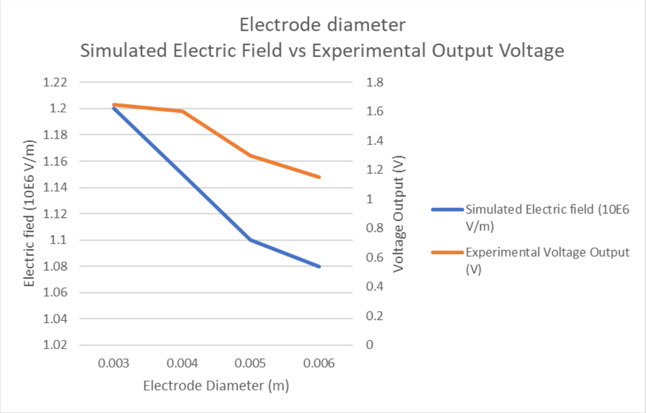

Figure 5.23: A figurative comparison of the simulated electric field intensity with the experimental output voltage for various electrode hole diameters

The simulated studies were used to modify the design of fabric in a way to make it suitable for optimal efficiency outputs. The use of a simple polymer strip attached to a fabric produced ‘good’ results, however, it did provide design and wearability issues (Waqar *et al*. 2013). Extruded PVDF yarns were used, thus making it much more convenient and durable in terms of its end use.

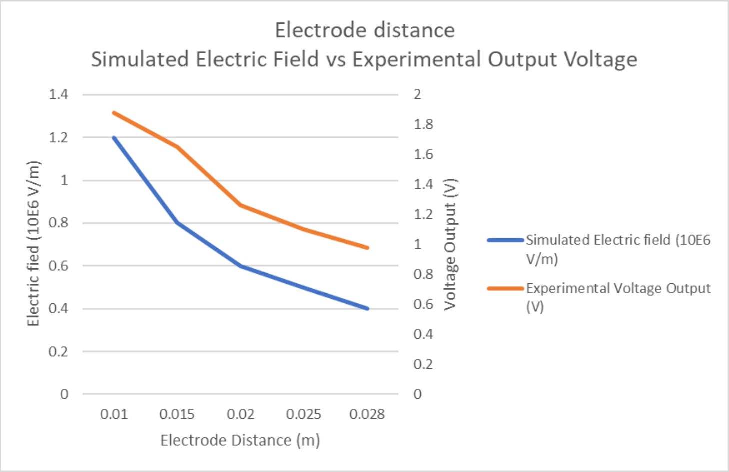

Figure 5.24 showing the comparison of the simulated results for electric field intensity on the output voltage for various electrode distances

5.5 Summary

The above results obtained show an enhanced β-phase achieved because of poling. The other parameters such as draw ratios and temperatures were also tested for phase changes. The FTIR obtained for the effect of poling voltages, the electrode distance, and electrode diameters were quite similar. The increase in β-fraction was quite marginal, such as 3.5% in case of electrode distances. The results suggest that the poling process mainly causes the reorientation of dipoles along the drawing direction and some transformation of α- into β-phase. The slight increase in β-phase associated with peaks at 840 cm^{-1} is the result of the effect of variation in electric field intensity. However, the effect is quite evident in FTIR spectra obtained by varying drawing ratio and varying temperature. The change in heights of peaks at 840 cm^{-1} is evidently visible resulting in an increase in β-content of about 32% at a temperature change of 70–80°C.

The open circuit voltage response and current obtained have been recorded. The power output calculated based on the acquired electrical response seems to augur the obtained results. The trends in β-content seem to be translated into resultant power output. Gomes *et al*. (2010) also reported a similar trend where a relation was drawn based on the β outputs translated into an electrical response. The strain induced in both longitudinal and transverse direction has resulted in varying electrical outputs. The power outputs are obtained in the range of microwatts with the peaks achieved at the start of each cycle. The obtained power can be stored in an integrated storage circuitry with a rectifier bridge attached, which can then be used to provide electrical power to a connected device.

The production of fibres, testing methods and the results of this study suggest that the overall objective of producing through fibres is met. Nevertheless, the power outputs shown in this chapter can be used to provide energy to low power and ultra-low power devices in the field of medical, defence and other consumer applications.

6 Conclusions and Recommendations

The main objective of this thesis was to develop a prototype for flexible energy harvesting using human motions based on displacement/strain-to-electricity conversion mechanism. Poled PVDF yarns were developed which were capable of generating up to 1.88 V voltage and 0.23 μW of mean power. The PVDF yarns were poled using a novel poling assembly design in the d_{33} direction to improve electrical outputs. The computational simulations were used to optimise the design of proposed energy harvester in the form of a spacer fabric configuration.

6.1 Computational simulations – piezo strip and yarns

The computational work was used to determine the electrical outputs from piezo fabric, piezo strip and yarns which, as far as the author is aware, is novel. In Chapter 3, simple harmonic motion (vibrational) analysis was carried out using a Finite Element Package, ANSYS to determine the effect of structural parameters on a harvester model. Mechanical ANSYS Parametric Design Language (MAPDL) was used to post process the flexible fabric to obtain outputs such as voltage, current, and power. Using the Design Modeller, a piezo patch (PVDF) was bonded to a flexible polyester fabric. Different parameters such as the area, aspect ratio, and input loading magnitude were studied at different frequencies and their effect on output power, voltage, current, and displacement were studied. For the parametric study carried out, an optimal dimension of about 400 mm^2 of PVDF was found. The operating frequency was about 5 Hz for maximum energy output in the microwatt range, making it viable as an energy scavenging system for powering many microwatt-based communications and medical devices such as a pacemaker, cardiac defibrillator, and neuro stimulator (Amar *et al.* 2015).

Another study was conducted to optimise the design of a sandwich structure fabric consisting of PVDF fibres co-joined in the lateral position. The model was designed to represent a knitted spacer fabric and was used to optimise the design, and structure of the fabric to obtain maximum outputs from fabric. The RVE of fabric was used consisting of four spacer yarns. The effect of damping was ignored. The mesh optimisation study found the medium size mesh to yield optimal results. It was found that the structural parameters of the fabric model directly affect the electrical outputs. The power outputs in d_{33} direction were found to be much higher than d_{31} direction. The yarn inclination at 15° to vertical was found to yield superior electrical outputs (power, voltage). These electrical outputs decrease with increasing the yarn inclination angle (45^0, 60°). The spacer yarn angle at 0° also produces lesser electrical outputs. The thickness of model was also discovered to be extremely critical, even though, the length of the PVDF yarn was increasing, the electrical outputs seemed to be decreasing. A similar fabric model with increased crosslinking spacer yarns was studied and the outputs were found to substantiate the results obtained earlier.

The PVDF fibres were drawn at various settings including draw ratio, temperatures, and poling setups. The drawing phase was found to be extremely critical in achieving a high β-content output. The drawing temperature of 80°C was found to yield a higher β-output. The drawing of fibres using the setup was a tedious job because of the breakages. The draw ratio of 5:1 gave a higher β-content.

6.2 Computational simulations – poling configurations

In Chapter 4, the key component of an energy harvesting fabric such as poling of yarns and design of the fabric, should lead to an enhanced electro-mechanical efficiency of these fabrics. Poled PVDF yarns were produced using poling assembly devised during this work. The assembly was validated using simulation work to determine the electric field intensity. The experimental results of testing the fibres were found to be in agreement with the trends in simulated results.

The characterisation of developed PVDF yarns has been carried out using SEM, FTIR, and XRD. The SEM was used to obtain the surface images of the yarns which shows a relatively smooth surface, without any voids. The FTIR spectra were obtained for various samples showing the distinct element of PVDF. Various peaks were observed in different heights and the β- fraction content was calculated based on the equation. The results show that β-content of PVDF yarns has been affected by applying a high electric field. The XRD diffractogram supports the results obtained by FTIR. The effect of various designs of a novel poling assembly was simulated and the fibres were poled accordingly. The increasing electric field intensity has been varied by varying the electrode distance, the hole diameter of electrodes, and the applied voltage. The results show an enhanced β-content of 4% on application of increasing plate distance which has a larger effect in terms of β-phase output. The result was substantiated by XRD diffractogram, showing the significant β-peak at 20.26° for the angle 2θ. The variation in electrode hole diameter was also found to affect the output, however, the effect was not as significant as increasing the plate distance. The applied voltage was found to effect intermittently, affecting the output fraction more at higher applied voltages. It was also observed that although the poling voltages are large, they are lower than the voltages used in the corona poling method, whereby, the parasitic discharge results in decreasing the fibre performance (Mahadeva *et al.* 2013). The increasing β-fraction of fibre because of applying voltages is suspected to be due to some α to β- conversion, but mostly because of dipole realignment, increasing the packing density and crystallinity. The FTIR spectra show a β-fraction of 0.69 of unpoled samples increase to 0.74 for fibres drawn at various applied voltages.

6.3 Experimental electro-mechanical performance of the poled PVDF yarns

The poled PVDF fibres were subjected to uniaxial testing in d_{31} and d_{33} modes. The open circuit voltage and the short circuit currents obtained have shown admittance of the simulated model. The power outputs calculated were found to be significantly higher in the d_{33} mode as compared to d_{31} mode, validating the simulation. The electrical results also show a decrease in mean power outputs on increasing the electrodes distance during poling process which supports the claims made in Chapter 3. The most important validation is related to the increasing electrode hole diameter which results in a decreased electrical output. The method shows a novel poling design that can be used to impart poling simultaneously while extruding fibres. The electrical outputs achieved peak voltage 1.88 V (mean power 0.23 µW) are lower than earlier reported peak voltage output values of 2.2 V (Hadimani *et al*. 2013), however, a more realistic result is presented based on a testing condition which mimics the on-person use of an energy harvesting fabric at a frequency which matches the range of frequency of human motion.

6.4 Summary

This work can be considered an important milestone towards on-person energy harvesting technologies. The work of this research was focused on the optimal design of fabric through computational simulation and poling of yarns to produce the simulated fabric model. Prior to this research, the use of computational simulations for energy harvesting fabrics had not been explored. Moreover, the design of a poling assembly in both d_{31} and d_{33} had hitherto, not been fully explored, particularly in relation to the extent of the effect of its β-characterisation. The testing method used in this work is novel to testing of fabrics, particularly for energy harvesting applications in areas of low frequency and low strains. It is expected that this research can pave the way for the enhancement of performance of energy harvesting fabrics through this approach.

6.4.1 Real world applications

The use of these fibres is limited to the applications using ultra-low power outputs owing to limited available current. The military and medical applications such as a soldier in combat for radio-frequency identification device (RFID) signalling and for powering on-garment sensors are of high interest where limited or no power is available.

6.5 Recommendations for further work in this area

The findings of this thesis have opened many interesting questions for researchers. The use of computational simulations for obtaining power outputs directly using ANSYS can lead to practically-designed energy harvesting fabrics for future harvesting applications. The extent of application of this work is not limited to the research outlined in this thesis and the author would like to suggest a few key areas that could show some promise for a fully functional energy harvesting device for future applications. These include:

1. Addition of further additives to the polymer, such as CNTs.
2. Time to poling of yarns in the continuous poling method which is crucial for optimal results.

3. The poling setup can be further enhanced by increasing using higher voltage and encasing the setup in a faraday cage. To prevent arcing due the strong electric field, a vacuum chamber can be used.
4. Despite several efforts, the effect of electrical noise was not completely isolated, hence obtaining outputs in complete isolation is recommended, preferably involving the use of a Faraday cage.

7 References

1. Bionic Power Inc., viewed 30th July 2017, <http://www.bionic-power.com/>.
2. Elektrisola Feindraht AG Textile wire, viewed 11 January 2014, <http://www.textile-wire.com/>.
3. X-STATIC Textiles, viewed 2nd August 2017, <http://noblebiomaterials.com/xstatic-textiles/what-x-static/>.
4. 'IEEE Standard on Piezoelectricity', 1988, ANSI/IEEE Std 176-1987, p. 0_1.
5. https://www.bluetooth.com/what-is-bluetooth-technology/how-it-works, 2017, viewed 2nd Feb 2017, <https://www.bluetooth.com/what-is-bluetooth-technology/how-it-works>.
6. 'Keep the doctor at bay', 2017, Nature Energy, vol. 2, p. 17068.
7. Abbasi, T, Premalatha, M & Abbasi, SA 2011, 'The return to renewables: Will it help in global warming control?', Renewable and Sustainable Energy Reviews, vol. 15, no. 1, pp. 891-4.
8. Abdelsayed, IM 2008, 'CHARACTERIZATION OF ELECTROSPRAYED POLY (VINYLIDENE FLUORIDE)/CNT NANOCOMPOSITE'.
9. Ahmed, R, Mir, F & Banerjee, S 2017, 'A review on energy harvesting approaches for renewable energies from ambient vibrations and acoustic waves using piezoelectricity', Smart Material Structures, vol. 26, no. 8.
10. Ahn, Y, Song, S & Yun, K-S 2015, 'Woven flexible textile structure for wearable power-generating tactile sensor array', Smart materials and structures, vol. 24, no. 7, p. 075002.
11. Alagirusamy, R, Eichhoff, J, Gries, T & Jockenhoevel, S 2013, 'Coating of conductive yarns for electro-textile applications', Journal of the Textile Institute, vol. 104, no. 3, pp. 270-7.
12. Allameh, SM, Akogwu, O, Collinson, M, Thomas, J & Soboyejo, WO 2007, 'Piezoelectric generators for biomedical and dental applications: effects of cyclic loading', J Mater Sci Mater Med, vol. 18, no. 1, pp. 39-45.

13. Almusallam, A, Torah, R, Zhu, D, Tudor, M & Beeby, S 2013, 'Screen-printed piezoelectric shoe-insole energy harvester using an improved flexible PZT-polymer composites', paper presented to Journal of Physics: Conference Series.
14. Amin Karami, M & Inman, DJ 2012, 'Powering pacemakers from heartbeat vibrations using linear and nonlinear energy harvesters', Applied Physics Letters, vol. 100, no. 4, p. 042901.
15. Amini, Y, Emdad, H & Farid, M 2015, 'Finite element modelling of functionally graded piezoelectric harvesters', Composite Structures, vol. 129, pp. 165-76.
16. Bai, S, Zhang, L, Xu, Q, Zheng, Y, Qin, Y & Wang, ZL 2013, 'Two dimensional woven nanogenerator', Nano Energy, vol. 2, no. 5, pp. 749-53.
17. Ballato, A 1996, 'Piezoelectricity: history and new thrusts', paper presented to Ultrasonics Symposium, 1996. Proceedings., 1996 IEEE.
18. Bedeloglu, A, Demir, A, Bozkurt, Y & Sariciftci, NS 2010, 'A photovoltaic fibre design for smart textiles', Textile Research Journal, vol. 80, no. 11, pp. 1065-74.
19. Beeby, S & White, N 2010, Energy harvesting for autonomous systems, Artech House.
20. Bernardes, A, Espinosa, DCR & Tenório, JS 2004, 'Recycling of batteries: a review of current processes and technologies', Journal of Power Sources, vol. 130, no. 1, pp. 291-8.
21. Bhaskaran, M, Sriram, S, Ruffell, S & Mitchell, A 2011, 'Nanoscale characterization of energy generation from piezoelectric thin films', Advanced Functional Materials, vol. 21, no. 12, pp. 2251-7.
22. Bodkhe, S, Rajesh, P, Kamle, S & Verma, V 2014, 'Beta-phase enhancement in polyvinylidene fluoride through filler addition: comparing cellulose with carbon nanotubes and clay', Journal of Polymer Research, vol. 21, no. 5, p. 434.
23. Bowen, C, Stevens, R, Nelson, L, Dent, A, Dolman, G, Su, B, Button, T, Cain, M & Stewart, M 2006, 'Manufacture and characterization of high activity piezoelectric fibres', Smart materials and structures, vol. 15, no. 2, p. 295.
24. Buckley, J, Cebe, P, Cherdack, D, Crawford, J, Ince, BS, Jenkins, M, Pan, J, Reveley, M, Washington, N & Wolchover, N 2006, 'Nanocomposites of poly (vinylidene fluoride) with organically modified silicate', Polymer, vol. 47, no. 7, pp. 2411-22.

25. Cady, WG 1946, Piezoelectricity: An introduction to the theory and application of electromechanical phenomena in crystals, McGraw-Hill.
26. Cass, RB, Khan, A & Mohammadi, F 2003, 'Innovative ceramic-fibre technology energizes advanced cerametrics', American Ceramic Society Bulletin, vol. 82, no. 11, pp. 14-5.
27. Cha, Y 2017, 'Energy harvesting using flexible piezoelectric materials from human walking motion: Theoretical analysis', Journal of Intelligent Material Systems and Structures, p. 1045389X17704917.
28. Chalasani, S & Conrad, JM 2008, 'A survey of energy harvesting sources for embedded systems', paper presented to Southeastcon, 2008. IEEE.
29. Chaudhari, VA & Bichile, GK 2013, 'Synthesis, structural, and electrical properties of pure PbTiO3 ferroelectric ceramics', Smart Materials Research, vol. 2013.
30. Chen, L, Lai, W, Wang, J, Jiang, G, Zhou, Y, Chen, Y, Liu, H, Qin, Z, Ke, L & Wang, L 2014, 'Study on Surface Electric Field Simulation of High Voltage Transmission Line Assembly', Journal of Power and Energy Engineering, vol. 2, no. 04, p. 554.
31. Chen, X 2013, 'Human motion analysis with wearable inertial sensors'.
32. Chen, X, Xu, S, Yao, N & Shi, Y 2010, '1.6 V nanogenerator for mechanical energy harvesting using PZT nanofibres', Nano letters, vol. 10, no. 6, pp. 2133-7.
33. Choi, D, Choi, MY, Choi, WM, Shin, HJ, Park, HK, Seo, JS, Park, J, Yoon, SM, Chae, SJ & Lee, YH 2010, 'Fully rollable transparent nanogenerators based on graphene electrodes', Advanced Materials, vol. 22, no. 19, pp. 2187-92.
34. Corbman, BP 1983, Textiles. Fibre to fabric, Gregg/McGraw-Hill Marketing Series; McGraw-Hill. Gregg Division.
35. Covert, T, Greenstone, M & Knittel, CR 2016, 'Will we ever stop using fossil fuels?', The Journal of Economic Perspectives, vol. 30, no. 1, pp. 117-37.
36. Curie, J & Curie, P 1881, 'Contractions et dilatations produites par des tensions électriques dans les cristaux hémièdres à faces inclinées', Compt. Rend, vol. 93, pp. 1137-40.
37. Damaraju, SM, Wu, S, Jaffe, M & Arinzeh, TL 2013, 'Structural changes in PVDF fibres due to electrospinning and its effect on biological function', Biomedical Materials, vol. 8, no. 4, p. 045007.

38. Damjanovic, D 1998, 'Ferroelectric, dielectric and piezoelectric properties of ferroelectric thin films and ceramics', Reports on Progress in Physics, vol. 61, no. 9, p. 1267.

39. Dargaville, TR, Celina, M & Chaplya, PM 2005, 'Evaluation of piezoelectric poly (vinylidene fluoride) polymers for use in space environments. I. Temperature limitations', Journal of Polymer Science Part B: Polymer Physics, vol. 43, no. 11, pp. 1310-20.

40. Das-Gupta, D & Doughty, K 1980, 'Piezoelectricity in uniaxially stretched and corona poled polyvinylidene fluoride', Journal of Physics D: Applied Physics, vol. 13, no. 1, p. 95.

41. Davis, G, McKinney, J, Broadhurst, M & Roth, S 1978, 'Electric-field-induced phase changes in poly (vinylidene fluoride)', Journal of Applied Physics, vol. 49, no. 10, pp. 4998-5002.

42. Delnavaz, A & Voix, J 2014, 'Energy harvesting for in-ear devices using ear canal dynamic motion', IEEE Transactions on Industrial Electronics, vol. 61, no. 1, pp. 583-90.

43. Edmison, J, Jones, M, Nakad, Z & Martin, T 2002, 'Using piezoelectric materials for wearable electronic textiles', paper presented to Wearable Computers, 2002. (ISWC 2002). Proceedings. Sixth International Symposium on.

44. Egusa, S, Wang, Z, Chocat, N, Ruff, Z, Stolyarov, A, Shemuly, D, Sorin, F, Rakich, P, Joannopoulos, J & Fink, Y 2010, 'Multimaterial piezoelectric fibres', Nature materials, vol. 9, no. 8, pp. 643-8.

45. Esterly, DM 2002, 'Manufacturing of Poly (vinylidene fluoride) and Evaluation of its Mechanical Properties'.

46. Esterly, DM & Love, BJ 2004, 'Phase transformation to β-poly (vinylidene fluoride) by milling', Journal of Polymer Science Part B: Polymer Physics, vol. 42, no. 1, pp. 91-7.

47. Fang, J, Wang, X & Lin, T 2011, 'Electrical power generator from randomly oriented electrospun poly (vinylidene fluoride) nanofibre membranes', Journal of Materials Chemistry, vol. 21, no. 30, pp. 11088-91.

48. Farnsworth, M, Tiwari, A & Dorey, R 2014, 'Modelling, simulation and optimisation of a piezoelectric energy harvester', Procedia CIRP, vol. 22, pp. 142-7.

49. French, JD & Cass, RB 1998, 'Developing innovative ceramic fibres', American Ceramic Society Bulletin, vol. 77, no. 5, pp. 61-5.
50. French, JD, Weitz, GE, Luke, JE, Cass, RB, Jadidian, B, Bhargava, P & Safari, A 1997, 'Production of continuous piezoelectric ceramic fibres for smart materials and active control devices', paper presented to Proceedings of SPIE.
51. Fukada, E 2000, 'History and recent progress in piezoelectric polymers', IEEE Transactions on ultrasonics, ferroelectrics, and frequency control, vol. 47, no. 6, pp. 1277-90.
52. Furukawa, T, Johnson, G, Bair, H, Tajitsu, Y, Chiba, A & Fukada, E 1981, 'Ferroelectric phase transition in a copolymer of vinylidene fluoride and trifluoroethylene', Ferroelectrics, vol. 32, no. 1, pp. 61-7.
53. Gemperle, F, Kasabach, C, Stivoric, J, Bauer, M & Martin, R 1998, 'Design for wearability', paper presented to Wearable Computers, 1998. Digest of Papers. Second International Symposium on.
54. Giannetti, E 2001, 'Semi-crystalline fluorinated polymers', Polymer international, vol. 50, no. 1, pp. 10-26.
55. Glauß, B, Steinmann, W, Walter, S, Beckers, M, Seide, G, Gries, T & Roth, G 2013, 'Spinnability and characteristics of polyvinylidene fluoride (PVDF)-based bicomponent fibres with a carbon nanotube (CNT) modified polypropylene core for piezoelectric applications', Materials, vol. 6, no. 7, pp. 2642-61.
56. Gniotek, K & Krucinska, I 2004, 'The basic problems of textronics', FIBRES AND TEXTILES IN EASTERN EUROPE., vol. 12, no. 1, pp. 13-6.
57. Gomes, J, Nunes, JS, Sencadas, V & Lanceros-Méndez, S 2010, 'Influence of the β-phase content and degree of crystallinity on the piezo-and ferroelectric properties of poly (vinylidene fluoride)', Smart materials and structures, vol. 19, no. 6, p. 065010.
58. Gong, R H., (2011), Specialist yarn and fabric structures, developments, and applications, Woodhead Publishing Limited, Part.
59. Gong, S & Cheng, W 2017, 'Toward Soft Skin-Like Wearable and Implantable Energy Devices', Advanced Energy Materials.

60. González, JL, Rubio, A & Moll, F 2002, 'Human powered piezoelectric batteries to supply power to wearable electronic devices', International journal of the Society of Materials Engineering for Resources, vol. 10, no. 1, pp. 34-40.
61. Gopalsamy, C, Park, S, Rajamanickam, R & Jayaraman, S 1999, 'The Wearable Motherboard™: The first generation of adaptive and responsive textile structures (ARTS) for medical applications', Virtual Reality, vol. 4, no. 3, pp. 152-68.
62. Granstrom, J, Feenstra, J, Sodano, HA & Farinholt, K 2007, 'Energy harvesting from a backpack instrumented with piezoelectric shoulder straps', Smart materials and structures, vol. 16, no. 5, p. 1810.
63. Gregorio, R 2006, 'Determination of the α, β, and γ crystalline phases of poly (vinylidene fluoride) films prepared at different conditions', Journal of applied polymer science, vol. 100, no. 4, pp. 3272-9.
64. Gregorio, R & Ueno, E 1999, 'Effect of crystalline phase, orientation and temperature on the dielectric properties of poly (vinylidene fluoride) (PVDF)', Journal of Materials Science, vol. 34, no. 18, pp. 4489-500.
65. Gusarov, B 2015, 'PVDF piezoelectric polymers: characterization and application to thermal energy harvesting', Université Grenoble Alpes.
66. Haertling, GH 1999, 'Ferroelectric ceramics: history and technology', Journal of the American Ceramic Society, vol. 82, no. 4, pp. 797-818.
67. Hännikäinen, J 2006, Electronic intelligence development for wearable applications.
68. Hansen, BJ, Liu, Y, Yang, R & Wang, ZL 2010, 'Hybrid nanogenerator for concurrently harvesting biomechanical and biochemical energy', ACS nano, vol. 4, no. 7, pp. 3647-52.
69. He, L, Sun, J, Wang, X, Wang, C, Song, R & Hao, Y 2013, 'Facile and effective promotion of β crystalline phase in poly (vinylidene fluoride) via the incorporation of imidazolium ionic liquids', Polymer international, vol. 62, no. 4, pp. 638-46.
70. He, R, Day, TD, Krishnamurthi, M, Sparks, JR, Sazio, PJ, Gopalan, V & Badding, JV 2013, 'Silicon p-i-n Junction Fibres', Advanced Materials, vol. 25, no. 10, pp. 1461-7.
71. Hearle, JW 2001, High-performance fibres, Elsevier.
72. Higashihata, Y, Sako, J & Yagi, T 1981, 'Piezoelectricity of vinylidene fluoride-trifluoroethylene copolymers', Ferroelectrics, vol. 32, no. 1, pp. 85-92.

73. Hong, J, Chen, J, Li, X & Ye, A 2005, 'Effects of the bias-controlled grid on performances of the corona poling system for electro-optic polymers', International Journal of Modern Physics B, vol. 19, no. 14, pp. 2205-11.
74. Huang, CT, Song, J, Tsai, CM, Lee, WF, Lien, DH, Gao, Z, Hao, Y, Chen, LJ & Wang, ZL 2010, 'Single-InN-Nanowire Nanogenerator with Upto 1 V Output Voltage', Advanced Materials, vol. 22, no. 36, pp. 4008-13.
75. Huang, C-T, Shen, C-L, Tang, C-F & Chang, S-H 2008, 'A wearable yarn-based piezo-resistive sensor', Sensors and Actuators A: Physical, vol. 141, no. 2, pp. 396-403.
76. Huang, P, Mao, C & Wang, D 2017, 'Electric Field Simulations and Analysis for High Voltage High Power Medium Frequency Transformer', Energies, vol. 10, no. 3, p. 371.
77. Jacobson, MZ 2009, 'Review of solutions to global warming, air pollution, and energy security', Energy & Environmental Science, vol. 2, no. 2, pp. 148-73.
78. Jones, GD, Assink, RA, Dargaville, TR, Chaplya, PM, Clough, RL, Elliott, JM, Martin, JW, Mowery, DM & Celina, MC 2005, Characterization, performance, and optimization of PVDF as a piezoelectric film for advanced space mirror concepts, Sandia National Laboratories.
79. Jun Sim, H, Choi, C, Jun Lee, C, Tae Kim, Y & Jeong Kim, S 2015, 'Flexible Two-ply Piezoelectric Yarn Energy Harvester', Current Nanoscience, vol. 11, no. 4, pp. 539-44.
80. Jung, W-S, Lee, M-J, Kang, M-G, Moon, HG, Yoon, S-J, Baek, S-H & Kang, C-Y 2015, 'Powerful curved piezoelectric generator for wearable applications', Nano Energy, vol. 13, pp. 174-81.
81. Kabir, E, Khatun, M, Nasrin, L, Raihan, MJ & Rahman, M 2017, 'Pure β-phase formation in polyvinylidene fluoride (PVDF)-carbon nanotube composites', Journal of Physics D: Applied Physics, vol. 50, no. 16, p. 163002.
82. KATZIR, S 2006, 'THE DISCOVERY OF THE PIEZOELECTRIC EFFECT', in S Katzir (ed.), THE BEGINNINGS OF PIEZOELECTRICITY: A Study in Mundane Physics, Springer Netherlands, Dordrecht, pp. 15-64.
83. ---- 2007, The beginnings of piezoelectricity: a study in mundane physics, vol. 246, Springer Science & Business Media.

84. Kaur, S, Graak, P, Gupta, A, Chhabra, P, Kumar, D & Shetty, A 2016, 'Effect of various shapes and materials on the generated power for piezoelectric energy harvesting system', paper presented to AIP Conference Proceedings.

85. Kholkin, A, Pertsev, N & Goltsev, A 2008, 'Piezoelectricity and crystal symmetry', in Piezoelectric and Acoustic Materials for Transducer Applications, Springer, pp. 17-38.

86. Kim, M-O, Oh, Y, Kang, Y, Cho, K-H, Choi, J & Kim, J 2017, 'Flexible piezoelectric strain energy harvester responsive to multi-directional input forces and its application to self-powered motion sensor', paper presented to Micro Electro Mechanical Systems (MEMS), 2017 IEEE 30th International Conference on.

87. Kong, L, Ma, J, Huang, H, Zhu, W & Tan, O 2001, 'Lead zirconate titanate ceramics derived from oxide mixture treated by a high-energy ball milling process', Materials Letters, vol. 50, no. 2, pp. 129-33.

88. Kong, LB, Li, T, Hng, HH, Boey, F, Zhang, T & Li, S 2014, 'Waste mechanical energy harvesting (I): piezoelectric effect', in Waste Energy Harvesting, Springer, pp. 19-133.

89. Kong, LB, Zhang, T, Ma, J & Boey, F 2008, 'Progress in synthesis of ferroelectric ceramic materials via high-energy mechanochemical technique', Progress in Materials Science, vol. 53, no. 2, pp. 207-322.

90. Kuwabara, M 1990, 'Lead titanate ceramics with positive temperature coefficients of resistivity', Journal of the American Ceramic Society, vol. 73, no. 5, pp. 1438-9.

91. Kymissis, J, Kendall, C, Paradiso, J & Gershenfeld, N 1998, 'Parasitic power harvesting in shoes', paper presented to Wearable Computers, 1998. Digest of Papers. Second International Symposium on.

92. Lam Po Tang, S & Stylios, G 2006, 'An overview of smart technologies for clothing design and engineering', International Journal of Clothing Science and Technology, vol. 18, no. 2, pp. 108-28.

93. Lanceros-Mendez, S, Mano, J, Costa, A & Schmidt, V 2001, 'FTIR and DSC studies of mechanically deformed β-PVDF films', Journal of Macromolecular Science, Part B, vol. 40, no. 3-4, pp. 517-27.

94. Lee, BY, Zhang, J, Zueger, C, Chung, W-J, Yoo, SY, Wang, E, Meyer, J, Ramesh, R & Lee, S-W 2012, 'Virus-based piezoelectric energy generation', Nature nanotechnology, vol. 7, no. 6, pp. 351-6.

95. Lee, J-H, Kim, J, Kim, TY, Al Hossain, MS, Kim, S-W & Kim, JH 2016, 'All-in-one energy harvesting and storage devices', Journal of Materials Chemistry A, vol. 4, no. 21, pp. 7983-99.
96. Lee, J-y, Kim, S, Kim, K, Kim, J & Choi, B 2009, 'An Experimental study on the energy harvesting system using piezoelectric elements (PVDF)', PowerMEMS 2009, pp. 324-7.
97. Lepro, X, Lima, MD & Baughman, RH 2010, 'Spinnable carbon nanotube forests grown on thin, flexible metallic substrates', Carbon, vol. 48, no. 12, pp. 3621-7.
98. Levi, N, Czerw, R, Xing, S, Iyer, P & Carroll, DL 2004, 'Properties of polyvinylidene difluoride− carbon nanotube blends', Nano letters, vol. 4, no. 7, pp. 1267-71.
99. Li, B, Zheng, J & Xu, C 2013, 'Silver nanowire dopant enhancing piezoelectricity of electrospun PVDF nanofibre web', paper presented to Proc. of SPIE Vol.
100. Li, J, Wang, C, Zhong, W, Zhang, P, Wang, Q & Webb, J 2002, 'Vibrational mode analysis of β-phase poly (vinylidene fluoride)', Applied Physics Letters, vol. 81, no. 12, pp. 2223-5.
101. Li, L, Zhang, M, Rong, M & Ruan, W 2014, 'Studies on the transformation process of PVDF from α to β phase by stretching', RSC Advances, vol. 4, no. 8, pp. 3938-43.
102. Li, P, Liu, Y, Wang, Y, Luo, C, Li, G, Hu, J, Liu, W & Zhang, W 2015, 'Low-frequency and wideband vibration energy harvester with flexible frame and interdigital structure', Aip Advances, vol. 5, no. 4, p. 047151.
103. Li, Q & Tao, XM 2014, 'Three-dimensionally deformable, highly stretchable, permeable, durable and washable fabric circuit boards', paper presented to Proceedings of the Royal Society of London A: Mathematical, Physical and Engineering Sciences.
104. Li, Z, Zhang, X & Li, G 2014, 'In situ ZnO nanowire growth to promote the PVDF piezo phase and the ZnO–PVDF hybrid self-rectified nanogenerator as a touch sensor', Physical Chemistry Chemical Physics, vol. 16, no. 12, pp. 5475-9.
105. Lin, L, Lai, C-H, Hu, Y, Zhang, Y, Wang, X, Xu, C, Snyder, RL, Chen, L-J & Wang, ZL 2011, 'High output nanogenerator based on assembly of GaN nanowires', Nanotechnology, vol. 22, no. 47, p. 475401.
106. Lin, Y-F, Song, J, Ding, Y, Lu, S-Y & Wang, ZL 2008, 'Piezoelectric nanogenerator using CdS nanowires', Applied Physics Letters, vol. 92, no. 2, p. 022105.

107. Lippmann, G 1881, 'Principe de la conservation de l'électricité, ou second principe de la théorie des phénomènes électriques', Journal de Physique Théorique et Appliquée, vol. 10, no. 1, pp. 381-94.

108. Liu, Z, Pan, C, Lin, L & Lai, H 2013, 'Piezoelectric properties of PVDF/MWCNT nanofibre using near-field electrospinning', Sensors and Actuators A: Physical, vol. 193, pp. 13-24.

109. Lovinger, AJ 1982, 'Annealing of poly (vinylidene fluoride) and formation of a fifth phase', Macromolecules, vol. 15, no. 1, pp. 40-4.

110. Lymberis, A & Paradiso, R 2008, 'Smart fabrics and interactive textile enabling wearable personal applications: R&D state of the art and future challenges', paper presented to Engineering in Medicine and Biology Society, 2008. EMBS 2008. 30th Annual International Conference of the IEEE.

111. Magniez, K, Krajewski, A, Neuenhofer, M & Helmer, R 2013, 'Effect of drawing on the molecular orientation and polymorphism of melt-spun polyvinylidene fluoride fibres: Toward the development of piezoelectric force sensors', Journal of applied polymer science, vol. 129, no. 5, pp. 2699-706.

112. Mahadeva, SK, Berring, J, Walus, K & Stoeber, B 2013, 'Effect of poling time and grid voltage on phase transition and piezoelectricity of poly (vinyledene fluoride) thin films using corona poling', Journal of Physics D: Applied Physics, vol. 46, no. 28, p. 285305.

113. Martin, TL 2002, 'Time and time again: Parallels in the development of the watch and the wearable computer', paper presented to Wearable Computers, 2002. (ISWC 2002). Proceedings. Sixth International Symposium on.

114. Martins, P, Lopes, A & Lanceros-Mendez, S 2014, 'Electroactive phases of poly (vinylidene fluoride): determination, processing and applications', Progress in polymer science, vol. 39, no. 4, pp. 683-706.

115. Massey, P 2001, 'GSM fabric antenna for mobile phones integrated within clothing', paper presented to Antennas and Propagation Society International Symposium, 2001. IEEE.

116. McCann, J & Bryson, D 2009, Smart clothes and wearable technology, Elsevier.

117. Meister, F, Vorbach, D, Niemz, F, Schulze, T & Taeger, E 2003, 'Functional high-tech-cellulose materials by the ALCER ((R)) process', Materialwissenschaft und Werkstofftechnik, vol. 34, no. 3, pp. 262-6.

118. Meitzler, A, Tiersten, H, Warner, A, Berlincourt, D, Couqin, G & Welsh III, F 1988, IEEE standard on piezoelectricity, Society.

119. Meoli, D & May-Plumlee, T 2002, 'Interactive electronic textile development: A review of technologies', Journal of Textile and Apparel, Technology and Management, vol. 2, no. 2, pp. 1-12.

120. Meyer, R, Shrout, T & Yoshikawa, S 1998, 'Lead Zirconate Titanate Fine Fibres Derived from Alkoxide-Based Sol-Gel Technology', Journal of the American Ceramic Society, vol. 81, no. 4, pp. 861-8.

121. Mitcheson, PD, Yeatman, EM, Rao, GK, Holmes, AS & Green, TC 2008, 'Energy harvesting from human and machine motion for wireless electronic devices', Proceedings of the IEEE, vol. 96, no. 9, pp. 1457-86.

122. Mohammadi, B, Yousefi, AA & Bellah, SM 2007, 'Effect of tensile strain rate and elongation on crystalline structure and piezoelectric properties of PVDF thin films', Polymer Testing, vol. 26, no. 1, pp. 42-50.

123. Moheimani, SR & Fleming, AJ 2006, Piezoelectric transducers for vibration control and damping, Springer Science & Business Media.

124. Mokhtari, F, Shamshirsaz, M, Latifi, M & Asadi, S 2017, 'Comparative evaluation of piezoelectric response of electrospun PVDF (polyvinilydine fluoride) nanofibre with various additives for energy scavenging application', The Journal of The Textile Institute, vol. 108, no. 6, pp. 906-14.

125. Origin (OriginLab, Northampton, MA)

126. Pi, Z, Zhang, J, Wen, C, Zhang, Z-b & Wu, D 2014, 'Flexible piezoelectric nanogenerator made of poly (vinylidenefluoride-co-trifluoroethylene) (PVDF-TrFE) thin film', Nano Energy, vol. 7, pp. 33-41.

127. Pinet, É 2008, 'Medical applications: Saving lives', Nature photonics, vol. 2, no. 3, pp. 150-2.

128. Poulsen, M & Ducharme, S 2010, 'Why ferroelectric polyvinylidene fluoride is special', IEEE Transactions on Dielectrics and Electrical Insulation, vol. 17, no. 4.

129. Proto, A, Penhaker, M, Bibbo, D, Vala, D, Conforto, S & Schmid, M 2016, 'Measurements of generated energy/electrical quantities from locomotion activities using piezoelectric wearable sensors for body motion energy harvesting', Sensors, vol. 16, no. 4, p. 524.
130. Pu, X, Li, L, Liu, M, Jiang, C, Du, C, Zhao, Z, Hu, W & Wang, ZL 2016, 'Wearable self-charging power textile based on flexible yarn supercapacitors and fabric nanogenerators', Advanced Materials, vol. 28, no. 1, pp. 98-105.
131. Qin, Y, Wang, X & Wang, ZL 2008, 'Microfibre-nanowire hybrid structure for energy scavenging', nature, vol. 451, no. 7180, p. 809.
132. Ray, CA & Anton, SR 2017, 'Multilayer piezoelectret foam stack for vibration energy harvesting', Journal of Intelligent Material Systems and Structures, vol. 28, no. 3, pp. 408-20.
133. Riemer, R & Shapiro, A 2011, 'Biomechanical energy harvesting from human motion: theory, state of the art, design guidelines, and future directions', Journal of neuroengineering and rehabilitation, vol. 8, no. 1, p. 22.
134. Romero-Ramirez, E 2010, Energy harvesting from body motion using rotational micro-generation, Michigan Technological University.
135. Salimi, A & Yousefi, A 2003, 'Analysis method: FTIR studies of β-phase crystal formation in stretched PVDF films', Polymer Testing, vol. 22, no. 6, pp. 699-704.
136. Sears, K, Skourtis, C, Atkinson, K, Finn, N & Humphries, W 2010, 'Focused ion beam milling of carbon nanotube yarns to study the relationship between structure and strength', Carbon, vol. 48, no. 15, pp. 4450-6.
137. Sebald, G, Lefeuvre, E & Guyomar, D 2008, 'Pyroelectric energy conversion: optimization principles', IEEE Transactions on ultrasonics, ferroelectrics, and frequency control, vol. 55, no. 3.
138. Selvan, KV & Ali, MSM 2016, 'Micro-scale energy harvesting devices: Review of methodological performances in the last decade', Renewable and Sustainable Energy Reviews, vol. 54, pp. 1035-47.
139. Sencadas, V, Gregorio Jr, R & Lanceros-Méndez, S 2009, 'α to β phase transformation and microestructural changes of PVDF films induced by uniaxial stretch', Journal of Macromolecular Science®, vol. 48, no. 3, pp. 514-25.

140. Seo, M-H, Choi, D-H, Kim, I-H, Jung, H-J & Yoon, J-B 2012, 'Multi-resonant energy harvester exploiting high-mode resonances frequency down-shifted by a flexible body beam', Applied Physics Letters, vol. 101, no. 12, p. 123903.

141. Sharapov, V 2011, Piezoceramic sensors, Springer Science & Business Media.

142. Shenck, NS & Paradiso, JA 2001, 'Energy scavenging with shoe-mounted piezoelectrics', IEEE micro, vol. 21, no. 3, pp. 30-42.

143. Siores, E, Hadimani, R & Vatansever, D 2010, 'Hybrid Energy Conversion Device', GB Patent No, vol. 1016193.

144. Soin, N, Shah, TH, Anand, SC, Geng, J, Pornwannachai, W, Mandal, P, Reid, D, Sharma, S, Hadimani, RL & Bayramol, DV 2014, 'Novel “3-D spacer” all fibre piezoelectric textiles for energy harvesting applications', Energy & Environmental Science, vol. 7, no. 5, pp. 1670-9.

145. Starner, T 1996, 'Human-powered wearable computing', IBM systems Journal, vol. 35, no. 3.4, pp. 618-29.

146. Straif, K, Cohen, A & Samet, J 2013, 'Air pollution and cancer', IARC scientific publication, vol. 161.

147. Strock, HB, Pascucci, MR, Parish, MV, Bent, AA & Shrout, TR 1999, 'Active pzt fibres: a commercial production process', paper presented to 1999 Symposium on Smart Structures and Materials.

148. Swallow, L, Luo, J, Siores, E, Patel, I & Dodds, D 2008, 'A piezoelectric fibre composite based energy harvesting device for potential wearable applications', Smart materials and structures, vol. 17, no. 2, p. 025017.

149. Takahashi, N & Odajima, A 1978, 'Fine Structures of Stretched PVDF and their Poling Effects', Reports on Progress in Polymer Physics in Japan, vol. 21, p. 141.

150. Tien, CMT & Goo, NS 2010, 'Use of a piezocomposite generating element in energy harvesting', Journal of Intelligent Material Systems and Structures, vol. 21, no. 14, pp. 1427-36.

151. Tilley, RJ 2006, Crystals and crystal structures, John Wiley & Sons.

152. Tressler, J, Alkoy, S, Dogan, A & Newnham, R 1999, 'Functional composites for sensors, actuators and transducers', Composites Part A: Applied Science and Manufacturing, vol. 30, no. 4, pp. 477-82.

153. Tuzzolino, A 1996, 'Applications of PVDF dust sensor systems in space', Advances in Space Research, vol. 17, no. 12, pp. 123-32.

154. Uchino, K 2010, Advanced piezoelectric materials: Science and technology, Elsevier.

155. Van Langenhove, L & Hertleer, C 2004, 'Smart clothing: a new life', International Journal of Clothing Science and Technology, vol. 16, no. 1/2, pp. 63-72.

156. Vatansever, D, Hadimani, R, Shah, T & Siores, E 2011, 'Piezoelectric Mono-Filament Extrusion for Green Energy Applications from Textiles', paper presented to Proceedings of the International Congress of Innovative Textiles, ICONTEX2011, Istanbul.

157. Vatansever, D, Siores, E, Hadimani, RL & Shah, T 2011, 'Smart woven fabrics in renewable energy generation', in Advances in modern woven fabrics technology, InTech.

158. Vatansever, D, Siores, E & Shah, T 2012, 'Alternative resources for renewable energy: piezoelectric and photovoltaic smart structures', in Global Warming-Impacts and Future Perspective, Intech.

159. Villafuerte-Castrejón, ME, Morán, E, Reyes-Montero, A, Vivar-Ocampo, R, Peña-Jiménez, J-A, Rea-López, S-O & Pardo, L 2016, 'Towards lead-free piezoceramics: Facing a synthesis challenge', Materials, vol. 9, no. 1, p. 21.

160. Wang, X 2012, 'Piezoelectric nanogenerators—Harvesting ambient mechanical energy at the nanometer scale', Nano Energy, vol. 1, no. 1, pp. 13-24.

161. Wang, ZL & Song, J 2006, 'Piezoelectric nanogenerators based on zinc oxide nanowire arrays', Science, vol. 312, no. 5771, pp. 242-6.

162. Waqar, S, McCarthy, JM, Deivasigamani, A, Wang, CH, Wang, L, Coman, F & John, S 2013, 'Dual field finite element simulations of piezo-patches on fabrics: a parametric study', paper presented to Proc. of SPIE Vol.

163. Williams, RB, Park, G, Inman, DJ & Wilkie, WK 2002, 'An overview of composite actuators with piezoceramic fibres', Proceeding of IMAC XX, vol. 47.

164. Winter, DA 2009, Biomechanics and motor control of human movement, John Wiley & Sons.

165. Wu, W, Du, H, Wang, DF & Itoh, T 2015, 'Resonating Characterization of Piezoelectric Fibres Applicable to Flexible Self-Powered Fabric', Procedia Engineering, vol. 120, pp. 1028-31.

166. Xu, C, Wang, X & Wang, ZL 2009, 'Nanowire structured hybrid cell for concurrently scavenging solar and mechanical energies', Journal of the American Chemical Society, vol. 131, no. 16, pp. 5866-72.
167. Yang, B & Yun, K-S 2012, 'Piezoelectric shell structures as wearable energy harvesters for effective power generation at low-frequency movement', Sensors and Actuators A: Physical, vol. 188, pp. 427-33.
168. Yang, R, Qin, Y, Li, C, Zhu, G & Wang, ZL 2009, 'Converting biomechanical energy into electricity by a muscle-movement-driven nanogenerator', Nano letters, vol. 9, no. 3, pp. 1201-5.
169. Yang, Y, Guo, W, Pradel, KC, Zhu, G, Zhou, Y, Zhang, Y, Hu, Y, Lin, L & Wang, ZL 2012, 'Pyroelectric nanogenerators for harvesting thermoelectric energy', Nano letters, vol. 12, no. 6, pp. 2833-8.
170. Yang, Y, Jung, JH, Yun, BK, Zhang, F, Pradel, KC, Guo, W & Wang, ZL 2012, 'Flexible Pyroelectric Nanogenerators using a Composite Structure of Lead-Free KNbO3 Nanowires', Advanced Materials, vol. 24, no. 39, pp. 5357-62.
171. Ye, Y, Jiang, Y, Wu, Z & Zeng, H 2006, 'Phase transitions of poly (vinylidene fluoride) under electric fields', Integrated Ferroelectrics, vol. 80, no. 1, pp. 245-51.
172. Yip, J & Ng, S-P 2008, 'Study of three-dimensional spacer fabrics:: Physical and mechanical properties', Journal of materials processing technology, vol. 206, no. 1, pp. 359-64.
173. Yuhuan, X 1991, 'Ferroelectric materials and their applications'.
174. Yuksel, R & Unalan, HE 2015, 'Textile supercapacitors-based on MnO2/SWNT/conducting polymer ternary composites', International Journal of Energy Research, vol. 39, no. 15, pp. 2042-52.
175. Yun, D & Yun, K-S 2013, 'Woven piezoelectric structure for stretchable energy harvester', Electronics Letters, vol. 49, no. 1, pp. 65-6.
176. Zabek, D, Taylor, J & Bowen, CR 2016, 'Characterization and Modelling of Meshed Electrodes on Free Standing Polyvinylidene Difluoride (PVDF) Films for Enhanced Pyroelectric Energy Harvesting', IEEE Transactions on ultrasonics, ferroelectrics, and frequency control, vol. 63, no. 10, pp. 1681-9.
177. Zatsiorsky, VM 2002, Kinetics of human motion, Human Kinetics.

178. Zeng, W, Tao, X-M, Chen, S, Shang, S, Chan, HLW & Choy, SH 2013, 'Highly durable all-fibre nanogenerator for mechanical energy harvesting', Energy & Environmental Science, vol. 6, no. 9, pp. 2631-8.

179. Zhang, M, Gao, T, Wang, J, Liao, J, Qiu, Y, Yang, Q, Xue, H, Shi, Z, Zhao, Y & Xiong, Z 2015, 'A hybrid fibres based wearable fabric piezoelectric nanogenerator for energy harvesting application', Nano Energy, vol. 13, pp. 298-305.

180. Zhang, X & Tao, X 2001, 'Smart textiles: Passive smart', Textile Asia, vol. 32, no. 6, pp. 45-9.

181. Zhao, J & You, Z 2014, 'A shoe-embedded piezoelectric energy harvester for wearable sensors', Sensors, vol. 14, no. 7, pp. 12497-510.

182. Zięba, J & Frydrysiak, M 2010, 'The Method of Human Frequency Breathing Measurement by Textronic Sesnors', paper presented to 7th International Conference– TEXSCI.

8 Appendix

8.1 Tables of Material properties

8.1.1 Properties for flexible polyester

Table 8.1: Material properties for flexible polyester[9]

Material properties for Polyester	
Property	Value
Young's Modulus (MPa)	4410
Poisson's Ratio,	0.403
Bulk Modulus (MPa)	7577.3
Shear Modulus (MPa)	1571.6
Density Kg/m^3	1400

Polymer Properties" available at http://engr.bd.psu.edu/rxm61/METBD470/Lectures/PolymerProperties%20from%20CES.pdf (05 May 2013)

8.1.2 Properties for piezoelectric material

Table 8.2: Material properties for piezoelectric material, PVDF[10]

Material properties for PVDF	
Property	Value
Young's Modulus (MPa)	4000
Poisson's Ratio	0.3
Bulk Modulus (MPa)	3333.3
Shear Modulus (MPa)	1538.5
Density Kg/m^3	1780
D_{31} 10^{-12} C/N	23
D_{32} 10^{-12} C/N	3
D_{33} 10^{-12} C/N	-33

Measurement Specialties Inc., [Technical Manual for Piezo Film Sensors], Hampton: Measurement Specialties. (2006).

8.1.3 Properties for polyamide

Table 8.3: Material properties for piezoelectric material polyamide used for analysis

Property	Polyamide
Young’s Modulus (MPa)	4000
Poisson’s Ratio	0.39
Bulk Modulus (MPa)	6060
Shear Modulus (MPa)	1438
Density kg/m^3	1130
D_{31} 10^{-12} C/N	-
D_{32} 10^{-12} C/N	-
D_{33} 10^{-12} C/N	-

8.2 Electric field density

In the table below, the minimum value represents the electric field density in the centre of the hole or slit between the two Aluminium plates.

8.4 Table showing electric field density in hole and plate setup

Simulation Configuration		Local Electric Field Density (m/V)	
		Min	Max
Centre Hole			
	10 mm thick; 10 mm diameter; 10 mm apart	57.0	2.9e7
	10 mm thick; 10 mm diameter; 3mm apart	57.4	2.9e7
	3 mm thick; 10 mm diameter; 10 mm apart	40.8	3.5e7
	3 mm thick; 10 mm diameter; 3mm apart	236	7.1e7
	3 mm thick; 5 mm diameter; 10 mm apart	5.3e6	2.5e7
	3 mm thick; 5 mm diameter; 3 mm apart	60.9	7.1e7
Slit			
	10 mm thick; 10 mm gap; 10 mm apart	36	1.8e7
	10 mm thick; 10 mm gap; 3 mm apart	-	-
	3 mm thick; 10 mm gap; 10 mm apart	57	2e7
	3 mm thick; 10 mm gap; 3 mm apart	70	4.2e7
	3 mm thick; 5 mm gap; 10 mm apart	73	1.8e7
	3 mm thick; 5 mm gap; 3 mm apart	5.9e2	5.1e7

8.3 ANSYS

ANSYS® is a multi-physics Finite Element Analysis (FEA) package, used for structural, thermal, fluid and electrical analyses. In this thesis, ANSYS® was used for determining the frequency response characteristics of the energy harvesting from yarns, fabric and a bonded PVDF piezo-strip. The geometries were created using ANSYS Design modeler and were exported and post processed in ANSYS Mechanical APDL.

The reports for these studies for both modal and harmonic response analyses is appended below. These reports present the details of the geometry, mesh, boundary conditions, solution methods and results for each study as discussed in Chapter 3.

8.3.1 Dual field analysis of poling design of Polyvinylidene fluoride fibres for energy harvesting applications

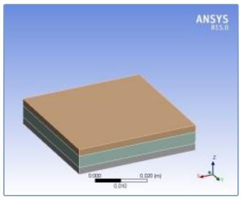

- a) TABLE 8.3.1.1 Units
- b) Model (A4)
    - (1) TABLE 8.3.1.2 Model (A4) > Geometry
        - (a) TABLE 8.3.1.3 Model (A4) > Geometry > Body Groups
        - (b) TABLE 8.3.1.4 Electrical Assembly Parts
    - (2) TABLE 8.3.1.5 Coordinate Systems
    - (3) Connections
        - (a) TABLE 8.3.1.6 Contacts
    - (4) TABLE 8.3.1.7 Mesh
    - (5) TABLE 8.3.1.8 Steady-State Electric Conduction (A5)
        - (a) TABLE 8.3.1.9 Analysis Settings
        - (b) TABLE 8.3.1.10 Loads
            - (i) TABLE 8.3.1.11 Solution (A6)
            - (ii) TABLE 8.3.1.12 Solution Information
            - (iii) TABLE 8.3.1.13 Results
- c) Material Data
    - (1) TABLE 8.3.1.14 Aluminium
    - (2) TABLE 8.3.1.15 Air

TABLE 8.3.1.1 Units

Unit System	Metric (m, kg, N, s, V, A) Degrees rad/s Celsius
Angle	Degrees
Rotational Velocity	rad/s

Temperature	Celsius

TABLE 8.3.1.2 Model (A4) > Geometry

Object Name	Geometry
State	Fully Defined
Definition	
Source	J:\Twin plate analysis\Twin plate analysis_50by100_files\dp0 \SYS\DM\SYS.agdb
Type	DesignModeler
Length Unit	Meters
Element Control	Program Controlled
Display Style	Body Color
Bounding Box	
Length X	5.e-002 m
Length Y	5.e-002 m
Length Z	1.1e-002 m
Properties	
Volume	2.75e-005 m³
Mass	0. kg
Scale Factor Value	1.
Statistics	
Bodies	3
Active Bodies	3
Nodes	33077
Elements	7200
Mesh Metric	None
Basic Geometry Options	
Parameters	Yes

TABLE 8.3.1.3 Model (A4) > Geometry > Body Groups

Object Name	Electrical Assembly
State	Meshed
Graphics Properties	
Visible	Yes
Definition	
Suppressed	No
Assignment	Multiple Materials
Coordinate System	Default Coordinate System

Bounding Box	
Length X	5.e-002 m
Length Y	5.e-002 m
Length Z	1.1e-002 m
Properties	
Volume	2.75e-005 m³
Mass	0. kg
Centroid X	0. m
Centroid Y	0. m
Centroid Z	0. m
Moment of Inertia Ip1	0. kg·m²
Moment of Inertia Ip2	0. kg·m²
Moment of Inertia Ip3	0. kg·m²
Statistics	
Nodes	33077
Elements	7200
Mesh Metric	None

TABLE 8.3.1.4 Model (A4) > Geometry > Electrical Assembly > Parts

Object Name	Bottom Plate	Top Plate	Air Gap
State	Meshed		
Graphics Properties			
Visible	Yes		
Glow	0		
Shininess	1		
Transparency	1		
Specularity	1		
Definition			
Suppressed	No		
ID (Beta)	18	20	22
Stiffness Behavior	Flexible		
Coordinate System	Default Coordinate System		
Reference Temperature	By Environment		
Material			
Assignment	Aluminium		Air
Nonlinear Effects	Yes		
Thermal Strain Effects	Yes		
Bounding Box			
Length X	5.e-002 m		

Length Y	5.e-002 m		
Length Z	3.e-003 m		5.e-003 m
Properties			
Volume	7.5e-006 m³		1.25e-005 m³
Mass	0. kg		
Centroid X	-1.4705e-019 m	-1.0294e-018 m	1.7647e-019 m
Centroid Y	2.9411e-019 m	-1.4705e-018 m	0. m
Centroid Z	-1.5e-003 m	6.5e-003 m	2.5e-003 m
Moment of Inertia Ip1	0. kg·m²		
Moment of Inertia Ip2	0. kg·m²		
Moment of Inertia Ip3	0. kg·m²		
Statistics			
Nodes	10385		17949
Elements	1800		3600
Mesh Metric	None		

TABLE 8.3.1.5 Model (A4) > Coordinate Systems > Coordinate System

Object Name	Global Coordinate System
State	Fully Defined
Definition	
Type	Cartesian

TABLE 8.3.1.6 Model (A4) > Connections > Contacts

Object Name	Contacts
State	Fully Defined
Definition	
Connection Type	Contact
Scope	
Scoping Method	Geometry Selection
Geometry	All Bodies
Auto Detection	
Tolerance Type	Slider
Tolerance Slider	0.
Tolerance Value	1.789e-004 m
Use Range	No
Face/Face	Yes
Face/Edge	No
Edge/Edge	No
Priority	Include All
Group By	Bodies

Search Across	Bodies

TABLE 8.3.1.7 Model (A4) > Mesh

Object Name	Mesh
State	Solved
Defaults	
Physics Preference	Electromagnetics
Relevance	0
Sizing	
Use Advanced Size Function	Off
Relevance Center	Coarse
Element Size	Default
Initial Size Seed	Active Assembly
Smoothing	Medium
Transition	Fast
Span Angle Center	Coarse
Minimum Edge Length	3.e-003 m
Inflation	
Use Automatic Inflation	None
Inflation Option	Smooth Transition
Transition Ratio	0.272
Maximum Layers	5
Growth Rate	1.2
Inflation Algorithm	Pre
View Advanced Options	No
Patch Conforming Options	
Triangle Surface Mesher	Program Controlled
Patch Independent Options	
Topology Checking	Yes
Advanced	
Number of CPUs for Parallel Part Meshing	Program Controlled
Shape Checking	Electromagnetics
Element Midside Nodes	Kept
Straight Sided Elements	Yes
Number of Retries	Default (4)
Extra Retries For Assembly	Yes
Rigid Body Behavior	Dimensionally Reduced
Mesh Morphing	Disabled
Defeaturing	

Pinch Tolerance	Please Define
Generate Pinch on Refresh	No
Automatic Mesh Based Defeaturing	On
Defeaturing Tolerance	Default
Statistics	
Nodes	33077
Elements	7200
Mesh Metric	None

TABLE 8.3.1.8 Model (A4) > Analysis

Object Name	Steady-State Electric Conduction (A5)
State	Solved
Definition	
Physics Type	Electric
Analysis Type	Steady-State Electric Conduction
Solver Target	Mechanical APDL
Options	
Environment Temperature	25. °C
Generate Input Only	No

TABLE 8.3.1.9 Model (A4) > Steady-State Electric Conduction (A5) > Analysis Settings

Object Name	Analysis Settings
State	Fully Defined
Step Controls	
Number Of Steps	1.
Current Step Number	1.
Step End Time	1. s
Auto Time Stepping	Program Controlled
Solver Controls	
Solver Type	Program Controlled
Nonlinear Controls	
Line Search	Program Controlled
Voltage Convergence	Program Controlled
Current Convergence	Program Controlled
Output Controls	
General Miscellaneous	No
Store Results At	All Time Points
Analysis Data Management	
Solver Files Directory	J:\Twin plate analysis\Twin plate analysis_50by100_files\dp0\SYS\MECH\
Future Analysis	None

Scratch Solver Files Directory	
Save MAPDL db	No
Delete Unneeded Files	Yes
Nonlinear Solution	No
Solver Units	Active System
Solver Unit System	mks

TABLE 8.3.1.10 Model (A4) > Steady-State Electric Conduction (A5) > Loads

Object Name	Voltage	Voltage 2
State	Fully Defined	
Scope		
Scoping Method	Geometry Selection	
Geometry	1 Face	
Definition		
ID (Beta)	68	79
Type	Voltage	
Magnitude	30000 V (ramped)	-30000 V (ramped)
Phase Angle	0. °	
Suppressed	No	

TABLE 8.3.1.11 Model (A4) > Steady-State Electric Conduction (A5) > Solution

Object Name	Solution (A6)
State	Solved
Adaptive Mesh Refinement	
Max Refinement Loops	1.
Refinement Depth	2.
Information	
Status	Done

TABLE 8.3.1.12 Model (A4) > Steady-State Electric Conduction (A5) > Solution (A6) > Solution Information

Object Name	Solution Information
State	Solved
Solution Information	
Solution Output	Solver Output
Update Interval	2.5 s
Display Points	All
FE Connection Visibility	
Activate Visibility	Yes
Display	All FE Connectors

Draw Connections Attached To	All Nodes
Line Color	Connection Type
Visible on Results	No
Line Thickness	Single
Display Type	Lines

TABLE 8.3.1.13 Model (A4) > Steady-State Electric Conduction (A5) > Solution (A6) > Results

Object Name	Electric Voltage	Total Electric Field Intensity
State	Solved	
Scope		
Scoping Method	Geometry Selection	
Geometry	All Bodies	1 Body
Shell		Top/Bottom
Layer		Entire Section
Definition		
Type	Electric Voltage	Total Electric Field Intensity
By	Time	
Display Time	Last	
Calculate Time History	Yes	
Identifier		
Suppressed	No	
Results		
Minimum	-30000 V	1.2e+007 V/m
Maximum	30000 V	1.2e+007 V/m
Minimum Occurs On	Bottom Plate	
Maximum Occurs On	Top Plate	
Minimum Value Over Time		
Minimum	-30000 V	1.2e+007 V/m
Maximum	-30000 V	1.2e+007 V/m
Maximum Value Over Time		
Minimum	30000 V	1.2e+007 V/m
Maximum	30000 V	1.2e+007 V/m
Information		
Time	1. s	
Load Step	1	
Substep	1	
Iteration Number	1	
Integration Point Results		
Display Option		Averaged

Average Across Bodies		No

TABLE 8.3.1.14 Aluminium > Constants

Resistivity	2.826e-008 ohm m

TABLE 8.3.1.15 Air > Constants

Resistivity	2.3e+016 ohm m

8.3.2 Dual Field Finite Element Simulations of Piezo-Patches on Fabrics: parametric study

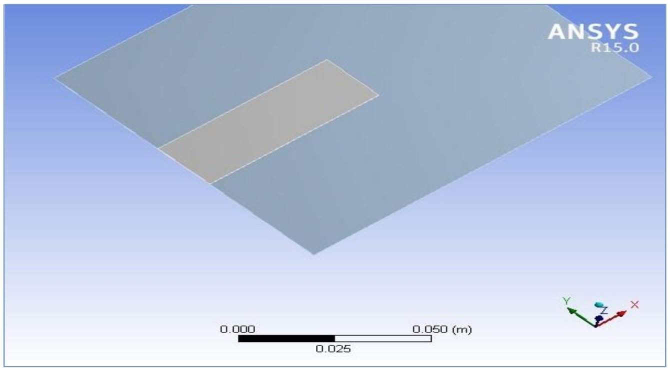

a) Model (A4)
i) TABLE 8.3.2.1 Geometry
(1) TABLE 8.3.2.2 Parts
ii) TABLE 8.3.2.3 Connections
(1) TABLE 8.3.2.4 Contact Regions
(2) Bonded - Piezo To Bottom_plate
iii) TABLE 8.3.2.5 Mesh
(1) TABLE 8.3.2.6 Mesh Controls
iv) Harmonic Response (A5)
(1) TABLE 8.3.2.7 Analysis
(2) TABLE 8.3.2.8 Initial Conditions
(3) TABLE 8.3.2.9 Analysis Settings
(4) TABLE 8.3.2.10 Loads
(5) TABLE 8.3.2.11 Solution (A6)
(6) TABLE 8.3.2.12 Solution Information
b) Material Data
i) TABLE 8.3.2.13 Structural Steel Constants
(1) TABLE 8.3.2.14 Structural Steel > Compressive Yield Strength
(2) TABLE 8.3.2.15 Structural Steel > Tensile Yield Strength
(3) TABLE 8.3.2.16 Structural Steel > Tensile Ultimate Strength
(4) TABLE 8.3.2.17 Structural Steel>Strain-Life Parameters
(5) TABLE 8.3.2.18 Structural Steel > Isotropic Elasticity
(6) TABLE 8.3.2.19 Structural Steel > Isotropic Relative Permeability

ii) TABLE 8.3.2.20 Polyethylene Constants

(1) TABLE 8.3.2.21 Polyethylene > Tensile Ultimate Strength
(2) TABLE 8.3.2.22 Polyethylene > Isotropic Secant Coefficient of Thermal Expansion
(3) TABLE 8.3.2.23 Polyethylene > Isotropic Elasticity

TABLE 8.3.2.1 Model (A4) > Geometry

Object Name	Geometry
State	Fully Defined
Definition	
Source	C:\Users\Imtiaz\AppData\Local\Temp\Piezo parametric analysis MESHING COMPLETED BUT SHM ANALYSIS.tmp\Piezo parametric analysis MESHING COMPLETED BUT SHM ANALYSIS_files\dp0\SYS\DM\SYS.agdb
Type	DesignModeler
Length Unit	Millimeters
Element Control	Program Controlled
Display Style	Body Color
Bounding Box	
Length X	0.12 m
Length Y	0.1 m
Length Z	4.e-004 m
Properties	
Volume	2.64e-006 m^3
Mass	4.164e-003 kg
Scale Factor Value	1.
Statistics	
Bodies	2
Active Bodies	2
Nodes	29399
Elements	5150
Mesh Metric	None
Basic Geometry Options	
Parameters	Yes
Parameter Key	DS
Attributes	No
Named Selections	No
Material Properties	No
Advanced Geometry Options	
Use Associativity	Yes

TABLE 8.3.2.2 Model (A4) > Geometry > Parts

Object Name	Piezo	Bottom_plate
State	Meshed	
Graphics Properties		
Visible	Yes	

Glow	0	
Shininess	1	
Transparency	1	
Specularity	1	
Definition		
Suppressed	No	
ID (Beta)	17	20
Stiffness Behavior	Flexible	
Coordinate System	Piezo_system	Default Coordinate System
Reference Temperature	By Environment	
Material		
Assignment	Structural Steel	Polyethylene
Nonlinear Effects	Yes	
Thermal Strain Effects	Yes	
Bounding Box		
Length X	6.e-002 m	0.12 m
Length Y	2.e-002 m	0.1 m
Length Z	2.e-004 m	
Properties		
Volume	2.4e-007 m³	2.4e-006 m³
Mass	1.884e-003 kg	2.28e-003 kg
Centroid X	3.e-002 m	6.e-002 m
Centroid Y	1.e-002 m	
Centroid Z	1.e-004 m	-1.e-004 m
Moment of Inertia Ip1	6.2806e-008 kg·m²	1.9e-006 kg·m²
Moment of Inertia Ip2	5.6521e-007 kg·m²	2.736e-006 kg·m²
Moment of Inertia Ip3	6.28e-007 kg·m²	4.636e-006 kg·m²
Statistics		
Nodes	2966	26433
Elements	486	4664
Mesh Metric	None	

TABLE 8.3.2.3 Model (A4) > Connections

Object Name	Connections
State	Fully Defined
Auto Detection	
Generate Automatic Connection On Refresh	Yes
Transparency	
Enabled	Yes

TABLE8.3.2.4 Model (A4) > Connections > Contacts > Contact Regions

Object Name	Bonded - Piezo To Bottom_plate
State	Fully Defined
Scope	
Scoping Method	Geometry Selection
Contact	1 Face
Target	1 Face
Contact Bodies	Piezo
Target Bodies	Bottom_plate
Definition	
Type	Bonded
Scope Mode	Automatic
Behavior	Symmetric
Trim Contact	Program Controlled
Trim Tolerance	3.9051e-004 m
Suppressed	No
Advanced	
Formulation	Pure Penalty
Detection Method	Program Controlled
Normal Stiffness	Program Controlled
Update Stiffness	Never
Pinball Region	Program Controlled
Geometric Modification	
Contact Geometry Correction	None
Target Geometry Correction	None

TABLE 8.3.2.5 Model (A4) > Mesh

Object Name	Mesh
State	Solved
Defaults	
Physics Preference	Mechanical
Relevance	0
Sizing	
Use Advanced Size Function	Off
Relevance Center	Fine
Element Size	Default
Initial Size Seed	Active Assembly
Smoothing	Medium
Transition	Fast
Span Angle Center	Coarse
Minimum Edge Length	2.e-004 m
Inflation	
Use Automatic Inflation	None

Inflation Option	Smooth Transition
Transition Ratio	0.272
Maximum Layers	5
Growth Rate	1.2
Inflation Algorithm	Pre
View Advanced Options	No
Patch Conforming Options	
Triangle Surface Mesher	Program Controlled
Patch Independent Options	
Topology Checking	Yes
Advanced	
Number of CPUs for Parallel Part Meshing	Program Controlled
Shape Checking	Standard Mechanical
Element Midside Nodes	Program Controlled
Straight Sided Elements	No
Number of Retries	Default (4)
Extra Retries For Assembly	Yes
Rigid Body Behavior	Dimensionally Reduced
Mesh Morphing	Disabled
Defeaturing	
Pinch Tolerance	Please Define
Generate Pinch on Refresh	No
Automatic Mesh Based Defeaturing	On
Defeaturing Tolerance	Default
Statistics	
Nodes	29399
Elements	5150
Mesh Metric	None

TABLE 8.3.2.6 Model (A4) > Mesh > Mesh Controls

Object Name	Edge Sizing	Edge Sizing 2
State	Fully Defined	
Scope		
Scoping Method	Geometry Selection	
Geometry	4 Edges	
Definition		
Suppressed	No	
Type	Number of Divisions	
Number of Divisions	2	
Behavior	Soft	
Bias Type	No Bias	

TABLE 8.3.2.7 Model (A4) > Analysis

Object Name	Harmonic Response (A5)
State	Solved
Definition	
Physics Type	Structural
Analysis Type	Harmonic Response
Solver Target	Mechanical APDL
Options	
Environment Temperature	22. °C
Generate Input Only	No

TABLE 8.3.2.8 Model (A4) > Harmonic Response (A5) > Initial Condition

Object Name	Modal (None)
State	Fully Defined
Definition	
Pre-Stress Environment	None
Modal Environment	None Available

TABLE 8.3.2.9 Model (A4) > Harmonic Response (A5) > Analysis Settings

Object Name	Displacement	Force
State	Fully Defined	
Scope		
Scoping Method	Geometry Selection	
Geometry	1 Face	
Definition		
ID (Beta)	58	60

TABLE 8.3.2.10 Model (A4) > Harmonic Response (A5) > Loads

Type	Displacement	Force
Define By	Components	
Coordinate System	Global Coordinate System	
X Component	0. m	0. N
Y Component	0. m	0. N
Z Component	0. m	1.e-004 N
Phase Angle	0. °	
Suppressed	No	

TABLE 8.3.2.11 Model (A4) > Harmonic Response (A5) > Solution

Object Name	Solution (A6)
State	Solved
Adaptive Mesh Refinement	
Max Refinement Loops	1.

Refinement Depth	2.
Information	
Status	Done

FIGURE 1
Model (A4) > Harmonic Response (A5) > Solution(A6)

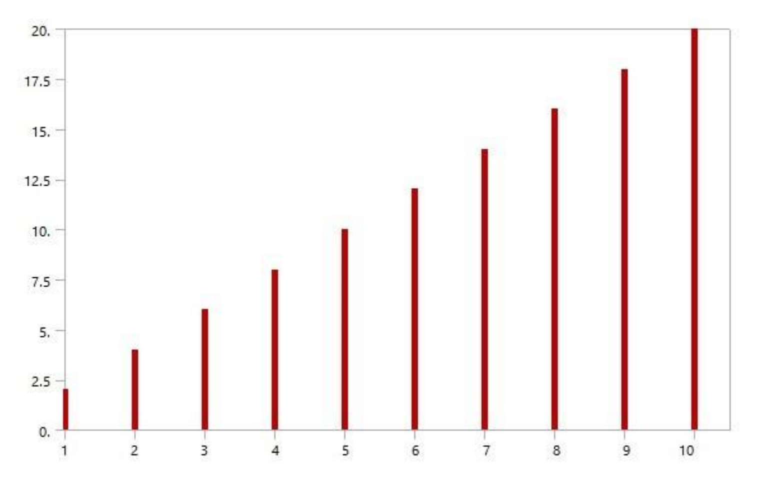

TABLE 8.3.2.12 Model (A4) > Harmonic Response (A5) > Solution (A6) > Solution Information

Object Name	Solution Information
State	Solved
Solution Information	
Solution Output	Solver Output
Newton-Raphson Residuals	0
Update Interval	2.5 s
Display Points	All
FE Connection Visibility	
Activate Visibility	Yes
Display	All FE Connectors
Draw Connections Attached To	All Nodes
Line Color	Connection Type
Visible on Results	No
Line Thickness	Single
Display Type	Lines

TABLE 8.3.2.13 Structural Steel > Constants

Density	7850 kg m^-3
Coefficient of Thermal Expansion	1.2e-005 C^-1
Specific Heat	434 J kg^-1 C^-1
Thermal Conductivity	60.5 W m^-1 C^-1
Resistivity	1.7e-007 ohm m

TABLE 8.3.2.14 Structural Steel > Compressive Yield Strength

Compressive Yield Strength Pa
2.5e+008

TABLE 8.3.2.15 Structural Steel > Tensile Yield Strength

Tensile Yield Strength Pa
2.5e+008

TABLE 8.3.2.16 Structural Steel > Tensile Ultimate Strength

Tensile Ultimate Strength Pa
4.6e+008

TABLE 8.3.2.17 Structural Steel > Strain-Life Parameters

Strength Coefficient Pa	Strength Exponent	Ductility Coefficient	Ductility Exponent	Cyclic Strength Coefficient Pa	Cyclic Strain Hardening Exponent
9.2e+008	-0.106	0.213	-0.47	1.e+009	0.2

TABLE 8.3.2.18 Structural Steel > Isotropic Elasticity

Temperature C	Young's Modulus Pa	Poisson's Ratio	Bulk Modulus Pa	Shear Modulus Pa
	2.e+011	0.3	1.6667e+011	7.6923e+010

TABLE 8.3.2.19 Structural Steel > Isotropic Relative Permeability

Relative Permeability
10000

TABLE 8.3.2.20 Polyethylene > Constants

Density	950 kg m^-3
Coefficient of Thermal Expansion	2.3e-004 C^-1
Specific Heat	296 J kg^-1 C^-1
Thermal Conductivity	0.28 W m^-1 C^-1

TABLE 8.3.2.21 Polyethylene > Tensile Ultimate Strength

Tensile Ultimate Strength Pa
3.3e+007

TABLE 8.3.2.22 Polyethylene > Isotropic Secant Coefficient of Thermal Expansion

Reference Temperature C
22

TABLE 8.3.2.23 Polyethylene > Isotropic Elasticity

Temperature C	Young's Modulus Pa	Poisson's Ratio	Bulk Modulus Pa	Shear Modulus Pa
	1.1e+009	0.42	2.2917e+009	3.8732e+008

8.3.3 Modelling and Analysis of Various Piezo Fibre Geometries on the Piezoelectric Properties for Energy Scavenging Applications

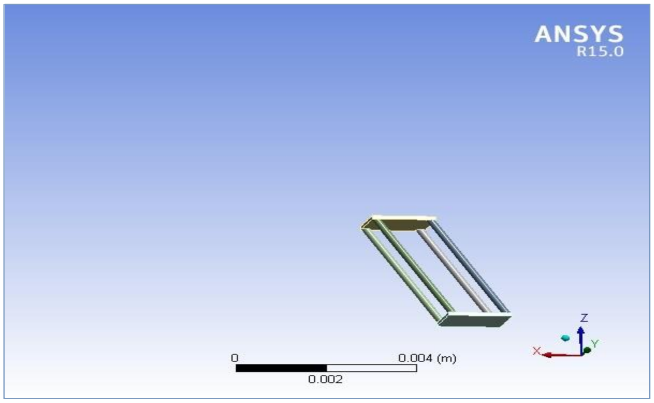

a) Model (A4)
  i) Geometry
    (1) TABLE 8.3.3.1 PVDF Fabric
    (2) TABLE 8.3.3.2 Body Groups
  ii) TABLE 8.3.3.3 Connections
    (1) TABLE 8.3.3.4 Contacts
  iii) Harmonic Response (A5)
    (1) Modal (None)
      (a) TABLE 8.3.3.5 Analysis
      (b) TABLE 8.3.3.6 Initial Conditions
      (c) TABLE 8.3.3.7 Analysis Settings
      (d) TABLE 8.3.3.8 Loads
      (e) TABLE 8.3.3.9 command Snippets
    (2) TABLE 8.3.3.10 Solution
      (a) TABLE 8.3.3.11 Solution Information
b) Material Data
  i) Plate material
    (1) TABLE 8.3.3.12 Contacts density
    (2) TABLE 8.3.3.13 Isotropic Elasticity

TABLE 8.3.3.1 Model (A4) > Geometry

Object Name	Geometry
State	Fully Defined
Definition	
Source	C:\Users\Khan\Desktop\ATC PROJECT\ATC-13 D\SP\PVDF Fabric Parametric Analysis_files\dp0\SYS-3\DM\SYS-3.agdb
Type	DesignModeler
Length Unit	Millimeters
Element Control	Program Controlled
Display Style	Body Color

Bounding Box	
Length X	3.079e-003 m
Length Y	1.4315e-003 m
Length Z	3.0581e-003 m
Properties	
Volume	7.9485e-010 m³
Mass	3.4236e-006 kg
Scale Factor Value	1.
Statistics	
Bodies	6
Active Bodies	6
Nodes	23206
Elements	4432
Mesh Metric	None
Basic Geometry Options	
Parameters	Yes
Parameter Key	DS
Attributes	No
Named Selections	Yes
Named Selection Key	
Material Properties	No
Advanced Geometry Options	
Use Associativity	Yes
Coordinate Systems	No
Reader Mode Saves Updated File	No
Use Instances	Yes
Smart CAD Update	No
Compare Parts On Update	No
Attach File Via Temp File	Yes
Temporary Directory	C:\Users\Imtiaz\AppData\Roaming\Ansys\v150
Analysis Type	3-D
Decompose Disjoint Geometry	Yes
Enclosure and Symmetry Processing	Yes

TABLE 8.3.3.2 Model (A4) > Geometry > Body Groups

Object Name	PVDF Fabric
State	Meshed
Graphics Properties	
Visible	Yes
Definition	
Suppressed	No
Assignment	Multiple Materials

Coordinate System	Multiple Coordinate Systems
Bounding Box	
Length X	3.079e-003 m
Length Y	1.4315e-003 m
Length Z	3.0581e-003 m
Properties	
Volume	7.9485e-010 m³
Mass	3.4236e-006 kg
Centroid X	1.5395e-003 m
Centroid Y	7.1577e-004 m
Centroid Z	1.4265e-003 m
Moment of Inertia Ip1	5.6112e-012 kg·m²
Moment of Inertia Ip2	5.242e-012 kg·m²
Moment of Inertia Ip3	2.0247e-012 kg·m²
Statistics	
Nodes	23206
Elements	4432
Mesh Metric	None

TABLE 8.3.3.3 Model (A4) > Connections

Object Name	Connections
State	Fully Defined
Auto Detection	
Generate Automatic Connection On Refresh	Yes
Transparency	
Enabled	Yes

TABLE 8.3.3.4 Model (A4) > Connections > Contacts

Object Name	Contacts
State	Fully Defined
Definition	
Connection Type	Contact
Scope	
Scoping Method	Geometry Selection
Geometry	All Bodies
Auto Detection	
Tolerance Type	Slider
Tolerance Slider	0.
Tolerance Value	1.1424e-005 m
Use Range	No
Face/Face	Yes
Face/Edge	No

Edge/Edge	No
Priority	Include All
Group By	Bodies
Search Across	Bodies

TABLE 8.3.3.5 Model (A4) > Analysis

Object Name	Harmonic Response (A5)
State	Solved
Definition	
Physics Type	Structural
Analysis Type	Harmonic Response
Solver Target	Mechanical APDL
Options	
Environment Temperature	22. °C
Generate Input Only	No

TABLE 8.3.3.6 Model (A4) > Harmonic Response (A5) > Initial Condition

Object Name	Modal (None)
State	Fully Defined
Definition	
Pre-Stress Environment	None
Modal Environment	None Available

TABLE 8.3.3.7 Model (A4) > Harmonic Response (A5) > Analysis Settings

Object Name	Analysis Settings
State	Fully Defined
Options	
Range Minimum	0. Hz
Range Maximum	2. Hz
Solution Intervals	4
Solution Method	Full
Variational Technology	Program Controlled
Output Controls	
Stress	Yes
Strain	Yes
Nodal Forces	Yes
Calculate Reactions	Yes
General Miscellaneous	Yes
Damping Controls	
Constant Damping Ratio	0.
Stiffness Coefficient Define By	Direct Input
Stiffness Coefficient	0.
Mass Coefficient	0.

Analysis Data Management	
Solver Files Directory	C:\Users\Imtiaz\Desktop\SANIA ANSYS BACKUP\SP\PVDF Fabric Parametric Analysis_files\dp0\SYS-3\MECH\
Future Analysis	None
Scratch Solver Files Directory	
Save MAPDL db	No
Delete Unneeded Files	Yes
Solver Units	Active System
Solver Unit System	mks

TABLE 8.3.3.8 Model (A4) > Harmonic Response (A5) > Loads

Object Name	Displacement	Displacement 2
State	Fully Defined	
Scope		
Scoping Method	Geometry Selection	
Geometry	1 Face	
Definition		
ID (Beta)	330	787
Type	Displacement	
Define By	Components	
Coordinate System	Global Coordinate System	
X Component	0. m	
Y Component	0. m	
Z Component	0. m	2.85e-005 m
Phase Angle	0. °	
Suppressed	No	

TABLE 8.3.3.9 Model (A4) > Harmonic Response (A5) > Command Snippet

Object Name	Commands (APDL)
State	Fully Defined
File	
File Name	X:\My Folders\PhD\ANSYS Computational Work\ANSYS Piezoelectric Analysis\Command Files\Mechanical to APDL Circuit Commands.txt
File Status	File not found
Definition	
Suppressed	No
Target	Mechanical APDL
Input Arguments	

TABLE 8.3.3.10 Model (A4) > Harmonic Response (A5) > Solution

Object Name	Solution (A6)
State	Not Solved
Adaptive Mesh Refinement	

Max Refinement Loops	1.
Refinement Depth	2.
Information	
Status	Solve Required

TABLE 8.3.3.11 Model (A4) > Harmonic Response (A5) > Solution (A6) > Solution Information

Object Name	Solution Information
State	Not Solved
Solution Information	
Solution Output	Solver Output
Newton-Raphson Residuals	0
Update Interval	2.5 s
Display Points	All
FE Connection Visibility	
Activate Visibility	Yes
Display	All FE Connectors
Draw Connections Attached To	All Nodes
Line Color	Connection Type
Visible on Results	No
Line Thickness	Single
Display Type	Lines

TABLE 8.3.3.12 Plate material > Constants Density

Plate Material Constants Density
1150 kg m^-3

TABLE 8.3.3.13 Plate material > Isotropic Elasticity

Temperature C	Young's Modulus Pa	Poisson's Ratio	Bulk Modulus Pa	Shear Modulus Pa
	4.e+009	0.39	6.0606e+009	1.4388e+009

8.3.4 Modelling of cross-linked spacer fibres

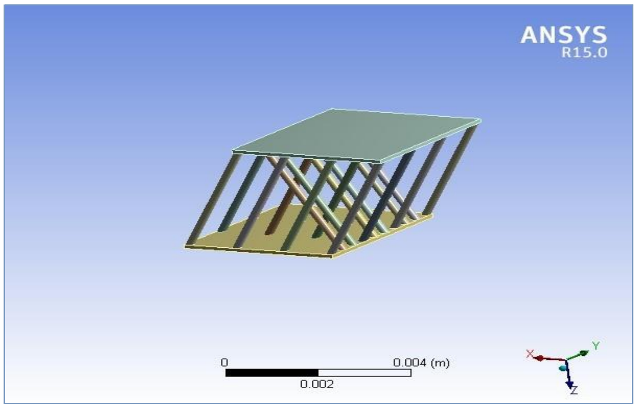

Contents

a) Model (A4)
  i) TABLE 8.3.4.1 Geometry
    (1) TABLE 8.3.4.2 Body groups
    (2) PVDF Fabric
      (a) TABLE 8.3.4.3 Rod Baseline2> Command Snippet
      (b) TABLE 8.3.4.4 Rod Baseline3> Command Snippet
      (c) TABLE 8.3.4.5 Rod Baselin4> Command Snippet
      (d) TABLE 8.3.4.6 Rod Baseline5> Command Snippet
      (e) TABLE 8.3.4.7 Rod Baseline6> Command Snippet
      (f) TABLE 8.3.4.8 Rod Baseline7> Command Snippet
      (g) TABLE 8.3.4.9 Rod Baseline8> Command Snippet
      (h) TABLE 8.3.4.10 Rod Baseline9> Command Snippet
      (i) TABLE 8.3.4.11 Rod Baseline10> Command Snippet
      (j) TABLE 8.3.4.12 Rod Baseline11> Command Snippet
    (3) Parts
      (a) TABLE 8.3.4.13 Rod Baseline1 > Command Snippet
      (b) TABLE 8.3.4.14 Rod Baseline 2> Command Snippet
      (c) TABLE 8.3.4.15 Rod Baseline 3> Command Snippet
      (d) TABLE 8.3.4.16 Rod Baseline 4> Command Snippet
  ii) TABLE 8.3.4.17 Coordinate Systems
    (1) TABLE 8.3.4.18 Coordinate Systems
  iii) TABLE 8.3.4.19 Connections
    (1) TABLE 8.3.4.20 Contacts
    (2) Contact Regions
  iv) TABLE 8.3.4.21 Mesh
    (1) TABLE 8.3.4.22 Mesh Controls
  v) TABLE 8.3.4.23 Named Selections
  vi) Harmonic Response (A5)
    (1) Modal (None)
      (a) TABLE 8.3.4.24 Analysis
      (b) TABLE 8.3.4.25 Initial Conditions

        - (c) TABLE 8.3.4.26 Analysis Settings
        - (d) TABLE 8.3.4.27 Loads
        - (e) TABLE 8.3.4.28 Command Snippet
    - (2) TABLE 8.3.4.29 Solution (A6)
    - (3) TABLE 8.3.4.30 Solution Information
- b) Material Data
  - i) Structural Steel
    - (1) TABLE 8.3.4.31
    - (2) TABLE 8.3.4.32 Isotropic Secant Coefficient of Thermal Expansion
    - (3) TABLE 8.3.4.33 Isotropic Elasticity
  - ii) Plate material
    - (1) TABLE 8.3.4.34 Isotropic Elasticity

TABLE 8.3.4.1 Model (A4) > Geometry

Object Name	Geometry
State	Fully Defined
Definition	
Source	J:\PVDF Fabric Parametric Analysis_files\dp0\SYS-3\DM\SYS-3.agdb
Type	DesignModeler
Length Unit	Millimeters
Element Control	Program Controlled
Display Style	Body Color
Bounding Box	
Length X	5.5331e-003 m
Length Y	3.8856e-003 m
Length Z	3.0581e-003 m
Properties	
Volume	5.1567e-009 m³
Mass	1.9733e-005 kg
Scale Factor Value	1.
Statistics	
Bodies	24
Active Bodies	24
Nodes	149843
Elements	29368
Mesh Metric	None
Basic Geometry Options	
Parameters	Yes
Parameter Key	DS
Attributes	No
Named Selections	Yes
Named Selection Key	
Material Properties	No

Advanced Geometry Options	
Use Associativity	Yes
Coordinate Systems	No
Reader Mode Saves Updated File	No
Use Instances	Yes
Smart CAD Update	No
Compare Parts On Update	No
Attach File Via Temp File	Yes
Temporary Directory	C:\Users\Imtiaz\AppData\Roaming\Ansys\v150
Analysis Type	3-D
Decompose Disjoint Geometry	Yes
Enclosure and Symmetry Processing	Yes

TABLE 8.3.4.2 Model (A4) > Geometry > Body Groups

Object Name	PVDF Fabric
State	Meshed
Graphics Properties	
Visible	Yes
Definition	
Suppressed	No
Assignment	Multiple Materials
Coordinate System	Multiple Coordinate Systems
Bounding Box	
Length X	5.5331e-003 m
Length Y	3.8856e-003 m
Length Z	3.0581e-003 m
Properties	
Volume	4.5948e-009 m^3
Mass	1.5322e-005 kg
Centroid X	2.7665e-003 m
Centroid Y	1.9428e-003 m
Centroid Z	1.4265e-003 m
Moment of Inertia Ip1	3.8402e-011 kg·m^2
Moment of Inertia Ip2	4.7486e-011 kg·m^2
Moment of Inertia Ip3	6.2376e-011 kg·m^2
Statistics	
Nodes	91373
Elements	17512
Mesh Metric	None

TABLE 8.3.4.3 Model (A4) > Geometry > PVDF Fabric > Rod Baseline 2 > Command Snippet

Object Name	Commands (APDL)

State	Fully Defined
File	
File Name	X:\My Folders\PhD\ANSYS Computational Work\ANSYS Piezoelectric Analysis\Command Files\PVDF Properties with Isotropic Model.txt
File Status	File not found
Definition	
Suppressed	No
Target	Mechanical APDL

TABLE 8.3.4.4 Model (A4) > Geometry > PVDF Fabric > Rod Baseline 3 > Command Snippet

Object Name	Commands (APDL)
State	Fully Defined
File	
File Name	X:\My Folders\PhD\ANSYS Computational Work\ANSYS Piezoelectric Analysis\Command Files\PVDF Properties with Isotropic Model.txt
File Status	File not found
Definition	
Suppressed	No
Target	Mechanical APDL

TABLE 8.3.4.5 Model (A4) > Geometry > PVDF Fabric > Rod Baseline 4 > Command Snippet

Object Name	Commands (APDL)
State	Fully Defined
File	
File Name	X:\My Folders\PhD\ANSYS Computational Work\ANSYS Piezoelectric Analysis\Command Files\PVDF Properties with Isotropic Model.txt
File Status	File not found
Definition	
Suppressed	No
Target	Mechanical APDL

TABLE 8.3.4.6 Model (A4) > Geometry > PVDF Fabric > Rod Baseline5 > Command Snippet

Object Name	Commands (APDL)
State	Fully Defined
File	
File Name	
File Status	File not found
Definition	
Suppressed	No
Target	Mechanical APDL
Input Arguments	

TABLE 8.3.4.7 Model (A4) > Geometry > PVDF Fabric > Rod Baseline6 > Command Snippet

Object Name	Commands (APDL)
State	Fully Defined
File	
File Name	
File Status	File not found
Definition	
Suppressed	No
Target	Mechanical APDL

TABLE 8.3.4.8 Model (A4) > Geometry > PVDF Fabric > Rod Baseline7 > Command Snippet

Object Name	Commands (APDL)
State	Fully Defined
File	
File Name	
File Status	File not found
Definition	
Suppressed	No
Target	Mechanical APDL
Input Arguments	

TABLE 8.3.4.9 Model (A4) > Geometry > PVDF Fabric > Rod Baseline 8> Command Snippet

Object Name	Commands (APDL)
State	Fully Defined
File	
File Name	
File Status	File not found
Definition	
Suppressed	No
Target	Mechanical APDL
Input Arguments	

TABLE 8.3.4.10 Model (A4) > Geometry > PVDF Fabric > Rod Baseline 9 > Command Snippet

Object Name	Commands (APDL)
State	Fully Defined
File	
File Name	
File Status	File not found
Definition	
Suppressed	No
Target	Mechanical APDL
Input Arguments	

TABLE 8.3.4.11 Model (A4) > Geometry > PVDF Fabric > Rod Baseline 10> Command Snippet

Object Name	Commands (APDL)
State	Fully Defined
File	
File Name	
File Status	File not found
Definition	
Suppressed	No
Target	Mechanical APDL
Input Arguments	

TABLE 8.3.4.12 Model (A4) > Geometry > PVDF Fabric > Rod Baseline11 > Command Snippet

Object Name	Commands (APDL)
State	Fully Defined
File	
File Name	
File Status	File not found
Definition	
Suppressed	No
Target	Mechanical APDL
Input Arguments	

TABLE 8.3.4.13 Model (A4) > Geometry > Rod Baseline1 > Command Snippet

Object Name	Commands (APDL)
State	Fully Defined
File	
File Name	
File Status	File not found
Definition	
Suppressed	No
Target	Mechanical APDL
Input Arguments	

TABLE 8.3.4.14 Model (A4) > Geometry > Rod Baseline2 > Command Snippet

Object Name	Commands (APDL)
State	Fully Defined
File	
File Name	
File Status	File not found
Definition	
Suppressed	No
Target	Mechanical APDL
Input Arguments	

TABLE 8.3.4.15 Model (A4) > Geometry > Rod Baseline 3> Command Snippet

Object Name	Commands (APDL)
State	Fully Defined
File	
File Name	
File Status	File not found
Definition	
Suppressed	No
Target	Mechanical APDL
Input Arguments	

TABLE 8.3.4.16 Model (A4) > Geometry > Rod Baseline4 > Command Snippet

Object Name	Commands (APDL)
State	Fully Defined
File	
File Name	
File Status	File not found
Definition	
Suppressed	No
Target	Mechanical APDL
Input Arguments	

TABLE 8.3.4.17 Model (A4) > Coordinate Systems > Coordinate System

Object Name	Global Coordinate System	Rod 1 CS	Rod 2 CS	Rod 3 CS	Rod 4 CS	Coordinate System	Coordinate System 2	Coordinate System 3	Coordinate System 4	Coordinate System 5	Coordinate System 6
State	Fully Defined										

Definition Origin

Z Axis Data	[0. 0. 1.]	[0.5 0. 0.86603]	[0.50114 0. 0.86536]	[0.50115 0. 0.86536]

TABLE 8.3.4.18 Model (A4) > Coordinate Systems > Coordinate System

Object Name	Coordinate System 18	Coordinate System 19
State	Fully Defined	
Definition		
Type	Cartesian	
Coordinate System	Program Controlled	
Suppressed	No	
Origin		
Define By	Geometry Selection	
Geometry	Defined	
Origin X	2.5504e-003 m	
Origin Y	9.2029e-004 m	5.1129e-004 m

Origin Z	1.4265e-003 m	
Principal Axis		
Axis	X	
Define By	Fixed Vector	
Orientation About Principal Axis		
Axis	Y	
Define By	Fixed Vector	
Directional Vectors		
X Axis Data	[0.86536 5.8752e-005 0.50115]	
Y Axis Data	[-5.0957e-005 1. -2.9243e-005]	
Z Axis Data	[-0.50115 0. 0.86536]	
Transformations		
Base Configuration	Absolute	
Transformed Configuration	[2.5504e-003 9.2029e-004 1.4265e-003]	[2.5504e-003 5.1129e-004 1.4265e-003]

TABLE 8.3.4.19 Model (A4) > Connections

Object Name	Connections
State	Fully Defined
Auto Detection	
Generate Automatic Connection On Refresh	Yes
Transparency	
Enabled	Yes

TABLE 8.3.4.20 Model (A4) > Connections > Contacts

Object Name	Contacts
State	Fully Defined
Definition	
Connection Type	Contact
Scope	
Scoping Method	Geometry Selection
Geometry	All Bodies
Auto Detection	
Tolerance Type	Slider
Tolerance Slider	0.
Tolerance Value	1.8551e-005 m
Use Range	No
Face/Face	Yes
Face/Edge	No
Edge/Edge	No
Priority	Include All
Group By	Bodies

Search Across	Bodies

TABLE8.3.4.21 Model (A4) > Mesh

Object Name	Mesh
State	Solved
Defaults	
Physics Preference	Mechanical
Relevance	0
Sizing	
Use Advanced Size Function	On: Curvature
Relevance Center	Medium
Initial Size Seed	Active Assembly
Smoothing	Medium
Transition	Fast
Span Angle Center	Coarse
Curvature Normal Angle	Default (70.3950 °)
Min Size	Default (1.8493e-006 m)
Max Face Size	Default (1.8493e-004 m)
Max Size	Default (3.6987e-004 m)
Growth Rate	Default (1.850)
Minimum Edge Length	1.0255e-004 m
Inflation	
Use Automatic Inflation	None
Inflation Option	Smooth Transition
Transition Ratio	0.272
Maximum Layers	5
Growth Rate	1.2
Inflation Algorithm	Pre
View Advanced Options	No
Patch Conforming Options	
Triangle Surface Mesher	Program Controlled
Patch Independent Options	
Topology Checking	Yes
Advanced	
Number of CPUs for Parallel Part Meshing	Program Controlled
Shape Checking	Aggressive Mechanical
Element Midside Nodes	Program Controlled
Straight Sided Elements	No
Number of Retries	0
Extra Retries For Assembly	Yes
Rigid Body Behavior	Dimensionally Reduced
Mesh Morphing	Disabled

Defeaturing	
Pinch Tolerance	Default (1.6644e-006 m)
Generate Pinch on Refresh	No
Automatic Mesh Based Defeaturing	On
Defeaturing Tolerance	Default (9.2467e-007 m)
Statistics	
Nodes	149843
Elements	29368
Mesh Metric	None

TABLE 8.3.4.22 Model (A4) > Mesh > Mesh Controls

Object Name	Sweep Method	Edge Sizing
State	Fully Defined	
Scope		
Scoping Method	Geometry Selection	
Geometry	16 Bodies	44 Edges
Definition		
Suppressed	No	
Method	Sweep	
Element Midside Nodes	Use Global Setting	
Src/Trg Selection	Automatic	
Source	Program Controlled	
Target	Program Controlled	
Free Face Mesh Type	Quad/Tri	
Type	Number of Divisions	
Sweep Num Divs	35	
Sweep Bias Type	No Bias	
Element Option	Solid	
Constrain Boundary	No	
Number of Divisions		15
Behavior		Hard
Bias Type		No Bias

TABLE 8.3.4.23 Model (A4) > Named Selections > Named Selections

Object Name	terminal1	terminal2	Selection
State	Fully Defined		
Scope			
Scoping Method	Geometry Selection		
Geometry	16 Faces		1 Face
Definition			
Send to Solver	Yes		
Visible	Yes		

Program Controlled Inflation	Exclude	
Statistics		
Type	Manual	
Total Selection	16 Faces	1 Face
Suppressed	0	
Used by Mesh Worksheet	No	

TABLE 8.3.4.24 Model (A4) > Analysis

Object Name	Harmonic Response (A5)
State	Solved
Definition	
Physics Type	Structural
Analysis Type	Harmonic Response
Solver Target	Mechanical APDL
Options	
Environment Temperature	22. °C
Generate Input Only	No

TABLE 8.3.4.25 Model (A4) > Harmonic Response (A5) > Initial Condition

Object Name	Modal (None)
State	Fully Defined
Definition	
Pre-Stress Environment	None
Modal Environment	None Available

TABLE 8.3.4.26 Model (A4) > Harmonic Response (A5) > Analysis Settings

Object Name	Analysis Settings
State	Fully Defined
Options	
Range Minimum	0. Hz
Range Maximum	2. Hz
Solution Intervals	4
Solution Method	Full
Variational Technology	Program Controlled
Output Controls	
Stress	Yes
Strain	Yes
Nodal Forces	Yes
Calculate Reactions	Yes
General Miscellaneous	Yes
Damping Controls	
Constant Damping Ratio	0.
Stiffness Coefficient Define By	Direct Input

Stiffness Coefficient	0.
Mass Coefficient	0.
Analysis Data Management	
Solver Files Directory	J:\PVDF Fabric Parametric Analysis_files\dp0\SYS-3\MECH\
Future Analysis	None
Scratch Solver Files Directory	
Save MAPDL db	No
Delete Unneeded Files	Yes
Solver Units	Active System
Solver Unit System	mks

TABLE 8.3.4.27 Model (A4) > Harmonic Response (A5) > Loads

Object Name	Displacement	Displacement 2
State	Fully Defined	

TABLE 8.3.4.28 Model (A4) > Harmonic Response (A5) > Command Snippet

Object Name	Commands (APDL)
State	Fully Defined
File	
File Name	X:\My Folders\PhD\ANSYS Computational Work\ANSYS Piezoelectric Analysis\Command Files\Mechanical to APDL Circuit Commands.txt
File Status	File not found
Definition	
Suppressed	No
Target	Mechanical APDL
Input Arguments	

TABLE 8.3.4.29 Model (A4) > Harmonic Response (A5) > Solution

Object Name	Solution (A6)
State	Not Solved
Adaptive Mesh Refinement	
Max Refinement Loops	1.
Refinement Depth	2.
Information	
Status	Solve Required

TABLE 8.3.4.30 Model (A4) > Harmonic Response (A5) > Solution (A6) > Solution Information

Object Name	Solution Information
State	Not Solved
Solution Information	
Solution Output	Solver Output

Newton-Raphson Residuals	0
Update Interval	2.5 s
Display Points	All
FE Connection Visibility	
Activate Visibility	Yes
Display	All FE Connectors
Draw Connections Attached To	All Nodes
Line Color	Connection Type
Visible on Results	No
Line Thickness	Single
Display Type	Lines

TABLE 8.3.4.31 Structural Steel > Constants

Density	7850 kg m^-3
Coefficient of Thermal Expansion	1.2e-005 C^-1
Specific Heat	434 J kg^-1 C^-1
Thermal Conductivity	60.5 W m^-1 C^-1
Resistivity	1.7e-007 ohm m

TABLE8.3.4.32 Structural Steel > Isotropic Secant Coefficient of Thermal Expansion

Reference Temperature C
22

TABLE 8.3.4.33 Structural Steel > Isotropic Elasticity

Temperature C	Young's Modulus Pa	Poisson's Ratio	Bulk Modulus Pa	Shear Modulus Pa
	2.e+011	0.3	1.6667e+011	7.6923e+010

TABLE 8.3.4.34 Plate material > Isotropic Elasticity

Temperature C	Young's Modulus Pa	Poisson's Ratio	Bulk Modulus Pa	Shear Modulus Pa
	4.e+009	0.39	6.0606e+009	1.4388e+009